

Probabilistic design of support structures for offshore wind turbines by means of non-Gaussian spectral analysis

Von der Fakultät für Bauingenieurwesen und Geodäsie
der Gottfried Wilhelm Leibniz Universität Hannover
zur Erlangung des akademischen Grades

Doktor der Ingenieurwissenschaften
– Dr.-Ing. –

genehmigte Dissertation
von

Dipl.-Ing. Sebastian Kelma

Promotionskommission

Referent: Prof. Dr.-Ing. Peter Schaumann
Korreferent: Prof. Dr.-Ing. Michael Beer
Vorsitzender: Prof. Dr.-Ing. Andreas Reuter

Tag der Promotion: 11. August 2023

Acknowledgements

This thesis results from my occupation as research associate at the Institute for Steel Construction of the Gottfried Wilhelm Leibniz Universität Hannover. The basic ideas arose during my research activities within the joint research projects “Probabilistische Sicherheitsbewertung von Offshore-Windenergieanlagen” and “GIGAWIND life”, which were financially supported by the Lower Saxony Ministry of Science and Culture and the Federal Ministry for Economic Affairs and Energy, respectively.

First of all, I express my gratitude to Prof. Dr.-Ing. Peter Schaumann for the possibility to learn and carry out research at the Institute for Steel Construction as well as for his guidance, patience, and constant motivation through the many years. The trust in my professional skills and the freedom to work on the topics of my thesis contributed significantly to the finalisation of my dissertation. I like to thank Prof. Dr.-Ing. Michael Beer for being the second examiner, for his interest, as well as for the valuable comments and discussions. Furthermore, I acknowledge Prof. Dr.-Ing. Andreas Reuter for chairing the doctoral committee and supporting the examination procedure.

I like to thank the colleagues at the Institute for Steel Construction for the pleasant and productive working atmosphere. I always enjoyed the fruitful and enjoyable discussions and talks, may they have been of work-related, scientific, or non-scientific nature. Special thanks go to Dr. rer. nat. Florian Kelma, Jan Kulikowski, and Joshua Possek, who proofread parts of the thesis and provided many helpful comments and proposals for improvements.

Last but not least, I thank my friends and especially my family. Thank you for all the support and encouragements which you gave to me in all the years and in so many various ways.

Danke für Euren Beitrag zu dieser Arbeit.

Sebastian Kelma

Abstract

Offshore wind energy is of special importance in order to meet the ambitious goals to produce climate-neutral energy. Therefore, an accelerated installation of offshore wind turbines is required. The design is to be achieved with respect to standards and guidelines. Especially probabilistic design methods allow an accurate and economic structural design.

Not only the environmental conditions vary during the lifetime, but the short-term loads are also subject of random scattering. For the design of offshore wind turbines, the required load simulations are usually carried out in time domain. In comparison, it is less time-consuming to obtain loads by means of frequency-domain analysis. This is very beneficial for the probabilistic design which requires significantly more load simulations in time domain. However, non-linearities and time-variant behaviour of offshore wind turbines cannot be represented well during the load simulation in frequency domain.

Extreme loads and fatigue loads can be calculated by means of frequency-domain analysis. The determination of the distribution functions of extreme values is well established on a theoretical background. As for the fatigue design, different empirical models exist which describe the distribution function of fatigue loads on the basis of frequency-domain analysis. In this thesis, a new model is introduced which leads to more accurate results.

Since frequency-domain analysis is not always suitable, the transformation of signals given in frequency domain is required to generate respective random time series. As for the design of offshore wind turbines, only limited recommendations are stated in standards on how to carry out this transformation. Detailed analysis shows that accurate results with respect to wave-induced loads are also obtained for coarser discretisation of spectra. The resulting loads and their statistical properties are still accurate, while the numerical effort can be reduced in comparison to the stated recommendations.

On the basis of theoretical findings, time series from load simulations of offshore wind turbines are analysed regarding their spectral properties. Investigations are carried out to evaluate the agreement between the extreme load and fatigue loads which are either simulated or calculated on the basis of the spectral properties. It is also shown that currents within sea states lead to increased fatigue loads.

Key words: Offshore wind energy, load simulation, frequency-domain analysis, fatigue, probabilistic design

Kurzfassung

Offshore-Windenergie ist von besonderer Bedeutung, um die ehrgeizigen Ziele der klimaneutralen Energieerzeugung zu erreichen. Diese machen den beschleunigten Ausbau von Offshore-Windenergieanlagen erforderlich. Die Strukturauslegung erfolgt unter der Berücksichtigung von Normen und Richtlinien. Hier ermöglichen probabilistische Bemessungsmethoden eine detaillierte und wirtschaftliche Strukturauslegung.

Nicht nur die Umweltbedingungen streuen während der Lebensdauer, sondern auch die Belastungen bei konstanten Umweltbedingungen unterliegen zufälligen Streuungen. Für den Entwurf von Offshore-Windenergieanlagen werden die erforderlichen Lastsimulationen meist im Zeitbereich durchgeführt. Im Vergleich dazu ist die Ermittlung der Lasten im Frequenzbereich weniger zeitaufwändig. Dies ist sehr vorteilhaft für den probabilistischen Entwurf, der deutlich mehr Lastsimulationen im Zeitbereich erfordert. Allerdings können Nichtlinearitäten und das sich im Kurzzeitbereich ändernde Strukturverhalten von Offshore-Windenergieanlagen bei der Lastsimulation im Frequenzbereich nicht gut dargestellt werden.

Extremlasten und Ermüdungslasten können mit Hilfe der Frequenzbereichsanalyse berechnet werden. Die Bestimmung der Verteilungsfunktionen von Extremwerten basiert auf theoretischen Grundlagen und ist schon bekannt. Für die Ermüdungsauslegung gibt es verschiedene empirische Modelle, die die Verteilungsfunktion von Ermüdungslasten auf der Grundlage der Frequenzbereichsanalyse beschreiben. Es wird ein neues Modell vorgestellt, das zu genaueren Ergebnissen führt.

Für den Fall, dass Lastsimulationen im Frequenzbereich nicht möglich sind, ist eine Übertragung der im Frequenzbereich gegebenen Signale erforderlich, um zufällige Zeitreihen zu erzeugen. Für die Auslegung von Offshore-Windenergieanlagen gibt es in den Normen nahezu keine Empfehlungen, wie diese Übertragung durchgeführt werden soll. Eine detaillierte Analyse zeigt, dass auch bei gröberer Diskretisierung der Spektren genaue Ergebnisse von Wellenlasten erzielt werden. Die resultierenden Lasten und ihre statistischen Eigenschaften haben eine hinreichende Genauigkeit, während der numerische Aufwand im Vergleich zu den angegebenen Empfehlungen reduziert ist.

Auf der Grundlage der theoretischen Erkenntnisse werden Zeitreihen aus Lastsimulationen von Offshore-Windenergieanlagen hinsichtlich ihrer spektralen Eigenschaften analysiert. Es werden Untersuchungen durchgeführt, um die Übereinstimmung zwischen den Extremlasten und den Ermüdungslasten zu ermitteln, die entweder aus Zeitreihen bestimmt oder auf Basis der spektralen Eigenschaften berechnet sind. Es wird zudem gezeigt, dass Strömungen im Seegang zu erhöhten Ermüdungsbelastungen führen.

Schlagwörter: Offshore-Windenergie, Lastsimulation, Frequenzbereichsanalyse, Ermüdung, probabilistische Strukturauslegung

Table of contents

Acknowledgements	i
Abstract	iii
Kurzfassung	v
1 Introduction	1
1.1 Motivation	1
1.2 Objective	4
1.3 Structure of the thesis	5
2 Analysis of signals	7
2.1 Analysis of random signals in time- and frequency domain	7
2.1.1 Fourier analysis	7
2.1.2 Characteristics of random signals in time- and frequency domain	11
2.2 Stochastic analysis of random variables and random signals	14
2.2.1 General definitions	15
2.2.2 Statistical methods for parameter estimation and statistical testing	16
2.2.3 Extreme value theory	18
2.2.4 Peak-over-threshold method	20
2.2.5 Relationship between generalized extreme value distribution and generalised Pareto distribution	21
3 Load acting on offshore wind turbines	23
3.1 Wind-induced loads	23
3.1.1 Wind field	23
3.1.2 Wind-induced loads on rotor blades	25
3.2 Wave-induced loads	25
3.2.1 Regular waves	27
3.2.2 Irregular waves	29
3.2.3 Currents	31
3.2.4 Calculation of wave-induced loads	32
3.2.5 Wave-induced loads in frequency domain	32
3.2.6 Load regimes of wave-induced drag and inertia loads	37
3.3 Long-term distribution of environmental data	40
3.3.1 Seasonal dependence of metocean data	41
3.3.2 Data availability	42
3.3.3 Long-term statistics	43

3.3.4	Extreme metocean values	44
3.4	Environmental-related structural alterations of offshore wind turbines .	45
3.4.1	Marine growth	45
3.4.2	Soil and scour development	47
3.4.3	Corrosion	49
3.4.4	Deterioration of structural components	51
3.5	Findings	52
4	Load simulation of offshore wind turbines	53
4.1	Design of offshore wind turbines	53
4.1.1	Safety concepts	54
4.1.2	Limit states	55
4.2	Load characterisation and load cases for offshore wind turbines	55
4.2.1	Effect of the rotor	56
4.2.2	Load events for offshore wind turbines	57
4.2.3	Standardisation of load simulation for offshore wind turbines . .	59
4.3	Load simulation of offshore wind turbines	64
4.3.1	Modal condensation	64
4.3.2	Load simulation in time domain	65
4.3.3	Load simulation in frequency domain	67
4.4	Findings	69
5	Estimation of extreme loads in frequency domain	71
5.1	Structural design against extreme loads	71
5.1.1	Effect of extreme loads on structural members	73
5.1.2	Structural design verification against extreme loads	73
5.2	Determination of extreme values in frequency domain	75
5.2.1	Extreme values within Gaussian signals	75
5.2.2	Comparison between results obtained from time simulations and from power spectral densities	76
5.2.3	Extreme values within non-Gaussian signals	78
5.3	Extreme values within combined signals	79
5.3.1	Extreme loads depending on one load type	79
5.3.2	Extreme loads within combination of different signals	80
5.4	Findings	80
6	Fatigue design in frequency domain	83
6.1	Structural design against fatigue loads	83
6.1.1	Effect of load cycles on structural members	85
6.1.2	Methods for counting of fatigue loads	85
6.1.3	Calculation of fatigue damage	87
6.1.4	Structural design verification against fatigue failure	88
6.2	Calculation of fatigue in frequency domain	92
6.2.1	Distribution of fatigue loads in frequency domain	92
6.2.2	Fatigue damage in frequency domain	96
6.3	Derivation of distribution functions for fatigue loads	97
6.3.1	Development of a new distribution function of fatigue loads based on power spectral densities	99

6.3.2	Goodness-of-fit of theoretical distribution functions for fatigue loads in frequency domain	106
6.4	Fatigue loads of non-Gaussian signals	111
6.5	Findings	113
7	Techniques for inverse Fourier transformation	115
7.1	Techniques for inverse Fourier transformation	115
7.1.1	Derivation of amplitudes	116
7.1.2	Randomness in time domain	116
7.1.3	Number of wavelets	117
7.1.4	Derivation of wave frequencies	117
7.2	Comparison of different approaches of inverse Fourier transformation	122
7.2.1	Impact on Gaussianity of time series	123
7.2.2	Impact on wave grouping	125
7.2.3	Impact on statistical properties of maximum loads acting on a monopile foundation	127
7.2.4	Impact on statistical properties of fatigue loads	129
7.3	Findings	135
8	Studies on analyses of load simulations for offshore wind turbines	137
8.1	Spectral properties from load simulations in time domain	137
8.1.1	Load simulations	137
8.1.2	Gaussianity of the signal	138
8.1.3	Power spectral densities	140
8.1.4	Spectral properties	141
8.1.5	Distribution functions of extreme loads	143
8.1.6	Distribution functions of fatigue loads	145
8.1.7	Conclusion	146
8.2	Impact of currents on the simulation of wave-induced loads	147
8.2.1	Load simulations	147
8.2.2	Impact of currents on power spectral densities of loads	148
8.2.3	Impact of currents on fatigue loads	150
8.2.4	Conclusion	151
9	Summary and outlook	153
9.1	Summary	153
9.2	Outlook	155
	Bibliography	169
	List of symbols	171
	List of Figures	175
	List of Tables	181
	A1 Reference design basis: environmental data	183
	A2 Removal of corrosion products from small steel specimens	187

A3	Fourier series of relevant functions	195
A4	Power spectral densities applied for analysis of distribution functions of fatigue loads	199

1 Introduction

1.1 Motivation

The environmental awareness of the climate change led to international and national agreements, aiming to reduce the emission of greenhouse gases. In order to achieve this aim, the further development of and expansion of renewable-energy supply devices for the electrical power production is substantial. For instance, the current version of the German Renewable Energy Sources Act (EEG, 2023) contains statutory targets of a share of renewable energy in gross final electricity consumption of at least 80% in 2030. Besides the further installation of renewable-energy supply devices onshore, the nominal power capacity of offshore wind turbines shall be raised to 30 *GW* in 2030 and to 40 *GW* in 2045 (WindSeeG, 2023). Since the erection of the first German offshore wind park alpha ventus in 2010 and until the end of 2022, offshore wind turbines with a cumulative electrical power of almost 8.1 *GW* were installed in the German North Sea and Baltic Sea (Deutsche WindGuard GmbH, 2023). In order to meet the targets stated by EEG (2023), both the technical development and the economical competitiveness of offshore wind turbines are essential.

Due to economical and technical reasons, bottom-fixed offshore wind turbines are preferred for water depth of up to 50 *m*. Monopiles and jackets are the preferred substructures for offshore wind turbines (Seidel, 2014a), which are shown in Fig. 1.1. The stated definitions of the components are in accordance with those of BSH (2015). Other types of substructures are tripods and gravity-based foundations. Nowadays these types are seldomly used as substructure for offshore wind turbines. Floating offshore wind turbines are considered as more economic for water depths greater than 50 *m*.

Monopile substructures, as shown in Fig. 1.1 (left) are steel tubes with diameters greater than approximately 5 *m*, which are driven into the seabed. The transition piece is connected to the monopile either by a grouted connection or by a ring-flange connection. Jacket substructures, shown in Fig. 1.1 (right) are lattice-type structures consisting of steel pipes which are connected via welded tubular joints. They are connected to foundation piles driven into the seabed via grouted joints. The transition piece is usually part of the jacket substructure. Instead of driven piles, so-called suction buckets can also be used for the connection of the substructures to the soil. Appurtenances such as boat landings for accessibility of the offshore wind turbine and J-tubes, containing and protecting power cables, are attached to the substructure.

The tower, consisting of tower segments with a height of about 30 *m*, is mounted on top of the transition piece. On top of the tower, the rotor-nacelle assembly consisting of the nacelle and the rotor with usually three rotor blades is installed. The connections between the transition piece, the tower segments, and the nacelle are usually connected

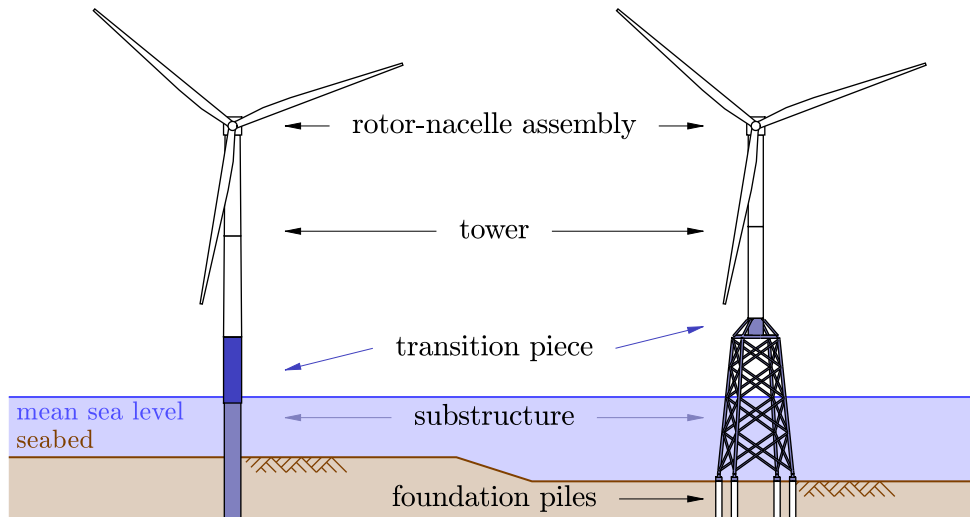


Figure 1.1: Offshore wind turbines with monopile substructure (left) and jacket substructure (right)

via ring-flange connections. The assembly of foundation piles, substructure, and tower is referred to as support structure.

Compared to onshore sites, steadier and less-turbulent wind conditions are found offshore, which is more favourable for the production of energy. However, the logistic, transport, installation, and maintenance of offshore wind turbines are more challenging and therefore require greater expenses. The harsh offshore conditions are also decisive for the structural design as the offshore wind turbines have to withstand the severe conditions of the sea states. Exemplarily, offshore wind turbines of the offshore wind park alpha ventus at various dates are shown in Fig. 1.2 to illustrate the different weather conditions which offshore wind turbines have to face.



Figure 1.2: Offshore wind turbines of the offshore wind park alpha ventus ©FuE-Zentrum FH Kiel GmbH

Offshore wind turbines are designed for a planned lifetime of at least 25 years. Due to the loads resulting from wind, wave, and operation of the offshore wind turbine, the support structures of offshore wind turbines are subjected to up to several hundreds of millions of load cycles. For the structural design, the structural members of offshore wind turbines are to be designed such that neither extreme loads or extreme deformations nor fatigue loads exceed the respective resistance. In order to determine the extreme loads and fatigue loads, load simulations in time domain are to be carried out. The load simulations are based on design load cases which are defined in respective standards (IEC 61400-3-1, 2019; DNV-ST-0437, 2016). Especially the design load cases covering the fatigue design require several tens of thousands of load simulations to cover the various combinations of different wind velocities, wind directions, sea-state conditions, and wave directions which potentially are to occur during the considered lifetime. This high number of simulations requires a very high computational effort.

Usually, the semi-probabilistic approach is applied for the structural design of offshore wind turbines. Here, inaccuracies of loads, material properties, and modelling are covered by design values which include partial safety factors. The probabilistic design allows a more accurate design and thus a more economic design (Hübler, 2019). Therefore, probabilistic models are to be defined which describe the random properties. In general, the probabilistic models to be considered can be divided into the following three classes:

- 1 *Structural and structural-dynamic properties* The structural properties cover the structure itself, here the offshore wind turbine, as well as its structural-dynamic interaction with the environment, e.g. the soil-structure interaction. Changes of the structural-dynamic properties of the offshore wind turbine during its lifetime include added masses, e.g. marine growth, and variable stiffness of the structural model. For example, stiffness changes occur due to scour development at the foundation piles. Examples of structural properties to be modelled are materials as well as soil and soil-structure interaction (Schmoor, 2017).
- 2 *Weather conditions* The describing parameters of wind fields and sea states are considered as constant for certain time spans. They change over the course of time. The occurrence frequencies of the different parameters to describe the weather conditions are usually summarised in scatter tables which show the long-term statistics as well as the combination occurrence frequencies of the different parameters.
- 3 *Random loads* The time series of wind fields and sea states for certain values of the describing parameters are not constant, but they are random processes, while the general parameters such as mean wind velocity or the severity of the sea state are constant within a specific weather window. The resulting load time series acting on an offshore wind turbine are also random processes, from which the extreme loads and fatigue loads are to be determined for the structural design.

The different probabilistic models within classes are to be simulated for the probabilistic design. As for the class 3, statistics of loads only can be derived from simulation results with the same structural properties and the same weather conditions. Therefore, the time series must be of sufficient length such that the decisive distribution functions of extreme loads and fatigue loads can be derived accurately from the signals. For

simulation in time domain, the number of required load simulations is enormous and leads to a strongly increased computational effort.

In comparison to time-domain simulations, load simulations in frequency domain require significantly less computational effort. Frequency-domain analysis is especially suitable for the calculation of the structural-dynamic response due to random Gaussian loads. So-called spectra of the structural-dynamic response are determined which describe the signal as superposition of sinusoidal wavelets with different wave energy and wave frequency. The distribution functions of extreme loads and of fatigue loads can be obtained on the basis of these resulting spectra. While several time series or one long time series is required for one set of certain structural properties and weather conditions, only one load simulation in frequency domain is required in order to determine the probabilistic models.

Frequency-domain analysis of offshore structures is well established in the offshore industry for oil- and gas applications (Barltrop and Adams, 1991). Linearised systems of equations are to be solved in frequency domain. Structural non-linearities, such as soil-structure interaction, cannot be modelled accurately. As for offshore wind turbines, the behaviour of the controller and the resulting wind-induced loads acting on the rotor are non-linear, too. The load assumptions are simplified. Up to now, load simulation in frequency domain is only applied for the very early design stages for a rough estimation of fatigue loads (Seidel et al., 2016).

1.2 Objective

The work carried out within this thesis aims to develop and improve methods to estimate the distribution functions of extreme loads and fatigue loads on the basis of frequency-domain analyses. Existing methods are only suitable for random signals which follow a Gaussian distribution. It is shortly analysed how the respective probabilistic models of extreme loads and of fatigue loads can be adjusted to random signals which are not Gaussian-distributed. Within the context of probabilistic design, variations of structural-dynamic behaviour over the lifetime of offshore wind turbines as well as the long-term weather conditions which offshore wind turbines have to face are also described.

It is not possible to carry out the load simulation of offshore wind turbines in frequency domain. Hence, simulations in time domain are required, while the random loading acting on the structural model is usually obtained via inverse Fourier transformation of signals provided in frequency domain. Only limited practical recommendation for the transformation of signals in frequency domain to time domain are provided in standards and guidelines. Hence, an extensive study is carried out to obtain suggestions on an accurate yet time-effective transformation. Due to the importance of extreme loads and fatigue loads for the structure design of offshore wind turbines, the transformation shall not effect the distribution function of these loads.

1.3 Structure of the thesis

Following this introduction, the basics of the analyses of signals in time- and frequency domain are presented in Chapter 2. Methods of stochastic analysis are described. A special emphasis is put on the statistical description of very high, rarely occurring values within signals.

Loads acting on offshore wind turbines are described in Chapter 3. Besides the meteorological and oceanographic conditions as well as their long-term statistics, the impact of structural alterations occurring during the lifetime of offshore wind turbines are shortly discussed. As continuation, Chapter 4 presents the methodologies of structural design and the load simulation of offshore wind turbines. Simulations in time domain and frequency domain are described for the load simulations.

The approaches to determine the extreme loads and fatigue loads on basis of load simulation in frequency domain are shown in the following chapters. Chapter 5 shortly presents the stochastic description of extreme loads in frequency domain. Fatigue loads in frequency domain are discussed in Chapter 6. A new approach to determine the distribution function of fatigue loads on the basis of frequency-domain analysis is introduced. It is compared to existing approaches. Both chapters also cover how non-Gaussian signals are to be handled.

Existing approaches to transfer signals presented in frequency domain into time domain are discussed in Chapter 7. Recommendations are stated for an efficient and appropriate transformation.

Studies of the load simulation of offshore wind turbines are carried out in Chapter 8. Different methods to extract spectral properties from time series and their effect on extreme and fatigue loads are discussed. Additionally, the impact of currents on fatigue loads is analysed.

The analyses performed within this thesis and the derived results are summarised in Chapter 9. Additionally, an outlook on possible future investigations is given.

2 Analysis of signals

Loads acting on offshore wind turbines and their structural responses vary in time. It is sufficient to model the behaviour of the respective time series as random or stochastic. General statistical information such as mean value, distribution type as well as minimum value, maximum value, and peak values can be extracted from given time series. Such information allows the structural design as well as further detailed analysis of the obtained data. An exact estimation of these statistical properties mentioned is almost impossible due to the stochastic nature of the time series. Especially the stochastic evaluation of the very high values and of the extreme values which are of special importance for the structural design requires special attention, but it is prone to uncertainties due to the commonly limited data set.

Random signals are presented as time series in time domain and as spectra in frequency domain, respectively. Considering the time series as superposition of sinusoidal wavelets, the spectra contain the information of these wavelets. Random time series which possess the same constant characteristics can be represented by one spectrum. Randomness of the time series is neglected in spectral representation of the signal.

In the following, basics of the description of time series in frequency domain as well as the basics of statistical analysis are introduced to the reader. The analysis of extreme values and the analysis of peak values for the determination of fatigue loads in frequency domain are described in detail in Chapter 5 and Chapter 6, respectively.

The signals mentioned in the following are described as time-dependent. The following relationships are also valid for spatial descriptions.

2.1 Analysis of random signals in time- and frequency domain

A random process is considered as stationary when its statistical parameters remain constant for every realisation and for a certain duration. For example, sea states are assumed to be stationary for a duration of three hours up to six hours (DNV-ST-0437, 2016). The characteristics of stationary processes and their analyses are described in the following. Here, it is distinguished between random processes in time domain and random processes in frequency domain.

2.1.1 Fourier analysis

Signals can be represented in time domain as well as in frequency domain. It is possible to transform a signal from time domain in frequency domain, and vice versa. This is referred to as Fourier transformation. Basics of the Fourier analysis are described in the

following. Detailed information on Fourier analysis is to be found in general textbooks such as Butz (2011) and Puente León et al. (2011).

Fourier series represent a signal as the superposition of single sinusoidal wavelets. They describe both periodically repeating signals as well as random signals, which are non-periodic. The Fourier series of a signal $g(t)$ can be stated in two ways, while each of these wavelets is defined by its wave frequency and amplitude,

$$g(t) = a_0 + \sum_{n=1}^N a_n \cdot \cos(\omega_n \cdot t + \varphi_n) \quad (2.1)$$

$$g(t) = a_0 + \sum_{n=1}^N a_{c,n} \cdot \cos(\omega_n \cdot t) + a_{s,n} \cdot \sin(\omega_n \cdot t), \quad (2.2)$$

with amplitudes $a_{c,n}$ and $a_{s,n}$, magnitude a_n , wave frequency ω_n , and phase angle φ_n associated to the sinusoidal wavelet n . The wave energy of a wavelet is calculated as $\frac{1}{2} \cdot a_n^2$. The wave frequencies are positive. a_0 denotes the mean value of the signal. The magnitudes $a_n = \sqrt{a_{c,n}^2 + a_{s,n}^2}$ and the phase angles $\varphi_n = \arctan(a_{s,n}/a_{c,n})$ according to Eq. (2.1) are obtained by combining the trigonometric terms with equal wave frequencies as given in Eq. (2.2). The coefficients $a_{c,n}$ and $a_{s,n}$ for each frequency ω_n with $\omega_n > 0$ are determined on the basis of the signal $g(t)$,

$$\begin{aligned} a_0 &= \frac{1}{T} \cdot \int_0^T g(t) \cdot dt \\ a_{c,n} &= \frac{2}{T} \cdot \int_0^T g(t) \cdot \cos(\omega_n \cdot t) \cdot dt \\ a_{s,n} &= \frac{2}{T} \cdot \int_0^T g(t) \cdot \sin(\omega_n \cdot t) \cdot dt, \end{aligned} \quad (2.3)$$

where T is the considered length. It is set as the period for periodic signals. For random non-periodic signals, the value is to be set sufficiently high. Eq. (2.3) is valid for non-negative wave frequencies in Eqs. (2.1) and (2.2). Otherwise, the Fourier coefficients for wave frequencies not equal zero are half the value as given in Eq. (2.3). The decomposition of a signal into the associated frequencies is referred to as Fourier transformation.

Power spectral densities

The amplitudes and magnitudes of the Fourier series are usually presented in so-called amplitude spectra. Here, the amplitudes are plotted against the associated wave frequencies. Similar to amplitude spectra, the wave energy of each wavelet can be plotted against the associated wave frequencies.

The presentation of the wave energy as power spectral density is especially convenient for random signals which consist of wavelets with frequencies over a continuous range. Power spectral densities represent the density of wave energy with respect to wave frequency, with the unit of wave energy per wave frequency. The density of wave energy is calculated as the ratio of the wave energy within a specific range of wave frequencies and this particular range.

Usually, the wavelets are considered as independent of the other wavelets. Hence, only the wave energies or the magnitudes of the wavelets are presented in spectra, but the information on phase angles is neglected. Information on potentially existing dependencies between specific wavelets is lost due to the presentation of signals as power spectral densities. However, it follows implicitly from this assumption that the signal follows a Gaussian distribution, as it can be derived from e.g. Rice (1944). The non-Gaussianity of signals is lost by the presentation as power spectral densities.

Fourier series for complex numbers

For completeness, the Fourier series is stated below for complex numbers,

$$g(t) = c_0 + \sum_{n=1}^N c_n \cdot \exp(i \cdot \omega_n \cdot t), \quad (2.4)$$

$$c_n = \frac{1}{T} \cdot \int_0^T g(t) \cdot \exp(-i \cdot \omega_n \cdot t) \cdot dt, \quad (2.5)$$

with the imaginary unit i . Here, the Fourier series and the Fourier coefficients are defined for wave frequencies with both positive and negative values, ω_n with $\omega_n \in \mathbb{R}$. The wave energy of one wavelet is half the squared norm of the complex Fourier coefficient, $\frac{1}{2} \cdot \|c_n\|^2$.

Discrete Fourier analysis

In engineering, time series are often obtained from experimental measurements or numerical simulations. They usually do not exist as a continuous function in time but as a discrete signal with values associated to time steps. The time-step width, which is the difference between two consecutive time steps, may vary, but it usually is kept constant. Additionally, measured time series have a finite length.

Fourier analysis and the determination of Fourier coefficients are obtained by means of numerical integration of Eq. (2.3) or Eq. (2.5), respectively. The facts that measured time series are of limited length and they are discrete signals may lead to corruption of the Fourier analysis and thus to inaccurate Fourier coefficients. These effects on the Fourier analysis of discrete, finite time series are known as aliasing effect and spectral leakage, which are shortly explained in the following.

Aliasing describes the effect that the magnitude of a wavelet with a period less than twice the time-step width is also erroneously associated to other wavelets when carrying out a Fourier analysis. The value of half of the reciprocal of the time-step width is called Nyquist frequency. The aliasing effect occurs when the time series contains wavelets with frequencies greater than the Nyquist frequency. It also occurs when the Nyquist-Shannon sampling theorem is violated. The Nyquist-Shannon sampling theorem states that the sampling frequency shall be not less than the Nyquist frequency. Considering a sinusoidal wave with a frequency f which is sampled with a frequency f_s smaller than the Nyquist frequency, aliases with frequencies of $f + z \cdot f_s$, $z \in \mathbb{Z}$ are found, each with the same magnitude as the original wave. Exemplarily, the aliasing effect is visualised in Fig. 2.1. Two aliases (grey lines) of the original sinusoidal wave (black line) are shown,

with all sinusoidal waves matching the values of the sampling rate (circles). Here, a sinusoidal wave with a frequency of 0.8 Hz is sampled with a sampling rate of 1 Hz . Two aliases with frequencies of 0.2 Hz and 1.8 Hz are shown.

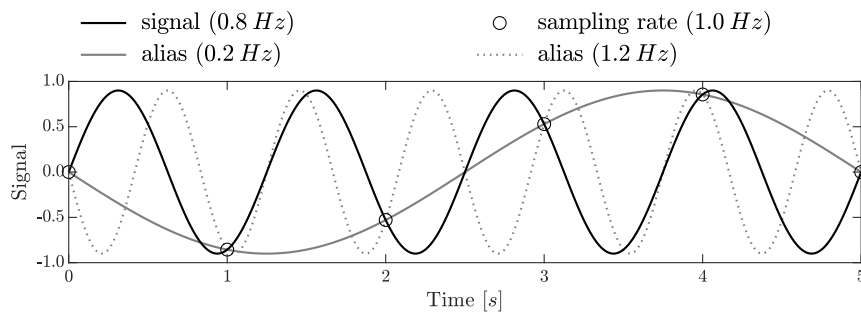


Figure 2.1: Aliasing effect of a sinusoidal wave

Prominent examples for the aliasing effect are fast rotating objects such as tires of moving vehicles or rotors of helicopters in motion pictures. These rotating objects seem to rotate with a lower speed, stand still, or even rotate backwards in case that the real rotational speed of the object is greater than half of the rate of recorded pictures per seconds. Anti-aliasing techniques exist which allow to minimize the aliasing effect. Further information on the aliasing effect is found in e.g. Kirchner (2005) and the aforementioned textbooks (Butz, 2011; Puente León et al., 2011).

Spectral leakage is also an effect which results in magnitudes of wavelets getting incorrectly associated to other wavelets. Spectral leakage occurs when the length of the time series is not a whole multiple of all periods of all sinusoidal wavelets which the time series consists of. Consequently, spectral leakage does not exist for time series of infinite length. The magnitude of the effect of the spectral leakage decreases with increased length of the time series.

In order to minimise the effect of spectral leakage for finite time series, so-called windowing is applied on the time series. Here, Fourier analysis is carried out on the time series which is multiplied with a specific window function instead of the original time series. Different window functions exist which all minimise spectral leakage to different extents. Information on spectral leakage and the application of window functions is given in e.g. van der Tempel (2006) and Puente León et al. (2011).

Inverse Fourier transformation

Signals in time domain are obtained by applying the inverse Fourier transformation, which reverses the Fourier transformation. Different techniques exist for the inverse Fourier transformation of a given power spectral density. Random time series based on the same power spectral density can also be computed by means of the inverse Fourier transformation. These techniques as well as their impact on the statistics of the resulting random time series are discussed in Chapter 7.

2.1.2 Characteristics of random signals in time- and frequency domain

Each random signal possesses certain characteristics and properties. These are usually statistical properties which allow the description of the randomness. Different properties can be extracted from a signal, depending on whether it is time domain or in frequency domain. Mostly statistical properties are extracted from signals in time domain. Different realisations of time series can be obtained from power spectral densities or amplitude spectra via inverse Fourier transformation. These time series may seem to be different, but their statistical properties are approximately equal. In frequency domain, spectral properties can be extracted from the respective power spectral density or amplitude spectrum. Certain relationships exist between the parameters in time domain and frequency domain. Hence, properties derived in time domain can be applied for the analysis of the signal in frequency domain, and vice versa.

Temporal averaging and spectral moments

Statistical properties in time domain are obtained from time series mostly by their general temporal behaviour. Here, the temporal average of any function f , which depends on the signal $g(t)$ in time domain, is analysed,

$$\langle f(g(t)) \rangle = \frac{1}{T} \cdot \int_0^T f(g(t)) \cdot dt. \quad (2.6)$$

Special values of the temporal average are the mean value as well as the variance or the standard deviation, respectively. The mean value is obtained for $f = g(t)$ in Eq. (2.6), and the variance of the time series is calculated with $f = g(t)^2 - \langle g(t) \rangle^2$ in Eq. (2.6).

In frequency domain, general properties can be derived from the power spectral densities or amplitude spectra. Here, the spectral moments are of special importance. The j -th-order spectral moment weights the power spectral density S by the wave frequency to the power of a number j ,

$$m_j = \int S(\omega) \cdot \omega^j \cdot d\omega. \quad (2.7)$$

Similarly, the spectral moments are obtained for a discrete amplitude spectrum,

$$m_j = \frac{1}{2} \cdot \sum a_n^2 \cdot \omega^j. \quad (2.8)$$

As shown below, certain characteristic values of the time series can be expressed by means of spectral moments in frequency domain. The spectral moment of order $2 \cdot j$ can be calculated as the variance of the j -th derivative of the function $g(t)$,

$$m_{2 \cdot j} = \left\langle \left(\frac{d^j g(t)}{dt^j} \right)^2 \right\rangle - \left\langle \frac{d^j g(t)}{dt^j} \right\rangle^2. \quad (2.9)$$

For example, the zeroth-order spectral moment m_0 in frequency domain is equal to the variance of the signal in time domain. Several characteristic periods are determined on the basis of spectral moments. The reciprocal of the weighted arithmetic mean of the wave frequencies is referred to as mean period T_m , the average time between consecutive

zero-up-crossings is referred to as zero-up-crossing period T_z , and the average time between consecutive local maxima or consecutive local minima is usually referred to as peak period T_c ,

$$T_m = T_{0,1} = 2\pi \cdot \frac{m_0}{m_1}, \quad (2.10)$$

$$T_z = T_{0,2} = 2\pi \cdot \sqrt{\frac{m_0}{m_2}}, \quad (2.11)$$

$$T_c = T_{2,4} = 2\pi \cdot \sqrt{\frac{m_2}{m_4}}, \quad (2.12)$$

$$T_{-1,0} = 2\pi \cdot \frac{m_{-1}}{m_0}. \quad (2.13)$$

For completeness, $T_{-1,0}$ denotes the weighted arithmetic mean of the wave periods. The reciprocal of the average peak-to-peak period is the number of local extrema per second and thus the range count per second, which is an important value for the evaluation of extreme loads and fatigue loads, as shown in detail in Chapter 5 and Chapter 6, respectively.

Spectral moments can also be stated as dimensionless values, which are referred to as spectral parameters in the following,

$$\alpha_j = \frac{m_j}{\sqrt{m_0 \cdot m_{2 \cdot j}}}. \quad (2.14)$$

The spectral parameters α_1 and α_2 are decisive for the estimation of fatigue loads, as shown in Chapter 6. The spectral parameter α_1 is the ratio of the zero-up-crossing period T_z and the mean period T_m , $\alpha_1 = \frac{T_z}{T_m}$. The spectral parameter α_2 is equal to the ratio of the peak-to-peak period T_c and the zero-up-crossing period T_z , $\alpha_2 = \frac{T_c}{T_z}$.

An important dimensionless value to describe spectral properties is the spectral width parameter ϵ , which was introduced by Cartwright and Longuet-Higgins (1956),

$$\epsilon = \sqrt{1 - \frac{m_2^2}{m_0 \cdot m_4}} = \sqrt{1 - \alpha_2^2}. \quad (2.15)$$

The spectral width parameter can also be calculated as $\epsilon = \sqrt{1 - \left(\frac{T_c}{T_z}\right)^2}$ on the basis of the zero-up-crossing period T_z and the peak-to-peak period T_c .

Cross-correlation and autocorrelation

Cross-correlation describes the correlation of a signal with another signal which is delayed by a certain time lag. The cross-correlation function measures the influence which a signal has on another signal delayed by a time lag τ ,

$$C(\tau) = \frac{\left\langle \left(g_1(t) - \mu_{g_1(t)} \right) \cdot \left(g_2(t + \tau) - \mu_{g_2(t+\tau)} \right) \right\rangle}{\sigma_{g_1(t)} \cdot \sigma_{g_2(t+\tau)}}, \quad (2.16)$$

with mean value μ and standard deviation σ of the signals of g_1 and g_2 , respectively. The codomain of the autocorrelation function is the interval $[-1, 1]$. Values close to

1 and -1 indicate correlation and anti-correlation, respectively. Values close to zero indicate no correlation.

As a special case of the cross-correlation, autocorrelation describes the correlation of a signal with the same signal delayed by a time lag. It is derived from signals in either time domain or frequency domain. Periodic behaviour of signals can be identified by means of the autocorrelation function. The autocorrelation function measures the influence which a signal at any time has on the same signal delayed by a time lag τ ,

$$C(\tau) = \frac{\left\langle \left(g(t) - \mu_{g(t)} \right) \cdot \left(g(t + \tau) - \mu_{g(t+\tau)} \right) \right\rangle}{\sigma_{g(t)} \cdot \sigma_{g(t+\tau)}}, \quad (2.17)$$

with mean value μ and standard deviation σ of the signals of g . For signals in frequency domain given by a power spectral density S , the autocorrelation function reads as follows,

$$C(\tau) = \frac{1}{m_0} \cdot \int S(\omega) \cdot \cos(\omega_n \cdot \tau) \cdot d\omega, \quad (2.18)$$

with the zeroth-order spectral moment m_0 according to Eq. (2.7). The deviation of Eq. (2.18) is given in e.g. Halfpenny (1998). For signals defined by an amplitude spectrum, the autocorrelation function solely depends on the given amplitudes a_n ,

$$C(\tau) = \frac{1}{2 \cdot m_0} \cdot \sum_{n=1}^N a_n^2 \cdot \cos(\omega_n \cdot \tau), \quad (2.19)$$

with the zeroth-order spectral moment m_0 according to Eq. (2.8). Eq. (2.19) is found by the general definition of the autocorrelation function according to Eq. (2.17) with a Fourier series according to Eq. (2.1) or Eq. (2.2).

Determination of spectral moments from random time series

As shown in Chapter 5 and Chapter 6, the spectral moments are of importance for the calculation of the distribution functions of fatigue loads and extreme loads which are observed within a Gaussian signal.

There are different possibilities to determine these spectral moments of a time series which is considered as zero-mean Gaussian signal. The Fourier transformation of a time series results in a power spectral density or an amplitude spectrum which is applied for the calculation of spectral moments according to Eq. (2.7) or Eq. (2.8), respectively. It is also possible to estimate the spectral moments solely on the basis of the time series itself. This is shortly explained in the following. The described method to determine the spectral moments from time series is only exact for a continuous time series of infinite length. For discrete time series or time series of finite length, numerical errors may occur during the calculation of spectral moments.

It is assumed that the time series is a Fourier series according to Eq. (2.1). The same findings are obtained for Eq. (2.2). The j -th derivative of the time series, denoted as $g^{(j)}(t)$ reads as follows,

$$g^{(j)}(t) =: \frac{d^j g(t)}{dt^j} = \sum_{n=1}^N a_n \cdot \omega_n^j \cdot \cos\left(\omega_n \cdot t + \varphi_n + j \cdot \frac{\pi}{2}\right). \quad (2.20)$$

The temporal average, referring to Eq. (2.6), of the product of two derivatives of arbitrary order of the same time series, with an arbitrary time lag, is analysed. This temporal average reads as follows for a time series of infinite length,

$$\langle g^{(j)}(t) \cdot g^{(k)}(t + \tau) \rangle = \frac{1}{2} \cdot \sum_{n=1}^N a_n^2 \cdot \omega_n^{j+k} \cdot \cos((k-j) \cdot \frac{\pi}{2} + \omega_n \cdot \tau). \quad (2.21)$$

In comparison to the definition of the spectral moment, each summand of Eq. (2.8) is multiplied by a cosine term $\cos((k-j) \cdot \frac{\pi}{2} + \omega_n \cdot \tau)$. Hence, the absolute value of Eq. (2.21) is equal to the spectral moment of order $j+k$ only when either all cosine terms are 1 or -1 . Therefore, either the arguments of all cosine terms must be even multiples of π , or they must be odd multiples of π . It easily follows that the spectral moments of even order are given for a time lag of zero. As a special case, the variance of the j -th derivative of the time series is equal to the spectral moment of order $2 \cdot j$. The variance of the time series itself is the zeroth-order spectral moment.

For spectral moments of odd order, the temporal average in Eq. (2.21) is zero for a time lag of zero. The time lag has to be chosen appropriately such that the absolute value of the temporal average is maximum. This time lag has to be found empirically, since no information on its value can be found analytically.

As another possibility to determine certain spectral moments, the second- and fourth-order spectral moment of a time series can be determined on the basis of the zero-up-crossing period, the peak-to-peak period, and the zeroth-order spectral moment, referring to Eq. (2.11) and Eq. (2.12). The values of the zero-up-crossing period and the peak-to-peak period can be extracted from the time series as average time between consecutive zero-up-crossings and the average time between consecutive local maxima or consecutive local minima, respectively.

Multiplication in frequency domain

The product of two time series is given by multiplication of those time series, $f(t) \cdot g(t)$. Multiplication of the respective signals in frequency domain is carried out by evaluation of the convolution integral of the respective spectra S_{gg} and S_{ff} ,

$$\langle S_{ff} * S_{gg} \rangle = \int S_{ff}(\omega) \cdot S_{gg}(\omega' - \omega) \cdot d\omega'. \quad (2.22)$$

For a signal to the power of n with $n \in \mathbb{N}$, the resulting spectrum is denoted as $\langle S \rangle^{*n}$. This term is equal to $\langle S * \langle S \rangle^{*n-1} \rangle$, with $\langle S \rangle^{*1} = S$. These formulae are valid for power spectral densities and amplitude spectra likewise.

2.2 Stochastic analysis of random variables and random signals

The analysis of the stochastic properties are of special interest for random processes and signals. The stochastic properties are e.g. the distribution function of the data as well as certain values such as the mean value or standard deviation. These properties allow to

evaluate the occurrence probability of certain events which may occur within a random process. Unless defined, they are determined on the basis of data sets. Since these data sets are usually of limited size, the determined values are subject of scattering and may be inaccurate. Especially for a safe structural design, it is of importance to estimate the error which is made due to the limited data set.

A short overview on important stochastic properties as well as on goodness-of-fit tests to evaluate the goodness-of-fit of assumed distribution functions are given in the following. More detailed information may be found in textbooks such as Bohm and Zech (2010).

2.2.1 General definitions

In order to evaluate the stochastic properties of variables, these variables have to be independent and identically distributed and random. Independent and identically distributed random variables follow the same probability distribution without being dependent on each other. Let X be a sample of independent and identically distributed random variables. Usually, the cumulative distribution function and probability density function are used to describe the occurrence probability of values from the data set statistically. The cumulative distribution function is the non-exceedance probability which denotes the probability that a random variable of X is less than or equal to a value x . The cumulative distribution function is a non-decreasing function with a codomain of $[0, 1]$. The probability density function is defined as the derivative of a continuous cumulative distribution function, $p(x) = \frac{dP(x)}{dx}$. By definition, the sum of all occurrence probabilities is unity, which is equivalent to the statement that the integration of the probability density function with respect to the domain of values is unity. Hence, the cumulative distribution function is expressed as follows,

$$P(x) = \text{Prob}[X \leq x] = \int_{-\infty}^x p(x') \cdot dx' , \quad (2.23)$$

with the probability $\text{Prob}[(\bullet)]$ that a certain event (\bullet) occurs. The expected value $E[g(X)]$ for any function g of independent and identically distributed random variables X is calculated as follows,

$$E[g(X)] = \int g(x) \cdot p(x) \cdot dx . \quad (2.24)$$

Typical and important values to describe a set of independent and identically distributed random variables X are the mean value μ_X , the variance Var_X , the standard deviation $\sigma_X = \sqrt{Var_X}$, the skewness γ_3 , and the kurtosis γ_4 ,

$$\begin{aligned} \mu_X &= E[X] , \\ Var_X &= E[(X - \mu_X)^2] , \\ \gamma_3 &= E[(X - \mu_X)^3] / \sigma_X^3 , \\ \gamma_4 &= E[(X - \mu_X)^4] / \sigma_X^4 . \end{aligned} \quad (2.25)$$

The skewness measures whether a probability density function is symmetrical. Its value is zero for symmetric probability density functions, negative if the left tail is stronger, and positive if the right tail is stronger. The kurtosis is a measurement whether the

probability density function is heavy- or light-tailed. As reference, the normal distribution has a kurtosis of 3. A heavy-tailed or platykurtic distribution function has a kurtosis with a value less than 3, and the kurtosis of a light-tailed or leptokurtic distribution function is greater than 3.

Values which are exceeded with a certain probability are also of interest in order to evaluate the statistical characteristics of a data set. These so-called quantiles are the inverse function of the cumulative distribution function, referring to Eq. (2.23). Besides the median, which is the 50%-quantile, quantiles associated to very low and very high probabilities are useful to describe the statistical behaviour of rarely occurring values. In structural engineering, quantiles are of importance for the semi-probabilistic safety concept, which is described in Section 4.1.

2.2.2 Statistical methods for parameter estimation and statistical testing

Different methods exist to determine the type of distribution functions and their defining parameters. A general overview on these methods is found in e.g. Embrechts et al. (1997) and Bohm and Zech (2010). Histograms, which are most commonly applied, and the methods applied within this thesis are shortly introduced in the following. The methods applied within this thesis are shortly introduced in the following. The applications of some of these methods are sketched in Fig. 2.2. Exemplarily, ten random values, which are normal-distributed, are compared to the underlying normal distribution with mean of zero and standard deviation of unity.

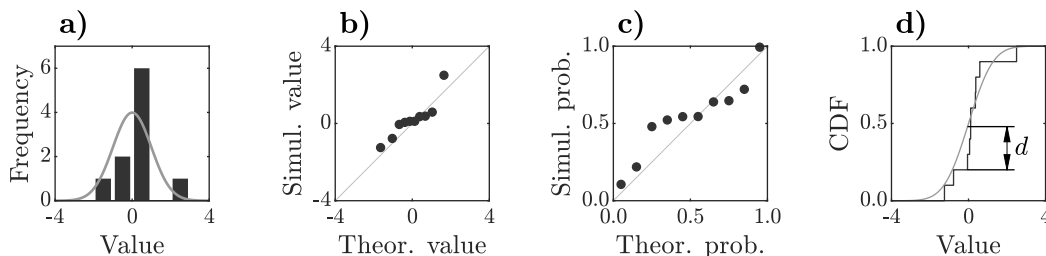


Figure 2.2: Graphical methods for estimation of distribution functions, here for normal-distributed values with mean of zero and standard deviation of unity: a) histogram, b) Q-Q plot, c) P-P plot, d) Kolmogorov-Smirnov test

Histograms

Histograms provide a graphical method which is often used to roughly estimate the underlying distribution. Here, the range of values is divided in non-overlapping intervals, usually referred to as bins, to which the data points are appointed. The counts within the bins are qualitatively compared to the assumed distribution function, referring to Fig. 2.2 (a).

Q-Q plots and P-P plots

Q-Q plots are a method to compare two probability distributions graphically. Within Q-Q plots, the quantiles of both distributions, each sorted in ascending order, are plotted against each other. Usually, Q-Q plots are applied to determine whether a given set of data follows an assumed distribution function with a certain accuracy. In case that the data pairs in the Q-Q plot lie close to the bisecting line within a certain confidence interval, the two distributions may be considered as similar.

In order to determine whether a given set of data follows an assumed distribution function, the data points sorted in ascending order are compared to the quantiles of the assumed distribution function with increasing probability. The quantiles of the assumed distribution function are calculated by the inverse of the respective cumulative distribution function. Different approaches exist for setting the values of the non-exceedance probability associated to the quantiles (Embrechts et al., 1997). Unless stated otherwise, the values of probability are set as $(n - 0.5) / N$, $n = 1 \dots N$, with the number of data N , for Q-Q plots within this thesis. Then, the set of data is plotted against the theoretical quantiles, both sorted in ascending order.

Instead of Q-Q plots, P-P plots can be applied. Here, the probabilities of two distributions are plotted against each other. The method to determine whether a given set of data follows an assumed distribution function is similar to the Q-Q plot. The non-exceeding probability of each value within the set of data is calculated by the assumed cumulative distribution function. These values are plotted against the values of probability, both sorted in ascending order.

Q-Q plots and P-P plot are shown in Fig. 2.2 (b) and (c).

Maximum-likelihood estimation

The maximum-likelihood estimation aims to find the values of the defining parameters of the underlying distribution function such that the likelihood function is maximised. Here, the likelihood function is given as the product of the probability density function evaluated for each data point of a given sample. Depending on the assumptions, it is more convenient to use the natural logarithm of the likelihood function, called the log-likelihood function,

$$\mathcal{L}((a_1, \dots); \underline{X}) = \sum_{n=1}^N \log(p(x_n)), \quad (2.26)$$

with the probability density function p depending on the parameters a_1, \dots .

Kolmogorov-Smirnov test and p -value

The Kolmogorov-Smirnov test is a statistical test for the hypothesis that two probability distributions are equal. It is used to compare a sample with a probability distribution, or to compare two samples. Comparing a sample with a probability distribution, the maximum difference between the empirical distribution function of the sample and the reference cumulative distribution function is quantified. The empirical distribu-

tion function is generated by assigning the non-exceeding probability, usually set as $(n - 0.5)/N$, $n = 1 \dots N$, to the N data points which are sorted in ascending order. The principal of the Kolmogorov-Smirnov test is shown in Fig. 2.2 (d).

The reference cumulative distribution function is calculated by means of the null hypothesis. The null hypothesis is to reject if the determined difference between the probability functions exceeds a certain value. This value depends on the number of the data points as well as on the chosen level of significance.

Moreover, the p -value can be determined in order to evaluate the hypothesis that the given data set fits the probability distribution with the determined parameters. The p -value is the probability, calculated with the studied hypothesis that the test statistic is equal to or more significant than its observed value (Wasserstein and Lazar, 2016). Small values cast doubt on the validity of the hypothesis. The hypothesis is to reject if the p -value is less than a chosen level of significance, which is typically set as 0.05. p -values greater than the level of significance do not prove that the studied hypothesis is true. They do not measure the probability that the studied hypothesis is true (Wasserstein and Lazar, 2016).

Kullback-Leibler divergence

The Kullback-Leibler divergence, introduced by Kullback and Leibler (1951), is a dimensionless parameter to assess how a probability distribution differs from another probability distribution. For discrete probability distributions of the variable x , here denoted as $P_1(x)$ and $P_2(x)$, the Kullback-Leibler divergence D_{KL} is calculated as follows,

$$D_{KL} = \sum_n P_1(x_n) \cdot \log \frac{P_1(x_n)}{P_2(x_n)}. \quad (2.27)$$

In case that continuous probability density functions p_1 and p_2 of the variable exist, the Kullback-Leibler divergence is stated in integral form, $D_{KL} = \int p_1(x) \cdot \log \frac{p_1(x)}{p_2(x)} \cdot dx$. The value of the Kullback-Leibler divergence can be understood as how much information of the original probability distribution is lost due to the assumption of the other probability distribution. Its values are non-negative. A value of zero indicates that the investigated distribution functions are identical.

2.2.3 Extreme value theory

The extreme value theory is a branch of statistics, which is concerned with the sample minimum and maximum of probability functions. Therefore, it deals with the asymptotic limit behaviour of the extreme values of independent and identically distributed random variables. The extreme value theory originally was developed by Gumbel (1958). Detailed information on the extreme value theory is given in e.g. Embrechts et al. (1997), Coles (2001), and de Haan and Ferreira (2006).

According to the extreme value theory (Gumbel, 1958), the stochastic behaviour of extreme values is described by the generalized extreme value distribution. Three different

types of the generalized extreme value distribution (index *GEV*) exist, with the type depending on the shape parameter ξ ,

$$P^{GEV}(x) = \begin{cases} \exp\left(-\exp\left(-\frac{x-\mu}{\sigma}\right)\right) & , \xi = 0, x \in \mathbb{R} \\ \exp\left(-\left(1 + \xi \cdot \frac{x-\mu}{\sigma}\right)^{-\frac{1}{\xi}}\right) & , \xi > 0, x \in \left[\mu - \frac{\sigma}{\xi}, \infty\right) \\ \exp\left(-\left(1 + \xi \cdot \frac{x-\mu}{\sigma}\right)^{-\frac{1}{\xi}}\right) & , \xi < 0, x \in \left(-\infty, \mu - \frac{\sigma}{\xi}\right] \end{cases}, \quad (2.28)$$

with the scale parameter $\sigma > 0$ and the location parameter μ . The respective cumulative distribution functions are given by Eq. (2.28). The three types of the generalized extreme value distribution are usually called Gumbel distribution, Fréchet distribution, and reverse-Weibull distribution, respectively (Eq. (2.28), from top to bottom).

Usually, only a small data set of independent and identically distributed extreme values is available due to the seldom occurrence of extreme values. Hence, its respective parameters of the generalized extreme value distribution are to be estimated carefully while also considering uncertainties due to the small sample sizes. Several methods to determine the generalized extreme value distribution and its parameters exist, as they are described in e.g. Embrechts et al. (1997), Coles (2001), and de Haan and Ferreira (2006).

A very common method to determine the distribution function of extreme values is the block-maxima method (Gumbel, 1958; de Haan and Ferreira, 2006). Here, independent and identically distributed data points are divided in several blocks of same size. The data points in all blocks shall be independent and identically distributed. The extreme values of each block are used for derivation of the generalized extreme value distribution. The respective parameters depend on the block size. Selecting a very small block size is not recommended because the selected extreme values of each set might not follow the generalized extreme value distribution. A great block size also results in a very limited data set of extreme values such that the generalized extreme value distribution and its parameters usually cannot be determined accurately. However, the generalized extreme value distributions for long periods are of special interest, i.e. the distribution function of annual extremes.

In case that the generalized extreme value distribution for a certain period T_{ref} is already known, the generalized extreme value distribution for any period T can be calculated on the basis of this period T_{ref} . The cumulative distribution function for the period T is given as $P_T^{GEV} = \left(P_{T_{ref}}^{GEV}\right)^\tau$, with $\tau = \frac{T}{T_{ref}}$. The generalized extreme value distribution for the period T is given by Eq. (2.28) with adapted parameters (index \prime),

$$\begin{aligned} \sigma' &= \sigma, & \mu' &= \mu + \ln \tau \cdot \sigma & , \xi &= 0 \\ \sigma' &= \sigma \cdot \tau^\xi, & \mu' &= \mu + \frac{1}{\xi} \cdot (\tau^\xi - 1) \cdot \sigma & , \xi &\neq 0 \end{aligned}, \quad (2.29)$$

with the parameters ξ , σ , and μ of the generalized extreme value distribution for the period T_{ref} . The shape parameter is independent of the period, $\xi' = \xi$.

Referring to generalized extreme value distributions for great block sizes and therefore small data sets of extreme values, the distribution function of the annual extremes can also be calculated on the basis of the distribution function of monthly extremes. The respective parameters are adapted according to Eq. (2.29). In order to carry out

this adaption, it has to be ensured that the values for all months are independent and identically distributed and that the monthly extremes can be described by a generalized extreme value distribution.

2.2.4 Peak-over-threshold method

As a method within the extreme-value analysis, the peak-over-threshold method is usually applied for the tail estimation of a probability distribution. Here, independent and identically distributed random variables which exceed a certain threshold are analysed. This method is well established in other disciplines such as hydrology or finance mathematics. Further information on the peak-over-threshold method is given in e.g. Embrechts et al. (1997) and Coles (2001). The method is described for values exceeding a certain threshold, but it is also valid for values falling below a certain threshold.

Assuming that a set of independent and identically distributed random variables X is described by a cumulative distribution function $P(x)$, the probability function of exceeding a certain threshold u is defined,

$$P_u(x) = \text{Prob}[X \geq x | X > u] = \frac{P(x) - P(u)}{1 - P(u)}. \quad (2.30)$$

According to the mathematical description of the peak-over-threshold method, the distribution of independent and identically distributed random variables exceeding a certain threshold according to Eq. (2.30) is given by the generalised Pareto distribution. The respective distribution functions (index *GPD*) depend on the shape parameter ξ , the scale parameter $\beta > 0$, and the threshold u ,

$$p^{GPD}(x) = \begin{cases} \frac{1}{\beta} \cdot \left(1 + \xi \cdot \frac{x-u}{\beta}\right)^{-\frac{\xi+1}{\xi}} & , \xi \neq 0 \\ \frac{1}{\beta} \cdot \exp\left(-\frac{x-u}{\beta}\right) & , \xi = 0 \end{cases}, x \in D(\xi, \beta, u), \quad (2.31)$$

with the domain of definition $D = [u, \infty)$ for $\xi \geq 0$, and $D = [u, u - \beta/\xi]$ for $\xi < 0$. Here, the probability density functions are shown.

The value of the threshold u is to be chosen carefully in order to determine the underlying generalised Pareto distribution for a given set of data $[X_1 \dots X_N]$. On the one hand, the number of data points may be small by setting a high value of the threshold. This eventually results in uncertainties with respect to the underlying generalised Pareto distribution. On the other hand, a small value of the threshold provides a greater set of data to evaluate. However, the application of the generalised Pareto distribution is doubtful by setting the value of the threshold too small. Hence, the quality and the uncertainties of the results are to be determined properly.

The parameters of the generalised Pareto distribution can be estimated by applying the maximum-likelihood estimation, as described above in Section 2.2.2. Then, the log-

likelihood function according to Eq. (2.26) reads as follows for the generalised Pareto distribution according to Eq. (2.31),

$$\mathcal{L}((\xi, \beta); \underline{X}) = \begin{cases} -N \cdot \ln \beta - \frac{\xi+1}{\xi} \cdot \sum_{n=1}^N \left(1 + \xi \cdot \frac{x_n - u}{\beta}\right) & , \xi \neq 0 \\ -N \cdot \ln \beta - \sum_{n=1}^N \frac{x_n - u}{\beta} & , \xi = 0 \end{cases}. \quad (2.32)$$

The log-likelihood function is usually to be calculated numerically. The maximum-likelihood estimation is suitable for the generalised Pareto distribution with the shape parameter $\xi > -0.5$ (Embrechts et al., 1997).

It is also possible to estimate the parameters of the generalised Pareto distribution by means of the mean-excess function, $me(u) = E[X - u | X > u]$. The mean-excess function is calculated for increasing values of the threshold u . Within the plot of the mean-excess function, a section of the graph is to be detected visually which is approximately linear. Then, the parameters of the generalised Pareto distribution can be determined on the basis of this linear section. Reference is made to e.g. Embrechts et al. (1997) and Coles (2001) for further details. However, it is often not possible to define a linear section with the mean-excess function with certainty. The analysis of the mean-excess function and the respective estimation of the parameters of the generalised Pareto distribution are to be carried out cautiously because they often are prone to misinterpretation (Embrechts et al., 1997).

2.2.5 Relationship between generalized extreme value distribution and generalised Pareto distribution

Assuming that the excesses over a high threshold can be modelled as a generalised Pareto distribution, the maximum of these excesses can be described as a generalized extreme value distribution (Embrechts et al., 1997, pp. 166). With a generalised Pareto distribution according to Eq. (2.31) with shape parameter ξ and scale parameter β , the distribution function of extreme values is a generalized extreme value distribution according to Eq. (2.28) with location parameter $\mu = \frac{\beta}{\lambda} \cdot (\lambda^\xi - 1)$ and scale parameter $\sigma = \beta \cdot \lambda^\xi$ for $\xi \neq 0$ and with location parameter $\mu = \beta \cdot \ln \lambda$ and scale parameter $\sigma = \beta$ for $\xi = 0$. λ denotes the ratio of total number of values to the number of values to be considered as maxima. The shape parameters of the generalised Pareto distribution and of the deviated generalized extreme value distribution are equal.

3 Load acting on offshore wind turbines

Offshore wind turbines are subjected to the harsh environment offshore. Meteorological and oceanographic parameters, referred to as metocean parameters, include parameters such as densities and temperatures of wind and water as well as severities and directions of wind fields, sea states, and currents. Metocean conditions describe the temporal variations and the occurrence frequencies of metocean parameters. Besides metocean conditions, further environmental conditions describe the interaction between the offshore structure itself and the offshore environment. Examples for these interactions typically occurring offshore are the settlement of marine fauna at the structure, scour development at embedded piles, and corrosion of structural components. The moving rotor and machinery as well as their wind-field- and loads-depending control also induce loads to the support structure of the offshore wind turbines.

3.1 Wind-induced loads

3.1.1 Wind field

Wind fields are described by the wind velocity which varies in space and time. A typical wind field to be observed is shown in Fig. 3.1. It consists of a wind-velocity profile, which varies over height, and of spatial and temporal fluctuations around the mean wind velocity at a certain height. Wind fields are usually considered as stationary for a duration of ten minutes.

Wind-velocity profile

Mean wind velocities are usually given for a certain height. Usually, the mean wind velocity increases with increasing height. The wind-velocity profile over height is usually described as a power-law profile in dependence of a reference height z_{ref} and the associated mean wind velocity,

$$v_{wind}(z) = v_{wind}(z_{ref}) \cdot \left(\frac{z}{z_{ref}} \right)^\alpha. \quad (3.1)$$

The wind-shear coefficient α depends on the surface roughness of the nearby landscape. Wind velocities near the surface are strongly decreased for an increased surface roughness. Hence, higher values of the wind-shear coefficient are observed for an increased surface roughness. Constant wind velocity over height is given for a wind-shear coefficient of zero. In general, smaller values are expected offshore in comparison to onshore sites, which are usually not plain, e.g. due to trees or hilly areas.

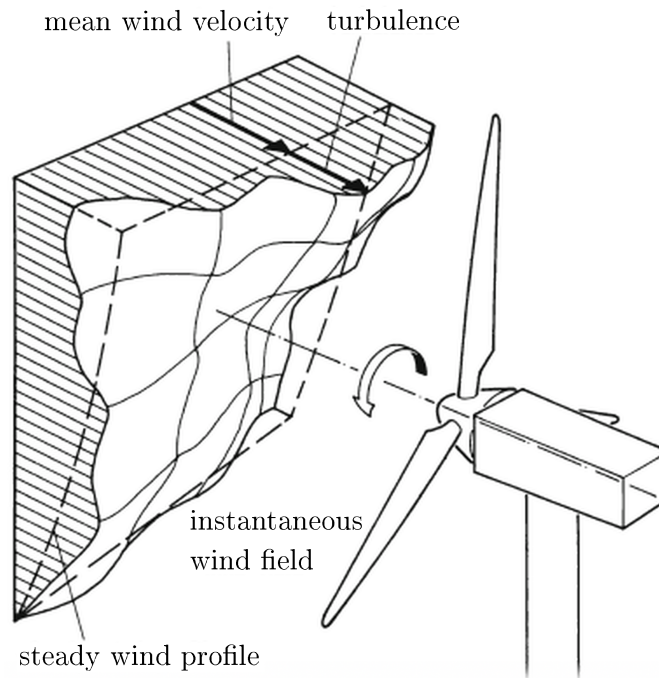


Figure 3.1: Wind field consisting of a vertical wind-shear profile and turbulence (adapted from Hau (2013))

The wind-shear coefficient at offshore sites also depends on the wind velocity, as shown by e.g. Türk et al. (2008) and Ernst and Seume (2012) on the basis of wind-velocity measurements at the research platform FINO1. Above wind velocities of 3 m/s , the wind-shear coefficient lies in the range of 0.12 up to 0.15 or in the range of 0.13 up to 0.19, depending on the evaluation method. Almost constant wind velocities over height are observed for wind velocities less than 3 m/s (Ernst and Seume, 2012). A detailed analysis regarding deviations from the power-law profile measured at the research platform FINO1 is carried out by Kettle (2014).

Unless site-specific wind-shear data are available, wind-shear coefficients of 0.20 for onshore sites (IEC 61400-1, 2005) and of 0.14 for offshore sites (IEC 61400-3-1, 2019) shall be applied for the load simulation of wind turbines, respectively.

Turbulence

Wind fields do not have a constant wind profile, but the wind velocity fluctuates spatially and temporarily in all dimensions. These fluctuations are usually referred to as turbulence. It is quantified with the turbulence intensity which is the coefficient of variance of the mean wind velocity in mean wind direction. The reference duration is ten minutes.

The turbulence intensity depends on the wind velocity. This is regulated in relevant standards, such as IEC 61400-1 (2005) and IEC 61400-3-1 (2019), where reference turbulence intensities are stated. The turbulence intensity decreases significantly with increasing wind velocity until average wind velocity. For greater wind velocities, the turbulence intensities increase slightly. Based on turbulence intensities measured at the research platform FINO1, Emeis and Türk (2008) and Ernst and Seume (2012) confirm

this characteristic for an offshore site. They also show that the turbulence intensities scatter significantly for all wind velocities.

For the wind-field simulation, the Kaimal spectrum or the von Kármán wind turbulence model is typically applied to model the turbulent wind field. The formulations of both models are stated in e.g. Gasch and Twele (2012).

Long-term behaviour of wind velocities

The long-term distribution function of the mean wind velocities can be described as a Weibull distribution function,

$$P_{wind}(v_{wind}) = 1 - \exp\left(-\left(\frac{v_{wind}}{A}\right)^k\right). \quad (3.2)$$

with site-specific scale parameter A and shape parameter k . In case that no site-specific long-term data exist, the long-term behaviour of the mean wind velocities is modelled as Rayleigh distribution function, which is a special case of the Weibull distribution function, referring to Eq. (3.2), with shape parameter $k = 2$ and scale parameter of $A = \frac{4}{\pi} \cdot v_{annual}$, with annual mean wind velocity v_{annual} .

3.1.2 Wind-induced loads on rotor blades

The blade-element-momentum theory is usually applied for the calculation of the wind-induced loads acting on the rotor blades.

Forces at each section of each rotor blade are calculated. Therefore, the lift- and drag coefficient of each blade section are to be known for the calculation of the respective forces. The wind velocity and wind direction attacking the profiles of the rotor blades are determined for each time step during the wind-load simulation. Here, the actual wind field, the rotational speed of the rotor as well as the positioning and flexibility of the rotor blades are taken into account. Positioning of the rotor blades includes the pitch angle of the rotor blades which is regulated by the controller of the wind turbine. The loads at each blade section of each rotor blade are summed in order to calculate the wind-induced loads acting on the rotor-nacelle assembly.

Further explanation on the blade-element-momentum theory is provided in relevant textbooks such as Burton et al. (2001), Gasch and Twele (2012), and Hau (2013).

3.2 Wave-induced loads

The flow conditions of the water particles around a structure result in loading of this structure. In order to determine these wave-induced loads, the flow conditions of the water particles, also referred to as water kinematics, are to be known. They are commonly described by the velocity potential Φ . The velocities of the water particles in space are given as the derivatives of the velocity potential with respect to the spatial directions,

$$\frac{d\Phi}{dx} = u, \quad \frac{d\Phi}{dy} = v, \quad \frac{d\Phi}{dz} = w. \quad (3.3)$$

Differentiation of the velocities with respect to time yields the accelerations of water particles. For two-dimensional flow conditions, the water kinematics can also be described by the stream function Ψ , which define the stream lines of the moving water particles. The stream function also relates to the velocities of water particles,

$$\frac{d\Psi}{dz} = u, \quad \frac{d\Psi}{dx} = -w. \quad (3.4)$$

The definition of the coordinate system and the respective velocities are shown in Fig. 3.2. The origin of the Cartesian coordinate system lies at the mean sea level, with the z -axis pointing upwards. When describing the water kinematics, the x -axis usually points towards the mean propagation direction of the wave or sea state. The axes are perpendicular to each other.

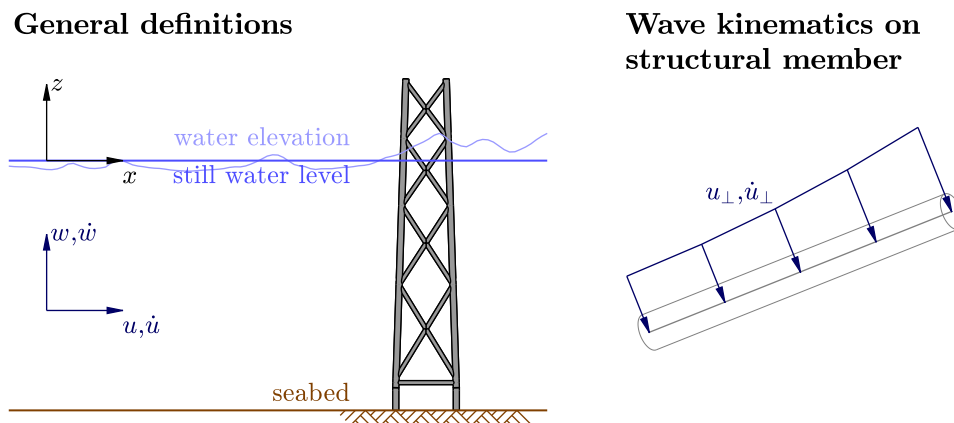


Figure 3.2: Definition of wave properties

The undisturbed flow conditions are described as a set of differential equations, Laplace's equation and Bernoulli's equation,

$$\frac{d^2\Phi}{dx^2} + \frac{d^2\Phi}{dy^2} + \frac{d^2\Phi}{dz^2} = 0, \quad (3.5)$$

$$\frac{d\Phi}{dt} + \frac{1}{2} \cdot (u^2 + v^2 + w^2) + g \cdot z + \frac{p}{\rho_w} = 0, \quad (3.6)$$

with Earth's acceleration g , static pressure p and density of water ρ_w . Additionally the following boundary conditions have to be satisfied,

$$w = 0, \quad z = -d, \quad (3.7)$$

$$\frac{d\Phi}{dt} + \frac{1}{2} \cdot (u^2 + v^2 + w^2) + g \cdot z = Q, \quad z = \eta, \quad (3.8)$$

$$\frac{d\eta}{dt} + u \cdot \frac{d\eta}{dx} + v \cdot \frac{d\eta}{dy} = w, \quad z = \eta, \quad (3.9)$$

with the water depth d and the water-surface elevation η . Assuming a constant atmospheric pressure at the water surface, the variable Q is constant. Eq. (3.8) and Eq. (3.9) are referred to as "dynamic free-surface boundary condition" and "kinematic free-surface boundary condition", respectively. General description of the boundary conditions are found in e.g. Hapel (1990). The term $u^2 + v^2 + w^2$ in Eqs. (3.6) and (3.8) and the terms $u \cdot \frac{d\eta}{dx}$ and $v \cdot \frac{d\eta}{dy}$ in Eq. (3.9) are non-linear. Therefore, no analyt-

ical solution of the set of differential equations can be found. Different approaches exist to solve the non-linear differential equations numerically.

3.2.1 Regular waves

A regular wave is a periodically repeating wave, defined by its wave period T , wave length L , and wave height H . Different methods exist to determine the shape of a periodic wave as well as the respective wave kinematics. The adequate selection of a suitable wave theory depends on the wave parameters as well as on the water depth, as recommended by e.g. DNV-RP-C205 (2019) and IEC 61400-3-1 (2019) and shown in Fig. 3.3. An overview on these wave theories is given in e.g. Dean and Dalrymple (1984). The approaches most commonly used are shortly given in the following. Without loss of generality, they are shown for a two-dimensional spatial field, with the y -direction being neglected.

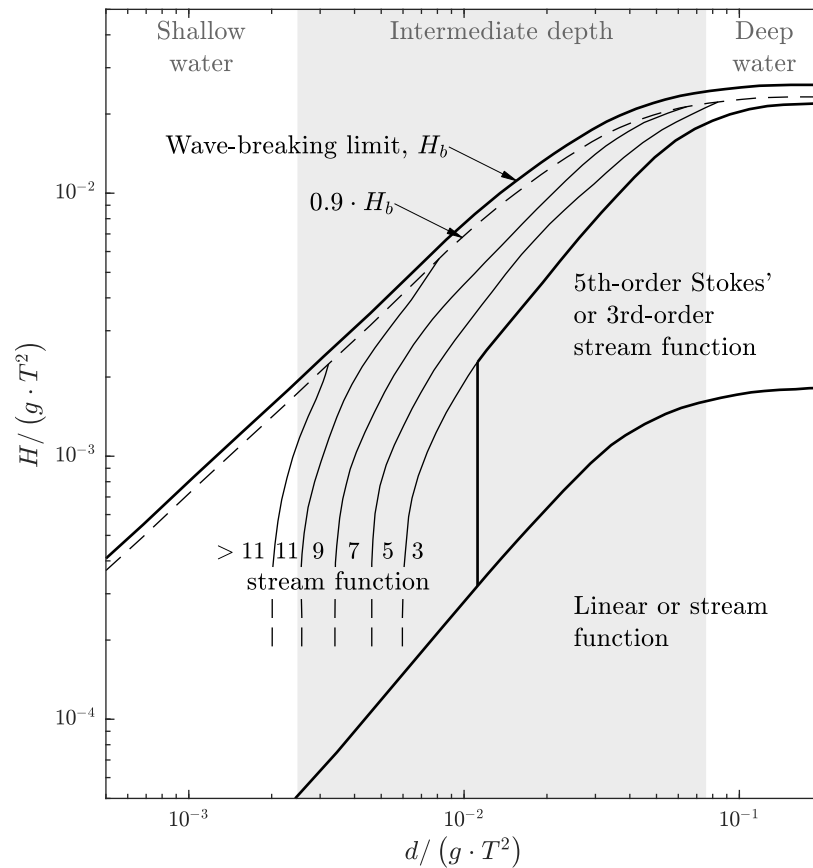


Figure 3.3: Selection of the applicable wave theory for regular waves, depending on wave height H , wave period T , and water depth d (adapted from DNV-RP-C205 (2019))

Airy waves

In case that the water-surface elevation is negligibly small in comparison to the water depth, and that the wave steepness, given as ratio of wave height and wave length, is small, the governing equations and boundary conditions can be simplified. Then, the

non-linear term $u^2 + v^2 + w^2$ in Eqs. (3.6) and (3.8) and the non-linear terms $u \cdot \frac{d\eta}{dx}$ and $v \cdot \frac{d\eta}{dy}$ in Eq. (3.9) are neglected, and the boundary conditions are evaluated at still water level instead of at water-surface elevation. An analytical solution for the water-surface elevation η and the velocity potential Φ is found for the set of the linearised equations,

$$\eta(t, x) = a \cdot \cos(k \cdot x - \omega \cdot t) , \quad (3.10)$$

$$\Phi(t, x, z) = c \cdot x + \frac{a \cdot g}{\omega} \cdot \frac{\cosh(k \cdot (d + z))}{\cosh(k \cdot d)} \cdot \sin(k \cdot x - \omega \cdot t) , \quad (3.11)$$

with amplitude $a = \frac{H}{2}$, wave frequency $\omega = \frac{2\pi}{T}$, current velocity c , and water depth d . The wave number k and the wave length $L = \frac{2\pi}{k}$, respectively, are given by the dispersion equation,

$$(\omega - k \cdot c)^2 = g \cdot k \cdot \tanh(k \cdot d) . \quad (3.12)$$

The linear wave theory is also called Airy wave theory, named after the British mathematician and astronomer Sir George Biddell Airy.

Since the Airy wave theory is defined from the seabed up to the still water level, the profile of the water-particle kinematics are stretched to the instantaneous water-surface elevation. Several stretching methods exist, as summarised in e.g. Couch and Conte (1997). The commonly-used stretching method is the so-called Wheeler stretching (Wheeler, 1969). The technique of Wheeler stretching is visualised in Fig. 3.4. Here, the kinematics at the instantaneous water-surface elevation are set as the kinematics at the still water level as given by the Airy wave theory. The vertical profile of the kinematics given by the Airy wave theory from seabed to still water level (grey) is stretched linearly from seabed to water-surface elevation (black). Wheeler stretching is to be applied for the design of offshore wind turbines (DNV-RP-C205, 2019; IEC 61400-3-1, 2019).

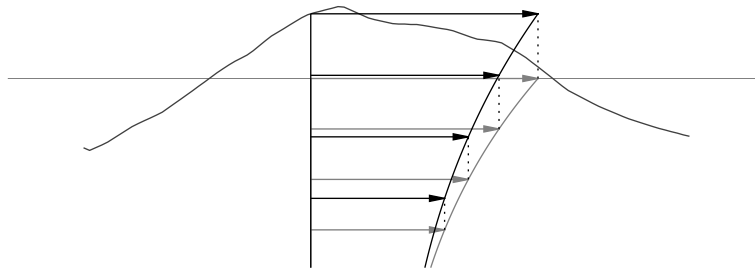


Figure 3.4: Wheeler stretching of water-particle kinematics (Wheeler, 1969): stretching of water-particle kinematics defined up to still water level according to linear wave theory (grey profile) up to water-surface elevation (black profile)

Non-linear waves

In case that the non-linear terms in Eqs. (3.6) and (3.8) are comparably great such that they cannot be neglected, higher-order wave theories are to be applied in order to describe the shape and kinematics of regular waves appropriately. The wave is described by superposition of sinusoidal terms, whose arguments are natural multiples of the base argument. They can be considered as Fourier series. Both analytical as well as numerical approaches to determine the shape and the kinematics of non-linear regular waves exist.

A commonly used approach is the so-called “stream function wave theory” (Dean, 1965), which is shortly described in the following. The stream function wave theory solves the non-linear equations by numerical approximation. Here, the stream function Ψ is modelled as a Fourier series,

$$\Psi(x, z) = \left(\frac{L}{T} - c \right) \cdot z + \sum_{n=1}^N X_n \cdot \sinh(n \cdot k \cdot (z + d)) \cdot \cos(n \cdot k \cdot x), \quad (3.13)$$

where c denotes a constant current velocity. The unknown coefficients X_n , $n = 1, \dots, N$ as well as the wave length are to be determined via iteration. The wave is considered as steady by selecting a coordinate system travelling with the speed of the wave. Therefore, the shape of the wave does not change within this coordinate system. First, the dynamic free-surface boundary condition (Eq. (3.8)) is evaluated for a certain number of chosen points along the water surface. Then, the mean square error of the dynamic free-surface boundary condition shall be minimized, with the constraints that both the given wave height and the mean sea level are maintained. The method of Lagrange multipliers, a strategy for finding the local maxima and minima of a function subject to constraints, is usually applied here. Each of the equations is linearised with respect to the initial values. Finally, the system of linear equations is solved, and the set of values to determine is updated. The iteration is stopped when the errors regarding the dynamic free-surface boundary condition, the wave height, and the mean sea level are sufficiently small. No stretching of the kinematics, as it is necessary for the Airy wave theory, is to be applied for non-linear waves.

3.2.2 Irregular waves

The water-surface elevation of a sea usually cannot be described by regular waves. Rather waves with different wave heights and distances between consecutive wave crest are observed. The sequence of these waves is described as random. Therefore, sea states are described as stochastic processes. They are assumed to be stationary over a time span of three hours up to six hours (DNV-ST-0437, 2016).

Sea states are usually represented by the significant wave height H_s and the mean zero-up-crossing period T_z . The significant wave height is defined as the mean value of the one-third greatest wave heights observed during a stationary sea state, and its value is almost exactly four times the standard deviation of the observed water-surface elevation. The mean zero-up-crossing period denotes the mean period of successive temporal up-crossings of the mean sea level by the water-surface elevation.

First-order sea state

For the simulation in time domain, the water-surface elevation and the wave kinematics are modelled as Fourier series by superposing an arbitrary number of linear waves (Eqs. (3.10) and (3.11)),

$$\eta(t, x) = \sum_{n=1}^N a_n \cdot \cos(k_n \cdot x - \omega_n \cdot t + \varphi_n), \quad (3.14)$$

$$\Phi(t, x, z) = c \cdot x + \sum_{n=1}^N \frac{a_n \cdot g}{\omega_n} \cdot \frac{\cosh(k_n \cdot (d + z))}{\cosh(k_n \cdot d)} \cdot \sin(k_n \cdot x - \omega_n \cdot t + \varphi_n), \quad (3.15)$$

with the water depth d . The respective properties of each superposed wavelet are derived from a power spectral density of the water-surface elevation, called wave-energy spectrum in the following. The determination of these properties as well as of the phase angles φ_n is discussed in Chapter 7. As for the Airy wave, the non-linear terms in the Eqs. (3.6), (3.8), and Eq. (3.9) are neglected. Stretching as described for regular Airy waves in Section 3.2.1 is also to be applied for irregular sea states.

Unless observed wave-energy spectra are available, theoretical models may be applied for the description of sea states. Different types of wave-energy spectra exist. An overview of different wave-energy spectra is given e.g. by Goda (2000). Most commonly applied wave-energy spectra are the Pierson-Moskowitz spectrum (Pierson and Moskowitz, 1964) and the JONSWAP spectrum (Hasselmann et al., 1973), here shown as one-sided spectra,

$$S_{PM}(\omega) = \frac{5}{16} \cdot H_s^2 \cdot \omega_p^4 \cdot \omega^{-5} \cdot \exp\left(-\frac{5}{4} \cdot \left(\frac{\omega}{\omega_p}\right)^{-4}\right) \quad \omega \geq 0, \quad (3.16)$$

$$S_{JS}(\omega) = nf(\gamma) \cdot S_{PM}(\omega) \cdot \gamma^{\exp\left(-\frac{1}{2 \cdot \sigma^2} \cdot \left(\frac{\omega - \omega_p}{\omega_p}\right)^2\right)}, \quad \omega \geq 0, \quad (3.17)$$

with peak-enhancement factor γ , normalising factor $nf(\gamma) = 1 - 0.287 \cdot \ln \gamma$, and bandwidth parameter σ . The peak frequency ω_p denotes the wave frequency associated with the maximum value of the wave-energy spectrum. The peak frequency and the peak period $T_p = \frac{2\pi}{\omega_p}$, respectively, depend on the mean zero-up-crossing period T_z , as stated e.g. in DNV-ST-0437 (2016). The Pierson-Moskowitz spectrum is especially applied for fully-developed sea states with unlimited fetch and unlimited duration of wind exposure. The JONSWAP spectrum was originally developed to consider limited fetch and duration, e.g. as required for the North Sea. Here, values of $\gamma = 3.3$ as well as $\sigma = 0.07$ for $\omega \leq \omega_p$ and $\sigma = 0.09$ for $\omega > \omega_p$ are usually set. DNV-ST-0437 (2016) recommends to apply the JONSWAP spectrum for the design of offshore wind turbines, unless data indicate otherwise.

The Pierson-Moskowitz spectrum and the JONSWAP spectrum, with a peak-enhancement factor of 3.3, are shown in Fig. 3.5 with $H_s = 2 \text{ m}$ and $T_p = 5 \text{ s}$.

Higher-order sea state

The linear sea state is often used in engineering practice due to its simplicity and adequate accuracy for most applications. Besides the linear sea state as superposition

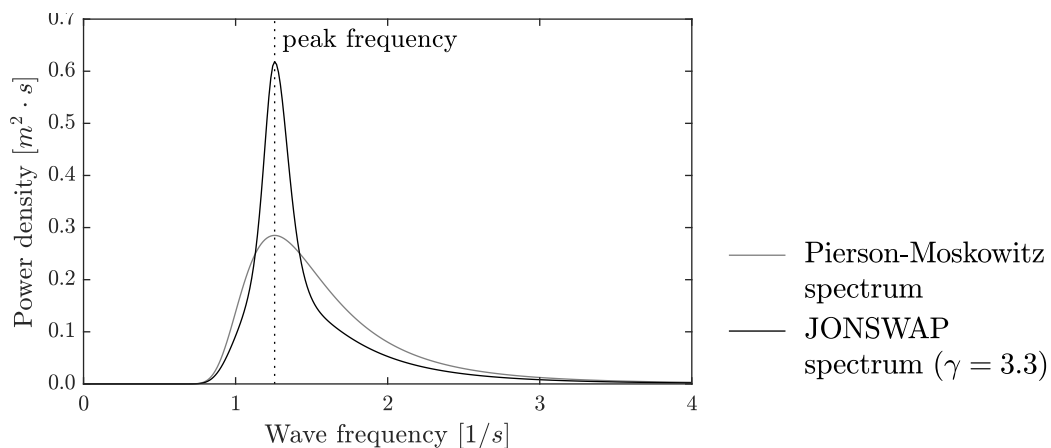


Figure 3.5: Pierson-Moskowitz spectrum and JONSWAP spectrum with $H_s = 2\text{ m}$ and $T_p = 5\text{ s}$

of multiple Airy waves, sea-state models exist which consider the non-linear terms in the governing equations, referring to Eqs. (3.6), (3.8), and (3.9).

Sharma and Dean (1981) proposed a sea-state model which solves the governing equations correctly for the second order. Second-order terms are added to the linear sea state. The properties of the second-order terms depend on the properties of the wavelets of the linear sea state. More information is given in the corresponding research report (Sharma and Dean, 1979). The guideline DNV-RP-C205 (2019) also refers to the second-order sea-state model according to Sharma and Dean (1981). Higher-order sea states can be modelled by means of the so-called “higher-order spectral method”. Even though the numerical effort is increased in comparison to the linear sea state and the second-order sea state, the sea state is modelled more accurately with respect to the governing equations. Sea states can be modelled up to fifth order. Detailed information on these higher-order sea states is given in e.g. Bonnefoy et al. (2010) and Desmars (2020).

Within the context of the thesis, only linear sea states are considered.

3.2.3 Currents

Different types of currents exist. The most common types of currents to be accounted for offshore structures are tidal currents and wind-generated currents. Rise and fall of sea levels as well as resulting tidal currents occur due to gravitational forces exerted by the Moon and the Sun. Wind-generated currents are caused by shear forces due to the interaction between wind and water surface.

Within the load simulation of offshore structures according to DNV-RP-C205 (2019), the vertical profile of tidal currents are to be modelled with a power-law profile,

$$c_{tidal}(z) = c_{tidal}(0) \cdot \left(\frac{d+z}{d}\right)^\alpha, \quad (3.18)$$

with the power-law exponent α . The vertical profile of wind-generated currents can be modelled as constant or linear.

Current velocities are considered in the determination of water-particle velocities, either by adding to the velocity term of linear waves or by including in the numerical approximation of non-linear waves.

3.2.4 Calculation of wave-induced loads

In offshore engineering, Morison's equation (Morison et al., 1950) is usually applied for the calculation of wave-induced loads acting on slender structural members,

$$f = f_d + f_m = 0.5 \cdot C_d \cdot \rho_w \cdot D \cdot u_{\perp} \cdot |u_{\perp}| + C_m \cdot \rho_w \cdot A \cdot \dot{u}_{\perp}, \quad (3.19)$$

with the diameter D and cross-section area A of the structural member. The index \perp denotes the wave kinematics perpendicular to the respective beam axis, referring to Fig. 3.2. Morison's equation consists of the drag term f_d and of the inertia term f_m . The values of the hydrodynamic coefficients, which include the drag coefficient C_d and the inertia coefficient C_m , are functions of the general flow regime around the structural member and of the surface roughness of the structural member. The flow regime around structural members is characterised mainly by the dimensionless quantity of the Keulegan-Carpenter number. The Keulegan-Carpenter number is the ratio of drag forces to inertia forces. Low Keulegan-Carpenter numbers mostly occur at fixed offshore structures, especially at those with increased diameters.

The flow regime around the primary structural member is alternated by potentially installed appurtenances. Their dimension, position, and orientation relative to the main member and the flow direction impact the additional loads due to the appurtenances. Detailed formulae to determine the local hydrodynamic coefficients for the primary structural member including the effects of appurtenances are given in e.g. IEC 61400-3-1 (2019, Annex C.6).

Morison's equation is only valid for slender structures with a maximum ratio of structural diameter to wave length of 0.2 (IEC 61400-3-1, 2019). Wave diffraction, which is the noticeable modification of the wave pattern due to the structure, is to be considered for greater ratios of structural diameter to wave length. Wave diffraction is usually accounted for by correcting the inertia term of Morison's equation in accordance with MacCamy and Fuchs (1954).

For the design of offshore wind turbines, the values for the hydrodynamic coefficients are to be set in accordance to the corresponding standards, e.g. DNV-RP-C205 (2019) and IEC 61400-3-1 (2019). Unless stated otherwise, values of $C_d = 0.7$ and $C_m = 2.0$ are used within this thesis. The selection of these values may be arguable, but it does not impair the findings of the thesis.

3.2.5 Wave-induced loads in frequency domain

Wave-induced loads in time domain are calculated with Morison's equation, referring to Eq. (3.19), and with local and temporal water-particle velocities and water-particle accelerations. For the calculation of wave-induced loads in frequency domain, the water-particle kinematics and the water-surface elevation are to be represented in frequency domain as well.

The drag term of Morison's equation is discussed in greater detail in the following due to the non-linearity of the term $u_{\perp} \cdot |u_{\perp}|$, referring to Eq. (3.19). The power spectral density of the linear inertia term is easily found on the basis of the linear power spectral density of the water-surface elevation.

Sea states and their water-particle kinematics are simulated up to the still water level in frequency domain. Therefore, alternating loading within the splash zone is not modelled. Stretching is not to be considered for the simulation of wave-induced loads in frequency domain. Stretching as described in Section 3.2.1 eventually results in additional non-linearities which are to be handled during the simulation in frequency domain.

Periodic Airy wave

For a periodic Airy wave, both the water-particle velocity and the water-particle acceleration are sinusoidal waves, referring to Eq. (3.11). Hence, the inertia term of Morison's equation is a sinusoidal wave as well. Due to its non-linear term $u \cdot |u|$, the drag term of Morison's equation is not a sinusoidal wave, but it can be modelled as superposition of several sinusoidal waves with natural multiples of the base wave frequency via Fourier analysis, referring to Eq. (2.2). Derivation of the Fourier series for the term $u \cdot |u|$ for periodic Airy waves without consideration of current is found in e.g. Clauss et al. (1992) and Naess and Moan (2012). Barltrop and Adams (1991) shortly discusses the impact of currents on the Fourier series of the non-linear drag term. Considering water-particle velocities including current velocity, $u = c + a_u \cdot \cos(-\omega \cdot t)$, with the amplitude of the sinusoidal wave a_u , the Fourier series of the term $u \cdot |u|$ reads as summarised in Appendix A3. The Fourier coefficients are shown in Fig. 3.6 for different ratios of current velocity c and amplitude of sinusoidal wave a_u . They are normalised by the value for the base wave frequency. Since the Fourier coefficients are presented in logarithmic scale, their respective signs are added, and Fourier coefficients with a value of zero are marked.

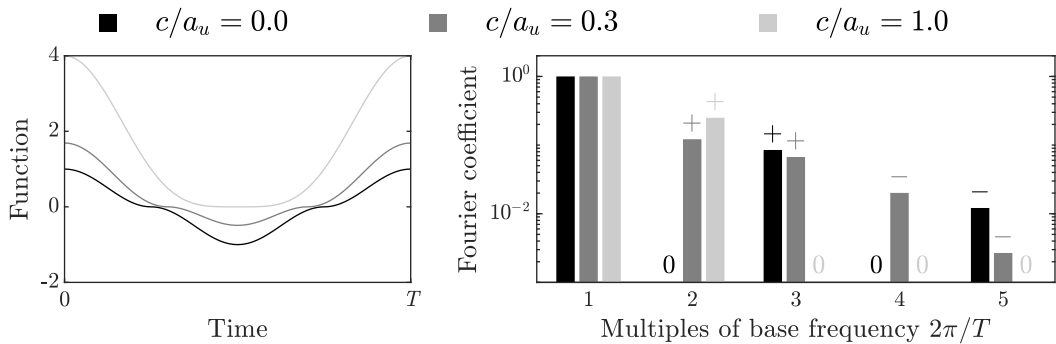


Figure 3.6: Periodic function $u \cdot |u|$ with $u = c + a_u \cdot \cos(-\omega \cdot t)$ (left) and corresponding Fourier coefficients normalised by the respective value for the base wave frequency ω (right) for different ratios of constant current c to amplitude of sinusoidal wave a_u

As visualised in Fig. 3.6 and stated in Eq. (A3.6), the non-linear drag term of Morison's equation for regular Airy waves consists of sinusoidal waves with odd multiples of the base frequency for no current existing. In case that the current velocity is equal to the amplitude of the sinusoidal wave, the drag term consists of a constant and two

sinusoidal wavelets with the base wave frequency and twice the base wave frequency, respectively. This is also true for current velocities greater than the amplitude of the sinusoidal wave, referring to Eq. (A3.5). For current velocities between these two limit states described, the drag term is described as the superposition of sinusoidal wavelets with all multiples of the base frequency. The one-sided Fourier coefficients of the term $u \cdot |u|$ with $u = c + a_u \cdot \cos(-\omega \cdot t)$ are dependent on the ratio of current velocity c to amplitude of sinusoidal wave a_u , as shown in Fig. 3.7. Here, the amplitude of the sinusoidal wave is set as unity.

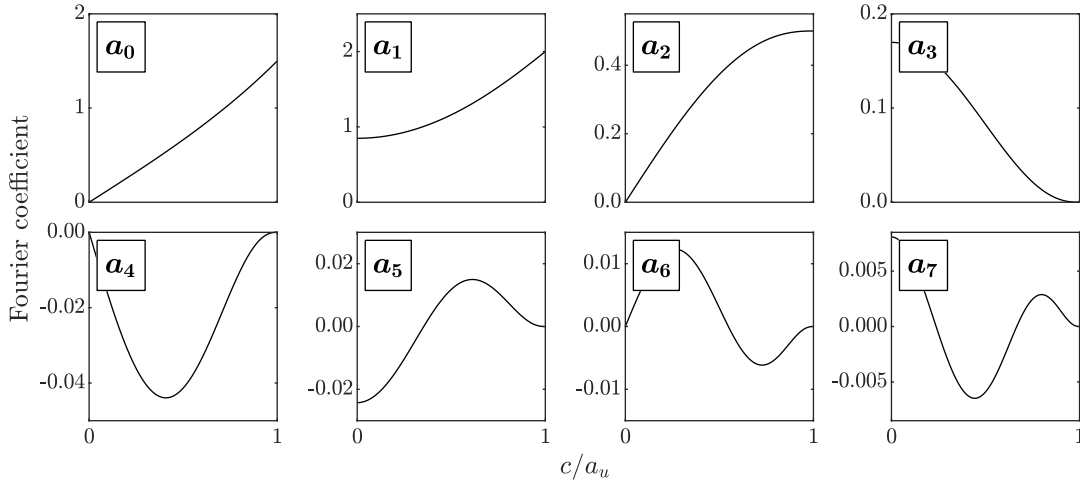


Figure 3.7: Fourier coefficients of the function $u \cdot |u|$ with $u = c + a_u \cdot \cos(-\omega \cdot t)$ in dependence of the ratio of constant current c to amplitude of sinusoidal wave a_u , here with $a_u = 1$, referring to Eq. (A3.5)

As already described for Fig. 3.6, Fourier coefficients for even multiples of the base frequency are zero for no existing current. The mean value a_0 increases with increasing ratio of current velocity to amplitude of sinusoidal wave. Most importantly, it can be noticed from Fig. 3.7 that the Fourier coefficients a_1 for the base frequency and a_2 for twice the base frequency increase with increasing ratio of current velocity to amplitude of sinusoidal wave for constant amplitude of sinusoidal wave. The Fourier coefficient for thrice the base frequency decreases. All the other Fourier coefficients for odd multiples of the base frequency have a non-zero value for no existing current and have a value of zero for a current velocity equal to the amplitude of the sinusoidal wave, and the Fourier coefficients for even multiples of the base frequency greater than two have a value of zero for no existing current and for a current velocity equal to the amplitude of the sinusoidal wave. In between these two limit cases, the behaviour of the Fourier coefficients over increasing ratio of current velocity to amplitude of sinusoidal wave may be described qualitatively as a decaying oscillation, and the number of zero-crossings increases with increasing multiple of the base frequency. The absolute maximum values of the Fourier coefficients decrease with increasing multiple of the base frequency.

The Fourier series is usually modelled with a limited number of Fourier coefficients. For example, root-mean-square errors of 0.1214, 0.0184, and 0.0065 are calculated for the Fourier series according to Eq. (A3.6) with $n \leq 1$, $n \leq 3$, and $n \leq 5$, respectively. The respective approximated maxima underestimate the theoretical maximum by 0.1512,

0.0184, 0.0057. Here, the amplitude of the sinusoidal wave a_u is unity, and the current c is zero.

Irregular sea states

The water-particle velocity and the water-particle acceleration of a linear sea state are random Gaussian signals. The water-surface elevation can be described by a power spectral density, e.g. by the Pierson-Moskowitz spectrum or the JONSWAP spectrum, referring to Eq. (3.16) and Eq. (3.17), respectively. The water-particle kinematics are also modelled as power spectral densities in frequency domain as well. Similar to the periodic Airy wave, as described above, the inertia term of Morison's equation in frequency domain is easily obtained. Again, the non-linear term $u \cdot |u|$ does not allow an analytical description of the drag term of Morison's equation, but the drag term is to be approximated.

Differentiation of the velocity potential of a linear sea state according to Eq. (3.15) with respect to horizontal direction yields the horizontal water-particle velocity, referring to Eq. (3.3). The vertical water-particle velocity as well as the corresponding water-particle accelerations are Gaussian signals as well. The power spectral density of the horizontal water-particle velocity reads as follows,

$$S_{uu}(\omega, z) = \left(\frac{g \cdot k(\omega)}{\omega} \cdot \frac{\cosh(k(\omega) \cdot (d+z))}{\cosh(k(\omega) \cdot d)} \right)^2 \cdot S_{\eta\eta}(\omega) , \quad (3.20)$$

with the power spectral density of the water-surface elevation $S_{\eta\eta}$. Based on the power spectral density of the horizontal water-particle velocity, the drag term of Morison's equation can be approximated as described by Borgman (1965). Gudmestad and Connor (1983) state an approximation of fourth order,

$$\begin{aligned} \frac{S_{fdfd}(\omega)}{\left(\frac{1}{2} \cdot \rho_w \cdot C_d \cdot D\right)^2 \cdot \sigma_u^4} &= a_0 + \sum_{n=1}^4 a_n \cdot \frac{\langle S_{uu}(\omega) \rangle^{*n}}{\sigma_u^{2 \cdot n}} \\ a_0 &= \left(\Phi \cdot \left(\frac{c}{\sigma_u}\right)^2 + \Phi + 2 \cdot \phi \cdot \frac{c}{\sigma_u} \right)^2 , \quad a_1 = 4 \cdot \left(\Phi \cdot \frac{c}{\sigma_u} + 2 \cdot \phi \right)^2 , \\ a_2 &= 2 \cdot \Phi^2 , \quad a_3 = \frac{8}{3} \cdot \phi^2 , \quad a_4 = \frac{2}{3} \cdot \left(\phi \cdot \frac{c}{\sigma_u} \right)^2 , \end{aligned} \quad (3.21)$$

with $\Phi = 2 \cdot \operatorname{erf}\left(\frac{c}{\sigma_u}\right)$ and $\phi = \frac{1}{\sqrt{2\pi}} \cdot \exp\left(-\frac{1}{2} \cdot \left(\frac{c}{\sigma_u}\right)^2\right)$. c is the current velocity, and σ_u is the standard deviation of the horizontal water-particle velocity. $\langle S_{uu}(\omega) \rangle^{*n}$ denotes the n -fold convolution with itself, referring to Section 2.1.2.

Exemplarily, the normalised power spectral density of the horizontal water-particle velocity as well as the normalised n -fold convolutions with itself are shown in Fig. 3.8 (left). The horizontal water-particle velocity is calculated at still water level for a JONSWAP spectrum according to Eq. (3.17) with $H_s = 2.0 \text{ m}$, $T_p = 5.0 \text{ m}$, and $\gamma = 3.3$ for a deep-water location. The corresponding normalised power spectral density of the drag force according to Eq. (3.21) is shown in Fig. 3.8 (right) for current velocities of zero (black line) and of half the standard deviation of the horizontal water-particle velocity (grey line). The standard deviation of the horizontal water-particle velocity has a value of $\sim 0.81 \text{ m/s}$ for the analysed sea state.

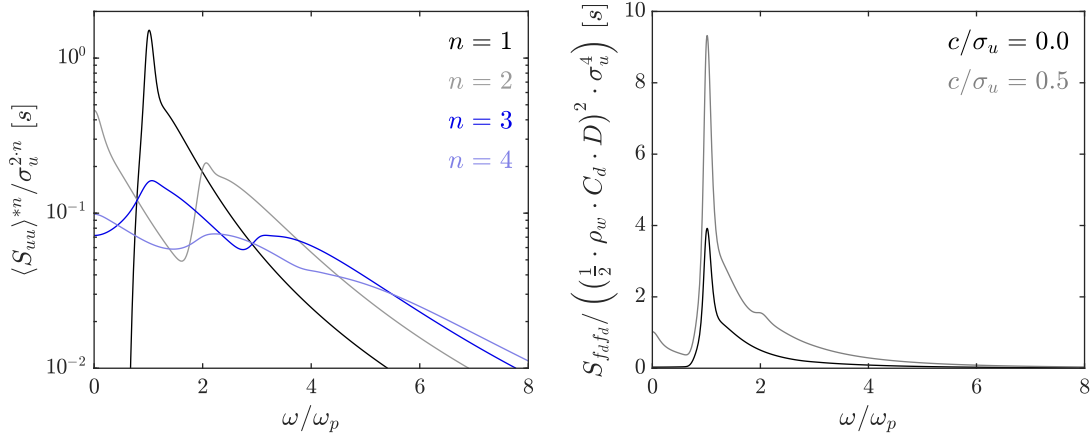


Figure 3.8: Normalised power spectral density of the horizontal water-particle velocity as well as its n -fold convolutions (left) and the normalised power spectral density of the drag force according to Eq. (3.21) for different current velocities (right)

Depending on the current velocity as well as on the standard deviation of the horizontal water-particle velocity, the terms of the n -fold convolutions contribute to the power spectral density of the drag force.

The power spectral density of the horizontal water-particle velocity S_{uu} has its maximum value close to the peak wave frequency of the respective wave-energy spectrum. For the n -fold convolutions of higher order, more than one peak within the power spectral densities are found. The 2-fold convolution and the 4-fold convolution have peaks at zero and close to twice the peak wave frequency, and the 3-fold convolution has peaks in vicinity of the peak wave frequency and of the trice the peak wave frequency. In general, it is observed that peaks of the n -fold convolutions of even order are close to even wave frequencies up to n -times the peak wave frequency, and that peaks of the n -fold convolutions of odd order are close to odd wave frequencies up to n -times the peak wave frequency.

The impact of currents on the power spectral density of the drag force can be observed in Fig. 3.8 (right). The power spectral density of the drag force including current contains an increased amount of energy. Additionally, an additional peak at twice the peak wave frequency is noticeable in comparison to the drag force without current.

The coefficients to be applied on the n -fold convolutions of the horizontal water-particle velocity S_{uu} depend on the ratio of current velocity c to the standard deviation of the horizontal water-particle velocity σ_u . The coefficients a_n , referring to Eq. (3.21), are shown in Fig. 3.9 in dependence of this ratio.

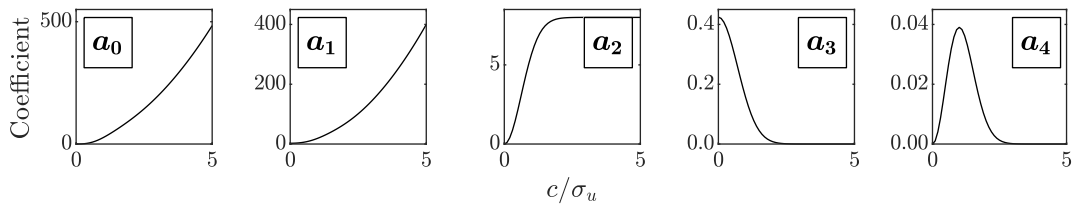


Figure 3.9: Coefficients of n -fold convolutions of the horizontal water-particle velocity for the power spectral density of the drag force according to Eq. (3.21)

For increasing current velocity, the term ϕ tends to zero, and Φ tends to 2, referring to Eq. (3.21). Similar to the results presented for the periodic Airy wave above, the terms for n -fold convolution with orders up to 2 of Eq. (3.21) increase with increasing current velocity, and the terms for higher order decrease.

The coefficient for the power spectral density of the horizontal water-particle velocity increases with increasing current velocity. Its value is always greater than the coefficients for n -fold convolutions of higher order. The coefficient for the 2-fold convolution increases with increasing current velocity as well. Its value is zero in case of no current, and its limit value is 8. For no current, the term of the 3-fold convolution is of secondary relevance, with a value of $\frac{4}{3\pi} \approx 0.4244$. It decreases and tends to zero with increasing current velocity. The coefficient for the 4-fold convolution is zero for no current, increases for up to $\frac{c}{\sigma_u} \approx 1.0$, and tends to zero for greater values. The maximum value of this coefficient is approximately a tenth of the maximum value of the coefficient of the 3-fold convolution.

In comparison to the normalised n -fold convolutions, the normalised power spectral density of the horizontal water-particle velocity contains the most energy and has the most decisive maximum value. It is also dominant as product with the corresponding coefficient. For the normalised power spectral density of the drag term of Morison's equation, only the peak close to the peak wave frequency is observed in case of no current. The power spectral density also possesses increased energy near twice the peak wave frequency and at zero for increased current velocities. No other peaks are noticeable at other multiples of the peak wave frequency.

In conclusion, not only the main wave frequencies of the water-particle velocity are to be considered for the load simulation but also the wave frequencies of the n -fold convolutions which are minor in the signal of the non-linear drag term of Morison's equation. This is of importance for the structural-dynamic analysis, since other Eigen modes may be excited, especially in case of currents. An study on the impact of currents is carried out in Section 8.2.

3.2.6 Load regimes of wave-induced drag and inertia loads

Mostly depending on the wave conditions and the dimension of the structure, either the drag term or the inertia term of Morison's equation predominates. These predominances are shown in e.g. Chakrabarti (1981) and Clauss et al. (1992) for periodic Airy waves. The main findings are concluded below. These researchers did not consider currents in their respective discussions. As presented in Section 3.2.5, currents may be significant for the structural-dynamic load simulation. Hence, the existence of currents is additionally included in the analysis.

The load regimes of horizontal load at water-surface elevation of regular Airy waves in deep water are shown in Fig. 3.10 for different current velocities. The ratio of maximum drag load and maximum inertia load is analysed on the left, and the ratio of maximum total load and maximum inertia load is analysed on the right. The load regimes are shown in dependence of the dimensionless parameters $\pi \cdot D/L$ and $\pi \cdot H/D$, with pile diameter D , wave length L , and wave height H . The latter parameter is the Keulegan-Carpenter number for a linear wave in deep water. Values of the hydro-

dynamic coefficients are $C_d = 1.0$ and $C_m = 2.0$. These values are typically applied for the presentation of the predominances, referring to e.g. Chakrabarti (1981) and Clauss et al. (1992). The breaking-wave limit for deep water, with wave breaking to be considered for $H/L > 1/7$, and the application limit of Morison's equation, $D/L = 0.2$ (IEC 61400-3-1, 2019), are also shown. The current velocities are given as dimensionless multiples of the term $\sqrt{g \cdot D}$. For diameters of 1 m and 10 m, the term equals ~ 3.13 m/s and ~ 9.90 m/s, respectively. The load regimes are shown for multiples of this term of 0 (dotted line), 0.10 (dashed line), and 0.32 (solid line). No current exist for a multiple of 0. Current velocities of ~ 1.0 m/s are considered for a pile diameter of 1 m and a multiple of 0.32 as well as for a pile diameter of 10 m and a multiple of 0.10.

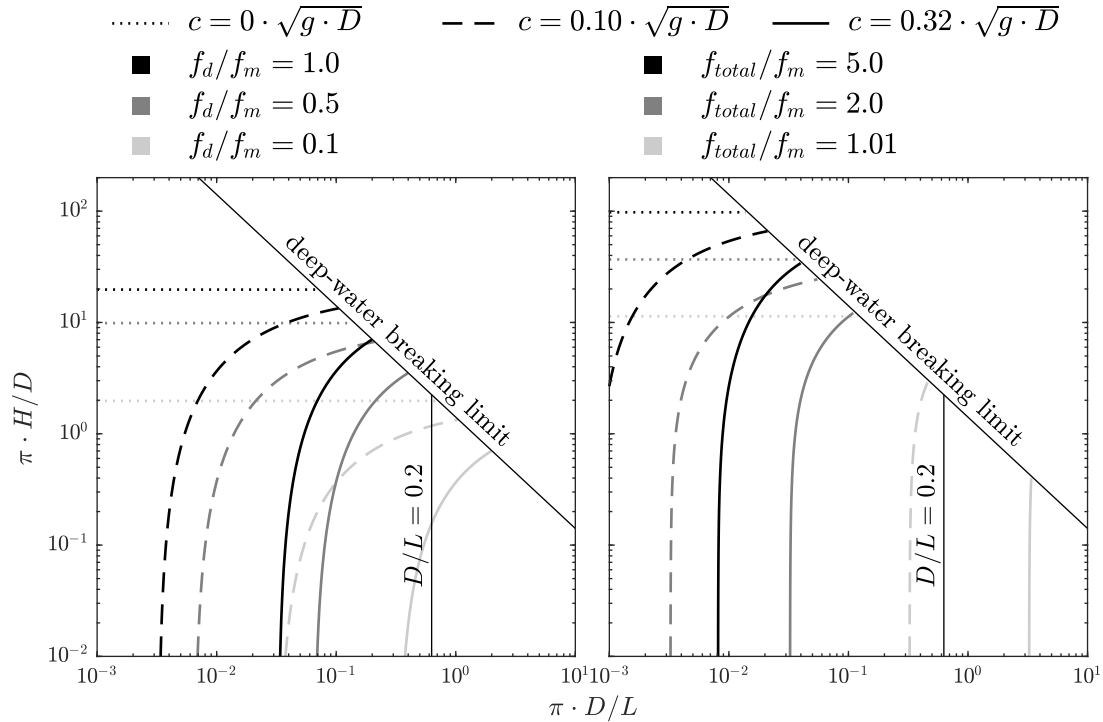


Figure 3.10: Load regimes of horizontal load at water-surface elevation of regular Airy waves in deep water for different current velocities with hydrodynamic coefficients $C_d = 1.0$ and $C_m = 2.0$: (left) ratio of maximum drag load and maximum inertia load, (right) ratio of maximum total load and maximum inertia load

In general, one can note in Fig. 3.10 (left) that the significance of the drag load increases with the wave height. As described in Chakrabarti (1981) and Clauss et al. (1992) for no current (dotted line), the amplitude of drag load and inertia load are equal for $\pi \cdot H/D \approx 20$. The drag load for $\pi \cdot H/D < 2$ may be neglected in wave-load calculation. Otherwise, it shall be considered as the predominance of the drag load increases with increasing wave height (Chakrabarti, 1981). Considering currents, the significance of the drag term increases with increasing current velocity. As the load regime for no currents only depends on the wave height, it depends on wave height as well as on wave period and wave length of the Airy wave for existing currents.

The load regimes of horizontal load at water-surface elevation of linear sea states in deep water are shown in Fig. 3.11 for diameters of 1 m (left) and of 10 m (right). These dimensions are representative for jacket legs and monopile substructures, respectively.

The load regimes are analysed for current velocities of 0.0 m/s , 0.5 m/s , and 1.0 m/s . The load regimes are shown in dependence of the dimensionless parameters $\pi \cdot D/L_p$ and $\pi \cdot H_s/D$, where the wave length L_p is calculated according to Eq. (3.12) with the peak period T_p . Here, the load regimes are defined as ratio of damage-equivalent horizontal drag loads and damage-equivalent horizontal total loads. On the basis of load simulations carried out for sea states with a peak-enhancement factor of 3.3, damage-equivalent loads are calculated according to Eq. (6.1) with the slope of the SN curve of $m = 4$. Again, values of the hydrodynamic coefficients are $C_d = 1.0$ and $C_m = 2.0$. The plotted breaking-wave limit is $H_s/L_p = 0.04$ for sea states according to Paulsen et al. (2019). In addition to different levels of load regimes, the occurrence frequencies of significant wave height and peak period at FINO1 for the period from 2003 to 2017 are shown. The occurrence frequencies are normalised by their maximum value. The respective wave lengths are calculated with Eq. (3.12) without current.

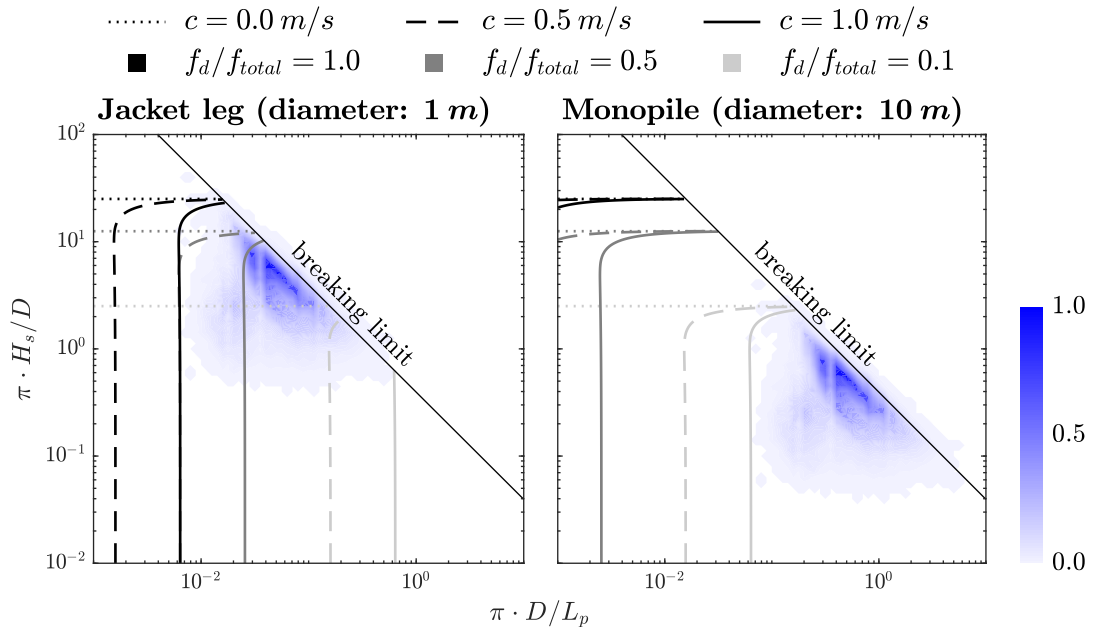


Figure 3.11: Load regimes of linear sea states in deep water for different current velocities with hydrodynamic coefficients $C_d = 1.0$ and $C_m = 2.0$ and peak-enhancement factor $\gamma = 3.3$: ratio of damage-equivalent horizontal drag load and damage-equivalent horizontal total load at water-surface elevation and the respective occurrence frequencies (blueish scale) (left) for jacket legs and (right) for monopile substructures

Similar to regular Airy waves shown in Fig. 3.10 (left), the significance of the drag load increases for greater significant wave heights. The levels of load regimes also shift to greater values of $\pi \cdot D/L_p$ and thus to greater peak periods for increasing current velocities. Comparison of the current-depending load levels for diameters of 1 m and of 10 m shows that the load levels shift to smaller values of $\pi \cdot D/L_p$ for increasing diameters. Visual interpretation indicates that the current-depending load levels may be inversely proportional to the diameter.

Significant differences regarding load levels and the shown occurrence frequency can be seen for the different diameters of 1 m and of 10 m . For smaller diameters, the same sea-state conditions occur in Fig. 3.11 at smaller values of $\pi \cdot D/L_p$ and greater values of

$\pi \cdot H_s/D$ and thus in regions where the drag term contributes more significantly to the wave load. For a diameter of 1 *m*, the ratio of damage-equivalent horizontal drag load and damage-equivalent horizontal total load at water-surface elevation of 0.1 is exceeded by $\sim 75\%$ of the considered sea states for no currents and by all considered sea states for a current velocity of 1.0 *m/s*. In comparison, the ratio of damage-equivalent horizontal drag load and damage-equivalent horizontal total load at water-surface elevation of 0.1 for a diameter of 10 *m* is exceeded by less than 0.03% of the considered sea states for no currents and by $\sim 0.05\%$ of the considered sea states for a current velocity of 1.0 *m/s*. The load regimes of Morison's equation as well as the impact of currents are shown in Fig. 3.10 and Fig. 3.11 for simplified assumptions regarding water depth, wave modelling and load calculation. Deviations from these assumptions lead to different load regimes and different occurrence probabilities of load regimes. Wave lengths increase for shallower waters, and greater current velocities also lead to increased wave lengths, referring to Eq. (3.12). Hence, the term $\pi \cdot D/L$ for regular waves and the term $\pi \cdot D/L_p$ for sea states decrease, which result in greater load levels of load regimes for currents. In case non-linear wave theories are applied instead of the Airy wave theory, the drag load contributes more significantly to the total wave load (Clauss et al., 1992). Hydrodynamic coefficients, which depend on surface roughness and flow conditions as described above, are also subject of change.

3.3 Long-term distribution of environmental data

For the load analysis of structures with a planned design lifetime of several decades, detailed environmental conditions, their long-term behaviour and long-term evolution as well as the correlations between different parameters are of importance. Long-term statistics of environmental conditions shall represent the annual statistics in appropriate manner. Long-term statistics are obtained either by means of weather simulations or from long-term measurements. Distribution functions of single parameters and joint distribution functions describing the combined occurrence of several parameters can be derived on the basis of these data sets.

Data series based on either measurements or simulations have advantages and disadvantages. Inaccuracies of the simulated data may occur due to modelling of the simulation process, whereas correctly-applied measurement data register the in-situ environmental conditions. However, potential failures of the measurement equipment result in missing data or erroneous data. Once validated against measurement data, simulations may model environmental conditions in a satisfactory manner.

In the following, metocean data measured at the research platform FINO1 are analysed and further discussed regarding the derivation of the respective statistical properties and subsequent definition of a design basis¹. Here, the chronological sequences of wind velocity at 90 *m* above mean sea level, of significant wave height, and of peak period are investigated. Measurement data for wind velocity at 90 *m* above mean sea level exist between 1 January 2004 and 30 September 2017, and measurement data for significant

¹The metocean data measured at the research platform FINO1 are kindly provided by the Bundesamt für Seeschifffahrt und Hydrographie (BSH, Federal Maritime and Hydrographic Agency). The research project FINO is funded by the German Federal Ministry for the Environment, Nature Conservation and Nuclear Safety (BMU) and the Project Management Jülich (PtJ).

wave height and peak period exist between 30 July 2003 and 31 October 2017. The wind velocity is measured with a cup anemometer, and the sea-state parameters are measured with a radar-based wave monitoring system (Herklotz, 2007; Leiding et al., 2016).

3.3.1 Seasonal dependence of metocean data

Environmental conditions mostly have a seasonal dependence. This dependency is shown in Fig. 3.12 for the wind velocity at 90 m above mean sea level (top) and for the significant wave height (bottom), showing non-exceedance probabilities for the months March, July, and November (left) and mean values and 95%-quantiles (right) as well as the respective annual properties. The monthly and annual statistic properties are derived from the measurement data of the research platform FINO1 for the years 2004 to 2016.

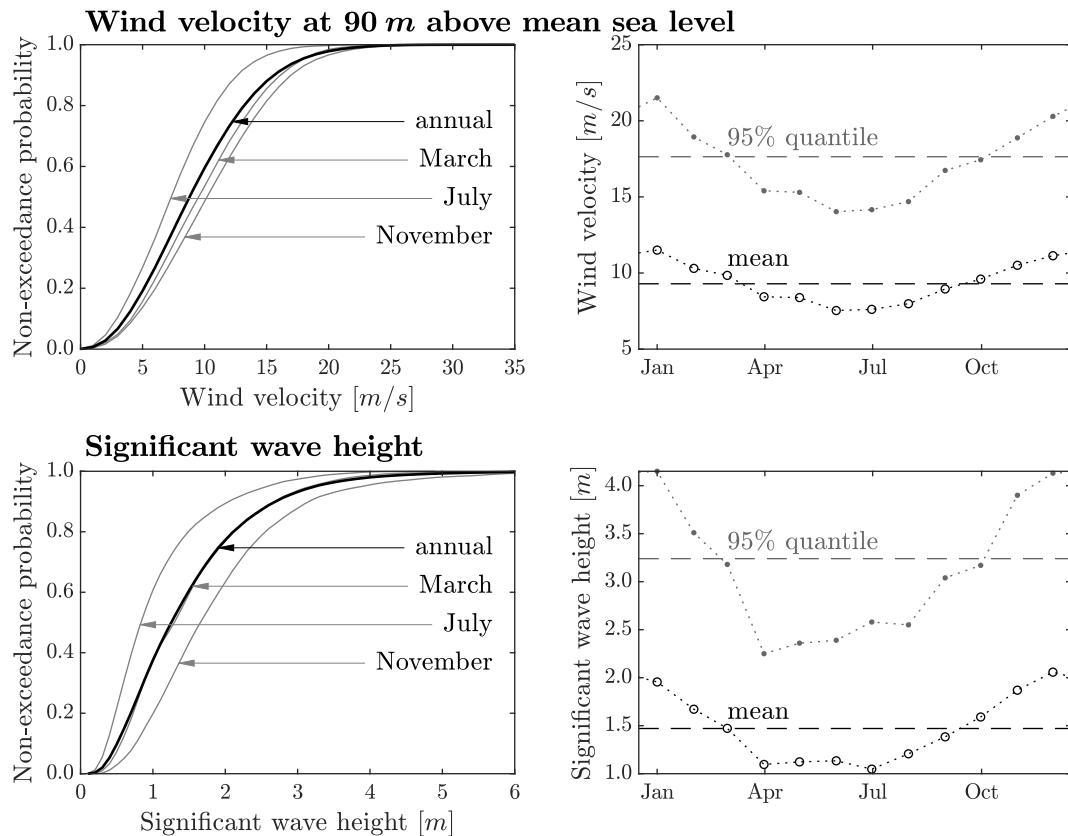


Figure 3.12: Monthly statistical properties at the research platform FINO1 for wind velocity at 90 m above mean sea level and significant wave height summarised for the years 2004 to 2016: (left) non-exceedance probabilities as well as (right) mean values and 95%-quantiles

One can see that the shown monthly distribution are not equal to the other monthly distributions. Annual distribution functions and monthly distribution functions also differ in general. Greater values for wind velocity at 90 m above mean sea level and significant wave height and therefore more severe metocean conditions are observed for autumn- and winter seasons. Mild metocean conditions and their statistical estimation

are important for the installation of offshore wind turbines, as mentioned by Lohaus et al. (2015) for grout-installation processes.

3.3.2 Data availability

In order to assess the data availability, wind velocity at 90 m above mean sea level, significant wave height, and peak period measured at the research platform FINO1 are exemplarily analysed. The derived annual data availabilities are presented in Tbl. 3.1 for the years 2003 to 2017. Monthly data availabilities for the years 2003 to 2017 are shown in Fig. 3.13.

Table 3.1: Yearly data availability at the research platform FINO1 for wind velocity at 90 m above mean sea level, significant wave height, and peak period for the years 2003 to 2017 (values in percentage)

	Year														
	2003	2004	2005	2006	2007	2008	2009	2010	2011	2012	2013	2014	2015	2016	2017
v_{wind}	–	97.6	95.0	99.4	90.6	94.2	99.7	99.9	95.8	95.6	89.5	87.4	88.0	98.1	73.7
H_s	14.9	52.6	88.5	72.6	74.5	88.8	62.7	71.9	92.1	90.8	97.3	69.1	90.3	67.2	83.3
T_p	15.5	53.0	88.8	72.9	74.5	88.8	62.7	71.9	92.1	90.8	97.3	69.1	90.3	67.2	83.2
$v_{wind} \& H_s$	–	52.3	83.7	72.5	66.3	83.6	62.4	71.8	88.0	86.4	88.4	61.2	79.4	65.7	73.7
$H_s \& T_p$	14.9	52.6	88.5	72.6	74.5	88.8	62.7	71.9	92.1	90.8	97.3	69.1	90.3	67.2	83.2

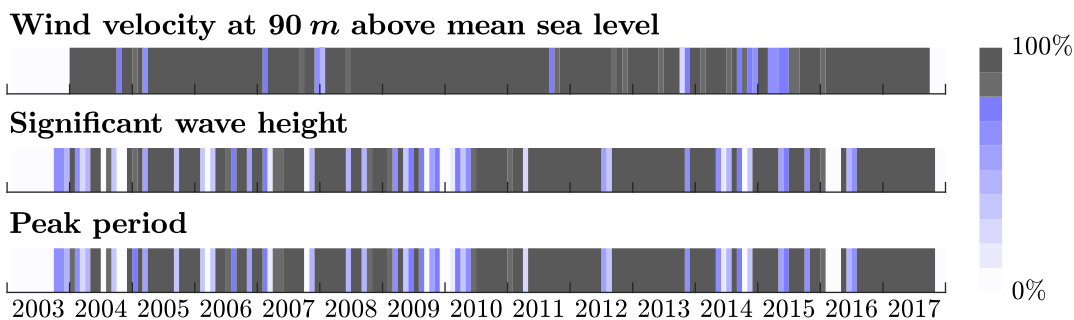


Figure 3.13: Monthly data availability at the research platform FINO1 for wind velocity at 90 m above mean sea level, significant wave height, and peak period for the years 2003 to 2017

Data for wind velocity at 90 m above mean sea level are available with a percentage of greater than 85% for each year. The years 2013 to 2015 are noticeable regarding the monthly data availability. Here, the monthly data availability is less than 80% in nine months and less than 60% in one month. At most two months with a data availability less than 80% are observed for all other years presented in Fig. 3.13. The annual and monthly data availabilities of significant wave height and of peak period are almost identical for the years 2003 to 2017. Excluding the year 2003, the annual availabilities are less than 75% within seven of the 14 years of measurements considered, with a minimum of 52.6% and 53.0% for the year 2004, respectively. Only for the years 2011 to 2013, at most two months with a data availability less than 80% are observed. Especially in the previous years, many months with reduced data availabilities are observed. The data availability of significant wave height is greater than 80% in 51 of the 84 months

in the years 2004 to 2010, while 21 and ten months have a data availability of less than 50% and less than 20%, respectively.

Daily data availabilities for wind velocity at 90 m above mean sea level, significant wave height and peak period, summarised for the years 2004 to 2016, are shown in Fig. 3.14. Here, the availability associated to a certain day is the summarised availability at all these particular days of each year considered. For example, the value associated to 5 October represents the data availability of each 5 October of the years 2004 to 2016.

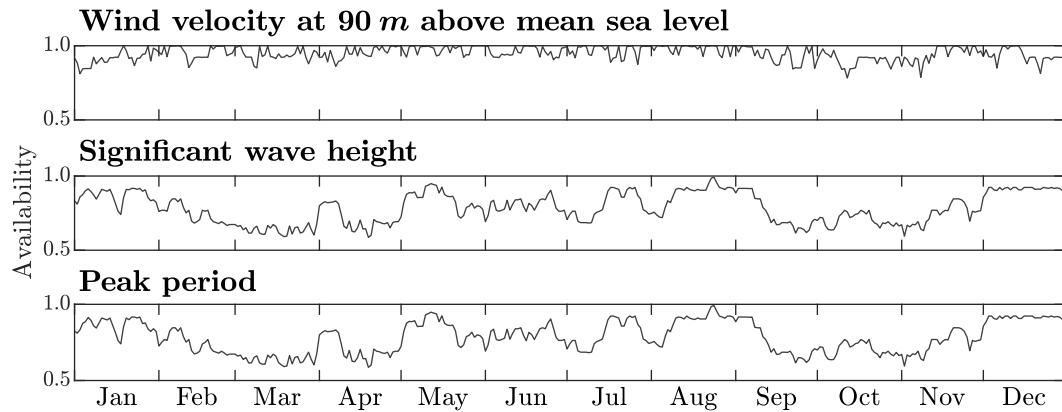


Figure 3.14: Daily data availabilities at the research platform FINO1 for wind velocity at 90 m above mean sea level, significant wave height, and peak period summarised for the years 2004 to 2016

The daily availability for wind velocity at 90 m above mean sea level is above 90% for almost every month. It is below 90% only from beginning of October to beginning of November and from middle of December to middle of January. As for significant wave height and peak period, the daily availabilities strongly scatter between 55% and 100%. Daily availabilities of less than 65% are observed especially for the periods of time from middle of February to end of March, from beginning of April to end of April, and from middle of September to middle of November.

3.3.3 Long-term statistics

At best, complete measurement data of several decades without any gaps are the basis of long-term statistics. At least all months and seasons as well as their respective statistical properties shall be represented in almost equal shares for the accurate deviation of the annual distribution. In case that certain months or seasons are over-represented or under-represented, the resulting annual distribution and the long-term statistics may be biased. Hence, long-term statistics for significant wave height and peak period derived from the presented measurements are to be critically assessed due to the scattering of availability over the course of a year, referring to Fig. 3.14. Due to the almost constant daily availability for wind velocity at 90 m above mean sea level, long-term statistics can be derived for this parameter.

Metocean parameters can be considered as invariant for certain periods of time. The long-term distribution of the environmental data are usually stated in so-called scatter diagrams. They provide the occurrence frequency of environmental parameters which are classified by bins. Usually, scatter tables show the joint distribution of two para-

meters. Exemplarily, the scatter tables of significant wave height and wind velocity at 90 m above mean sea level as well as of significant wave height and peak period are visualised in Fig. 3.15. They are based on the measurements at the research platform FINO1. Instead of evaluating all available years, only the year 2013 is analysed due to the high annual and monthly data availability, referring to Tbl. 3.1 and Fig. 3.13. Detailed scatter tables are given in Appendix A1.

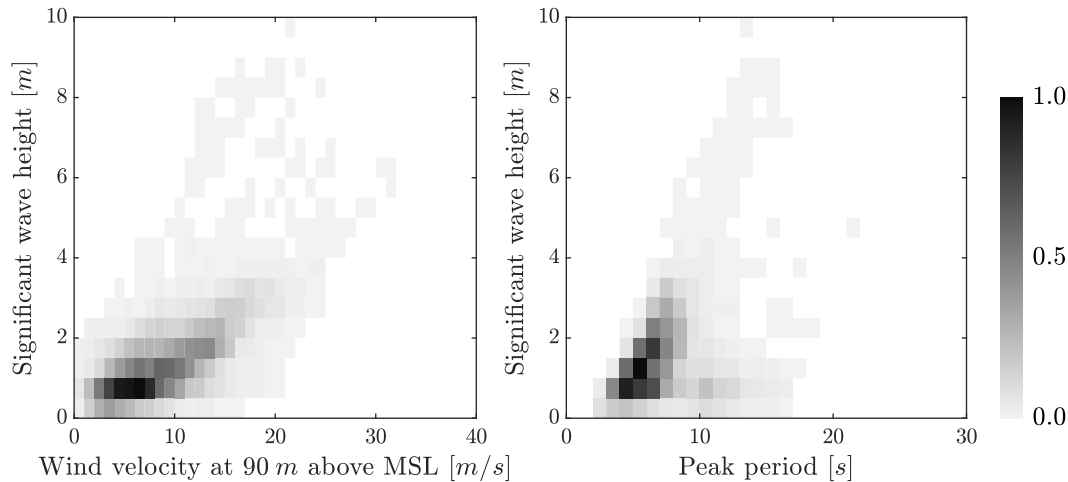


Figure 3.15: Scatter tables of (left) significant wave height and wind velocity at 90 m above mean sea level and of (right) significant wave height and peak period

3.3.4 Extreme metocean values

In order to deduce the distribution function of annual extremes on the basis of measurement data, referring to the block-maxima method as described in Section 2.2.3, complete data sets for several years shall exist such that each annual extreme is included. Otherwise, the parameters of the derived distribution function may be inaccurate or underestimated in case that actual annual extreme values were not recorded. The extrapolation of extreme values with return periods of several years or decades may also be strongly affected by ignoring missing seasonal data. Due to the seasonal dependence of monthly statistics, only annual extremes can be analysed. Analysing maxima of blocks which are smaller than a year does not satisfy the requirement that the analysed values must be independent and identically distributed. Exemplarily, greater values of the significant wave height are measured during autumn and winter in comparison to summer at the research platform FINO1 in the German North Sea (Lohaus et al., 2015). Neglecting these values of autumn- or winter months leads to an underestimation of annual extremes.

Extreme values with certain return periods may be estimated on the basis of the distribution function of high values above a certain threshold via the peak-over-threshold method. Here, the distribution function has the type of the generalised Pareto distribution, referring to Section 2.2.4. Once the generalised Pareto distribution to describe the values above a certain threshold is found, the generalized extreme value distribution can be determined as described in Section 2.2.5. Contrarily to the distribution function of annual extreme, the distribution function of high values above a certain threshold and the respective generalised Pareto distribution depend on the annual distribution

of values. As described above for the long-term statistics, the monthly and seasonal availability of the data shall be approximately constant in order to obtain an unbiased distribution function.

In general, the deviation of the distribution functions for extreme values is very sensitive, i.a. due to often small data sets. Hence, it shall be carried out with care. Further information on extreme metocean conditions is given by e.g. Haselsteiner et al. (2021) and Haselsteiner (2022).

3.4 Environmental-related structural alterations of offshore wind turbines

Structural dynamics and loading on the structure may change during course of time due to the progressive effects of the marine environment. Exemplarily, the submerged structures change the flow regime of the sea water, and they form an artificial habitat for marine life. The impact of marine growth, scour development, and corrosion, which result from the marine environment, on offshore wind turbines are described in the following. The findings for marine growth and scour development were already published by the author in Rolfes et al. (2018, Section 5.5). Structural alterations due to structural damage probably occurring at support structures and at typical structural connections are briefly discussed.

Only a qualitative description of structural alterations is given. No detailed calculations are provided within the thesis. Due to their impact on the structural-dynamic properties of offshore wind turbines, the scattering of the structural alteration over lifetime shall be considered within the probabilistic design. Therefore, the joint occurrence frequencies of different scattering parameters shall also be considered in order to achieve an optimised design.

3.4.1 Marine growth

Offshore structures can be considered as artificial reefs, which are settled by marine fauna and flora. Marine growth, or biofouling, is already observed shortly after installation of offshore structures. The species and the thickness of marine growth depend i.a. on the local position in relation to the mean sea level as well as on the salinity, pH value, temperature, and oxygen content of the seawater. Marine growth varies over the course over a year due to seasonal effects. The volume of marine growth usually stagnates after a few years.

Marine growth results in additional mass, and changes the geometry and surface of structural components. This influences the hydrodynamic loads and the dynamic response of offshore structures. Hence, it is to be considered during the design process of offshore wind turbines and is to be documented in each periodic inspection (BSH, 2015). The thickness of marine growth, which is to be modelled for simulations, is regulated by the standard DNV-ST-0437 (2016). Unless measurement data are available, profiles for marine growth as stated in DNV-ST-0437 (2016) are to be applied. For instance, thicknesses of 150 mm up to a depth of 10 m below lowest astronomical tide and of 100 mm between depths of 10 m below lowest astronomical tide to 40 m below

lowest astronomical tide are to be applied the Southern North Sea (south of latitude of 56°N). In absence of more accurate data, the density of marine growth is set equal to $1,325 \text{ kg} \cdot \text{m}^{-3}$.

Several investigations cover the marine growth for the region of the German offshore wind park alpha ventus. For the research platform FINO1, erected in July 2003 and located 400 m west of alpha ventus, records of marine growth exist for spring, summer and autumn from 2005 to 2007 (Krone et al., 2013). Marine growth was documented for four substructures within the German offshore wind park alpha ventus, erected in the summer 2009, during the period from 2009 to 2012 (Kazmierczak et al., 2010, 2011; Preuß et al., 2012, 2013). It is measured for various depth below the mean sea level. The research studies show that blue mussels (*mytilus edulis*) mostly populate the support structures up to a depth of 5 m below sea level. Studies at the Dutch offshore wind park *Egmond aan Zee* show a qualitatively similar population of the respective substructures (i.a. Bruijs, 2010; Bouma and Lengkeek, 2012). The thicknesses of marine growth are shown in Fig. 3.16 for both the research platform FINO1 as well as for the substructures of the offshore wind turbines R1, R6, M7, and M12 within the offshore wind park alpha ventus. Depths of 1 m , 5 m , and 10 m below the mean sea level are considered. The thicknesses of marine growth are derived on the basis of the biomass as documented in the aforementioned studies and a density of $1,325 \text{ kg} \cdot \text{m}^{-3}$.

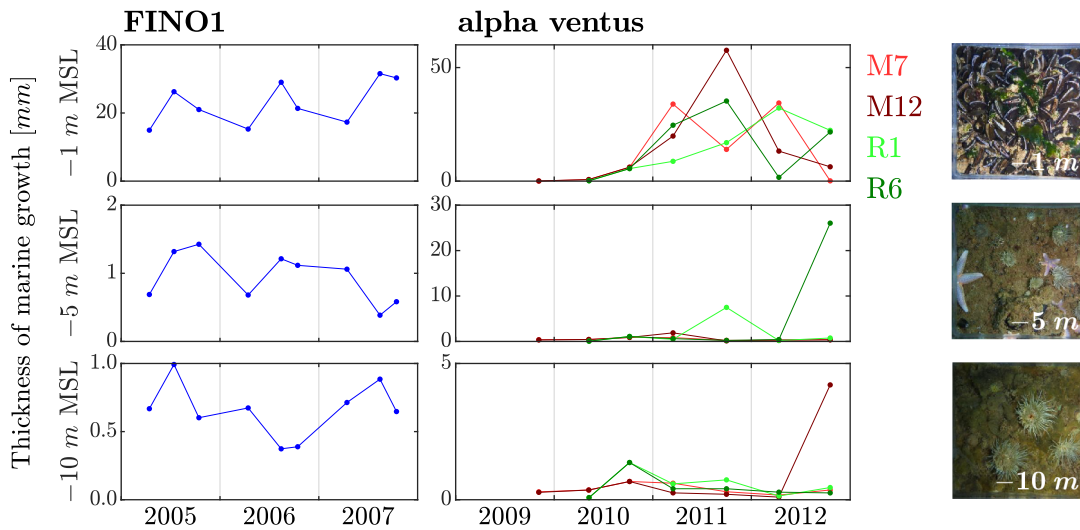


Figure 3.16: Thicknesses of marine growth at the research platform FINO1 and at offshore wind turbines R1, R6, M7, and M12 of the offshore wind park alpha ventus for different depths below mean sea level (MSL) as well as respective photographs of marine growth, observed at alpha ventus, adapted from Preuß et al. (2012, Fig. 100)

Seasonal fluctuations of the biomass is especially notable for a depth of 1 m below mean sea level at FINO1. The thicknesses of marine growth observed during spring and autumn is reduced in comparison to summer. The reasons for seasonal fluctuations are not investigated sufficiently: parts of marine growth may be torn off the substructures during storms, which usually occur during autumn and winter, and new populations of marine fauna and flora are settling during spring. Documenting marine growth since shortly after erection, the initial settling of marine fauna and flora is observed at each

substructure within alpha ventus. It is notable that the thicknesses of marine growth vary at each substructure within alpha ventus. In comparison to the data of marine growth at FINO1, no clear regularities regarding seasonal fluctuations can be derived for alpha ventus during the first three years after erection of the offshore wind turbines.

The Eigen frequencies of the offshore wind turbine are lowered due to marine growth which is mostly an additional mass with almost no additional stiffness. Due to the increased diameter and increased surface roughness, the hydrodynamic loads acting on structural components covered by marine growth are increased.

3.4.2 Soil and scour development

Geotechnical soil investigations at offshore sites are carried out in order to determine the soil layers, their composition, and their physical properties. Load-bearing behaviour of soil and soil-structure interaction are described with reference to corresponding standards (API RP 2A-WSD, 2014; API RP 2GEO, 2014) on the basis of these results. Therefore, non-linear springs along the pile embedded in the soil are usually modelled. Depending on the types of soil layers, different models are stated in API RP 2GEO (2014). Load-deflection curves (p - y curves) describe the soil reaction of laterally-loaded piles, and the soil-structure interaction of axially-loaded piles is modelled by means of axial-load transfer curves (t - z curves) and tip-load-displacement curves (Q - z curves). As an important parameter, the vertical effective stress is used to calculate the shaft friction of piles in cohesionless soils and the end bearing (API RP 2GEO, 2014, Section 8.1.4). Details on soil modelling are found in e.g. Thieken (2015) and Schmoor (2017). Schmoor also proposes an approach to model the soil by means of a probabilistic model. Load-bearing behaviour of soil and soil-structure interaction are impaired due to the development of scour.

Unless appropriate measures are taken, scour develops at offshore structures which are placed at the seabed. The erosion of the seabed sediment results from the interaction of the flow field, the soil, and the structure itself. The flow of water particles due by waves and currents is affected by the structure, which causes increased vortex shedding or wave reflection. Subsequently, enhanced movement of the sediment and hence scour development occur in vicinity of the structure. Global scour and local scour may occur (DNV-ST-0437, 2016). Global scour covers the overall seabed erosion as well as the scour due to pile groups, covering a greater field around the structure. Local scour occurs at single piles. Both types are shown in Fig. 3.17 (left). Scour may result in reduced stability of the respective structures. Therefore, it is to be considered in the design. Protection against scour development is especially required for piles with great diameters placed into the seabed. Monopiles and gravity-based foundations require appropriate measures against scour development. Usually, no scour protection is applied for jacket substructures, whose foundation piles typically have comparatively small diameters.

Requirements for consideration of local scour at offshore wind turbines located at sites with cohesiveless sediment, such as sand, are given in DNV-ST-0126 (2021). For single piles, relative scour depth, which is the ratio of scour depth to pile diameter, of up to 1.3 is observed. Full-scale- oder model-scale test are to be carried out for other structures, such as jackets, or structures installed at sites with cohesive soils in order to

determine the scour development (DNV-ST-0126, 2021). According to API RP 2GEO (2014), scour is not considered as a problem for cohesive soils. Model tests of a tripod substructure, as i.a. installed at the offshore wind park alpha ventus, suggest relative scour depths of 1.1 up to 1.6 (Stahlmann and Schlurmann, 2012; Stahlmann, 2014). Relative scour depths of 0.3 up to 2.0 are observed for experiments with a model of a jacket substructure in different conditions of the sea state (Yang et al., 2010). The temporal scour development at monopiles due to combined loading of waves and currents is studied by Schendel (2018) and Welzel (2021).

There is no general accepted method to model the soil properties of laterally-loaded piles due to scour development. API RP 2GEO (2014) suggests the reduction of the vertical effective stress for laterally-loaded piles as shown in Fig. 3.17, but the standard also allows other methods derived from practice and experience. The vertical effective stress is reduced linearly with depth below the local scour. A slightly different approach is proposed by Zaaijer et al. (2002). Here, the vertical effective stress is reduced linearly by global scour, and it is linearly reduced by local scour until the overburden reduction depth. The effect of local scour is not considered below the overburden reduction depth. The value of the overburden reduction depth is usually taken as six times the respective pile diameter. In comparison, the approach stated in API RP 2GEO (2014) yields a greater reduction of the vertical effective stress due to scour development. In general, scour development yields reduced load-bearing capacities and stiffnesses of cohesiveless soils with respect to the soil modelling according to API RP 2GEO (2014).

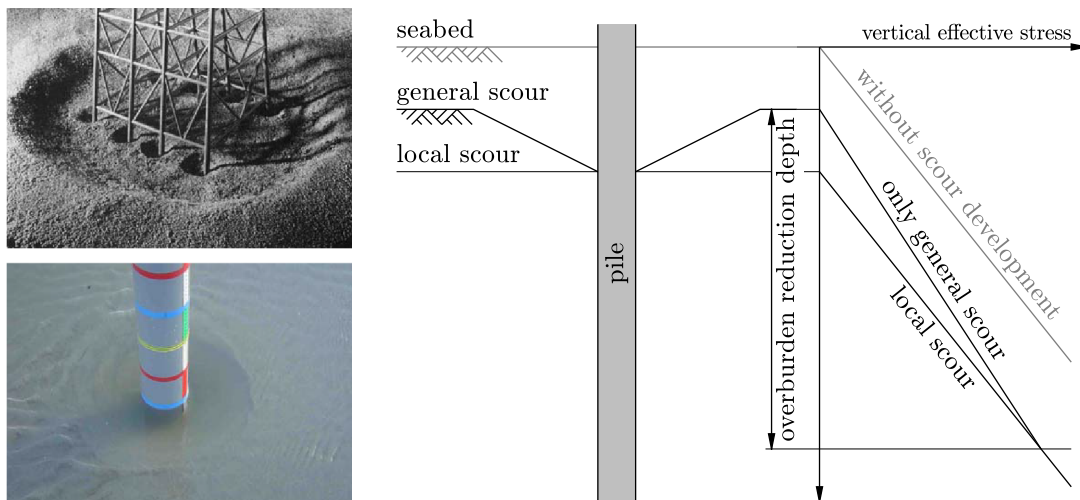


Figure 3.17: Scour at jacket and monopile substructures (van der Tempel et al., 2004) (left) and overburden reduction depth determination for global and local scour according to API RP 2GEO (2014) (right)

Scour development directly impacts the structural response of offshore structures. Increased scour depth leads to reduced Eigen frequencies. Exemplarily, the first bending Eigen frequency of an offshore wind turbine with monopile substructure is reduced by approximately 6% for a relative scour depth of 1.3 (Prendergast et al., 2015). First and second bending Eigen frequencies reduced by 1.4% and 2.1% for a relative scour depth of 1.3 are calculated for an offshore wind turbine with tripod substructure (Ma et al., 2018). Numerical investigations by the author (Rolfes et al., 2018) for an offshore wind

turbine with jacket substructure show that the first bending Eigen frequency is almost constant for relative scour depth up to 2.0.

Concerning fatigue life, investigations on an offshore wind turbine with monopile substructure show a significantly decreased fatigue lifetime in case of scour (van der Tempel et al., 2004; van der Tempel, 2006). Numerical simulations of an offshore wind turbine with tripod substructure and a relative scour depth of 1.3 are evaluated with respect to limit states (Ma et al., 2018). Increased maximum loads and lateral deflection of foundation piles are observed. Additionally, the structure is exposed to increased fatigue loads, resulting in significantly reduced fatigue lives. Increased fatigue loads are also calculated by the author (Rolfes et al., 2018) for the foundation piles of an offshore wind turbine with jacket substructure.

3.4.3 Corrosion

Corrosion is a natural process. It is the chemical or electrochemical reaction of materials with their environment, which results in alternated properties and deterioration of the materials. Especially metals are prone to corrosion. General information on corrosion of metals is given in e.g. Bergmann (2013).

The severity of corrosion depends on the environmental conditions. Comparing offshore to onshore sites, corrosion of steel components is more severe due to greater humidity and salinity. Corrosion is also supported by high oxygen concentration in water. Marine growth may influence the corrosion rate. Especially microbiologically-influenced corrosion results in a rapid corrosion of steel components (Videla and Characklis, 1992; Blackwood, 2018). Considering offshore wind turbines, the values of corrosion rates depend on the vertical location. High corrosion rates are observed in the splash zone, defined as the part of a support structure which is frequently exposed to seawater due to tide and waves (IEC 61400-3-1, 2019). For monopiles, microbiologically-influenced corrosion was observed at internal steel surfaces of monopiles (Hilbert et al., 2012). Depending on the vertical location and the corrosion to be expected, different techniques for protection against corrosion are to be applied in accordance with the respective standards (BSH, 2015; DNV-RP-0416, 2016). Corrosion control includes coatings, cathodic protection, corrosion allowance, and selection of corrosion-resistant materials. However, complete protection against corrosion cannot be ensured due to various reasons as stated in Momber and Marquardt (2018). Marine growth usually modifies the corrosive environment locally. No clear findings regarding the interaction of marine growth and protection against corrosion still are not found yet (Momber and Marquardt, 2018). Hence, corrosion is to be considered during the design of offshore wind turbines. A more detailed overview of corrosion and of protection systems against corrosion for offshore wind turbines is given in e.g. Momber (2011).

Considering steel structures exposed to external loads, the loss of material due to corrosion results in reduced cross-section properties. This leads to increased internal loads and to changed structural dynamics of the structures. Here, the Eigen frequencies are reduced. In general, different models exist to describe the surface topology of corroded steel components. The surface topologies due to uniform corrosion, irregular corrosion, and pitting corrosion are shown in Fig. 3.18. The grey lines indicate the original cross section before corrosion.



Figure 3.18: Uniform corrosion, irregular corrosion, and pitting corrosion (from left to right)

The impact of corroded, irregular steel surfaces on the load-bearing behaviour of steel components and their modelling as well as experimental fatigue investigation of corroded steel components are still topic of research (Teixeira et al., 2013; Momber et al., 2019; Shojai et al., 2022a,b). Significantly increased stress concentration exists at pits in structural components, which is equivalent to a reduction of load-bearing capacities and of the respective fatigue life. Several experimental investigations on steel specimens exposed to corrosion show a reduced fatigue strength in comparison to uncorroded specimens (Adedipe et al., 2015; Ummenhofer et al., 2017; Collmann and Wefer, 2017; Gkatzogiannis et al., 2019). Especially the acquisition of respective corroded specimens is of importance. Methods to generate corroded steel specimens in laboratory in considerably less time, which shall possess similar properties as specimens exposed to natural corrosion, are discussed in Gkatzogiannis et al. (2019).

For the structural design of offshore wind turbines, SN curves and partial safety factors are to be selected depending on location as well as accessibility for inspection and maintenance (DNV-ST-0126, 2021). The SN curves for steel components are specified in DNV-RP-C203 (2019) in dependence of the risk of corrosion. Here, distinction is made between steel components in air, in seawater with cathodic protection, as well as for free corrosion. The fatigue strength descends for the stated order of classifications. The SN curves stated for the fatigue design according to DIN EN 1993-1-9 (2010) explicitly are only valid for steel components which are not exposed to corrosion.

Exemplarily, a steel specimen² with the dimensions of $150\text{ mm} \times 20\text{ mm} \times 10\text{ mm}$ is analysed. It was placed below mean sea level at a harbour at the German North Sea for two years. Its surface was covered mainly by barnacles (*Balanidae*). The steel specimen was placed in acetic acid, which has a concentration of 10%, for twelve hours in order to remove the calcareous remains of the barnacles. No chemical reaction between the steel surface and the acetic acid is noted. Afterwards, electrolysis of the steel specimen was performed in order to remove the remaining corrosion products. Detailed information on the methods applied to remove the corrosion products is given in Appendix A2.

The steel specimen before removal of the calcareous remains of the barnacles and of the corrosion products and its measured surface profile after removal are shown in Fig. 3.19. The red-coloured contour plots in the photography of the steel specimen covered by barnacles indicate the depths of 0.25 mm , 0.50 mm , and 0.75 mm to mark the locations of corrosion pits. The profile of the steel surface was optically measured with a profilometer “VR-3200” of *KEYENCE*.

Notable corrosion pits are detected between neighbouring barnacles as well as at locations which are not covered by barnacles. These areas were exposed directly to the seawater, which eventually led to corrosion. Based on this steel specimen, no reliable statement cannot be made that corrosion occurred at locations covered by barnacles. Nevertheless, the steel surface below the barnacles is notably smooth.

²The steel specimen as shown in Fig. 3.19 (top) was kindly provided by Fraunhofer IWES.

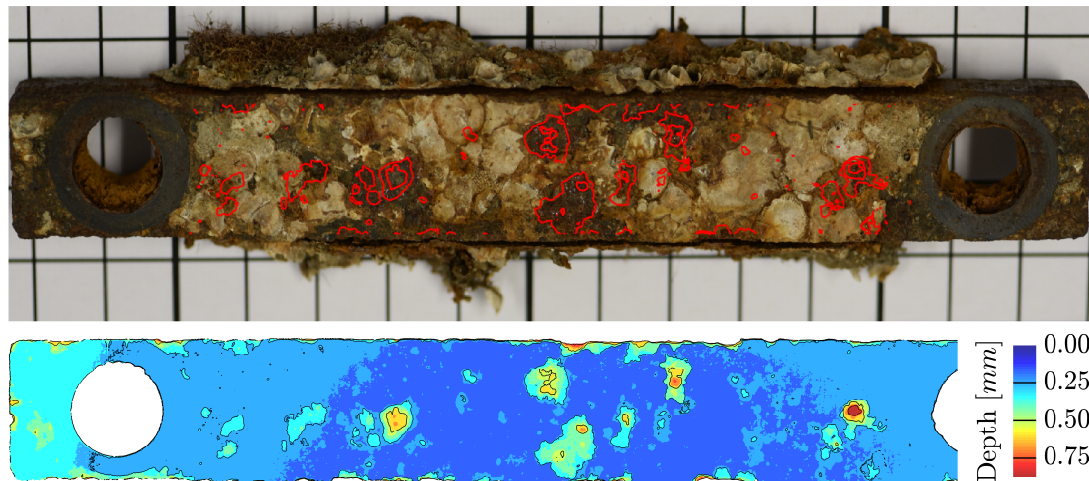


Figure 3.19: Corroded steel specimen² covered by calcareous remains of the barnacles (top) and the measured profile of its surface after removal of the calcareous remains of the barnacles and of the corrosion products (bottom)

3.4.4 Deterioration of structural components

Local damages of structural components may lead to changed structural behaviour of structures. Especially components exposed to increased local stresses are prone to damage. Components and structural details, which are typically found at offshore wind turbines, include welding seams, tubular joints, and structural connections, such as ring-flange connections and grouted connections. Additionally, increased local stresses occur at irregular steel surfaces, i.a. due to corrosion.

Initial fatigue cracks at steel structures and at their details, such as welding seams and tubular joints, have a depth of less than a millimetre and a length of a few millimetres. This is equivalent to a rupture of a laboratory test specimen (Radaj and Vormwald, 2007). Both values are considerably small in comparison to the thicknesses of and overall dimensions of steel components used for support structures of wind turbines. Since fatigue design of structures according to standards at most permit cracks of this dimension, no cracks are to occur which may change the general structural properties significantly and notably. Further crack propagation may lead to an accelerated failure of the respective component.

Preloaded high-strength bolt assemblies are applied in ring-flange connections between tower segments and for the connection between tower and transition piece. About hundred bolts or more are used for ring-flange connections as used for wind turbines. Damages of a few single bolts within ring-flange connections, leading to a significant reduction of the preload, hardly affect the general structural properties of ring-flange connections. Damaged bolts are subsequently exchanged during periodic inspections in order to ensure a safe and stiff connection furthermore.

Grouted joints are applied to realise the form closure between substructures and the foundation piles. The connection between transition piece and monopile is realised either by grouted connections or newly by ring-flange connections. Slipping of grouted connections was observed at cylindrical monopiles and transition pieces of offshore wind turbines within several offshore wind parks in Europe. Here, no shear keys have been attached to monopiles and transition pieces, which caused the slipping (Schaumann

et al., 2010). No degradation of the stiffness of grouted connections with shear keys is observed (Raba, 2018).

In conclusion, no structural deterioration by means of a significantly reduced stiffness of the respective component can be observed, unless severe local damage or failure of a component has already occurred.

3.5 Findings

Within this chapter, the reader is introduced to the simulation of wind fields and sea states which are applied for the load simulation of offshore wind turbines. A special emphasis is put on the characteristics of waves and sea states as well as on the wave-induced loads.

The wave-induced loads, usually calculated with Morison's equation, consist of a drag- and inertia term, whereas bottom-fixed offshore structures are preliminary loaded by inertia forces. However, the drag term becomes more relevant in case that currents occur. Due to the quadratic term of the water-particle velocity within the drag term of Morison's equation, the local maxima within the load time series are increased for increased current velocities. The ranges from a local minimum to the consecutive local maximum are also greater. For certain peak periods of the sea state, dynamic amplification of the drag term including current may become even more significant. A corresponding analysis on the impact of currents is carried out in Section 8.2.

Besides the introduction to modelling of sea states and wind fields, the long-term statistics of the decisive parameters to describe sea states and wind fields as well as their combined occurrence frequencies are shortly discussed. The respective scatter tables are derived from the measurement data from the research platform FINO1.

Additionally, variations of the structure as well as of the structural-dynamic properties are described. Mostly the variations occur due to the special environment offshore. Substructures can be considered as artificial reefs, as they are settled by marine fauna, such as mussels or barnacles. The soil-structure interaction may be subject of change due to the scour development around the foundation piles. Even though corrosion is about to occur within the harsh environment, the loss of material is almost not notable, mostly due to the corrosion protection systems attached to offshore wind turbines. The effects on the structural-dynamic behaviour is almost not notable. Deterioration of structural components also does not result in significant changes of the structural-dynamic behaviour.

4 Load simulation of offshore wind turbines

The design of offshore wind turbines is usually based on the semi-probabilistic design approach. The probabilistic design approach may result in a more economic structural design. As for the probabilistic design, three classes of probabilistic models are to be considered. They cover variations of the structure and structural-dynamic properties, long-term weather conditions, as well as the randomness of signals, as introduced in Section 1.1. The variations of the structure and structural-dynamic properties as well as the long-term weather conditions are described in Chapter 3. The estimation of distribution functions for extreme loads and fatigue loads is given in Chapter 5 and Chapter 6, respectively.

For the structural design of offshore wind turbines, certain load cases as specified in the relevant standards are to be simulated. These load cases shall represent the operational states which offshore wind turbines face during their considered lifetime. The regular operation of the offshore wind turbines, which produces power, covers most of the lifetime. Additionally, parked offshore wind turbines as well as offshore wind turbines with fault conditions during different environmental conditions are to be considered because these conditions of the rotor-nacelle assembly result in different structural responses of the offshore wind turbine.

For the load simulations, a system of equations, consisting of characteristic matrices, is set up which represents the structural behaviour of the offshore wind turbine as well as the acting loads. The load simulations are usually carried out in time domain in order to model non-linearities appropriately. These non-linearities result in time-dependent matrices of the system of equations to be solved for each time step. Frequency-domain simulations require significantly less computational effort, but it is not possible to model non-linearities. Only linearised models can be used.

4.1 Design of offshore wind turbines

The Federal Maritime and Hydrographic Agency of Germany (in German: Bundesamt für Seeschifffahrt und Hydrographie, BSH) is responsible for the approval of offshore wind turbines within the exclusive economic zone of Germany. The structural design of offshore wind turbines is regulated by the standard BSH (2015), which refers to national and international standards and guidelines.

4.1.1 Safety concepts

The effects of actions E shall not exceed the respective resistance R of any structural component. This is equivalent to state that the limit-state function g is greater than zero,

$$g(E, R) = R - E \stackrel{!}{>} 0. \quad (4.1)$$

Due to the stochastic scattering of the effects of actions and of the structural resistance, the probability of failure P_f is defined as the probability that the limit-state function is not fulfilled,

$$P_f = \int_{g(E,R)<0} p(E, R) \cdot dE \cdot dR, \quad (4.2)$$

with the joint probability density function $p(E, R)$ of effects of actions and resistance. Complementary, the survival probability is the probability that the limit-state function is fulfilled, $P_s = 1 - P_f$. The target values for probability of failure are set in dependence of the so-called reliability classes according to DIN EN 1990 (2010). The reliability classes may be associated to the so-called consequences classes. The consequences classes and the associated target probabilities of failure are concluded in Tbl. 4.1. Here, the target values for an one-year reference period are listed. Instead of the maximum probability of failure, the minimum values for the reliability index are stated in DIN EN 1990 (2010). The probability of failure is the value of the cumulative distribution function of the normalised Gaussian distribution for the negative value of the reliability index.

Table 4.1: Definition of consequences classes and their associated probabilities of failures according to DIN EN 1990 (2010)

Consequences class	Definition	Probability of failure
CC3	High consequence for loss of human life, or economic, social or environmental consequences very great	10^{-7}
CC2	Medium consequence for loss of human life, economic, social or environmental consequences considerable	10^{-6}
CC1	Low consequence for loss of human life, and economic, social or environmental consequences small or negligible	10^{-5}

Contrarily to DIN EN 1990 (2010), an annual probability of failure of 10^{-4} is stated for offshore wind turbines in DNV-ST-0126 (2021). The survival probability for a period of n years depends on the annual survival probability, $P_{s,n} = P_s^n$. Hence, the probability of failure for a period of n years is $P_{f,n} = 1 - P_{s,n}$.

The design standards regarding the design of offshore wind turbines follow the semi-probabilistic safety concept. Here, design values of the effects of actions as well as of the resistances are defined. The values of the effects of actions must not exceed the respective design values of resistance, $E_d < R_d$. The target probability of failure is already included in the design values via partial factors and combination factors to consider

simultaneously occurring effects of actions. These factors are usually obtained by applying the first-order reliability method. Further information on the semi-probabilistic safety concept is given in e.g. DIN EN 1990 (2010).

No design values are required for the probabilistic design, but the distribution functions of the effects of actions as well as of the resistances are to be known. For a reliability-based design or probabilistic design, the probability of failure according to Eq. (4.1) is to be calculated and evaluated. The integral in Eq. (4.2) may be solved by applying Monte Carlo simulations. Further information on the reliability-based design is given in e.g. DIN EN 1990 (2010). Additionally, a detailed description of the safety concepts is found in e.g. Al Shamaa (2015).

4.1.2 Limit states

Especially the verifications of the ultimate limit state and the fatigue limit state are of importance for the structural design of offshore wind turbines. For the design against ultimate limit state, the extreme load effects are compared to the correspondent ultimate resistance of the structural component. The verification of the fatigue limit state is carried out by calculating the fatigue damage caused by the cycling effects of actions. Additionally, verification of the accidental limit state and of the serviceability limit state are to be carried out. An example for the accidental limit state is the verification of the structural behaviour in case of a collision of a ship with an offshore wind turbine. The verification of the serviceability limit state is required to evaluate that the operation of offshore wind turbines is not disturbed by events not covered by the previously stated limit states. Further requirements and required verifications for the design of offshore wind turbines are listed in BSH (2015).

Details on the verifications of the ultimate limit state and fatigue limit state are stated in Chapter 5 and Chapter 6, respectively.

4.2 Load characterisation and load cases for offshore wind turbines

In general, load types can be classified as constant, periodic, random, and transient, referring to Böker (2010). Additionally, the random transient load type is introduced. These different load types are sketched in Fig. 4.1. Loads of different types may occur simultaneously.

Constant loads mostly occur due to the self weight of the components of a structure and due to constant mean wind or constant sea currents.

Periodic loads are caused by i.a. the rotation of the rotor whose rotational speed is usually constant during operation. Reasons are the imbalances of the rotor plane, such as different mass or stiffness of the blades, as well as loads along the blades, which pass through a temporally changing wind field. Periodic loads also occur due to regular waves.

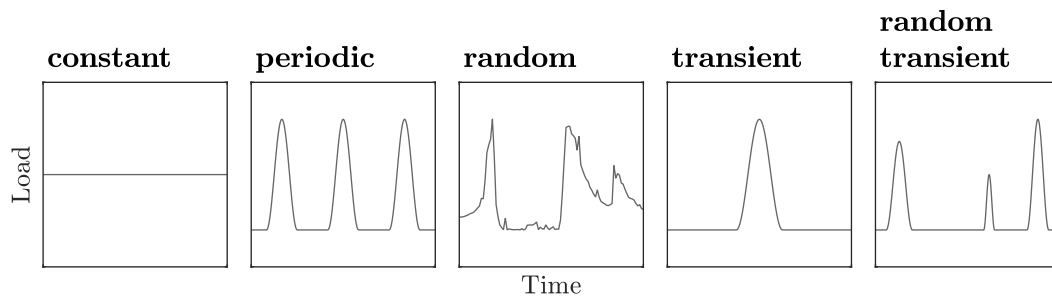


Figure 4.1: Classification of load types: constant, periodic, random, transient, and random transient (from left to right)

Irregular waves and turbulent wind fields result in random loads. Only characteristics such as statistical properties, distribution functions, spectral moments, and power spectral densities may be obtained for describing this load type.

Transient loads are impact loads with sudden changes in magnitude or direction. Examples are wind gusts, operational loads due to start of or shutdown of a wind turbine, and breaking-wave impact at the substructure. Start describes the process from standstill- or idling situation to power production, and vice versa, shutdown is the process from power production to standstill- or idling situation. Breaking waves are modelled as impact forces, referring to Paulsen et al. (2019). Their impact duration is in the range of tenths of seconds.

Random transient loads are identified as a special form of the transient loads. In comparison to transient loads, they occur frequently, but their magnitudes and the time gap between consecutive transient loads are considered as random. An example for offshore structures is the wave-induced loading due to sea states in the splash zone. The wave-induced loading is only acting below the temporally changing water-surface elevation. Hence, the substructure is either loaded in this area by waves with random height and random magnitude, or it is not loaded at all when the wave though passes.

4.2.1 Effect of the rotor

The rotor itself has a significant impact on the loads acting on the support structure of the offshore wind turbine. The wind acting on the single blades of the rotor causes a rotation. The generated torque is transferred to electrical power. All loads acting on the blades and thus on the rotor are transferred by the support structure into the soil.

Usually, the rotor speed is approximately constant. The loads acting on a single blade are not constant, but they vary periodically due to the mean wind field. The mean wind field, here considered without turbulence for reasons of simplification, is affected by wind shear and the tower-shadow effect. Due to the wind shear, referring to Section 3.1.1, the absolute wind velocity and the angle of attack at the blade section varies along a whole rotation. The tower-shadow effect describes that the wind velocity is reduced in front of the tower due to the presence of the tower. Passing of the blades through this local field of reduced wind velocity alters the loads acting on the blades. The resulting loads acting on a blade are periodical with a base frequency equal to the rotor speed.

The load acting on the rotor hub is the superposition of all periodic loads acting on all blades. Assuming that the periodic loads acting on the blades are equal with a time lag due to their installed angular positions, this load is a periodic signal whose base frequency is the rotor speed multiplied by the number of blades. The rotor speed itself is not a component of the superposed signal. These load effects due to the rotating blades are referred to as nP for a rotor with n blades.

Additionally, imbalances of the rotor as a whole, which may exist because the blades attached to the rotor hub may have different masses or different geometries due to manufacture and installation, cause periodic loads. These periodic loads may also consist of natural multiples of the base frequency which is equal to the rotor speed. Effects due to rotor imbalances are referred to as $1P$.

Natural multiples of the $1P$ - and nP -frequencies are to be considered as well for the design of offshore wind turbines. Such a periodic signal is usually not a sinus wave, but it consists of several wavelets with wave periods being natural multiples of the base wave frequency. The absolute values of the amplitudes of the components associated to the natural multiples usually are less than this of the base frequency, without consideration of the dynamic amplification. However, dynamic amplification may increase certain amplitudes within the resulting dynamic load effect. General description on the the $1P$ - and nP -frequencies is also found in textbooks such as Gasch and Tvele (2012) and Hau (2013).

This effect is exemplarily shown in the Campbell diagram in Fig. 4.2. The Campbell diagram plots the rotor speed against the Eigen frequencies. It is used to identify potential resonance effects which occur when the rotor speed as an excitation frequency is close to the Eigen frequencies of the offshore wind turbine. Here, it is shown for a rotor with three blades. It is state of the art that offshore wind turbines operate in between the $1P$ - and $3P$ frequencies. This configuration is called “soft-stiff design”. The offshore wind turbine is to be designed such that the Eigen frequencies do not match the $1P$ - and $3P$ frequencies including some safety margins for any operational rotor speed. Here, a safety margin of $\pm 10\%$ is considered, shown as grey area. In case that a periodic load with a base wave frequency of the $1P$ frequency due to the rotation of the rotor also consists of a wavelet with a wave frequency equal to two time the base wave frequency, this frequency lies within the allowable area of Eigen frequencies. This frequency is denoted as $2*1P$ frequency and shown as dashed line. Therefore, dynamic excitation of the wavelet with a wave frequency of $2*1P$ frequency is possible.

This effect is exemplarily described for the $2*1P$ frequency. Greater multiples of the $1P$ frequency as well as multiples of the $3P$ frequency may also interfere with other Eigen frequencies of the offshore wind turbine.

4.2.2 Load events for offshore wind turbines

The loads acting on offshore wind turbines depend on the severity of environmental conditions as well as on soil-structure interaction, the selected support structure and control mechanisms of the rotor-nacelle assembly.

Most of the lifetime of an offshore wind turbine, power production is possible for operational wind turbines and for wind velocities which lie within the range of cut-in wind

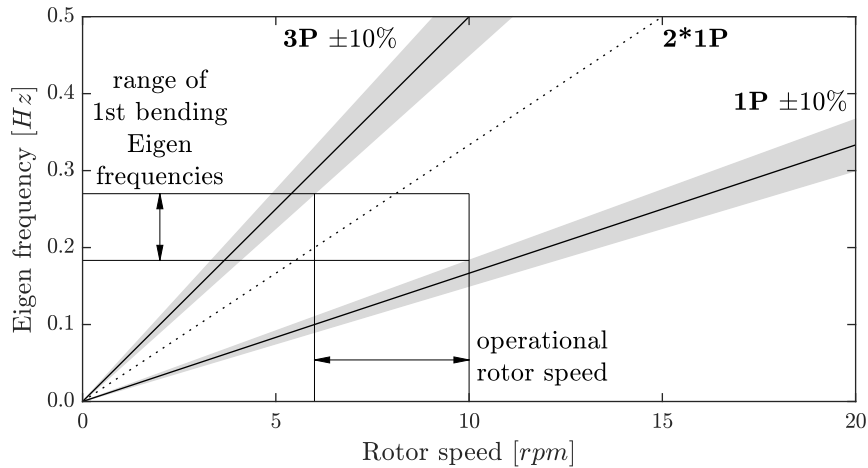


Figure 4.2: Campbell diagram for a three-bladed wind turbine, with an exemplary range of first bending Eigen frequencies for offshore wind turbines and of rotor speeds

velocity and cut-out wind velocity. Outside of this range, the rotor-nacelle assembly is in parked or idling condition such that no power production is possible. For wind velocities less than the cut-in wind velocity, the resulting loads acting on the rotor blades are too small to cause a rotation of the rotor. For wind velocities greater than the cut-out wind velocity, the resulting loads acting on the offshore wind turbines are too great such that a safe and reliable operation of the offshore wind turbine is not possible. The values for the cut-in wind velocity and the cut-out wind velocity depend on the technical demands for the machinery of the offshore wind turbine. The cut-in wind velocity usually has a value of 2 m/s up to 5 m/s , and the cut-out wind velocity usually has a value of 25 m/s up to 30 m/s . The percentage of power-production status depends on the site-specific wind distribution as well as on the technical specification and technical availability of the offshore wind turbine. Technical availability of the rotor-nacelle assembly is not given during the whole lifetime of an offshore wind turbine. Due to various reasons such as technical malfunctions or maintenance, the inoperable rotor-nacelle assembly is consequently driven in idling or parked position. No safe operation can be guaranteed otherwise. The technical availability of an offshore wind turbine is assumed to have a value of approximately 90%. These load events are relevant for the design against fatigue. Due to the reduced aerodynamic damping for load events with idling or parked rotor-nacelle assembly and thus greater dynamic excitation, the fatigue damage is increased in comparison to a similar load event of an operating offshore wind turbine with same duration. Even though the technical availability is very high, the load events due to technical non-availability may contribute noticeably to the total fatigue damage.

Besides the operational stages of offshore wind turbines described above, high loads acting on support structures of offshore wind turbines may be caused by environmental events which either rarely occur or are considered as abnormal. Operation of the offshore wind turbine itself and faults during the operation may result in high loads as well. These load events are to be additionally analysed for the design against ultimate limit states.

During storms with wind velocities less than the cut-out wind velocity, power production is still possible. Both great wind-induced loads as well as great wave-induced loads

act on the rotor and the substructure, respectively. During storms with wind velocities greater than the cut-out wind velocity, the offshore wind turbines are in idling or parked conditions. Even though the wind-induced loads action on the rotor are reduced in comparison to the operational stages, no aerodynamic damping exists. This may cause an increased dynamic excitation, especially when the exciting frequency is close to the Eigen frequencies of the offshore wind turbine. Very high waves and slamming waves may occur during storms which act for a few seconds or few tenth of seconds, respectively, with a high magnitude on the substructure. They cause sudden extreme transient loading.

Other rare events include environmental conditions or faults of the rotor-nacelle assembly which cause transient loading at the offshore wind turbine. Examples are sudden change in mean wind directions or wind gusts. Sudden wind-direction change results in a reduced wind-induced force acting on the rotor-nacelle assembly perpendicularly to the rotor, but the side-to-side force, acting parallel to the rotor plane, is increased due to the inclined flow direction. Almost no aerodynamic damping exists for the side-to-side excitation.

Start processes of offshore wind turbines occur when the offshore wind turbine starts to operate from parked or idling stage. This is the case the mean wind velocity exceeds the cut-in wind velocity or it falls below the cut-out wind velocity. Vice versa, stop processes occur when the mean wind velocity falls below the cut-in wind velocity or it exceeds the cut-out wind velocity. Emergency stops may occur during sudden faults which require a sudden stop of the rotor. Therefore, the blades are pitched such that the wind-induced loads suddenly vanish. This causes a transient excitation of the offshore wind turbine. The rotational speed also passes the nP -frequency of a n -bladed wind turbine and multiples of the $1P$ - and nP -frequency during these processes. This passing causes a dynamic excitation of the offshore wind turbine.

4.2.3 Standardisation of load simulation for offshore wind turbines

The standards IEC 61400-3-1 (2019) and DNV-ST-0437 (2016) define the load simulations which are to be carried out for the design of offshore wind turbines. These so-called design load cases (DLCs) are classified into several groups, as can be seen in Tbl. 4.2. They cover the different operational and environmental stages which the offshore wind turbine has to withstand during its lifetime. The load types which are to be expected to occur for the design load cases, referring to Section 4.2, are associated to the design load cases. The design load cases covering sea-ice simulation are excluded from this overview. Further details on these design load cases are found in IEC 61400-3-1 (2019), DNV-ST-0437 (2016), as well as in e.g. Popko (2020).

Periodic loads are observed for all design load cases which simulate the offshore wind turbine during operation. As described above, periodic loads occur due to the passing of the blades with almost constant rotational speed through wind fields, which include wind shear and tower-shadow effect. These design load cases are summarised in the groups of design load cases 1 and 2. Periodic load effects are also observed for start-up- and shutdown processes, which are listed within the groups of design load cases 3 and 4. Here, periodic excitation is caused when the changing rotational speed of the

Table 4.2: Design load cases (DLCs) for the design of support structures of offshore wind turbines according to IEC 61400-3-1 (2019) and associated load types

DLC	Description	Load type			
		P	T	RT	R
1) Power production					
1.1	Normal conditions (for rotor-nacelle assembly only)	x		(x)	x
1.2	Normal conditions	x		(x)	x
1.3	Extreme wind turbulence	x		(x)	x
1.4	Extreme wind-direction change	x		(x)	x
1.5	Extreme wind shear	x		(x)	x
1.6	Severe sea state	x		x	x
1.7	Ice at rotor blades	x		(x)	x
2) Power production plus occurrence of various faults					
2.1	Normal conditions	x		(x)	x
2.2	Normal conditions	x		(x)	x
2.3	Extreme operating gust	x	x	(x)	x
2.4	Normal conditions	x		(x)	x
2.5	Normal wind profile, no turbulence	x		(x)	(x)
3) Start up					
3.1	Normal wind profile, no turbulence	x	(x)		(x)
3.2	Extreme operating gust	x	x	(x)	x
3.3	Extreme wind-direction change	x	x	(x)	x
4) Normal shutdown					
4.1	Normal wind profile, no turbulence	x	x		(x)
4.2	Extreme operating gust	x	x		x
5) Emergency stop					
5.1	Normal conditions	x			x
6) Parked (standing still or idling)					
6.1	50-years storm			x	x
6.2	50-years storm plus yaw misalignment due to electrical fault			x	x
6.3	One-year storm			x	x
6.4	Normal conditions, wind velocities below cut-in vel.				x
	Normal conditions, wind velocities above cut-out vel.			(x)	x
7) Parked and fault conditions					
7.1	One-year storm			x	x
7.2	Normal conditions			(x)	x
8) Transport, installation, maintenance and repair					
8.x	...	x		(x)	x

Load type: periodic (P), transient (T), randomly transient (RT), random (R)

x: notable load type, (x): minor or randomly observed load type

rotor meets an Eigen frequency or its multiples. The sudden excitation of certain Eigen modes can also be considered as transient load.

As explained above, transient load effects are caused by sudden changes within the wind field, sea state or due to faults during the operation. For examples, wind gusts are to be simulated for various design load cases DLC 2.3, DLC 3.2, and DLC 4.2, and extreme wind-direction changes are considered with the design load cases DLC 1.4 and DLC 3.3.

Random transient loads occur for all design load cases due to sea states. Hence, alternating loads occur within the splash zone. Their contribution to the total loads depends on the severity of the respective sea states. Strong sea states especially occur for great wind velocities. Hence, high random transient loads are to be expected for the simulation of severe sea states, referring to DLC 1.6, as well as of extreme sea states during an one-year storm and 50-years storms, referring to DLC 6.3 as well as DLC 6.1 and DLC 6.2, respectively.

Random loads occurs for all design load cases, since either random sea states, random wind fields or both are to be simulated for those.

Design load cases for fatigue design

The design load cases DLC 1.2, DLC 6.4, and DLC 7.2 are most governing for the fatigue design. They cover the operational lifetime of the offshore wind turbine during operation under normal conditions for wind velocities between cut-in- and cut-out wind velocity, during parked conditions due to wind velocities less than the cut-in wind velocity and wind velocities greater than the cut-out wind velocity, and during parked conditions due to faults, respectively.

As recommended by the respective standards, all wind velocities and wind directions as well as the associated sea states are to be considered with their respective occurrence frequency. The sea states are defined by their spectral density, significant wave height, peak period, and wave direction. Currents are not to be considered for the design load cases DLC 1.2, DLC 6.4, and DLC 7.2 (IEC 61400-3-1, 2019; DNV-ST-0437, 2016).

Usually, the design load cases DLC 3.1 and DLC 4.1, which cover the start-up- and normal shutdown processes of the offshore wind turbine, are included for the calculations of the fatigue loads. The count of start- and shutdown processes during the lifetime can be estimated on the basis of the metocean data. These design load cases do not contribute as much to the fatigue damage as the design load cases DLC 1.2, DLC 6.4, and DLC 7.2 do.

Lumping of sea states

Generally, the full scatter tables of wind velocity, wind direction, significant wave height, peak period, and wave direction are to be considered for the simulation of the design load cases DLC 1.2, DLC 6.4, and DLC 7.2. The maximum number of required simulations is the product of considered wind velocities, wind directions, significant wave heights, peak periods, and wave directions as given in the scatter tables. Even with excluding those combinations with an occurrence frequency of zero, several ten-thousands of different combinations are to be simulated and analysed. The required computational effort is enormous.

Therefore, it is beneficial to reduce the number of combinations of environmental variables. Different lumping approaches exist which allow to reduce the number of combinations. An overview of these approaches is provided by Katsikogiannis et al. (2021). Following these lumping approaches, only one sea state to be simulated is derived for the combination of wind velocity, wind direction, and wave direction. Then, the number of required simulations is reduced to several thousands in comparison to the full-scatter approach. No lumping approach and no corresponding note are not referenced in design standards until now.

Different approaches to reduce the number of load cases for fatigue-load evaluation exist. The approaches aim to condense a scatter table of significant wave height and peak period for each wind velocity, wind direction, and wave direction to a single sea state. With the exception of using averaged values of significant wave height and peak period, as mentioned by Passon (2015), the approaches aim to find a sea state which eventually causes the same fatigue damage as the scatter table itself. They are usually referred to as damage-equivalent wave lumping approaches. In general, there is not one but several sea states which may cause the same fatigue damage as the scatter table. For each combination in the scatter table of significant wave height and peak period, the fatigue damage caused by each combination of significant wave height and peak period is calculated. The total fatigue damage due to this scatter table is obtained by weighting the fatigue damages with the respective occurrence probability of each combination of significant wave height and peak period. The line on which these sea states with the same fatigue damage as the complete scatter table lie is referred to as “damage contour line” by Passon (2015).

Kühn (2001) describes an iterative lumping approach which is based on quasi-static simulations of the sea states given in the scatter table. These load simulations are carried out in time domain. A lumped sea state is found with an iteration process which is applied to find a lumped sea state with respect to the fatigue damage at a reference height. Structural-dynamic effects are not included.

Seidel (2014b) introduced a damage-equivalent wave lumping method which considers the structural-dynamic response. The fatigue damage is calculated in frequency domain. The value of the equivalent significant wave height is determined such that the quasi-static fatigue damage is maintained. The value of the equivalent peak period depends on the first-bending Eigen frequency and lies on the damage contour line. The formulae stated by Seidel (2014b) and Seidel (2014a) only consider one damping value for the first-bending Eigen frequency and simplified fatigue-damage calculation. These formulae could be extended for more than one damping value and for higher sophisticated fatigue-damage calculation methods in frequency domain, as they are described in Section 6.2.1.

The lumping approach introduced by Passon (2015) is based on structural-dynamic wave-load simulations in time domain. The author notes that the lengths of the simulated time series shall be of sufficient length such that the fatigue damage is calculated appropriately without being prone to scatter. Damage contour lines are determined for several locations along the monopile substructure. The intersection point of all damage contour lines defines the values of the lumped sea state.

Katsikogiannis et al. (2021) state that the shortcomings of the previously described lumping approaches are the lack of wind-wave interaction as well as of appropriate damping assumptions which take the current operation status of the offshore wind turbine into account. The authors extended the proposed approach of Passon (2015) by including advanced damping assumptions. In order to analyse the impact of wind-wave interaction on the lumped sea states, damage-equivalent sea states are derived by means of fully-integrated simulations in time domain, considering wind- and wave induced loads. Additionally, wave-induced load simulations were carried out in frequency domain. Almost the same parameters for the lumped sea states are derived by both time-domain- as well as frequency-domain simulations. Katsikogiannis et al. (2021) also analysed the impact of different soil-structure interactions for an offshore wind turbine with a power capacity of 10 MW. For each soil-structure interaction considered, a distinct lumped sea state is found. As a continuance of their previous work, Katsikogiannis et al. (2022) analysed different turbine classes, namely offshore wind turbines with a power capacity of 5 MW, 10 MW, and 15 MW. The authors observed that the lumping approach yields different lumped sea states for the different power capacities of the offshore wind turbines. They also noted that different lumped sea states are found for different elevations along the monopile.

In general, all lumping approaches described above are developed for monopile substructures. The application of the lumping methods on more complex substructures such as jackets are yet to be analysed and discussed. In comparison to monopiles, more structural details such as the welding seams at the tubular joints are to be considered. Due to the increased complexity and thus increased number of relevant design positions, the risk that no distinct lumped sea state is found is eventually higher.

Design load cases for design against extreme loads

For the design against ultimate limit state, rarely occurring events are to simulated. The design load cases for the design against ultimate limit state cover severe conditions of wind fields and sea states as well as fault conditions of the machinery. Rarely and suddenly occurring events within wind fields and sea states are also considered, which cause transient load effects. These load events are already described in Section 4.2.2. These extreme situations may implicitly exist in the design load cases used for the fatigue design, which are already described above. For example, extreme direction changes or extreme wind gust may already be included in the random wind fields.

It is not predictable which design load case is governing for the design of the different components of the support structure. The most important ones are shortly described. The design load case DLC 6.1 models an idling or parked offshore wind turbine during a storm with a reoccurrence period of 50 years, and the design load case DLC 6.3 models an offshore wind turbine during a storm with a reoccurrence period of one year. The design load case DLC 1.6 describes an operating offshore wind turbine during a storm with wind velocities less than the cut-out wind velocity. Extreme wind fields and extreme events within the wind fields are covered by the design load case DLC 1.3, DLC 1.4, and DLC 1.5. Start-up and shutdown of offshore wind turbines are simulated within the groups of design load cases 3, 4, and 5.

4.3 Load simulation of offshore wind turbines

Load simulations of offshore wind turbines are usually carried out with finite-element software. A linear system of equations is set up which represents the structure, the structural behaviour, and the acting loading. For structural-dynamic simulations, the equations of motion are to be solved,

$$\underline{\underline{M}} \cdot \underline{\ddot{y}} + \underline{\underline{C}} \cdot \underline{\dot{y}} + \underline{\underline{K}} \cdot \underline{y} = \underline{f}(t) , \quad (4.3)$$

with the mass matrix $\underline{\underline{M}}$, damping matrix $\underline{\underline{C}}$, stiffness matrix $\underline{\underline{K}}$, vector of deformation \underline{y} , and vector of loads \underline{f} . The matrices describe the finite-element model of the structure. The matrices may depend on time and on the structural response \underline{y} and its derivatives. This is in particular the case for wind turbines. Especially the rotation of the rotor as well as the positioning of the blades, which is regulated by the control mechanisms of the rotor-nacelle assembly, cause a non-linear, time-variant structural behaviour of the rotor blades and thus non-linear loading acting on the blades.

Damping describes the energy dissipation due to the movement of the structure. Oscillations are either reduced or prevented by damping. For offshore structures, soil damping due to soil-structure interaction, hydrodynamic damping due to the movement within the water, as well as material damping are to be considered.

A special form of damping for wind turbines is the aerodynamic damping. It occurs during the operational stages of the wind turbine. High loads on the rotor blades cause a bending deformation of the rotor blades and support structure in wind direction. Due to the moving in wind direction, the angles of attacks along the rotor blades are decreasing such that the wind-induced loads are reduced which decelerates the movement. Vice versa, the wind-induced loads increase for a movement against the wind direction which again damps the movement. Aerodynamic damping only occurs for loads acting perpendicular to the rotor plane. Side-to-side movements of wind turbines do not experience aerodynamic damping. General information on aerodynamic damping is given by Kühn (2001).

Aerodynamic damping is implicitly covered in the load simulation which also simulate the flexibility of the structure explicitly. Values for aerodynamic damping are usually stated in dependence of wind velocities for structural systems which are considered rigid and do not simulate the flexible structure (Kühn, 2001).

Damping within the equations of motion can be modelled as Rayleigh damping. It describes a damping matrix which is linearly composed of the mass matrix and the stiffness matrix. Damping is defined for two arbitrary wave frequencies, and its course depends on the wave frequency. Wave frequencies less than the lower selected wave frequency and greater than the upper selected wave frequency are heavily damped.

4.3.1 Modal condensation

It is possible to reduce the computational effort to solve by transforming the equations of motion to modal coordinates such that the response is described by the Eigen vectors of the system.

The Eigen frequencies ω_n or the Eigen values ω_n^2 are found for satisfying the equation $\det(-\omega^2 \cdot \underline{\underline{M}} + \underline{\underline{K}}) = 0$. The Eigen vectors are given as non-trivial solution of $(-\omega_n^2 \cdot \underline{\underline{M}} + \underline{\underline{K}}) \cdot \underline{u}_n = \underline{0}$, with $\underline{u}_n \neq \underline{0}$. Usually, Eigen vectors are presented as normalised vectors $\hat{\underline{u}}_n = \alpha_n \cdot \underline{u}_n$, $\alpha_n \in \mathbb{R}$ such that the terms $\hat{\underline{u}}_n^T \cdot \underline{\underline{M}} \cdot \hat{\underline{u}}_n$ are equal to unity for all Eigen vectors. The normalised Eigen vectors are summarised as modal matrix $\hat{\underline{\underline{U}}} = [\hat{\underline{u}}_1, \dots, \hat{\underline{u}}_N]$. Hence, the equations of motion can be transformed to the following formulation,

$$\hat{\underline{\underline{M}}} \cdot \ddot{\underline{u}} + \hat{\underline{\underline{C}}} \cdot \dot{\underline{u}} + \hat{\underline{\underline{K}}} \cdot \underline{u} = \hat{\underline{\underline{U}}}^T \cdot \underline{f}, \quad (4.4)$$

with the modal mass matrix $\hat{\underline{\underline{M}}}$, the modal damping matrix $\hat{\underline{\underline{C}}}$, the modal stiffness matrix $\hat{\underline{\underline{K}}}$, and the vector of modal deformation \underline{u} . The modal mass matrix is equal to the identity matrix, and the modal stiffness matrix has entries of $\hat{k}_{ij} = 0$ for $i \neq j$ and of the Eigen values at the main diagonal otherwise, $\hat{k}_{ii} = \omega_{n,i}^2$. Hence, each equation of Eq. (4.4) can be considered as a single-degree-of-freedom system.

As stated by Böker (2010), it is sufficient to reduce the modal equations of motion by eliminating modes which possess a small amount of energy. Modal condensation is applied by most software packages for the simulation of wind turbines due to its numerical efficiency.

4.3.2 Load simulation in time domain

Load simulations of offshore wind turbines in time domain are well established. General overviews over finite-element software for the simulation of offshore wind turbines are found in e.g. Böker (2010), Popko (2020), or Leimeister (2020).

The time-variant matrices of the equations of motion are updated for each time step of the structural-dynamic simulation. Hence, a solution of the equations of motion, referring to Eq. (4.3) and Eq. (4.4), is obtained for each time step which includes the non-linear and time-variant behaviour of the structure. Various time-integration schemes of different accuracy and computational efficiency can be applied for the load simulations (Böker, 2010).

Different approaches exist to carry out the simulation of offshore wind turbines in time domain to determine the loads and internal loads of the support structure. A general overview and respective principle schemes are provided by Böker (2010). These approaches are shortly summarised in the following. The numerical effort for the load simulation increases for the given order, as does the accuracy of the load simulation and of the resulting loads.

Superposition approach

The superposition approach is a very simple approach to determine the loads at an offshore wind turbine. It is very commonly applied within the early design stages during an offshore-wind project (Seidel et al., 2016). The structural-dynamic interaction between support structure and rotor-nacelle assembly is not considered by the superposition approach.

Here, the simulation of the wave-induced loads with a software package for offshore applications and the simulation of the wind turbine with an aerodynamic-aeroelastic software package are carried out independently. It is convenient to model the structures within the software packages such that the structural-dynamic properties such as Eigen frequencies and Eigen modes approximately match those of the offshore wind turbine. The loads from the aerodynamic-aeroelastic simulation are transferred to the support structure at the interface node in order to determine the structural response of the support structure. Aerodynamic damping of the support structure which is decisive of the load simulation can be modelled by means of specified damping values (Kühn, 2001).

Afterwards, the loads from the offshore software package and from the aerodynamic-aeroelastic software package are superposed. For the determination of the extreme loads, Böker (2010) suggests to add the extreme loads from each simulation. Combination rules, such as Turkstra's rule, are also convenient for the extreme-load determination (Seidel and Kelma, 2012; Schmidt, 2017). For the calculation of the combined fatigue loads, Kühn (2001) proposes the following superposition of the damage-equivalent loads,

$$s_{DEL,total} = \sqrt{s_{DEL,wind}^2 + s_{DEL,wave}^2}, \quad (4.5)$$

with the damage-equivalent loads $s_{DEL,wind}$ and $s_{DEL,wave}$ from the aerodynamic-aeroelastic software package and from the offshore software package, respectively, and the combined damage-equivalent load $s_{DEL,total}$.

Semi-integrated approach

The semi-integrated approach is described by Seidel et al. (2004). This approach includes the structural-dynamic interaction between support structure and rotor-nacelle assembly. Again, different software packages are applied for the simulation of the structural response of the offshore wind turbine due to wind- and wave-induced loads.

For the semi-integrated approach, the support structure is modelled within the aerodynamic-aeroelastic software package as an equivalent monopile which possesses structural-dynamic properties similar to the actual support structure. Equivalent wave-induced loads are applied during the aerodynamic-aeroelastic simulation. Either the resulting loads or the resulting deformations are applied on the interface node for the following simulation with the offshore software package. In case that loads are applied, the load simulation is to be carried out as static. Hence, Eigen modes of the support structure may be neglected. This especially leads to inaccurate results for complex structures, such as jackets. In case that deformations are applied, dynamic load simulation can be carried out. However, since the support structure is modelled as equivalent monopile within the aerodynamic-aeroelastic software package, not all Eigen modes of the original support structure may be represented appropriately. For example, the torsional stiffness of a jacket and this of the equivalent monopile vary significantly.

Sequential approach

Instead of modelling the substructure as equivalent monopile, as it is done for the semi-integrated approach, it is represented by reduced mass-, damping, and stiffness matrices within the aerodynamic-aeroelastic software package for the sequential approach. Otherwise, the procedure is similar to this of the semi-integrated approach. These matrices include the main structural-dynamic properties of the support structure.

Here, the main structural-dynamic properties are modelled with a higher degree of accuracy. Hence, the aerodynamic-aeroelastic load simulation leads to more accurate loads which are applied at the interface node for the simulation with the offshore software package. However, a detailed analysis by Böker (2010) has shown that the responses of local Eigen modes are overestimated in comparison to those obtained with the fully-coupling approach and that the Eigen frequencies may differ. Again, complex structures such as jackets are subject of these inaccuracies, while they are minor for tripods and negligibly small for monopiles. Overall, it cannot be concluded whether the sequential approach leads to conservative loads (Böker, 2010).

Fully-coupling approach

Böker (2010) presented an improved approach to couple the different software packages required for an accurate load simulation of offshore wind turbines. Here, one of the software packages solves the whole system of equations. As described by Böker (2010), it is more practical to represent the rotor-nacelle assembly as superelement and the acting loads within the offshore simulation package.

First, the offshore wind turbine is set up within the offshore simulation package as well as within the aerodynamic-aeroelastic software package. The model of the rotor-nacelle assembly is transferred to the general system matrices to be solved. Based on the kinematics of the previous time step, the system matrices, representing the current stage of the rotor-nacelle assembly, and the currently acting loads on the rotor-nacelle assembly are updated for each time step of the time-domain simulation. The hydrodynamic loads are calculated within the offshore simulation package. Finally, the response of the system is calculated within the offshore simulation package.

Fully-integrated approach

The simulation approaches previously described make use of several of several software packages for the load simulation of an offshore wind turbine. Instead, the whole load simulation can be carried out within one simulation package. Here, all non-linearities and interaction effects between offshore wind turbine and environmental conditions can be modelled appropriately and accurately.

4.3.3 Load simulation in frequency domain

Load simulations for offshore structures in frequency domain are well established in the offshore industry for oil- and gas applications (Barltrop and Adams, 1991). This is

mostly applicable, since these kind of substructures are located in very deep waters such that the water-surface elevation hardly is to be accounted for in the load simulation.

As for load simulation of offshore wind turbines in frequency domain, the non-linear behaviour of the controller is hardly to handle. It causes time-variant structural variations. Additionally, it is almost not possible to describe the wind-induced loads acting on the rotor blades in frequency domain. Load simulation of offshore wind turbines in frequency domain are only possible by considering simplifications and linearisation of the structural model and acting loads. Halfpenny (1998) carries out a linearisation of the wind-induced loads and of the controller's response such that load simulation in frequency domain is possible. No time-variant structural properties are considered. Within the work carried out by van der Tempel (2006), the power spectral densities of wind-induced loads are determined via Fourier transformation from time-domain simulations, and the wave-induced loads are calculated in frequency domain. Lupton (2014) analyses the response of a floating offshore wind turbine. A linear model is used to describe the behaviour of the controller. Errors of up to 10% for the thrust forces are reported for wind velocities not being close to the rated wind velocity. However, the error increases to up to 40% for wind velocities close to the rated wind velocity.

Equations of motion in frequency domain

A rough sketch on the equations of motion in frequency domain is given here. Further details on the equations of motion in frequency domain as well as load simulation of structures in frequency domain is provided in general textbooks, e.g. Crandall and Mark (1967), Preumont (1994), and Roberts and Spanos (2003). A short overview is provided by Kleineidam (2005).

Fourier transformation of Eq. (4.3) yields the equations of motion in frequency domain. Loads and deformations are represented as matrices of power spectral densities. The spectrum of deformations $\underline{\underline{S}}_{yy}$ is calculated on the basis of the spectrum of external loads $\underline{\underline{S}}_{ff}$ and the transfer function $\underline{\underline{H}}$,

$$\underline{\underline{S}}_{yy}(\omega) = \bar{\underline{\underline{H}}}(\omega) \cdot \underline{\underline{S}}_{ff}(\omega) \cdot \underline{\underline{H}}^T(\omega) . \quad (4.6)$$

The transfer function $\underline{\underline{H}}$ consists of the structural properties of each element of the finite-element model, $\underline{\underline{H}} = \left[-\omega^2 \cdot \underline{\underline{M}} + i \cdot \omega \cdot \underline{\underline{C}} + \underline{\underline{K}} \right]^{-1}$. $\bar{\underline{\underline{H}}}$ is the complex conjugate of $\underline{\underline{H}}$. The spectrum of deformations $\underline{\underline{S}}_{yy}$ is determined via matrix multiplication of the matrices given on the right side of Eq. (4.6).

Eq. (4.6) reads as follows for a single-degree-of-freedom system,

$$S_{yy}(\omega) = |H(\omega)|^2 \cdot S_{ff}(\omega) . \quad (4.7)$$

Dynamic amplification factor

Following Eq. (4.7), the amplification of the static structural response is calculated as follows for a single-degree motion of equation,

$$V(\omega) = \frac{1}{\sqrt{\left(1 - \left(\frac{\omega}{\omega_n}\right)^2\right)^2 + 4 \cdot D^2 \cdot \left(\frac{\omega}{\omega_n}\right)^2}}, \quad (4.8)$$

with excitation frequency ω , Eigen frequency ω_n , and damping ratio D . The function V is referred to dynamic amplification factor. The value of the dynamic amplification factor at the Eigen frequency is $\frac{1}{2 \cdot D}$. Exemplarily, the dynamic amplification factor has a value of 50 for a damping value of 1%, which is a typical value for offshore wind turbine excluding aerodynamic damping. The dynamic amplification factor is shown in Fig. 4.3 for different values of the damping ratio.

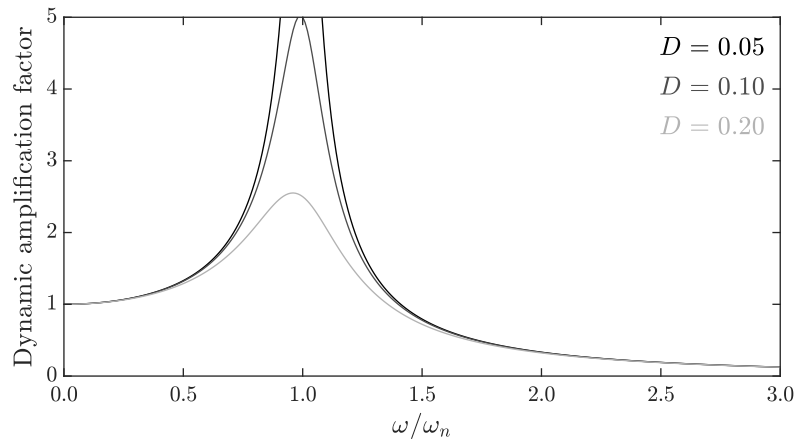


Figure 4.3: Dynamic amplification factor for different damping ratios

4.4 Findings

It is state-of-the-art to carry out the design of offshore wind turbines by means of the semi-probabilistic design approach. The probabilistic design approach may result in a more economic structural design. Yet, it is more time-consuming to the increased number of load simulations to be carried out in order to meet the required probability of failure for the structural verification.

As for the design of offshore wind turbines, design load cases are defined which are to be simulated in order to determine the extreme loads and fatigue loads which the offshore wind turbines have to resist. Mostly the signals consist of random load type due to the sea states and wind fields acting on the offshore wind turbine. Periodic loads are observed for the simulation during operation. Transient loads occur due to sudden changes within the otherwise random time series.

Load simulations are usually carried out in time domain, even though the simulations are very time-consuming. The computational effort for load simulations in frequency domain is reduced significantly. However, the time-variant structural model as well

as the non-linearities, which are mostly caused by the controller of the rotor-nacelle assembly, cannot be covered appropriately such that simulations in frequency domain cannot be applied for a detailed and accurate design of offshore wind turbines. Up to now, load simulations in frequency domain are used to estimate preliminary loads for the early design stages of an offshore-wind project (Seidel et al., 2016).

5 Estimation of extreme loads in frequency domain

Structural components are to be designed such that no load exceeds their load-bearing capacity.

Loads acting on structures may exceed the load-bearing capacity of structural components such that a sudden damage may occur. Extreme loads may also cause deformations which cause an unsafe operational stage. Therefore, it is of importance to determine the very high loads which may occur during the lifetime of the structure and which may cause damage. The design against extreme loads is usually referred to as ultimate limit state design. These extreme loads usually subject of scatter. The statistical properties of the extreme loads can be determined on the basis of multiple time series as well as on the basis of power spectral densities. The derivation of extreme loads for offshore wind turbines, both as characteristic value and as respective distribution function, is challenging and still topic of ongoing research activities (Haselsteiner, 2022).

Besides scattering of the extreme loads, the load-bearing behaviour of structural components and of materials is also subject of scattering, which is mostly due to the manufacturing process.

5.1 Structural design against extreme loads

For the structural design, it has to be evaluated whether the maximum occurring load or deformation exceeds the respective values which the structure can withstand. The load-bearing behaviour depends very much on the selected material. The following description concentrates on steel structures. Other materials, which are applied for offshore wind turbines, such as concrete or cast iron, show different material behaviour when loaded.

Exceeding of the load-bearing capacity of structural components causes irreversible deformation of the structure and eventually damage. Loads may also cause deflections or rotations of structural components which exceed predefined limits while the load-bearing capacity is not exceeded yet. For example, only a certain value of deflection is allowed for a rotor-blade tip. Otherwise, it touches the tower of a wind turbine, which causes damage to blade and tower or eventually results in the total loss of the wind turbine.

The load-bearing capacity is determined based on experimental testing. Of importance are stress-strain curves, which show the relation between stress and strain rate within the test specimen. Here, the steel probe is axially loaded until rupture. Usually, the strain rate is constantly increased until rupture of the probe. The shape of the stress-strain curve depends on the tested material. General information on stress-strain tests

of steel probes and on its normative regulations is found in e.g. Bergmann (2013). The stress-strain curve includes several parameters which are characteristic for the tested material. The yield strength is the point on a stress-strain curve which indicates the end of the elastic behaviour. If the stress acting on the steel component exceeds the yield strength, plastic deformation of the steel probe is observed. The modulus of elasticity or Young's modulus is the constant slope of the stress-strain relationship until plastic deformation of the steel probe occurs. The maximum stress which the steel probe can withstand without rupture is referred to as ultimate strength. An idealised stress-strain curve for a steel probe as it is retrieved from tensile testing is shown in Fig. 5.1, with the relevant parameters stated.

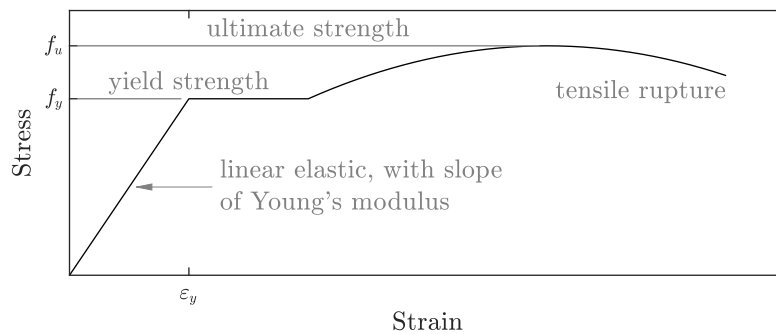


Figure 5.1: Idealised stress-strain curve for a steel probe

The resulting stress-strain curves of several experimental tests usually do not match, but they scatter mostly due to the manufacturing process of the steel specimens and of steel itself. As for the latter one, the micro-structure of steel is usually inhomogeneous which results in scattering material properties. Extensive investigations on the statistical properties of the stress-strain curves of structural steel are found in Melcher et al. (2004) and Sadowski et al. (2015). The distribution functions of the yield strength and of the ultimate strength is to be modelled as log-normal, as suggested by several research groups and scientific consortia, i.a. JCSS (2001), Melcher et al. (2004), Sørensen and Toft (2010), and Sadowski et al. (2015). However, these research groups propose different characteristic values for the underlying log-normal distribution functions of the yield strength and the ultimate stress. Melcher et al. (2004) and Sadowski et al. (2015) investigated steel probes from different regions and from different decades, which are the reasons for the stated differences.

Young's modulus is found to be subject to scattering as well. Its distribution type is a log-normal distribution (JCSS, 2001; Sørensen and Toft, 2010; Sadowski et al., 2015). Again, the values of the parameters describing the distribution function of Young's modulus differ slightly.

The yield strength, the ultimate strength, and Young's modulus correlate to each other. Inter alia JCSS (2001) states a correlation matrix which allows to model the properties of structural steel appropriately for stochastic analyses.

5.1.1 Effect of extreme loads on structural members

Loading acting on a component causes both stress and strain within the material. Until the yield strength is reached, structural components only deform elastically. This means that the original shape of the structural component is reached after relaxing of the load. If the yield strength is exceeded, plastic deformation of structural components occurs. This plastic deformation of the steel component is still noticeable after relaxing of the load.

Additionally, buckling of steel structures may occur due to compression loads. Buckling describes sudden deformation due to compression load. Especially thin-walled and slender structural steel members are prone to buckling. The value of the critical buckling load is usually less than the yield strength of steel. This value depends strongly on the slenderness and potential imperfections of the geometry. Further information on buckling is given in e.g. Gottschalk (2017).

5.1.2 Structural design verification against extreme loads

For the design of steel structures, the yield strength is one limiting load-bearing capacity. Usually, plastic deformation which occurs for higher stresses than the yield strength is not allowed. Besides the proof against yield strength, the structural design against buckling is of special importance. Especially wind turbines may be prone to buckling, since the respective support structures usually are slender steel tubes which are loaded by axial compression loads to the self weight of its different components.

Semi-probabilistic safety concepts

The ultimate limit state design against failure due to extreme loads of offshore wind turbines is regulated by various standards. Inter alia DNV-ST-0126 (2021) is applied for European and international offshore-wind projects. DNV-ST-0126 (2021) makes reference to other standards and guidelines, such as DIN EN 1993-1-6 (2017) for shell buckling. The design against ultimate limit state for offshore wind turbines for German projects is based on DIN 18088-3 (2019) which refers to different parts of the Eurocode, most relevantly to DIN EN 1993-1-1 (2010) and DIN EN 1993-1-6 (2017). Here, the different methods as well as different characteristic and design values for the design against failure due to extreme loads are stated.

As one of the most important parameters, the characteristic value of the yield strength is defined as the 5%-quantile, meaning that 95% of all tests shall exceed this limit. As explained above, scattering of the yield strength may occur during the manufacturing process of steel with a predefined nominal steel grade. The nominal yield strength of structural steel matches approximately the characteristic yield strength, as described by Melcher et al. (2004) and Sadowski et al. (2015). No difference is made by DIN EN 1993-1-1 (2010) between characteristic and nominal value.

Different steel grades with supplementary properties, such as minimum toughness, test temperature, or delivery conditions, are applicable for the structural design. The selection of the steel grade depends on the aimed field of application and the design requirements. The nominal yield strength and potentially supplementary properties are part

of the notation of the steel grades, with the notations being defined in DIN EN 10025-1 (2005) and its accompanying standards. Structural steel with nominal yield strengths of 235 MPa, 275 MPa, 355 MPa, 420 MPa, 460 MPa, and 690 MPa are applicable according to DIN EN 1993-1-1 (2010). The nominal yield strength is to be reduced for steel plates with increased wall thickness, as it is regulated in the governing standard DIN EN 1993-1-1 (2010).

For both the proof against failure due to exceeding of the yield strength as well the proof against failure due to buckling, the acting design stresses caused by external loads shall not exceed the design load-bearing capacity of the structural component, referring to Section 4.1. Partial safety factors as defined in the relevant standards are applied on the characteristic values of loads and of resistance to calculate the design values. For the proof against failure due to exceeding of the yield strength, the acting design stress is compared against the design yield strength. Different methods exist for the proof against failure due to buckling. The most-common approach is the stress-based proof against buckling. Here, the ideal buckling stress is reduced which a structural member can withstand. Important parameters for the determination of the reduction factors are the slenderness ratio of the structure as well as imperfections due to the manufacturing process, considering different levels of manufacturing quality. Formulae and values for the relevant parameters are provided in the relevant standards, i.e. DIN EN 1993-1-1 (2010). Besides this approach, several methods exist which are based on finite-element analysis of the structural component (DIN EN 1993-1-6, 2017). Different levels of accuracy and complexity can be applied to model the required shell theory, material law, and the shell geometry. Shell theory and material law may be linear or non-linear, and the shell geometry can be modelled as either perfect or with imperfections included. Gottschalk (2017) provides details on these different methods for the design of steel structures against buckling.

The nominal value of Young's modulus is the mean value of the distribution function, as stated by JCSS (2001) and in the relevant standards and guidelines.

Probabilistic safety concepts

For the probabilistic design against extreme loads, both the distribution functions of the load-bearing capacity as well as of the extreme loads must be known. The probabilistic description of the extreme loads may be based on extrapolation of measurements or on load simulations. The probabilistic description of the extreme loads on the basis of frequency-domain analysis is given in the following sections.

Different statistical models exist to describe the scattering of yield strength of the structural components. As mentioned above, the yield strength follows a log-normal distribution which is stated by various consortia and researchers, i.a. JCSS (2001), Melcher et al. (2004), Sørensen and Toft (2010), and Sadowski et al. (2015). However, different values for the parameters describing the log-normal distribution function are proposed by these researchers. This is also observed by JCSS (2001). It is to be noted that the mentioned researchers analysed different data sets of steel specimens which were produced in different decades of the 20th century and in different regions of the world. These facts may be a reason for the differences described.

For the buckling analysis of shells and plates, the geometric imperfections of the structural components or their characteristic values are to be described stochastically. It is a common approach to model the structural components as a random field. This can be done by inverse Fourier transformation if applicable. Exemplarily, Böhm and Schaumann (2022) describe the shell geometries of suction buckets for offshore wind turbines as random field. Buckling may be most likely initiated at locations of the shell geometry which are either most loaded or which have the greatest deviation from the theoretically-perfect shell geometry. However, no detailed analysis of extreme deviations from the theoretically-perfect shell geometry exists which describes the extreme deformations by means of the extreme value theory. The correlation between loads, geometry, and imperfect shell geometry is to be considered within the probabilistic analysis especially for indifferently-loaded structures and complex geometries.

5.2 Determination of extreme values in frequency domain

Extreme loads can be determined both in time domain as well as in frequency domain. For the analysis in time domain, usually only one extreme value can be extracted per time series. Distribution functions of extreme values can be estimated on the basis of several extreme values which stem from different random realisations of otherwise constant conditions such that the extreme values can be considered as independent and identically distributed. Methods to estimate the distribution functions of extreme loads are described in Section 2.2.2. The deviation of extreme values in frequency domain is described in detail in the following.

5.2.1 Extreme values within Gaussian signals

The distribution functions of local minima and maxima can be derived in frequency domain by means of the spectral moments of the underlying signal. Considering that the analysed signal is a zero-mean Gaussian process, Rice (1945) stated a general theory regarding local minima and maxima within random noise. Based on this theory, the application for irregular sea states is shown by Cartwright and Longuet-Higgins (1956). The authors introduced the spectral width parameter ϵ , referring to Eq. (2.15), to describe the distribution function of the elevation of wave crests. The authors also provided a method to estimate the mean value of the greatest water-surface elevation observed during a specific period.

The deviation of the distribution function of the local maxima is explained by i.a. Rice (1945) and Cartwright and Longuet-Higgins (1956). The probability density function of the local maxima x is given as follows,

$$p^c(x_*) = \frac{\epsilon}{\sqrt{2\pi}} \cdot \exp\left(-\frac{x_*^2}{2 \cdot \epsilon^2}\right) + \frac{\sqrt{1-\epsilon^2}}{2} \cdot x_* \cdot \exp\left(-\frac{x_*^2}{2}\right) \cdot \left(1 + \operatorname{erf}\left(\sqrt{\frac{1-\epsilon^2}{2 \cdot \epsilon^2}} \cdot x_*\right)\right), \quad (5.1)$$

with $x_* = x/\sqrt{m_0}$ and the spectral width parameter ϵ . $\operatorname{erf}((\bullet))$ denotes the error function, which is defined as $\operatorname{erf}((\bullet)) = \frac{2}{\sqrt{\pi}} \cdot \int_0^{(\bullet)} \exp(-t^2) \cdot dt$. The distribution function for the peak values x_* solely depends on the spectral width parameter ϵ . On the basis of the

distribution functions of peak values, referring to Eq. (5.1), the distribution functions of the extreme values within a certain duration are obtained,

$$\begin{aligned} P^{\max}(x_*) &= P^c(x_*)^{N_c}, \\ p^{\max}(x_*) &= N_c \cdot p^c(x_*) \cdot P^c(x_*)^{N_c-1}, \end{aligned} \quad (5.2)$$

with N_c denoting the number of peaks within a certain duration T . The number of peaks is equal to T/T_c . For increasing number of peaks, the distribution function tends to the Gumbel distribution function, referring to Eq. (2.28). Cartwright and Longuet-Higgins (1956) state an equation to determine the expected mean value of extreme values occurring during a certain duration,

$$\begin{aligned} E[x_{*,\max}] &\approx \sqrt{\ln((1-\epsilon^2) \cdot N_c^2)} + \gamma / \sqrt{\ln((1-\epsilon^2) \cdot N_c^2)} \\ &= \sqrt{2 \cdot \ln N_z} + \gamma / \sqrt{2 \cdot \ln N_z}, \end{aligned} \quad (5.3)$$

where γ is the Euler-Mascheroni constant, $\gamma = 0.5772\dots$ N_z denotes the number of zero-up-crossings during a certain period.

5.2.2 Comparison between results obtained from time simulations and from power spectral densities

The distribution function of extreme values on the basis of power spectral densities is theoretically sound such that no differences are to be expected between the distribution functions of extreme values derived from power spectral densities and from respective random time series. Due to the transformation of the power spectral density into time domain, numerical errors are made which have an impact on the distribution function of extreme values. The inverse Fourier transformation of power spectral densities is discussed in further detail in Chapter 7. Reference is made to Section 7.1 for the definitions of different discretisation concepts of power spectral densities, including explanation of equidistant discretisation and equienergetic discretisation. The impact of discretisation on the spectral properties and on the respective distribution functions of extreme values is already discussed here for a Gaussian signal.

The derivation of distribution functions of local minima and maxima in frequency domain is shown for local minima and maxima occurring during irregular waves. The signal of the water-surface elevation is Gaussian. Exemplarily, a JONSWAP spectrum according to Eq. (3.17) with $H_s = 2 \text{ m}$, $T_p = 5 \text{ s}$, and $\gamma = 3.3$ is analysed. The simulated time series of the resulting water-surface elevation consists of 1,000 wavelets. Both the equidistant as well as equienergetic discretisation are applied. Two specific kinds of integration limits are investigated. The limits are chosen such that 0.5% as well as 0.0005% of the area are cut off at both tails of the power spectral density, respectively. The random time series of the water-surface elevation are generated with an executable program written by the author in the numeric computing environment *MATLAB*.

The probability density functions of the peak values according to Eq. (5.1) are shown in Fig. 5.2 (left). Additionally, Q-Q plots, with the extreme values as quantiles according to Eq. (5.2) plotted against simulated extreme values, are given in Fig. 5.2 (right). Five-hundred extreme values extracted from random time series are analysed. The analysis

is carried out for different utilised areas of 99% and 99.999% of the power spectral density. A duration of 600 s is considered. The 95% confidence intervals are calculated on the basis of the Kolmogorov-Smirnov test. Only the findings for the equienergetic discretisation with 1,000 wavelets are shown here.

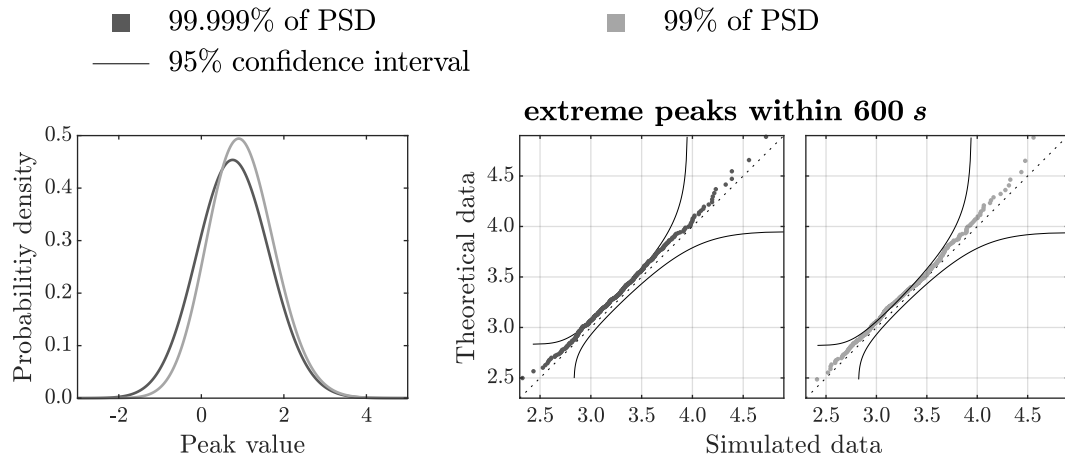


Figure 5.2: Probability density functions of peak values (left) and Q-Q plots of extreme peaks (right) obtained by different integration limits of the power spectral density (PSD) for a duration of 600 s

Due to the different values of the spectral width parameter ϵ for different utilised areas of the power spectral density, referring to Tbl. 5.1, the distribution functions for the peak values according to Eq. (5.1) also differ. The mode of the probability density function is greater and shifted to greater peak values for smaller values of the spectral width parameter. Smaller peak values are more probable to occur for greater values of the spectral width parameter.

As can be observed in Fig. 5.2 (right), the simulated extreme values are close to and parallel to the bisection line for both the utilised areas of the power spectral density considered. The values between 3.0 and 3.5 lie slightly outside the limit of the 95% confidence interval. The simulated extreme values are slightly underestimated in comparison to the theoretical extreme values according to Eq. (5.2). Nevertheless, a good agreement between the simulated and theoretical extreme values can be noticed.

Table 5.1 lists the statistical properties of the extreme values of a power spectral density, of its discrete power spectral density, and of the respective time series. The expected mean of extreme values according to Eq. (5.3) is calculated for the power spectral density as well as for the discrete power spectral density. The mean and standard deviation for the power spectral density as well as for the discrete power spectral density are determined by means of the distribution function according to Eq. (5.2). The mean and standard deviation of the time series are calculated on the basis of 500 independent and identically distributed extreme values, each extracted from random time series. The given values are obtained for different discretisation types and different utilised areas of 99% and 99.999% of the power spectral density with 1,000 wavelets. A duration of the time series of 600 s is considered for the analysis.

The expected mean values of the extreme values according to Eq. (5.3) which are calculated either on the basis of the power spectral density or on the basis of the discrete

Table 5.1: Statistical properties of the extreme values of a power spectral density, of its discrete power spectral density, and of the respective time series by obtained for different discretisation types and different integration limits of the power spectral density for a duration of 600 s

	99.999% of PSD			99% of PSD		
	PSD	D-PSD	TS ^a	PSD	D-PSD	TS ^a
ϵ	0.8456	0.8439 <i>0.7786</i>	0.8439 <i>0.7818</i>	0.6309	0.6309 <i>0.6308</i>	0.6333 <i>0.6315</i>
T_c [s]	2.0777 ^b	2.0789 ^b <i>2.4522^b</i>	2.0794 <i>2.4368</i>	3.1263 ^b	3.1263 ^b <i>3.1268^b</i>	3.1226 <i>3.1210</i>
E [$x_{*,\max}$] ^c	3.3561	3.3574 <i>3.3549</i>		3.3458	3.3458 <i>3.3458</i>	
Mean	3.3322 ^d	3.3335 ^d <i>3.3304^d</i>	3.3022 <i>3.2645</i>	3.3211 ^d	3.3211 ^d <i>3.3211^d</i>	3.3126 <i>3.2625</i>
St. dev.	0.3678 ^d	0.3677 ^d <i>0.3682^d</i>	0.3467 <i>0.3629</i>	0.3691 ^d	0.3691 ^d <i>0.3691^d</i>	0.3852 <i>0.3612</i>

PSD: power spectral density, D-PSD: discrete power spectral density,
TS: time series

Non-italic: equidistant discretisation, italic: equienergetic discretisation

^a Extracted from random time series

^b Peak-to-peak period according to Eq. (2.12)

^c Expected mean value of extreme values according to Eq. (5.3)

^d Calculated by means of distribution functions according to Eq. (5.2)

power spectral densities are nearly equal for each utilised area of the power spectral density. The expected values of the extreme values according to Eq. (5.3) are slightly greater in comparison to the mean values determined by means of the distribution functions according to Eq. (5.2), with a relative difference of approximately 0.7%.

The mean values calculated on the basis of the extreme values of random time series are smaller than the mean values calculated by means of the distribution function. The mean value for the time series obtained by the equidistant discretisation is less than 1% smaller in comparison to the respective mean values determined by Eq. (5.2). The mean value for the time series obtained by the equienergetic discretisation is about 2% smaller. The standard deviations are almost constant for each discretisation type considered in Tbl. 5.1.

In general, comparison of both utilised areas considered shows that the mean values for a relative utilised area of the power spectral density of 99% is slightly less than the value for a relative utilised area of the power spectral density of 99.999%.

5.2.3 Extreme values within non-Gaussian signals

The distribution function of extreme loads in frequency domain, referring to Eq. (5.1), is only valid for random Gaussian signals. In order to apply these formulae also for a non-Gaussian signal, it must be transformed to a Gaussian signal first. Then, the respective spectral moments required can be extracted either from the power spectral density, from the amplitude spectrum, or from the transformed time series itself. Finally, as the retrieved distribution function is a function of the transformed variable,

the transformation must be reversed for the distribution function of extreme values. The calculation of the mean extreme value according to Eq. (5.3) is generally not valid for non-Gaussian signals due to the back-and-forth transformation of the variables.

Winterstein (1985) states a method to transform the non-Gaussian signal to a Gaussian. This transformation is based on the mean value, standard deviation, skewness, and kurtosis of the signal. A non-Gaussian signal X_{NG} can be transformed to a Gaussian signal X_G with mean of zero and standard deviation of unity by applying the following formulae, with Eq. (5.4) being valid for leptokurtic signals and Eq. (5.5) being valid for platykurtic signals,

$$\begin{aligned}
 X_G &= \left(\sqrt{\xi^2(X_{NG}) + c + \xi(X_{NG})} \right)^{\frac{1}{3}} - \left(\sqrt{\xi^2(X_{NG}) + c - \xi(X_{NG})} \right)^{\frac{1}{3}} - a, \\
 \xi(X_{NG}) &= 1.5 \cdot b \cdot \left(a + \frac{X_{NG} - \mu_{X_{NG}}}{\kappa \cdot \sigma_{X_{NG}}} \right) - a^3, \\
 a &= \frac{h_3}{3 \cdot h_4}, \quad b = \frac{1}{3 \cdot h_4}, \quad c = (b - 1 - a^2)^3, \\
 h_4 &= \frac{\left(\sqrt{1 + 1.5 \cdot (\gamma_4 - 3)} - 1 \right)}{18}, \quad h_3 = \frac{\gamma_3}{6 \cdot (1 + 6 \cdot h_4)}, \quad \kappa = \frac{1}{\sqrt{1 + 2 \cdot h_3^2 + 6 \cdot h_4^2}},
 \end{aligned} \tag{5.4}$$

$$\begin{aligned}
 X_G &= X_{NG,0} - h_3 \cdot \left(X_{NG,0}^2 - 1 \right) - h_4 \cdot \left(X_{NG,0}^3 - 3 \cdot X_{NG,0} \right), \\
 X_{NG,0} &= \frac{X_{NG} - \mu_{X_{NG}}}{\sigma_{X_{NG}}}, \quad h_3 = \frac{\gamma_3}{6}, \quad h_4 = \frac{\gamma_4 - 3}{24},
 \end{aligned} \tag{5.5}$$

with the mean value $\mu_{X_{NG}}$, standard deviation $\sigma_{X_{NG}}$, skewness γ_3 , and kurtosis γ_4 of the non-Gaussian signal. It has to be checked whether the transformation is applicable. For certain values of the skewness and the kurtosis, the transformation according to Eq. (5.4) and Eq. (5.5) is not a monotonic function. Non-monotonic transformations cannot be handled such that other transformation functions must be applied (Benasciutti and Tovo, 2005a).

5.3 Extreme values within combined signals

As described in Section 4.2, the time series of loads acting on an offshore wind turbine may be a superposition of constant, periodic, transient, random, and random-transient functions.

5.3.1 Extreme loads depending on one load type

In case that the signal consists of only one load type, the respective extreme loads and their distribution function are determined as follows.

For a constant load type, the extreme value is equal to the constant value itself. The extreme value is constant as well for a periodic load, which has a constant amplitude. For a transient load, either the structural response is either an oscillation with constant amplitude or a decaying oscillation. The oscillation is constant in case that no damping exists, or it is decaying due to damping. Just as transient loads, random transient loads either have constant amplitudes or are a declining oscillation, and the extreme value

of the oscillation can be determined analytically or numerically. Randomness of load amplitudes as well as potential random superposition are to be considered. The extreme value of the oscillation can be determined analytically or numerically. The distribution function of extreme values of a random Gaussian process is calculated as described in Section 5.2.1. For random non-Gaussian, the approach as described in Section 5.2.3 can be applied in order to determine the distribution function of extreme loads.

5.3.2 Extreme loads within combination of different signals

Usually, several load types occur simultaneously. Considering that the respective signals are independent of each other, combination rules can be applied to determine the extreme value which is to be expected within the combined signal. The greatest possible value is observed when extremes within the different signals occur simultaneously. However, this event is highly unlikely, and a consideration of this event leads to a conservative but non-economic design of offshore wind turbines.

Several combination rules exist. An overview on the most common approaches is provided by Schmidt (2017). Of these different approaches, Turkstra's rule (Turkstra and Madsen, 1980) is shortly explained in the following. Inter alia Turkstra's rule is applied for the probabilistic description of the extreme loads which occur due to wind-induced and wave-induced loads within a 50-years storm acting on an offshore wind turbine (Seidel and Kelma, 2012).

Turkstra's rule is based on the assumption that the extreme value of one for the superposed signals occurs simultaneously with the mean value of the other signals. The mean values and extreme values have to be determined for each signal. Then, the greatest combined value f_{\max} according to Turkstra's rule is calculated as follows,

$$f_{\max} = \max_j \left(\max(f_j) + \sum_{i \neq j} \mu_{f_i} \right), \quad (5.6)$$

where μ_{f_i} is the mean value of the superposed signal f_i .

Turkstra's rule is mainly derived for the determination of design extreme values, but it is also suited for the probabilistic load determination. Therefore, the mean value as well as the distribution function of extreme values of each signal are to be known. For example, Monte Carlo simulations can be carried out in order to determine the extreme value of the combined signal and the respective distribution function of combined extreme values.

5.4 Findings

In time domain, extreme loads are extracted from random time series to model an appropriate distribution function of these loads. In frequency domain, the distribution function of extreme loads can be determined on the basis of the spectral moments. This method is theoretically proven and well established for Gaussian signals. An adequate transformation of signals which are not Gaussian-distributed is to be carried out in order

to apply this method as well. The non-Gaussianity of time series and its impact on the extreme values are shortly discussed in Section 8.1

It is observed that the extreme values extracted from time series slightly underestimate those obtained from the respective power spectral densities. Despite the smaller mean value of the extreme values, a very good agreement between the simulated and theoretical extremes regarding the type of distribution function is confirmed.

6 Fatigue design in frequency domain

The scattering loads, which act on structures, may cause fatigue damage. In order to evaluate the potential fatigue damage, both the resistance of the material and of the structural component as well as the decisive fatigue-load distribution are to be known. Models to describe the fatigue loads in both time domain as well as in frequency domain exist. Especially the frequency-domain analysis of fatigue loads is presented in the following. A new model is presented which has extended application boundaries in comparison to previously existing models and which provides more accurate results.

6.1 Structural design against fatigue loads

According to ASTM E1823-13 (2013), fatigue of materials is the process of local permanent structural damage which is caused by fluctuating stress or strain at some point. This process may lead to cracks or complete fracture after a sufficient number of load cycles. Concerning the design against fatigue failure of a structure or component, the time history of loading, geometry, material behaviour, and environmental conditions are to be considered.

The resistance of materials or structural components against fatigue failure is usually derived on the basis of laboratory tests with constant load amplitudes. Test specimens are cyclically loaded until a previously defined level of failure occurs, such as a defined crack size or fracture. Multiple tests of one specimen type with different loading amplitudes are required. Usually, the load amplitude is constant during each fatigue test. On the basis of these laboratory tests, the resistance against fatigue failure is usually characterised by SN curves which show the relationship of endurable numbers of fatigue loads and load ranges. The endurable number of fatigue loads decreases with increasing load ranges. For steel specimen, the relation of endurable number of fatigue loads N and load range s is given as a power-law function,

$$N(s) = C \cdot s^{-m} . \quad (6.1)$$

The slope of the SN curve m and the parameter C depend on properties of the material and the specimen. SN curves as defined by Eq. (6.1) are linear when plotted with both endurable number of fatigue loads and fatigue load being in logarithmic scale. The parameters C and m are usually not constant for all load ranges, but they are constant for certain intervals of load ranges and endurable numbers of fatigue loads, respectively. These SN curves are continuous at the boundaries of the intervals. The SN curve as given in Eq. (6.1) with constant parameters for all load ranges is referred to as “simplified SN curve” in the following.

The shape of the SN curve and its defining parameters depend on i.a. the load type and environmental conditions. Gudehus and Zenner (1999) provide a detailed overview, which is summarised in Fig. 6.1.

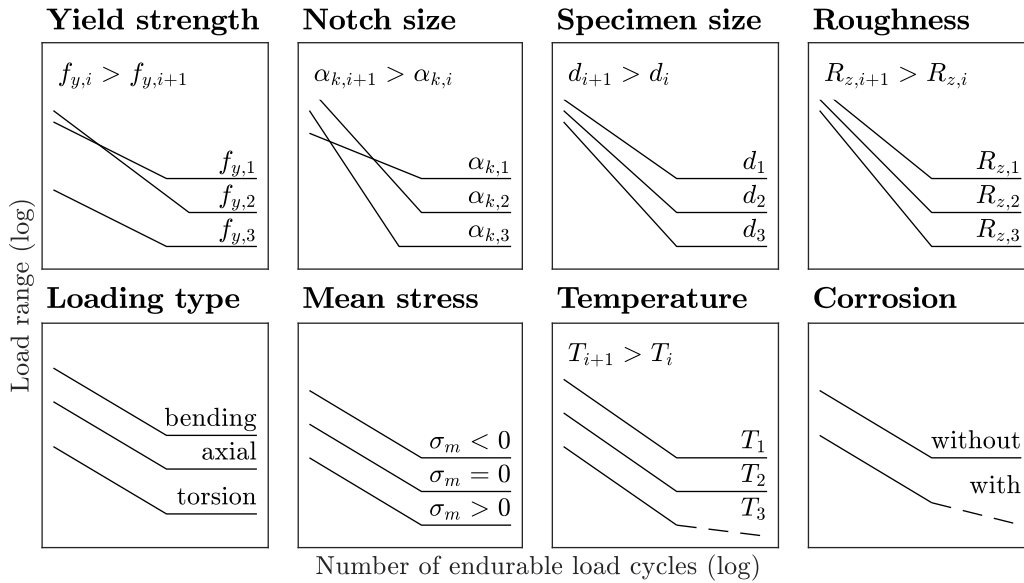


Figure 6.1: Influencing factors on SN curves of steel (adapted from Gudehus and Zenner (1999))

Fatigue tests on the same specimens carried out under identical environmental conditions and identical load conditions do not necessarily result in the same endurable number of fatigue loads. Rather the endurable numbers of fatigue loads are subject to scatter due to slight differences in geometry and microstructure of the specimen, which exist due to manufacturing process. This is especially notable for steel specimens with welding seams because the geometry of welding seams hardly can be controlled during the welding process.

Exemplarily, a collection of fatigue-test data is given in Sonsino et al. (2005). Here, the authors normalised the data of multiple fatigue tests by their corresponding detail categories such that the mean detail category of all test series is unity. The data are shown in Fig. 6.2 (left). The dashed line is the mean SN curve of all test data, and the solid line is the characteristic SN curve which is applied for the structural design. Here, the test data are adapted such that the detail category is 90 MPa , with the detail category being the characteristic load range at an endurable number of fatigue loads of $2 \cdot 10^6$ (DIN EN 1993-1-9, 2010). The derivation of the characteristic detail category is shortly discussed in Section 6.1.4. The characteristic detail category is required for the verification against fatigue failure when applying the semi-probabilistic safety concept. The presented SN curve has a slope of $m = 3$ for endurable number of fatigue loadss up to $5 \cdot 10^6$ and of $m = 5$ for endurable number of fatigue loadss greater than $5 \cdot 10^6$.

Additionally, the theoretical distribution function of the detail category, which is derived from the test data, is shown in Fig. 6.2 (right). The detail category follows a log-normal distribution, which is equivalent to a normal distribution in logarithmic scale.

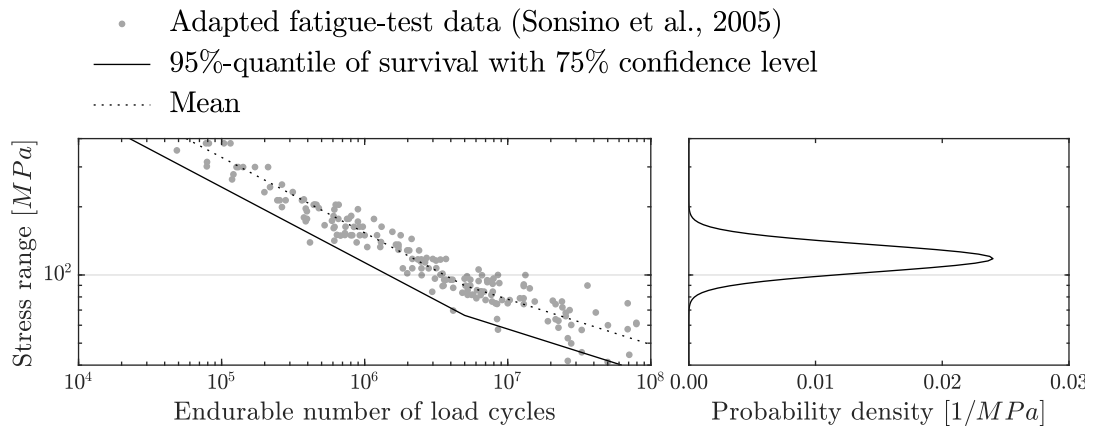


Figure 6.2: SN curve with detail category of 90 MPa (left) and probability density function of the detail category (right), based on the fatigue-test data collected by Sonsino et al. (2005) (figure adapted from Kelma and Schaumann (2015))

6.1.1 Effect of load cycles on structural members

Loading acting on a component causes both stress and strain within the material. The relation between stress and strain usually is not linear, but strain is disproportional to stress. It is assumed that the material behaviour consists of both elastic deformation and plastic deformation. The elastic deformation is usually modelled as linear. Different models exist to describe the plastic deformation, as described i.a. by Eichstädt (2019).

A load cycle is defined as a closed stress-strain hysteresis loop. A closed stress-strain hysteresis loop, consisting of both elastic and plastic deformation, is shown in Fig. 6.3 (left). A closed stress-strain hysteresis loop means that the initial strain for an initial stress is reached again. The stress-strain hysteresis loop due to a load time series of consecutive peaks with different values are shown in Fig. 6.3 (right). Stress-strain hysteresis loops of time series are considered as fatigue loads.

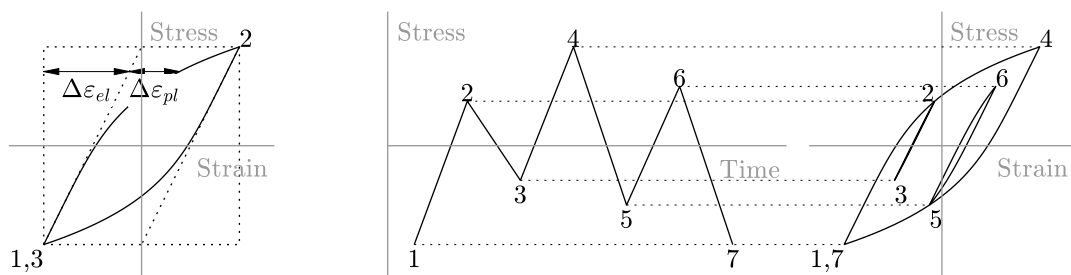


Figure 6.3: Stress-strain relationship for a single load cycle (left) and for a random load time series (right)

6.1.2 Methods for counting of fatigue loads

Counting methods are applied on time series for the derivation of stress-strain hysteresis loops. Here, smaller stress-strain hysteresis loops are considered as interrupting greater stress-strain hysteresis loops, referring to Fig. 6.3 (right). For specimens or structural components subjected to random loading, counting methods are applied to obtain a set

of representative fatigue loads. Different counting methods exist, with the most common being shortly described in the following. Detailed information on these counting methods is given in e.g. Radaj and Vormwald (2007) and ASTM E1049-85 (2017).

Peak counting All local minima (valleys) and local maxima (peaks) are extracted from a time series. Ranges are defined as the difference between a valley and a peak. Different approaches exist to form a range on the basis of a peak and a valley (ASTM E1049-85, 2017). Most commonly, the n -th greatest peak and the n -th smallest valley are combined.

Range counting The differences between local minima and the consecutive local maxima form the ranges which define the distribution of fatigue loads.

Level-crossing counting The cases in which the positive-sloped portion of a time series exceeds a load level are counted for previously set load levels. Load ranges are extracted from this cumulative frequency distribution.

Rainflow counting This widely-used method is commonly used for determination of fatigue loads. It captures the stress-strain hysteresis loops of a time series correctly. Rainflow counting, which is extensively applied for the analyses in this thesis, is explained in greater detail below.

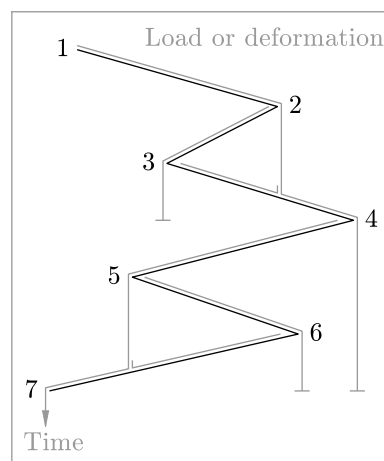


Figure 6.4: Example of rainflow-counting algorithm (further explanation is given in text)

For the rainflow-counting algorithm, only local extrema of a time series, i.e. peaks and valleys, are considered. As shown in Fig. 6.4, the time series is rotated such that the time axis points down, which may remind someone of pagoda roofs. Each local extremum is considered as a source of water which runs down the pagoda roof. This thought experiment is eponymous for the rainflow-counting algorithm. Rainflow counting is carried out by the rules listed below. Examples for applications of these rules are given in brackets with reference to Fig. 6.4.

- (i) Rainflows are consecutively started for earliest to latest local extremum.
- (ii) For a rainflow starting at a valley, it is interrupted if a following valley has a smaller value than the value of the starting valley [rainflow starting at 5, interrupted by 7]. For a rainflow starting at a peak, it is interrupted if a following peak has a greater

value than the value of the starting peak [rainflow starting at 2, interrupted by 4].

- (iii) A rainflow is interrupted if it meets a previous rainflow [rainflow starting at 3, interrupted by rainflow starting at 1].
- (iv) If not interrupted previously, a rainflow ends at the end of the time series [rainflow starting at 4].

Two rainflows form a closed stress-strain hysteresis loop if the following properties of both rainflows are applicable. Both rainflows possess the same range and same mean value, and both flow in opposite directions. The first rainflow of a closed stress-strain hysteresis loop is always interrupted by rule (ii). The latter rainflow is always interrupted by rule (iii). It starts at the range-defining extremum of the first rainflow and is interrupted by the rainflow which flows over the starting extremum of the first rainflow. Referring to Fig. 6.4, the rainflow flowing from 2 and interrupted by 4 and rainflow flowing from 3 and interrupted by the rainflow which starts at 1 and flows over 2 form a closed stress-strain hysteresis loop. Rainflows which do not form a pairing with another rainflow are considered as open stress-strain hysteresis loops. They are usually considered in fatigue-damage calculation. An open stress-strain hysteresis loop is assigned to half the probability of occurrence of a closed stress-strain hysteresis loop.

6.1.3 Calculation of fatigue damage

In order to evaluate the fatigue damage, the Palmgren-Miner linear damage hypothesis is usually applied for nearly all fatigue evaluation methods. The damage which would cause failure in a fatigue test with constant load amplitude after a specific endurable number of fatigue loads is proportional to the number of load cycles acting on the test specimen. The Palmgren-Miner linear damage hypothesis states that each load cycle (index i) contributes to the fatigue-damage accumulation,

$$D = \sum_i \frac{n_i}{N_i}, \quad (6.2)$$

with the number of applied load cycles n_i with the fatigue load s_i and the corresponding endurable number of fatigue loads N_i . Fatigue damage occurs when the fatigue-damage accumulation of all load cycles exceeds the permissible fatigue damage D_{lim} , $D > D_{lim}$. The value of the permissible fatigue damage depends on the assumptions and requirements made for the verification against fatigue failure. Further comments on selection of its value are given in Section 6.1.4. The load-sequence effect is not covered by the Palmgren-Miner linear damage hypothesis. Hence, a load cycle with a specific load range s at the beginning of the load time series contributes to the accumulated fatigue damage with the same amount as a load cycle with the same load range at any other point in time.

Usually, a fatigue load during a random time series has a different value than all other fatigue loads. Hence, each fatigue load with a number n_i of unity is considered in Eq. (6.2). In order to minimise the numerical effort, histograms of fatigue loads are often analysed. Here, fatigue loads are allocated to bins with previously defined ranges. Representative endurable numbers of fatigue loads are assigned to all bins. If the distri-

bution function of fatigue loads is known, the fatigue-damage accumulation according to the Palmgren-Miner linear damage hypothesis can be calculated as follows,

$$D = n \cdot \int \frac{p(s)}{N(s)} \cdot ds, \quad (6.3)$$

with the total number of applied load cycles n and the probability density function of load ranges $p(s)$. The integral in Eq. (6.3) is numerically solved if it is not integrable. For example, Eq. (6.2) is a numerical approximation of Eq. (6.3).

In dependence of the counting algorithm applied to determine fatigue loads, the expected values of the fatigue damage differ. Considering the counting methods stated in Section 6.1.2, rainflow counting causes an equal or greater calculated fatigue damage than range counting and an equal or smaller calculated fatigue damage than level-crossing counting (Tovo, 2002),

$$D_{RC} \leq D_{RFC} \leq D_{LCC} \leq D_{PC}, \quad (6.4)$$

with the indexes RC for range counting, RFC for rainflow counting, LCC for level-crossing counting, and PC for peak counting. The fatigue damage due to peak counting is the upper limit of the other three counting methods.

Often, a damage-equivalent load is given instead of the distribution of fatigue loads. Here, Palmgren-Miner linear damage hypothesis is assumed with the SN curve according to Eq. (6.1) with a single slope m . A damage-equivalent load (DEL) is defined as the fatigue load s_{DEL} with an occurring frequency of n_{ref} which causes the same damage as a set of fatigue loads s_i with corresponding occurring frequencies n_i does,

$$s_{DEL} = \sqrt[m]{\frac{\sum_i n_i \cdot s_i^m}{n_{ref}}}. \quad (6.5)$$

The value of n_{ref} can be chosen arbitrarily. For the structural design of offshore wind turbines, it is typically a characteristic endurable number of fatigue loads of the SN curve as given by the governing standard. The damage-equivalent load does not contain any information regarding the distribution of fatigue loads. Similar to Eq. (6.2) and Eq. (6.3), Eq. (6.5) can be expressed by means of an integral. Then, the term $\sum_i n_i \cdot s_i^m$ is substituted by $n \cdot \int p(s) \cdot s^m \cdot ds$.

6.1.4 Structural design verification against fatigue failure

The structural design has to be carried out so that no fatigue failure may occur during the considered lifetime. Therefore, the limit state function, which compares the load effects and structural resistance, has to be evaluated, as described in Section 4.1. The limit state function for fatigue is the difference between the permissible fatigue damage and the fatigue-damage accumulation. As stated in Section 4.1, the limit state function has to be fulfilled for design values for the semi-probabilistic safety concept. In case that the probabilistic safety concept is applied, the probability of the limit state function being less than zero must be less than a predefined probability of failure.

Fatigue-design concepts

Different fatigue-design concepts exist. These are the nominal-stress concept, the structural-stress concept, the notch-stress concept, the notch-strain concept, and fracture mechanics. The level of detail and the required computational effort increase in the given order of the short descriptions. Only a short overview on fatigue-design concepts is given. General information on these concepts is given in e.g. Radaaj et al. (2006) and Radaaj and Vormwald (2007). Deeper knowledge as well as profound background information on the different fatigue-design concepts are provided by i.a. Eichstädt (2019), Collmann (2021), and Schürmann (2021).

Nominal-stress approach Due to its relative simplicity in comparison to the approaches described in the following, the nominal-stress approach is commonly applied for the verification against fatigue failure of common structural details, such as longitudinal or circumferential weld seams. The verification against fatigue failure is carried out with the nominal stresses and the respective SN curves. The nominal load does not include any local stress peaks due to geometrical or material discontinuities. As described above, SN curves are derived from laboratory tests of the aforementioned common structural details, which are usually defined in the relevant standards and guidelines.

Structural-stress approach The structural-stress approach is applied for more complex structural components which are not covered by the SN curves defined for the nominal-stress approach. The structural-stress approach is commonly applied for welded tubular joints, which are components of jacket substructures. Here, the percentage stress increase at the structural discontinuity, usually referred to as “stress concentration factor”, is calculated by means of extrapolation of stresses which are either measured or numerically simulated at predefined locations close to the structural discontinuity. The value of the stress concentration factor depends on the geometry as well as on the load type. The geometry of the weld seam is not considered directly. The fatigue assessment is carried out with the structural stress at the component and SN curves defined for structural-stress approach.

Notch-stress approach The geometry of the weld seam is considered to determine the associated stress peaks at the notch. Therefore, a fictive notch radius is implemented to model the local stresses appropriately. The notch stress usually is calculated numerically. The verification against fatigue failure is carried with the determined notch stress and the specific SN curve for notch-stress approach.

Notch-strain approach The approaches previously described only consider the elastic material behaviour. The notch-strain approach additionally takes the plastic deformations at the notch into account for the verification against fatigue failure. Cyclic stress-strain behaviour of the material, as shown in Fig. 6.3, is derived from fatigue tests of plain steel specimens without any notches. Strain Wöhler curve with strain instead of stress are applied. The stress-strain relationship as well as of the stress at the notch are applied for the calculation of specific fatigue-damage parameters. The fatigue assessment is carried out on the basis of these parameters.

Fracture mechanics Within fracture mechanics, fatigue-crack growth is investigated. It is assumed that the shape and depth of an already existing crack is known. The growth of this crack due to cyclic loading is simulated until a predefined allowable crack depth is exceeded.

The scheme for the verification against fatigue failure by applying SN curves is exemplarily described in the following for a circumferential weld seam at a monopile substructure, referring to Fig. 6.5 (bottom, left). It concludes the previous sections. The scheme mainly describes the fatigue design by means of the nominal-stress approach. It can be adapted and be understood for the structural-stress approach, the notch-stress approach and partly for the notch-strain approach as well. In order to adapt the scheme for fracture mechanics, the SN curve (bottom, middle) is to be replaced with a material law to describe the fatigue-crack propagation.

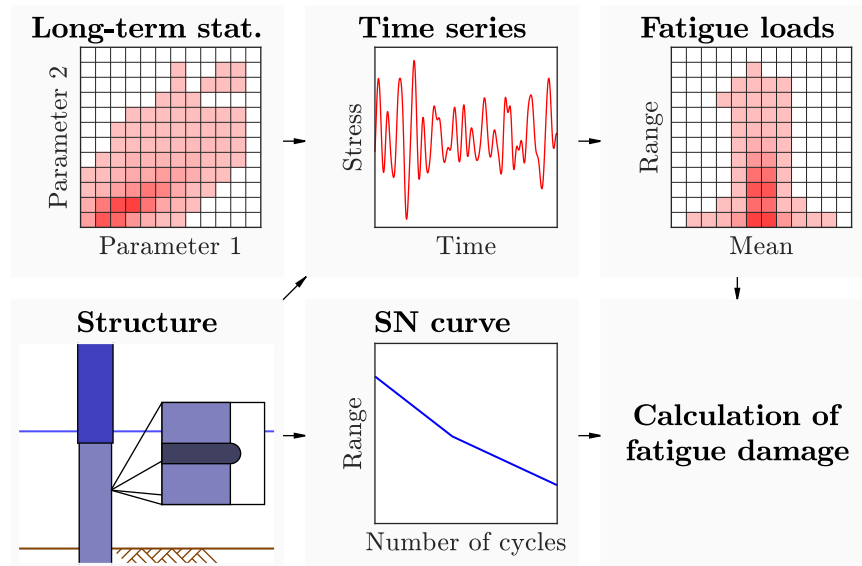


Figure 6.5: Scheme for the verification against fatigue damage by means of SN curves

The long-term statistics of environmental impacts are to be considered which are expected to act on the structure during its lifetime. Here, a histogram of two unspecified parameters is shown exemplarily (top, left). For all possible environmental conditions to be considered, time series of the load effects (top, center) are determined for each structural component, usually by means of load simulations. Fatigue loads are derived from these time series, e.g. by counting algorithms such as the rainflow-counting method, referring to Section 6.1.2. These load cycles can be understood as short-term statistics, determined for each case of the long-term statistics. The pairings of means and ranges as well as their frequency are usually stored in Markov matrices (top, right). For each pairing of mean and range of the load effects, the endurable number of fatigue loads which a component can resist until a defined failure mode is determined via the respective SN curves (bottom, center). Finally, the fatigue damage is calculated (bottom, right), e.g. via the Palmgren-Miner linear damage hypothesis, referring to Section 6.1.3.

Semi-probabilistic safety concepts

The fatigue design of offshore wind turbines is regulated by various standards and guidelines, which mostly rely on the regulations established in offshore oil- and gas industry DIN EN ISO 19902 (2014). The standards and guidelines DNV-RP-C203 (2019) and API RP 2A-WSD (2014) are commonly applied for the certification of European and international offshore-wind projects, while both are in accordance with DIN EN ISO 19902 (2014). The fatigue design of offshore wind turbines according to the German standard DIN 18088-3 (2019) refers to DIN EN 1993-1-9 (2010). These standards state SN curves for the base material as well as for configurations of geometries and welding seams which are commonly applied in structural engineering. Small differences exist for the SN curves for the same configuration stated within the mentioned standards and guidelines. Exemplarily, a detailed comparison for the SN curves for tubular joints, as they are stated in various standards, is given in Schürmann (2021).

For the semi-probabilistic design approach, which is commonly applied for the design of offshore wind turbines or structures in general, characteristic SN curves are usually stated in the respective standards and guidelines. As described above, they are based on laboratory tests. According to DNV-RP-C203 (2019), the characteristic SN curve is defined as the value associated to a probability of survival of 97.7% of all test data. Considering a log-normal distribution of the detail category, the characteristic value is equivalent to the mean SN curve minus two times the standard deviation in logarithmic scale. Within DIN EN 1993-1-9 (2010), the SN curve is labelled with the characteristic detail category. In case that fatigue-test results were applied to define the SN curve, the characteristic detail category is the value at an endurable number of fatigue loads of $2 \cdot 10^6$ with a probability of survival of 95% with a confidence level of 75% (DIN EN 1993-1-9, 2010). The characteristic SN curve with a probability of survival of 97.7% (DNV-RP-C203, 2019) is shown as solid line in Fig. 6.2 (left).

According to DIN EN 1993-1-9 (2010), either the nominal stress approach or the structural stress approach shall be applied for the fatigue assessment. The fatigue damage is calculated by means of the Palmgren-Miner linear damage hypothesis. Material partial safety factors are to be applied on the respective SN curves. The value of these partial safety factor is to be selected in dependence of the assessment method (damage-tolerant method or safe-life method) and of the consequence of failure (low consequence or high consequence). The permissible fatigue damage is unity. Three levels of consequence of failure are defined in the upcoming revision of DIN EN 1993-1-9 (2010), which is already published as draft version (DIN EN 1993-1-9, 2023).

DNV-RP-C203 (2019) also recommends to carry out the fatigue design with either the nominal stress approach or the structural stress approach. A guideline for fracture mechanics is additionally provided. In comparison to DIN EN 1993-1-9 (2010), no partial safety factors are applied on the SN curves. Instead, a design fatigue factor according to DNV-OS-C101 (2019) is applied to the permissible fatigue damage. It accounts for accessibility, possibility of inspections, and type of structure. The value of the design fatigue factor is either 1, 2, or 3, where higher values indicate a more critical or less accessible structural component. For the Palmgren-Miner linear damage hypothesis, the permissible fatigue damage is adapted in dependence of the design

fatigue factor, here as the reciprocal of the design fatigue factor. DNV-RP-C203 (2019) refers to the permissible fatigue damage as usage factor.

Probabilistic safety concepts

For a probabilistic fatigue design, distribution functions for material properties to model the resistance against fatigue failure as well as for the occurrence frequencies of the fatigue loads are required. The occurrence frequencies of fatigue loads on the basis of frequency-domain analysis are subject of the following sections.

JCSS (2013) provides statistical models to describe the scattering of the SN curves, for the verification concept of fracture mechanics, as well as for the permissible fatigue damage. As for SN curves, JCSS (2013) proposes to describe the parameter C of Eq. (6.1) with a log-normal distribution. The analysis of the fatigue-test data collected by Sonsino et al. (2005) supports this assumption, as can be seen for the detail category in Fig. 6.2 (right). The slopes of the SN curve are set as constant for steel (JCSS, 2013). The values of the parameters describing the log-normal distribution of the detail category are to be determined on the basis of fatigue tests. According to JCSS (2013), the permissible fatigue damage is log-normal distributed with mean value of unity and coefficient of variance of 0.3. A detailed analysis is provided by Al Shamaa (2015), who analysed the applicability of the Palmgren-Miner linear damage hypothesis as well as the statistical scattering of the permissible fatigue damage on the basis of broad data sets of fatigue tests of welded connections.

6.2 Calculation of fatigue in frequency domain

Different approaches exist to determine the distribution function of fatigue loads and the fatigue damage in frequency domain, assuming that the signals are Gaussian. The most commonly used are listed in the following. Additionally, a new distribution function of fatigue loads developed by the author is introduced.

6.2.1 Distribution of fatigue loads in frequency domain

For a time series which is Gaussian and narrow-banded, the values of peaks can be described with a Rayleigh distribution,

$$p(s) = \frac{z}{2 \cdot \sqrt{m_0}} \cdot \exp\left(-\frac{z^2}{2}\right), \quad (6.6)$$

with $z = \frac{s}{2 \cdot \sqrt{m_0}}$. Here, the distribution function is given for load ranges s whose values are twice the load peaks. The Rayleigh distribution of load ranges is only based on the zeroth-order spectral moment. Hence, it is preferably applied for approximate fatigue-load estimation. For time series which are Gaussian and cannot be considered as broad-banded, the load peaks follow the distribution function of local maxima, referring to Eq. (5.1).

Only the load peaks and the load ranges, which are twice the load peaks, are modelled with the Rayleigh distribution function and the Rice distribution function. The

distribution functions of load peaks usually overestimate the resulting fatigue damages which are usually determined by means of counting algorithms, such as the rainflow-counting algorithm. Different approaches were derived by various researchers in order to describe the distribution function of fatigue loads by means of power spectral densities. No theoretical motivation exists for these distribution functions of fatigue loads. They are fitted to corresponding distribution functions of fatigue loads which are extracted from numerous time-domain simulations.

Selected, most-commonly applied distribution functions of fatigue loads as well as a new distribution function developed by the author are shortly described in the following. All these distribution functions of fatigue loads depend on the spectral parameters α_1 and α_2 , according to Eq. (2.14). With both α_1 and α_2 tending to unity, the underlying power spectral densities become narrow-banded. Hence, these distribution functions of fatigue loads tend to the narrow-band distribution function, referring to Eq. (6.6). Details on the background and on their derivation are given in Section 6.3.

It can be shown that the spectral parameter α_2 does not exceed α_1 (Benasciutti and Tovo, 2006). In order to provide a clearer presentation, the spectral parameter α_2 is shown as multiple of the spectral parameter α_1 within the thesis. Hence, both α_1 as well as α_2/α_1 have a codomain of $[0, 1]$.

Fatigue loads according to Dirlik (1985)

The distribution function of fatigue loads according to Dirlik (1985) is widely established for engineering disciplines such as offshore- and automotive applications. The distribution function of fatigue loads according to Dirlik (1985) consists of one exponential distribution function and two Rayleigh distribution functions, here given as probability density function,

$$\begin{aligned}
 p(s) &= \frac{1}{2 \cdot \sqrt{m_0}} \cdot \left(\frac{w_1}{t} \cdot \exp\left(-\frac{z}{t}\right) + \frac{w_2 \cdot z}{a^2} \cdot \exp\left(-\frac{z^2}{2 \cdot a^2}\right) + w_3 \cdot z \cdot \exp\left(-\frac{z^2}{2}\right) \right), \\
 w_1 &= \frac{2 \cdot \alpha_2 \cdot (\alpha_1 - \alpha_2)}{1 + \alpha_2^2}, \quad w_2 = \frac{1 - \alpha_2 - w_1 + w_1^2}{1 - a}, \quad w_1 + w_2 + w_3 = 1, \\
 t &= 1.25 \cdot w_1, \quad a = \frac{\alpha_2 - \alpha_1 \cdot \alpha_2 - w_1^2}{1 - \alpha_2 - w_1 + w_1^2},
 \end{aligned} \tag{6.7}$$

with $z = \frac{s}{2 \cdot \sqrt{m_0}}$ and load range s . Originally, the coefficients of the distribution function of fatigue loads were described in dependence on the spectral parameter α_2 and the so-called ‘‘irregularity factor’’ $\alpha_1 \cdot \alpha_2$ (Dirlik, 1985). The irregularity factor is the ratio of peak-to-peak period to mean period. The coefficients are shown in Fig. 6.6, here in dependence of the spectral parameters α_1 and α_2 . As marked, the scale parameter a of the first Rayleigh distribution function according to Eq. (6.7) is negative for values of α_1 close to unity. The scale factor of the exponential distribution function, which is a multiple of the weighting of the exponential distribution function, is not shown.

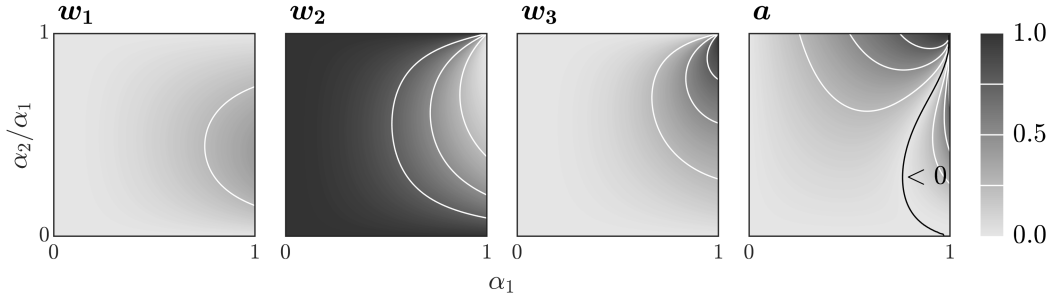


Figure 6.6: Weightings and parameters for the distribution function of fatigue loads according to Eq. (6.7) (Dirlik, 1985) in dependence of α_1 and α_2

Fatigue loads according to Zhao and Baker (1992)

Zhao and Baker (1992) described the probability density function of fatigue loads as a combination of a Rayleigh distribution function and a Weibull distribution function,

$$p(s) = \frac{1}{2 \cdot \sqrt{m_0}} \cdot \left(w \cdot a \cdot b \cdot z^{b-1} \cdot \exp(-a \cdot z^b) + (1-w) \cdot z \cdot \exp\left(-\frac{z^2}{2}\right) \right), \quad (6.8)$$

$$w = \frac{1-\alpha_2}{1-\sqrt{\frac{2}{\pi}} \cdot \Gamma\left(1+\frac{1}{b}\right) \cdot a^{-\frac{1}{b}}},$$

$$a = \max(1.1, 9 \cdot \alpha_2 - 7), \quad b = 8 - 7 \cdot \alpha_2,$$

with $z = \frac{s}{2 \cdot \sqrt{m_0}}$, load range s and the gamma function $\Gamma(\bullet)$. This distribution function is only valid for $\alpha_2 > 0.130$. Otherwise, the weighting w is greater unity for the spectral parameter $\alpha_2 \leq 0.130$. The distribution function can be used in almost every case, since there are only very few applications with $\alpha_2 \leq 0.130$ in practise. This calculation is applied in the following, even though Zhao and Baker (1992) also provided an improved calculation of the scale factor a . Here, the scale factor is calculated iteratively in dependence of the spectral parameters $\alpha_{0.75}$ and α_2 . This calculation is especially developed for a slope of the SN curve of 3. However, unrealistic values for the weighting w exist for certain values of $\alpha_{0.75}$ and α_2 (Zhao and Baker, 1992).

Fatigue loads according to Tovo (2002) and Benasciutti and Tovo (2005b)

Referring to Section 6.1.3, the fatigue loads extracted with the rainflow counting cause an expected fatigue damage which lies between the fatigue damage due to fatigue loads extracted with range counting and with level-crossing counting. Tovo (2002) introduced a distribution function of fatigue loads which consists of two Rayleigh distribution functions, which are the respective distribution functions for fatigue loads extracted with range counting and with level-crossing counting,

$$p(s) = \frac{1}{2 \cdot \sqrt{m_0}} \cdot \left(w_1 \cdot \delta(0) + w_2 \cdot z \cdot \exp\left(-\frac{z^2}{2}\right) + w_3 \cdot \frac{z}{\alpha_2^2} \cdot \exp\left(-\frac{z^2}{2 \cdot \alpha_2^2}\right) \right), \quad (6.9)$$

$$w_2 = b \cdot \alpha_2, \quad w_3 = 1 - b, \quad w_1 + w_2 + w_3 = 1,$$

with $z = \frac{s}{2 \cdot \sqrt{m_0}}$ and load range s . $\delta(\bullet)$ is the Dirac function. The term $w_1 \cdot \delta(0)$ is not given in previous publications which introduced this distribution function of fatigue loads or referred to it. This term is added by the author such that the cumulative

distribution function tends to unity for increasing fatigue loads, referring to Section 2.2. Adding this term does not alter the results presented by Tovo (2002), Benasciutti and Tovo (2005b), or fellow researchers, since fatigue loads of zero do not contribute to the fatigue damage. The Rayleigh distribution functions have scale parameters of unity and the spectral parameter α_2 , respectively. The term b is calculated to adjust the fatigue loads, which lie between fatigue loads extracted with range counting only and level-crossing counting only.

Based on multiple numerical simulations, Tovo (2002) suggested to calculate the term b as follows,

$$b = \frac{\alpha_1 - \alpha_2}{1 - \alpha_1} . \quad (6.10)$$

Benasciutti and Tovo (2005b) obtained an advanced analytical formula to determine the value of the term b , which depends on the spectral parameters α_1 and α_2 ,

$$b = \frac{\alpha_1 - \alpha_2}{(1 - \alpha_2)^2} \cdot (1.112 \cdot (1 + \alpha_1 \cdot \alpha_2 - (\alpha_1 + \alpha_2)) \cdot \exp(2.11 \cdot \alpha_2) + (\alpha_1 - \alpha_2)) . \quad (6.11)$$

The weightings according Eq. (6.11) are shown in Fig. 6.7 dependant on the spectral parameters α_1 and α_2 .

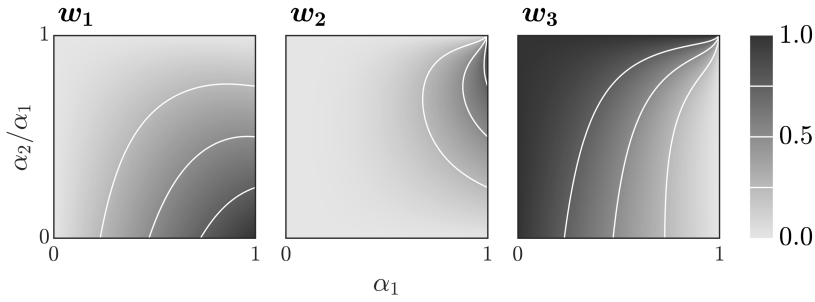


Figure 6.7: Weightings for the distribution function of fatigue loads according to Eq. (6.9) and Eq. (6.11) (Benasciutti and Tovo, 2005b) in dependence of α_1 and α_2

Newly-developed distribution function for fatigue loads in frequency domain

The author of this thesis developed a new distribution function for fatigue loads in frequency domain. The procedure to derive the newly-developed distribution function of fatigue loads is explained in detail in Section 6.3. This distribution function consists of two Rayleigh distribution functions,

$$p(s) = \frac{1}{2 \cdot \sqrt{m_0}} \cdot \left(w_1 \cdot z \cdot \exp\left(-\frac{z^2}{2}\right) + w_2 \cdot \frac{z}{\beta^2} \cdot \exp\left(-\frac{z^2}{2 \cdot \beta^2}\right) \right) ,$$

$$w_1 = \begin{cases} \alpha_1 \cdot \alpha_2 \cdot \left(\frac{1 - \alpha_2}{1 - \alpha_1}\right)^{1 - \alpha_1} & , \alpha_1 < \frac{\alpha_2}{\alpha_1} \\ \alpha_1 \cdot \alpha_2 & , \text{otherwise} \end{cases} , \quad w_1 + w_2 = 1 , \quad (6.12)$$

$$\beta = \alpha_2 \cdot \frac{1 - \alpha_1}{1 - \alpha_2} ,$$

with $z = \frac{s}{2\sqrt{m_0}}$ and load range s . The scale parameter of the first term in Eq. (6.12) has a value of unity. The scale parameter as well as the weightings of both terms depend on the spectral parameters α_1 and α_2 . The value of this scale parameter and the corresponding values of weightings are shown in Fig. 6.8 in dependence of the spectral parameters α_1 and α_2 .

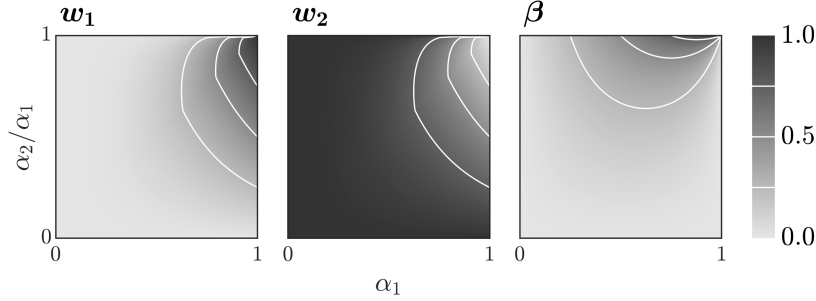


Figure 6.8: Coefficients for the newly-developed distribution function of fatigue loads according to Eq. (6.12) in dependence of α_1 and α_2 : (left and middle) weightings of Rayleigh distribution functions, (right) scale parameter of the second Rayleigh distribution function

6.2.2 Fatigue damage in frequency domain

Considering a simplified SN curve according to Eq. (6.1), which is linear in log-log scale, Eq. (6.3) yields analytical expressions for the fatigue damage with continuous distribution functions of fatigue loads. The mean fatigue damages per load cycle are listed in Tbl. 6.1 for the distribution functions introduced in Section 6.2.1.

Table 6.1: Mean fatigue damage per load cycle of various distribution functions of fatigue loads for linear SN curve according to Eq. (6.1)

Distribution function of fatigue loads	Mean fatigue damage per load cycle
Narrow band, Eq. (6.6)	$\left(\frac{8}{m_0}\right)^{\frac{m}{2}} \cdot C^{-1} \cdot \Gamma\left(1 + \frac{m}{2}\right)$
Dirlik (1985), Eq. (6.7)	$\left(\frac{4}{m_0}\right)^{\frac{m}{2}} \cdot C^{-1} \cdot \left(w_1 \cdot t^m \cdot \Gamma(1+m) + (w_2 \cdot \beta^m + w_3) \cdot 2^{\frac{m}{2}} \cdot \Gamma\left(1 + \frac{m}{2}\right)\right)$
Zhao and Baker (1992), Eq. (6.8)	$\left(\frac{4}{m_0}\right)^{\frac{m}{2}} \cdot C^{-1} \cdot \left(w \cdot a^{-\frac{m}{b}} \cdot \Gamma\left(1 + \frac{m}{b}\right) + (1-w) \cdot 2^{\frac{m}{2}} \cdot \Gamma\left(1 + \frac{m}{2}\right)\right)$
Benasciutti and Tovo (2005b), Eq. (6.9)	$\left(\frac{8}{m_0}\right)^{\frac{m}{2}} \cdot C^{-1} \cdot \left(b \cdot \alpha_2 + (1-b) \cdot \alpha_2^m\right) \cdot \Gamma\left(1 + \frac{m}{2}\right)$
Kelma, Eq. (6.12)	$\left(\frac{8}{m_0}\right)^{\frac{m}{2}} \cdot C^{-1} \cdot (w + (1-w) \cdot \beta^m) \cdot \Gamma\left(1 + \frac{m}{2}\right)$

In addition to the fatigue damages derivated from the power spectral densities of loads, formulae exist which calculate the fatigue damage of any wide-band power spectral density as a portion of the fatigue damage caused by a narrow-band power spectral density (index NB) as given by the first entry of Tbl. 6.1 (index NB),

$$D = \rho \cdot D^{NB} . \quad (6.13)$$

Different proposals of the correction factor for the narrow-band assumption ρ exist. Wirsching and Light (1980) introduced a correction factor which depends on the slope of the SN curve m ,

$$\rho = a(m) + (1 - a(m)) \cdot \left(1 - \sqrt{1 - \alpha_2^2}\right)^{b(m)}, \quad (6.14)$$

with $a(m) = 0.926 - 0.033 \cdot m$ and $b(m) = 1.587 \cdot m - 2.323$. Wirsching and Light found this expression for the correction factor by fitting it to the fatigue damages of several simulated time series. They applied the Palmgren-Miner linear damage hypothesis and rainflow counting for the fatigue analysis. Benasciutti (2005) proposed an empirical correction factor of $\rho = \alpha_{0.75}^2$, which is independent of the slope of the SN curve. The resulting fatigue damage approximates the actual fatigue damage quite well, but it lacks any theoretical background (Benasciutti, 2005).

6.3 Derivation of distribution functions for fatigue loads

In general, the basic methodology applied by researchers to determine distribution functions of fatigue loads and fatigue-damage models, which are described above in Section 6.2, is very similar. This methodology is described by five steps, which are listed below. The differences between the distribution functions of fatigue loads as described in Section 6.2 arise from differences regarding initial assumptions, methods applied within the steps of the methodology and evaluation of the error.

- (1) Based on certain spectral properties of the underlying Gaussian signal, power spectral densities of the signal are defined, which possess these certain spectral properties.
- (2) These power spectral densities are transferred into time domain, usually via inverse Fourier transformation.
- (3) A fatigue-loads counting algorithm is applied on the time series.
- (4) Either the fatigue damage caused by the extracted fatigue loads is calculated by means of a specific fatigue-damage model, or the distribution of the simulated fatigue loads is derived.
- (5) A model which describes either the fatigue damage or the fatigue-load distribution is fitted to the simulated fatigue damage or the simulated fatigue-load distribution determined in step (4), respectively, such that the error made by the model is small. This model solely depends on the spectral parameters which are used to describe the power spectral densities in step (1).

The various power spectral densities which are used by the researchers introduced in Section 6.2 are shown in Fig. 6.9, with the assignment given in the following. These power spectral densities possess two clear distinctive peaks. Hence, they are usually referred to as “bimodal”. The distribution functions of fatigue loads presented in Section 6.2 depend on spectral parameters of the underlying power spectral densities, while the type of the power spectral densities is not taken into account. No studies exist which discuss the impact of different types on the distribution functions of fatigue loads.

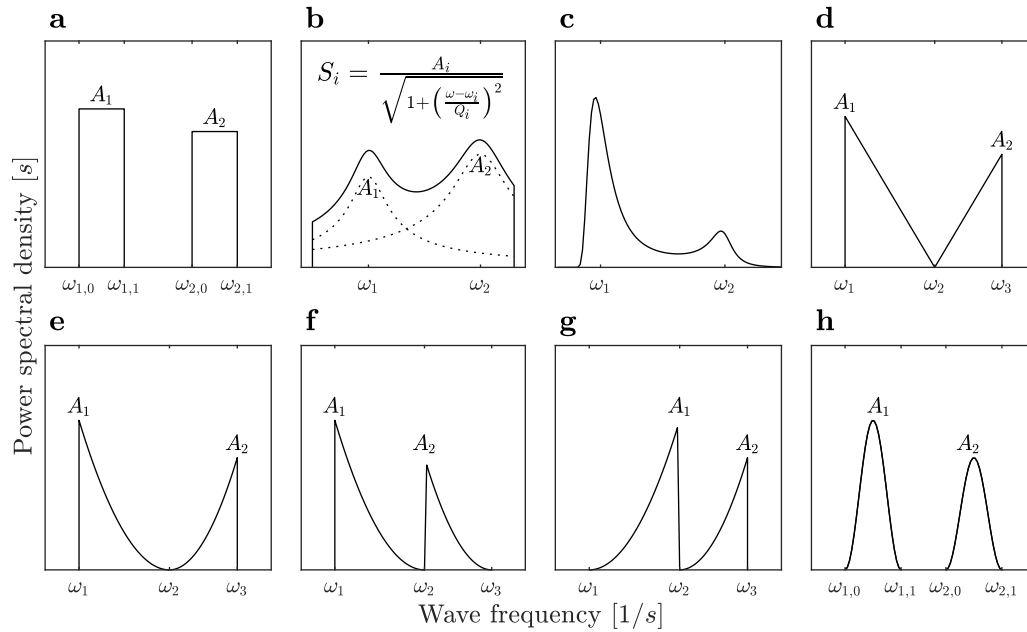


Figure 6.9: Types of power spectral densities used for derivation of distribution functions of fatigue loads

Dirlik (1985) used 70 different pairings of the spectral parameter α_1 and the irregularity factor $\alpha_1 \cdot \alpha_2$ for generation of power spectral densities, shown in Fig. 6.10. Fifty-six power spectral densities consisting of two constant terms and 14 smooth power spectral densities were analysed, with the shapes shown in Fig. 6.9(a) and (b). In order to evaluate the impact of the irregularity factor, Dirlik investigated several sets of power spectral densities with constant irregularity factors and random values for α_1 . Random time series were generated via inverse Fourier transformation of the power spectral densities. Equidistant discretisation was applied, and 1,024 wavelets were determined for each power spectral density. Each resulting time series consisted of approximately 108 peaks and 108 troughs. Twenty time series randomly generated for a certain power spectral density were concatenated to one block, from which fatigue loads were extracted via rainflow counting. Probability density functions were determined on the basis of the simulated fatigue loads. Ten blocks, each containing approximately 2,160 peaks and 2,160 troughs, were analysed for each power spectral density. The weightings and coefficients of Eq. (6.7) were numerically determined via the least-square estimation of the error between the probability density function of the simulated fatigue loads and the theoretical probability density function. Dirlik found analytical approximations for the numerically determined weightings and coefficients.

Zhao and Baker (1992) analysed 16 different power spectral densities with three different shapes, respectively, which are characterised by the spectral parameters $\alpha_{0.75}$ and α_2 . The authors used two types of uniform spectra, as shown in Fig. 6.9(a) with only one term, three Pierson-Moskowitz spectra, given by Eq. (3.16) and shown in Fig. 3.5, as well as eleven types of response spectra which are typical for offshore structures (Zhao and Baker, 1990), as shown in Fig. 6.9(c). Inverse Fourier transformation of the power spectral densities was applied to obtain time series. Each power spectral density was discretised such that 200 wavelets describe the signal in time domain. The wave frequencies of these wavelets are chosen randomly to avoid periodic effects.

These random values follow an uniform distribution limited by two boundary wave frequencies. Each simulated time series included 11,000 to 14,000 load cycles. Fatigue loads were extracted from the simulated time series via the rainflow-counting algorithm. The fatigue damage for each time series was determined for a SN curve according to Eq. (6.1) with a slope of unity. Least-square estimation of the error between simulated fatigue damage and corresponding fatigue damage caused by the theoretical distribution function was applied to determine the weight and the coefficient of the Weibull term in Eq. (6.8).

Benasciutti and Tovo (2005b) used 286 different pairings of the spectral parameters α_1 and α_2 to describe the investigated power spectral densities, shown in Fig. 6.10 (left). Values of 0.1, 0.3, 0.5 and 0.7 are chosen for α_2 , and the values for α_1 are scattering. The shapes of the power spectral densities consist of two terms which are either constant, linear with either negative or positive slope, or parabolic with negative or positive gradient, as shown in Fig. 6.9(a) and (d) to (g). The upper boundary of first term is the lower boundary of the second term. Rainflow counting was applied to derive the fatigue loads from the simulated time series. However, no information is provided by Benasciutti and Tovo regarding the techniques which were used to derive time series from the power spectral densities. The coefficients of the proposed distribution function as given by Eq. (6.9) are fitted to the corresponding fatigue damage according to Eq. (6.1) with a slope of $m = 3$. The error between simulated and theoretical fatigue damage is minimised via least-square estimation.

The pairings of spectral parameters which are used by Dirlik (1985), Zhao and Baker (1992) and Benasciutti and Tovo (2005b) are shown in Fig. 6.10. As one can see in Fig. 6.10, only a limited range of all possible pairings for spectral parameters of power spectral densities is covered by the studies of Dirlik (1985), Zhao and Baker (1992), and Benasciutti and Tovo (2005b). This is especially true for Dirlik (1985) and Zhao and Baker (1992), identified with black circles and grey squares, respectively. For the study by the author and the derived distribution function of fatigue loads in frequency domain, referring to Eq. (6.12), all possible pairings of spectral parameters α_1 and α_2/α_1 , which cover the whole codomains of these spectral parameters, are applied such that a universal distribution functions of fatigue loads is determined.

Again, the spectral parameter α_2 is shown as multiple of the spectral parameter α_1 or of the spectral parameter $\alpha_{0.75}$ to provide a clearer presentation of the results within the thesis. Both α_1 as well as α_2/α_1 and $\alpha_2/\alpha_{0.75}$ have a codomain of $[0, 1]$.

6.3.1 Development of a new distribution function of fatigue loads based on power spectral densities

Based on the findings of the reanalysis of existing approaches, the new approach to determine the distribution function of fatigue loads based on power spectral densities is developed, referring to Eq. (6.12).

The time series analysed by the author are longer and contain more peaks and troughs and thus more stress-strain hysteresis loops. The simulated distribution functions of simulated fatigue loads are more accurate than those of previous studies. The applied method of inverse Fourier transformation is also described in detail. The newly-

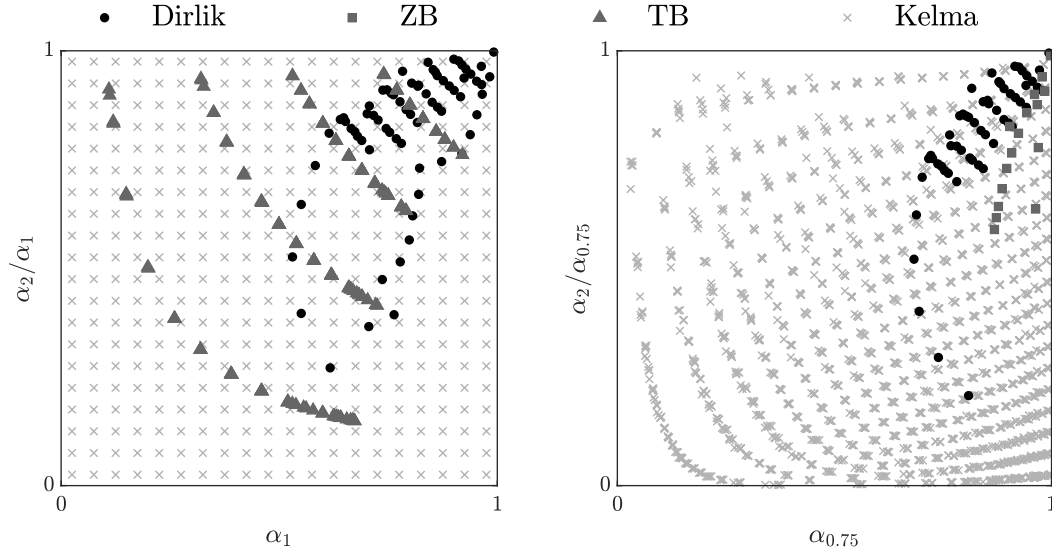


Figure 6.10: Pairings of α_1 and α_2/α_1 (left) and pairings of $\alpha_{0.75}$ and $\alpha_2/\alpha_{0.75}$ (right) used for the derivation of different theoretical distribution functions of fatigue loads. Acronyms for analytical distribution functions: Dirlik (Dirlik, 1985), ZB (Zhao and Baker, 1992), TB (Tovo, 2002; Benasciutti and Tovo, 2005b), Kelma (Eq. (6.12))

developed distribution function of fatigue loads based on power spectral densities also depends on the spectral parameters α_1 and α_2 . Their values are selected such that all possible values of the respective codomains are covered.

Power spectral densities applied for derivation of the newly-developed distribution function of fatigue loads

The power spectral densities used to derive a new distribution function of fatigue loads are classified by pairing of the spectral parameters α_1 and α_2/α_1 . Here, both parameters have values of $\frac{1}{40}, \frac{3}{40}, \frac{5}{40}, \dots, \frac{37}{40}, \frac{39}{40}$. Hence, 400 different pairings of α_1 and α_2/α_1 are used. As can be seen in Fig. 6.10, these pairings cover the codomains of all possible combinations of α_1 and α_2/α_1 extensively. The power spectral densities are set as the sum of two sinusoidal terms,

$$S(\omega) = \sum_{n=1}^2 S_n(\omega)$$

$$S_n(\omega) = \begin{cases} \frac{A_n}{2} \cdot \left(1 - \cos\left(\frac{\omega - \omega_{n,0}}{\omega_{n,1} - \omega_{n,0}}\right) \right) & , \omega \in [\omega_{n,0}, \omega_{n,1}] \\ 0 & , \text{otherwise} \end{cases}, \quad (6.15)$$

with coefficients A_n and boundary wave frequencies $\omega_{n,0}$ and $\omega_{n,1}$ for each term n . The shape of these power spectral densities is plotted in Fig. 6.9(h). Five sets of coefficients and boundary wave frequencies are analysed for each pairing of α_1 and α_2/α_1 . Since the values of each set cannot be expressed on the basis of the target values of the pairings, the values defining each power spectral density according to Eq. (6.15) are chosen randomly. Only those sets which are the closest to a given pairing are used to derive a new distribution function of fatigue loads. Due to the random selection of the values,

the values of the parameters α_1 and α_2/α_1 may not be equal to the target values. The maximum permissible deviation from the target pairing of α_1 and α_2/α_1 is set as 0.01. The random selection of the values defining each is carried out until five different sets of coefficients and boundary wave frequencies are determined for each pairing of α_1 and α_2/α_1 . The average deviation from the target pairing is $5.85 \cdot 10^{-4}$. The greatest deviations occur especially for small values of α_1 and α_2/α_1 , with a maximum deviation of $4.93 \cdot 10^{-3}$. The coefficients of each term are chosen such that the first-order spectral moment is unity. The values for the coefficients and boundary wave frequencies applied for this study are given in Appendix A4. Inverse Fourier transformation of the power spectral densities is carried out to generate corresponding time series. Equienergetic discretisation is applied for each term of the power spectral density according to Eq. (6.15), with 250 wavelets each. A study on discretisation techniques and the applicability of the equienergetic discretisation is given in Chapter 7. The length of the time series are chosen such that each time series contains approximately 1,000,000 local extrema. The simulation of the random time series is carried out with an executable program written by the author in the programming language *C#*. The rainflow-counting algorithm and the further evaluation are carried out with the numeric computing environment *MATLAB*.

Characteristics of time series

The time series, resulting from inverse Fourier transformation of the power spectral densities, are described shortly in the following. They are shown in Fig. 6.11 for different pairings of the spectral parameters α_1 and α_2/α_1 . They are chosen such that the domain of the spectral parameters are covered fairly to provide an adequate overview of the time series and their characteristics in dependence of the spectral parameters. The time series are plotted over different durations. Here, the durations are multiples of the peak-to-peak period of 20, 10,000 and 400,000. This allows short-term- and long-term characterisations of the time series.

Referring to Section 2.1.2, the spectral moment α_1 is the ratio of zero-up-crossing period and mean period of the signal, and α_2 is the ratio of peak-to-peak period and zero-up-crossing period. These characteristics can be best observed in the time series with $\alpha_1 = 0.025$. Here, the wavelets with very high periods, or equivalently with very low wave frequencies, are dominant in the time series of very long duration, referring to Fig. 6.11 (right). The amplitudes of the wavelets with high wave frequencies are very small in comparison to those of the wavelets with low wave frequencies, as can be seen in Fig. 6.11 (left) and (middle). The amplitudes of the wavelets with high wave frequencies increase with increasing α_2 , which can be seen for all α_1 shown in Fig. 6.11 (left). No clear distinction between the energy contents of wavelets with low and high wave frequencies can be made for the time series with $\alpha_1 = 0.975$ and $\alpha_2/\alpha_1 = 0.975$. It is observed for this time series in Fig. 6.11 (left) that the number of peaks is approximately the number of zero-up-crossings which follows from the definition of the spectral parameter α_2 . This cannot be observed for the other time series presented due to the selected domains of the graphs. For the time series with $\alpha_1 = 0.025$ and $\alpha_2/\alpha_1 = 0.025$, the ratio of number of peaks and number of zero-up-crossings is 1,600.

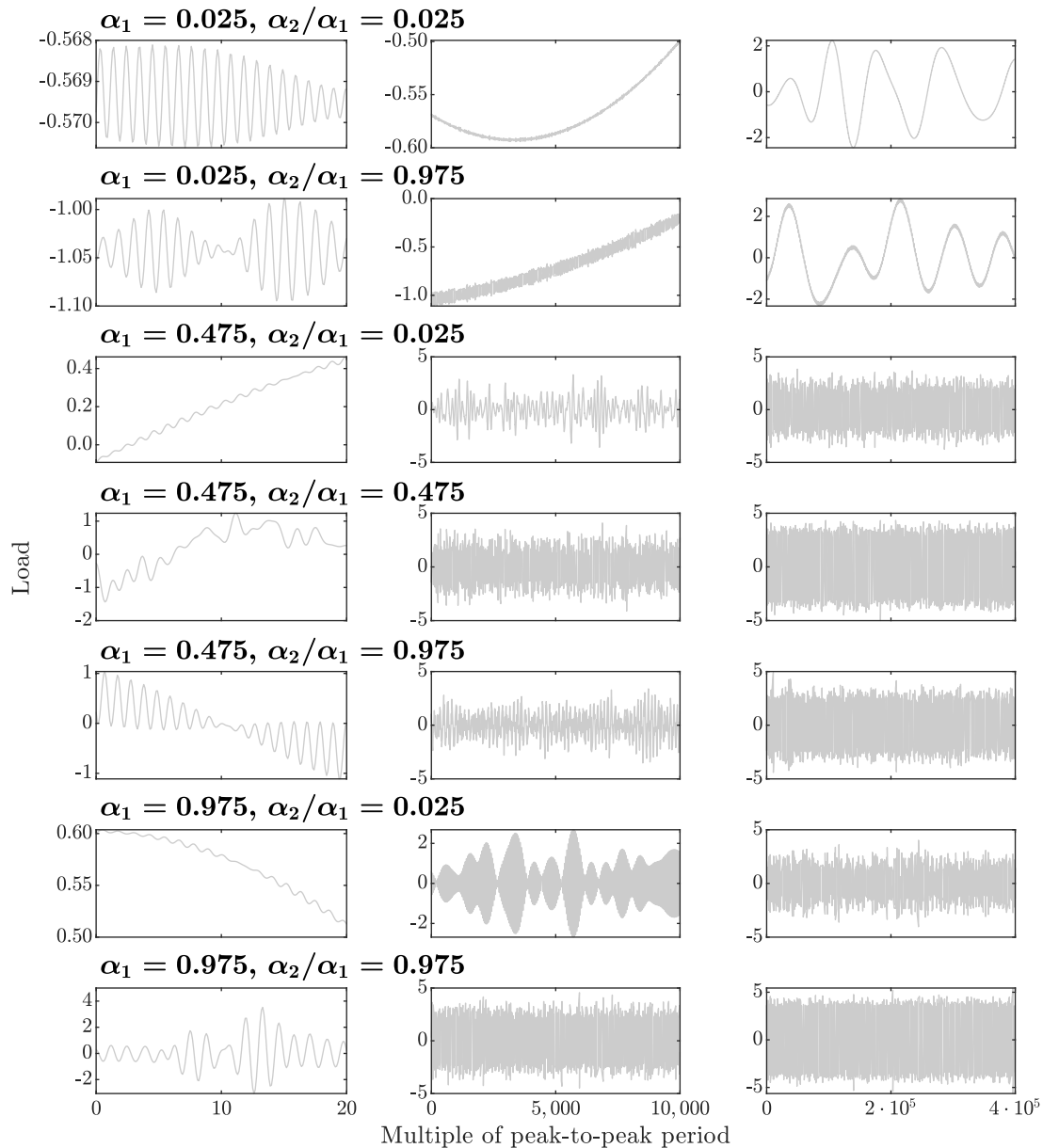


Figure 6.11: Examples of time series for different pairings of α_1 and α_2/α_1 for durations of multiples of the peak-to-peak period of (left) 20, (middle) 10,000, and (right) 400,000

Distribution functions of fatigue loads

Fatigue loads are determined with the rainflow-counting algorithm. Hence, approximately 500,000 fatigue cycles are extracted. Both full cycles and half cycles are considered.

The occurring probability associated to each full cycle is equal, and each half cycle possesses half the occurring probability of a full cycle. An empirical cumulative distribution function of fatigue loads is determined for each simulated time series. For this purpose, the fatigue cycles are sorted by their magnitude in ascending order. The probability of not exceeding a certain value is given by summing the occurring probabilities of all fatigue cycles which are smaller than this value.

The reverse cumulative distribution functions of fatigue loads are shown in Fig. 6.12 for different pairings of the spectral parameters α_1 and α_2/α_1 . The distribution functions for all five different realisations of each pairing of spectral parameters are plotted. The exceedance probability is shown in logarithmic scale.

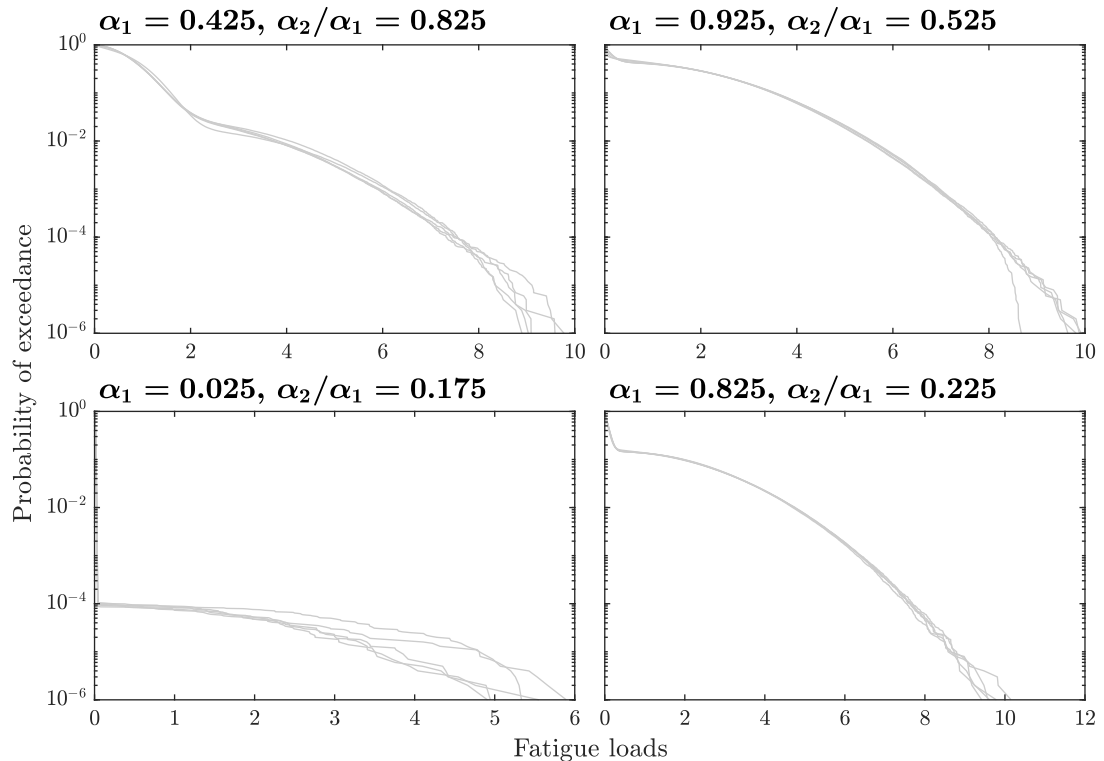


Figure 6.12: Simulated reverse cumulative distribution functions of fatigue loads for various pairings of α_1 and α_2

In general, it can be noted that the distribution functions of fatigue loads seem to consist of two distribution functions which are superposed and weighted. This can be seen by means of the transition between both distribution functions. This transition point is at a value of fatigue loads of ~ 2 and at a probability of exceedance of $\sim 10^{-2}$ for the reverse cumulative distribution functions with $\alpha_1 = 0.425$ and $\alpha_2/\alpha_1 = 0.825$, and at a value of fatigue loads of ~ 0.25 and at a probability of exceedance of ~ 0.2 for the reverse cumulative distribution functions with $\alpha_1 = 0.825$ and $\alpha_2/\alpha_1 = 0.225$. This transition point becomes less notable with increasing α_1 and α_2 .

Especially the curves of the simulated reverse cumulative distribution functions with an exceedance probability of less than 10^{-4} scatter for each set of pairings of spectral parameters. This is due to the stochastic scattering of very high, rarely-occurring values. Even when the fatigue loads with an exceedance probability of less than 10^{-4} are not considered, the distribution functions for one set of pairings of spectral parameters are not congruent, but they possess small differences in their general shape. Exemplarily, this can be seen in Fig. 6.12 for the reverse cumulative distribution functions with $\alpha_1 = 0.425$ and $\alpha_2/\alpha_1 = 0.825$. These differences also show up in the analysis of the fatigue damages which are calculated for each realisation of time series. The fatigue damages are calculated according to Eq. (6.2) for a SN curve with a slope of 4. The minimum and maximum value relative to the average fatigue damages as well as the

coefficients of variance of the fatigue damages are shown in Fig. 6.13 for all analysed pairings of the spectral parameters α_1 and α_2/α_1 . Even though the set of five different realisations for each pairing of the spectral parameters is small, the scattering is noticeable, and they allow the following qualitative conclusions.

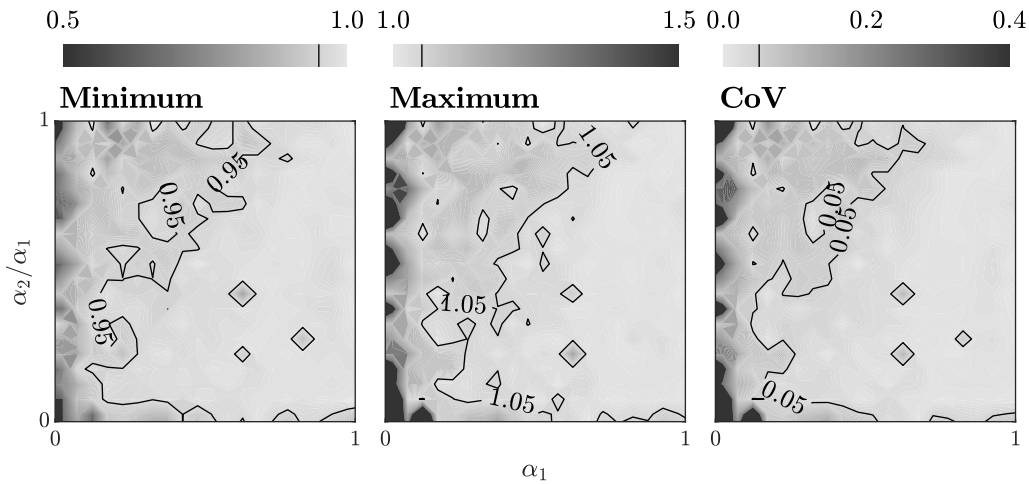


Figure 6.13: Relative minima and relative maxima as well as coefficients of variance (CoV) of the fatigue damage of the five time series simulated for each pairing of α_1 and α_2 , with the slope of the SN curve of $m = 4$

It is notable that the fatigue damage is not constant for each time series of each pairing of the spectral parameters α_1 and α_2/α_1 . Otherwise, the relative minimum and maximum values would be equal to unity, and the coefficients of variance would be equal to zero. For α_1 close to zero, the deviations results from the scattering of the very high with a low exceedance probability of less than 10^{-4} . For increasing α_1 , the relative minimum and maximum values tend to unity, and the coefficients of variance tend to zero. With increasing α_2/α_1 , deviations of 5% from the mean fatigue damages are exceeded for greater α_1 . As can be seen in Fig. 6.14 in comparison to Fig. 6.13, almost identical relative minima and relative maxima as well as coefficients of variance are determined when only the fatigue loads up to the 99.9%-quantiles are considered. Only exceptions are the statistics for values of α_1 close to zero where the very high fatigue loads above the 99.9%-quantiles contribute significantly to the fatigue damage. This means that only the very high, rarely occurring fatigue loads do not account significantly to the statistics of the fatigue damage. Furthermore, it is concluded that the spectral parameters α_1 and α_2 are not the only parameters which are required to describe the distribution functions of fatigue loads clearly. Further analysis of the time series and their respective spectral properties, such as spectral moments, may result in a more detailed description of the distribution functions of fatigue loads. This analysis is not carried out within this thesis.

Fitting of simulated distribution functions of fatigue loads to theoretical distribution functions

The assumption is that the underlying distribution function of fatigue loads consists of the sum of two weighted Rayleigh distributions. The sum of the weightings is equal

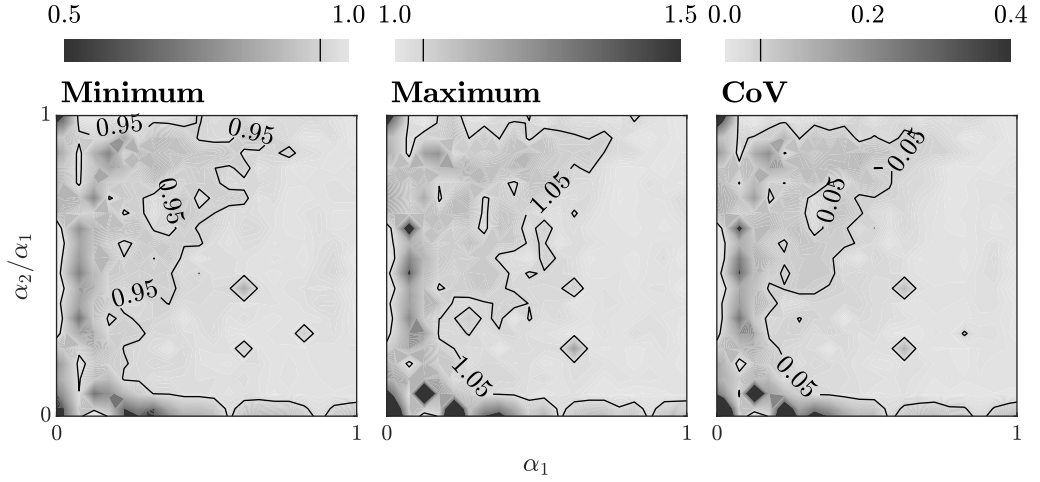


Figure 6.14: Relative minima and relative maxima as well as coefficients of variance (CoV) of the fatigue damage of the five time series simulated for each pairing of α_1 and α_2 , with the slope of the SN curve of $m = 4$, for the fatigue loads up to the 99.9%-quantile

to unity, and the scale parameter of the first Rayleigh distribution is unity. The scale parameter of the second Rayleigh distribution is considered as depending on the spectral parameters α_1 and α_2 . The approach is similar to this of Benasciutti and Tovo (2005b). Similarly, they assumed a distribution function of a sum of two weighted Rayleigh distributions, with the scale parameters set as unity and the spectral parameter α_2 , respectively, referring to Eq. (6.9).

Least-square estimation is applied to determine the scale parameter of the second Rayleigh distribution as well as the weightings. Therefore, the average difference between simulated distribution function and assumed distribution function is to be minimised by adapting the parameters to be determined. In order to emphasise the rarely occurring, very high fatigue loads, the average error of the logarithm of the exceedance probability function R is evaluated,

$$\frac{1}{\|X\|} \int_X (\log_{10} R_{sim}(x) - \log_{10} R_{theo}(x))^2 \cdot dx, \quad (6.16)$$

where the indices *sim* and *theo* refer to the simulated and to the analytical exceedance probability function, respectively. The exceedance probability function is the reverse of the non-exceedance probability function which is the cumulative distribution function. This emphasising of the very high fatigue loads is made, since especially these fatigue loads contribute significantly to the fatigue damage (Kelma and Schaumann, 2015). A brief calculation example shows the emphasising by applying the logarithmic function. Consider a small fatigue load with a simulated exceedance probability of 0.990 and a theoretical exceedance probability of 0.995. The absolute difference is 0.005, and the absolute difference of logarithmic values is $|\log_{10} 0.995 - \log_{10} 0.990| \approx 0.02$. For a great fatigue load with a simulated exceedance probability of 0.010 and a theoretical exceedance probability of 0.005, the absolute difference is 0.005, and the absolute difference of logarithmic values is $|\log_{10} 0.010 - \log_{10} 0.005| \approx 0.30$. In comparison, the absolute difference is equal for the small and high fatigue load, but the absolute differ-

ence of logarithmic values of the high fatigue load is larger by a factor of approximately 15.

The trapezoidal rule is applied to solve Eq. (6.16) numerically. The average difference between simulated distribution function and assumed distribution function according to Eq. (6.16) is non-linear. It is linearised for a set of values for the weightings and the scale parameter. Hence, a linear system of equations, which depends solely on the weightings and the scale parameter, is given. The linear system of equations as well as the constrain that the sum of weightings is unity is solved by means of the method of Lagrange multipliers. The values the weightings and the scale parameter are updated iteratively until the average difference is minimal.

Finally, analytical expressions for the weightings and the scale parameter are found on the basis of the respective values which are determined for each pairing of α_1 and α_2/α_1 by means of the least-square estimation as described above. The analytical expressions solely depend on the spectral parameters α_1 and α_2 , referring to Eq. (6.12).

6.3.2 Goodness-of-fit of theoretical distribution functions for fatigue loads in frequency domain

In order to evaluate the goodness-of-fit of the different analytical distribution functions for fatigue loads in frequency domain, both the distribution functions as well as the fatigue damages are compared to the respective properties of simulated fatigue loads in the following. All possible pairings of the spectral parameters α_1 and α_2 are considered.

Goodness-of-fit of theoretical reverse cumulative distribution functions for fatigue loads in frequency domain

The exceedance probability functions for four various pairings of α_1 and α_2 are shown in Fig. 6.15. The five empirical exceedance probability functions, simulated for each pairing, are in grey colour. The same empirical exceedance probability functions as in Fig. 6.12 are plotted here. Additionally, the reverse cumulative distribution functions according to Dirlik (1985), Zhao and Baker (1992), Benasciutti and Tovo (2005b), and as proposed by the author, referring to Eq. (6.12), are plotted. No distribution function according to Zhao and Baker (1992) is given for the pairing of $\alpha_1 = 0.025$ and $\alpha_2/\alpha_1 = 0.175$ because this pairing does not lie within the domain of the distribution function.

In general, the distribution functions according to Dirlik (1985), Benasciutti and Tovo (2005b), and as proposed by the author, referring to Eq. (6.12), match the simulated distribution functions of fatigue loads well. Small differences exist between those three distribution functions. As one can see, the distribution function as proposed by the author describes the simulated distribution functions at the transition point, as referred to in the description of Fig. 6.12, very well in comparison to the other theoretical distribution functions. This is especially notable for the reverse cumulative distribution functions with $\alpha_1 = 0.825$ and $\alpha_2/\alpha_1 = 0.225$ and for the reverse cumulative distribution functions with $\alpha_1 = 0.925$ and $\alpha_2/\alpha_1 = 0.525$. For the reverse cumulative distribution functions with $\alpha_1 = 0.925$ and $\alpha_2/\alpha_1 = 0.525$, it can be seen that the reverse cumulative distribution function according to Dirlik (1985) overestimates the simulated ex-

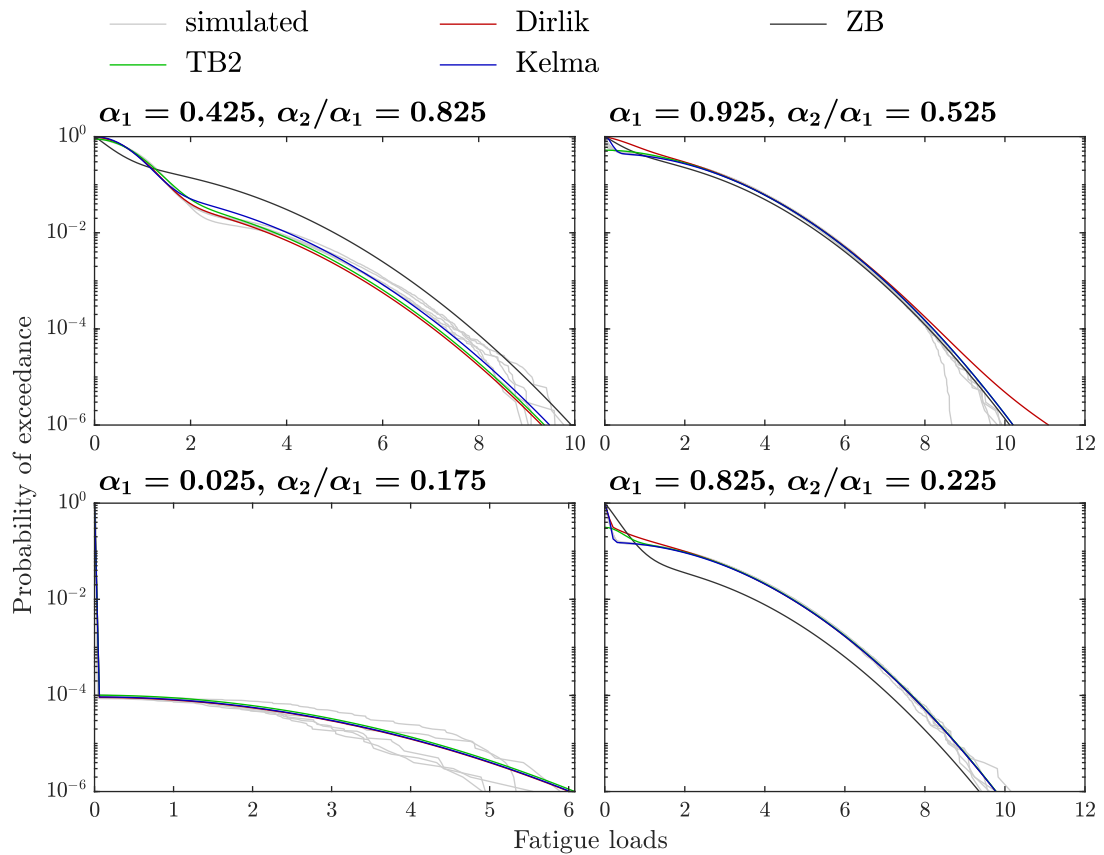


Figure 6.15: Simulated and analytical reverse cumulative distribution functions of fatigue loads for various pairings of α_1 and α_2 . Acronyms for analytical distribution functions: Dirlik (Dirlik, 1985), ZB (Zhao and Baker, 1992), TB2 (Benasciutti and Tovo, 2005b), Kelma (Eq. (6.12))

ceedance probabilities for ranges of fatigue loads less than 2 and greater than 8. Hence, the damage-equivalent load and fatigue damage are underestimated as it is shown in the following. In comparison to the other distribution functions shown in Fig. 6.15, the differences between the reverse cumulative distribution function according to Zhao and Baker (1992) and the simulated reverse cumulative distribution functions are the greatest, especially for reverse cumulative distribution functions with $\alpha_1 = 0.425$ and $\alpha_2/\alpha_1 = 0.825$ and with $\alpha_1 = 0.825$ and $\alpha_2/\alpha_1 = 0.225$.

Besides the optical measure of the error due to the theoretical distribution functions of fatigue loads in frequency domain, the deviation between theoretical and simulated distribution functions is analysed in the following. Therefore, the deviation is calculated according to Eq. (6.16), which was applied to derive the newly developed distribution function of fatigue loads based on power spectral densities, referring to Eq. (6.12). The errors for the narrow-band distribution function of fatigue loads, referring to Eq. (6.6), as well as for the analytical distribution functions of fatigue loads according to Dirlik (1985), Zhao and Baker (1992), Benasciutti and Tovo (2005b), and the new approach, referring to Eq. (6.12), are shown in Fig. 6.16. In order to evaluate the impact of the very high fatigue loads on the error according to Eq. (6.16), the deviation is also determined for fatigue loads with a non-exceedance probability less than 0.01. The results are presented in Fig. 6.17. Light colours denote a small values of the deviation according to Eq. (6.16) and thus a small error, and dark colours represent a greater

deviation between the analytical and simulated distribution functions of fatigue loads. For the distribution functions according to Zhao and Baker (1992), the errors are only shown for the spectral parameters for which the distribution functions are defined.

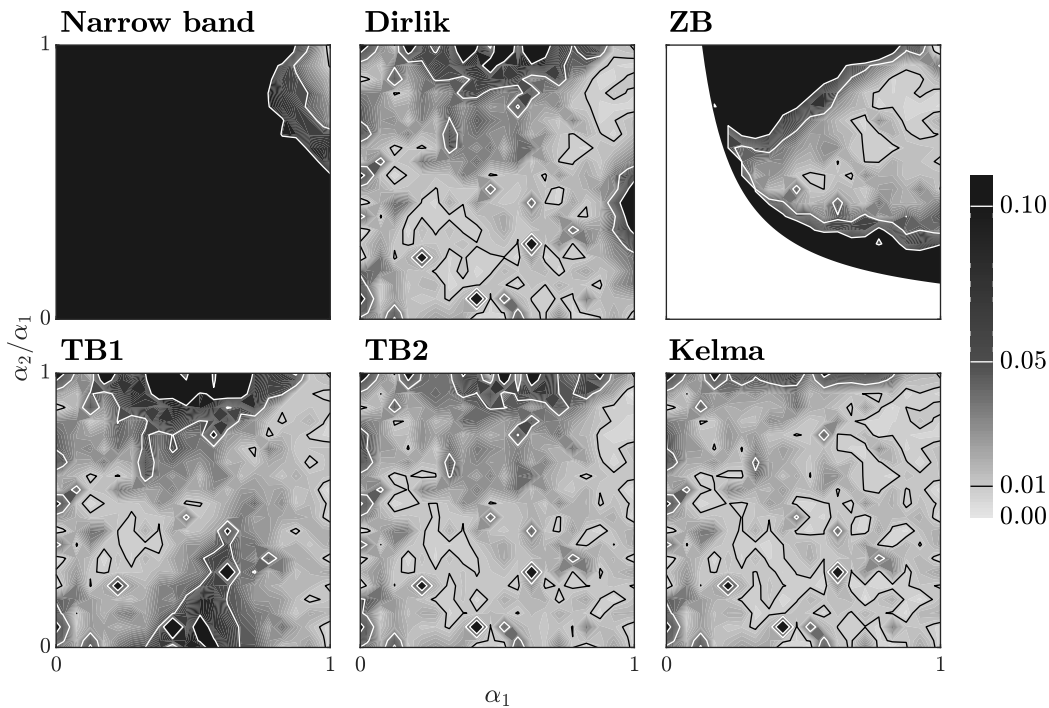


Figure 6.16: Error of different analytical reverse cumulative distribution functions according to Eq. (6.16) in dependence of α_1 and α_2 . Acronyms for analytical distribution functions: narrow band (Eq. (6.6)), Dirlik (Dirlik, 1985), ZB (Zhao and Baker, 1992), TB1 (Tovo, 2002), TB2 (Benasciutti and Tovo, 2005b), Kelma (Eq. (6.12))

The deviation between the narrow-band distribution function and the simulated distribution functions of fatigue loads is significant for almost all pairings of α_1 and α_2/α_1 . It reduces for increasing α_1 and for increasing α_2/α_1 and tends to zero as α_1 and α_2/α_1 tend to unity. The deviation for Zhao and Baker (1992) is less than 0.05 for α_1 greater than α_2/α_1 and α_2/α_1 greater 0.4. The error is significant outside of this area. The errors in dependence of α_1 and α_2/α_1 are similar for the distribution functions of fatigue loads according to Dirlik (1985), Tovo (2002), Benasciutti and Tovo (2005b), and the new approach, referring to Eq. (6.12). For most pairings of α_1 and α_2/α_1 , the error is less than 0.05. Only for α_2/α_1 close to unity, the error is greater than 0.05. The respective area is the smallest for the distribution functions of fatigue loads according to Benasciutti and Tovo (2005b) and especially for the new approach according to Eq. (6.12). The error is also greater than 0.05 for α_1 less than α_2/α_1 and α_1 less than 0.7 for the distribution functions of fatigue loads according to Tovo (2002).

In comparison to Fig. 6.16, similar findings are observed when the errors above the 99%-quantiles are analysed. This is especially true for the narrow-band distribution function and the distribution function of fatigue loads according to Zhao and Baker (1992). The errors are still similar for the distribution functions of fatigue loads according to Dirlik (1985), Tovo (2002), Benasciutti and Tovo (2005b), and the new approach developed by the author, referring to Eq. (6.12). However, the area with the error greater than

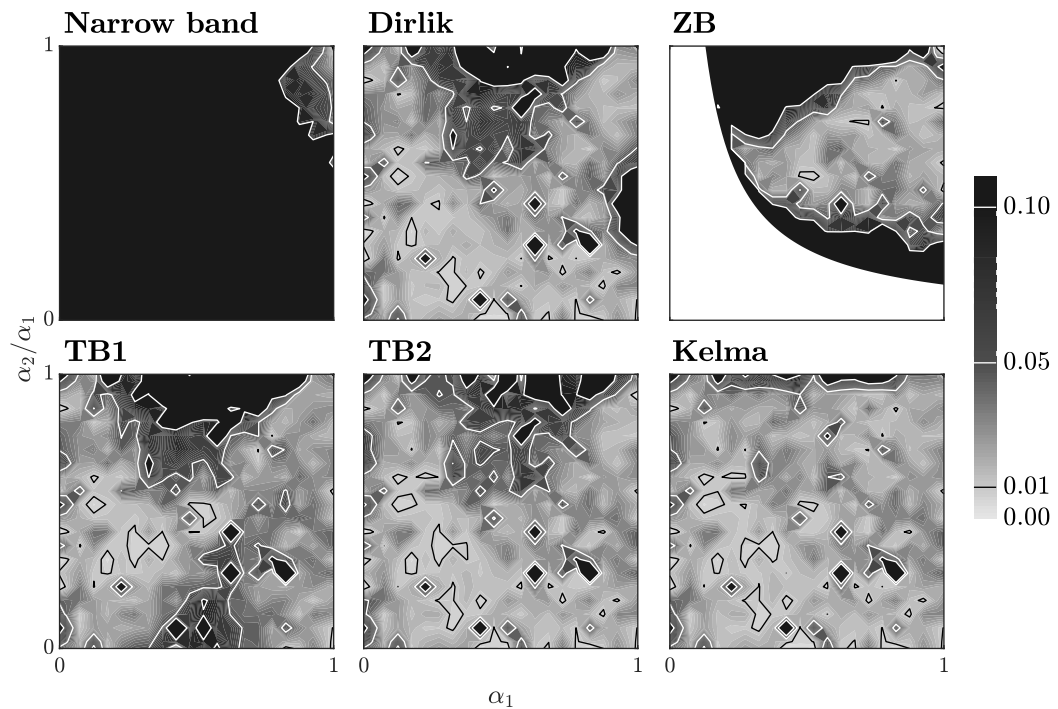


Figure 6.17: Error of different analytical reverse cumulative distribution functions according to Eq. (6.16) with an exceedance probability greater than 0.01 in dependence of α_1 and α_2 . Acronyms for analytical distribution functions: narrow band (Eq. (6.6)), Dirlik (Dirlik, 1985), ZB (Zhao and Baker, 1992), TB1 (Tovo, 2002), TB2 (Benasciutti and Tovo, 2005b), Kelma (Eq. (6.12))

0.1 is enlarged for Dirlik (1985), Tovo (2002) and Benasciutti and Tovo (2005b). Here, roughly the area with α_1 less than α_2/α_1 and α_1 greater than $1 - \alpha_2/\alpha_1$ has an error of greater 0.05. As for the distribution functions of fatigue loads according to Eq. (6.12), the error is similar to this when considering all fatigue loads, referring to Fig. 6.16.

In general, the new approach developed by the author, referring to Eq. (6.12), shows the best agreement between the analytical and simulated distribution functions of fatigue loads. Of the analysed theoretical distribution functions, the new approach also yields the most accurate match between the theoretical and simulated reverse cumulative distribution function of the very high, rarely occurring fatigue loads.

Goodness-of-fit of theoretical fatigue damages in frequency domain

As an additional measure to evaluate the goodness-of-fit of theoretical distribution functions of fatigue loads in frequency domain, the fatigue damages are analysed. Only the ratios of analytical and simulated fatigue damages are shown. The ratios of analytical and simulated damage-equivalent loads are the m -th root of the ratios of analytical and simulated fatigue damages. For slender steel tubes, as they are used for the support structures of offshore wind turbines, the section moduli are approximately proportional to the wall thickness. For example, the ratio of analytical and simulated damage-equivalent loads is 0.974 for a ratio of analytical and simulated fatigue damages of 0.9 and a slope of the SN curve of $m = 4$. Hence, the required wall thickness is underestimated by 2.6%.

The ratio of analytical fatigue damage to simulated fatigue damage in dependence of α_1 and α_2 are shown in Fig. 6.18 for the slope of the SN curve of $m = 4$. Here, the narrow-band distribution function of fatigue loads, referring to Eq. (6.6), as well as the analytical distribution functions of fatigue loads stated by Dirlik (1985), Zhao and Baker (1992), Benasciutti and Tovo (2005b), and by the author, referring to Eq. (6.12), are analysed. The black contour line denotes a perfect match between analytical fatigue damage and simulated fatigue damage, light colours represent an underestimation by the theoretical fatigue damage, and dark colours represent an overestimation by the theoretical fatigue damage.

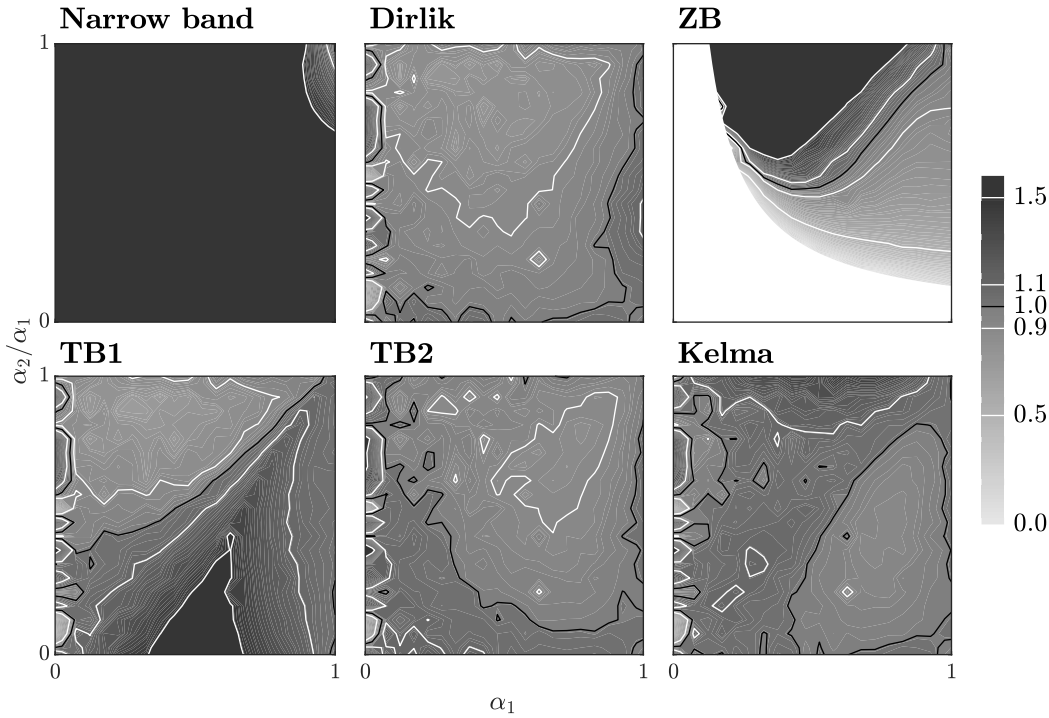


Figure 6.18: Ratio of analytical fatigue damage to simulated fatigue damage in dependence of α_1 and α_2 , with the slope of the SN curve of $m = 4$. Acronyms for analytical distribution functions: narrow band (Eq. (6.6)), Dirlik (Dirlik, 1985), ZB (Zhao and Baker, 1992), TB1 (Tovo, 2002), TB2 (Benasciutti and Tovo, 2005b), Kelma (Eq. (6.12))

The results for small values of α_1 are not discussed in detail in the following. Following the explanation given for Fig. 6.12 and Fig. 6.13, the scattering of the very high loads contributes significantly to the fatigue damage here, and it results in scattering fatigue damage as well. The fatigue damage for the narrow-band distribution function overestimates the simulated fatigue damage significantly. The ratio of analytical fatigue damage to simulated fatigue damage decreases for increasing α_1 and for increasing α_2/α_1 . The fatigue damage according to Dirlik (1985) slightly underestimate the simulated fatigue damage for most pairings of α_1 and α_2/α_1 . Only for values of α_1 close to unity, the fatigue damage is slightly greater than the simulated fatigue damage. The fatigue damage according to Zhao and Baker (1992) deviates from the simulated fatigue damage by $\pm 10\%$ for α_1 close to α_2/α_1 . In general, the ratio of analytical fatigue damage to simulated fatigue damage decreases for increasing α_1 and increases for increasing α_2/α_1 . The fatigue damage according to Tovo (2002) overestimated the simulated fa-

tigue damage by at least 10% for α_1 less than α_2/α_1 and α_1 less than 0.9. For α_1 greater than α_2/α_1 and α_2/α_1 greater 0.5, the simulated fatigue damage is underestimated. The fatigue damage according to Benasciutti and Tovo (2005b) yields a deviation from the simulated fatigue damage of $\pm 10\%$ for almost all pairings of α_1 and α_2/α_1 . Only exception is the area with α_1 greater than 0.5 and less than 0.9 and α_2/α_1 greater than 0.5 and less than 0.9 where the fatigue damage is underestimated by more than 10%. With a few exceptions, the absolute deviation of the fatigue damage according to the new approach, referring to Eq. (6.12), from the simulated fatigue damage is less than 10% for all pairings of α_1 and α_2/α_1 . For α_1 greater than α_2/α_1 , the simulated fatigue damage is underestimated. The simulated fatigue damage is overestimated by more than 10% only for α_2/α_1 close to unity.

In general, the fatigue damage according to Benasciutti and Tovo (2005b) and the fatigue damage according to the new approach developed by the author, referring to Eq. (6.12), show a good agreement between analytical fatigue damage and simulated fatigue damage. The new model according to Eq. (6.12) yields more conservative fatigue damage in comparison to this of Benasciutti and Tovo (2005b).

The ratio of analytical fatigue damage to simulated fatigue damage in dependence of α_1 and α_2 are shown in Fig. 6.19 for values of $m = 3$, $m = 5$, and $m = 10$ for the slope of the SN curve. Here, the analytical distribution functions of fatigue loads stated by Dirlik (1985), by Benasciutti and Tovo (2005b), and by the author, referring to Eq. (6.12), are analysed. Again, the black contour line denotes a perfect match between analytical fatigue damage and simulated fatigue damage, light colours represent an underestimation by the theoretical fatigue damage, and dark colours represent an overestimation by the theoretical fatigue damage.

The number of pairings α_1 and α_2/α_1 with the ratio of analytical fatigue damage to simulated fatigue damage less than unity (light-grey) increases with increased slope of the SN curve for all three analytical distribution functions of fatigue loads. This is especially true for the distribution functions according to Dirlik (1985) and Benasciutti and Tovo (2005b). Here, the ratio of analytical fatigue damage to simulated fatigue damage may have values of less than 0.5 for a slope of the SN curve of $m = 10$. Even though the distribution function of fatigue loads proposed by the author leads to ratios which are not as small, the fatigue damage is overestimated for values of α_2/α_1 close to unity. All three distribution functions may lead to non-conservative fatigue loads in dependence of α_1 and α_2 . The distribution function of fatigue loads proposed by the author is more conservative in comparison to those stated by Dirlik (1985) and Benasciutti and Tovo (2005b).

6.4 Fatigue loads of non-Gaussian signals

As explained in Section 4.2, the loads acting on offshore wind turbines may consist of several different load types. Superposition of several of the load types generally result in a non-Gaussian signal. The random load type may be non-Gaussian, too.

If the signal only consists of one load type, the respective fatigue loads are determined without great effort. For a periodic load, the distribution function of fatigue loads is equal to this of one period. Transient loading leads to an oscillation which can be

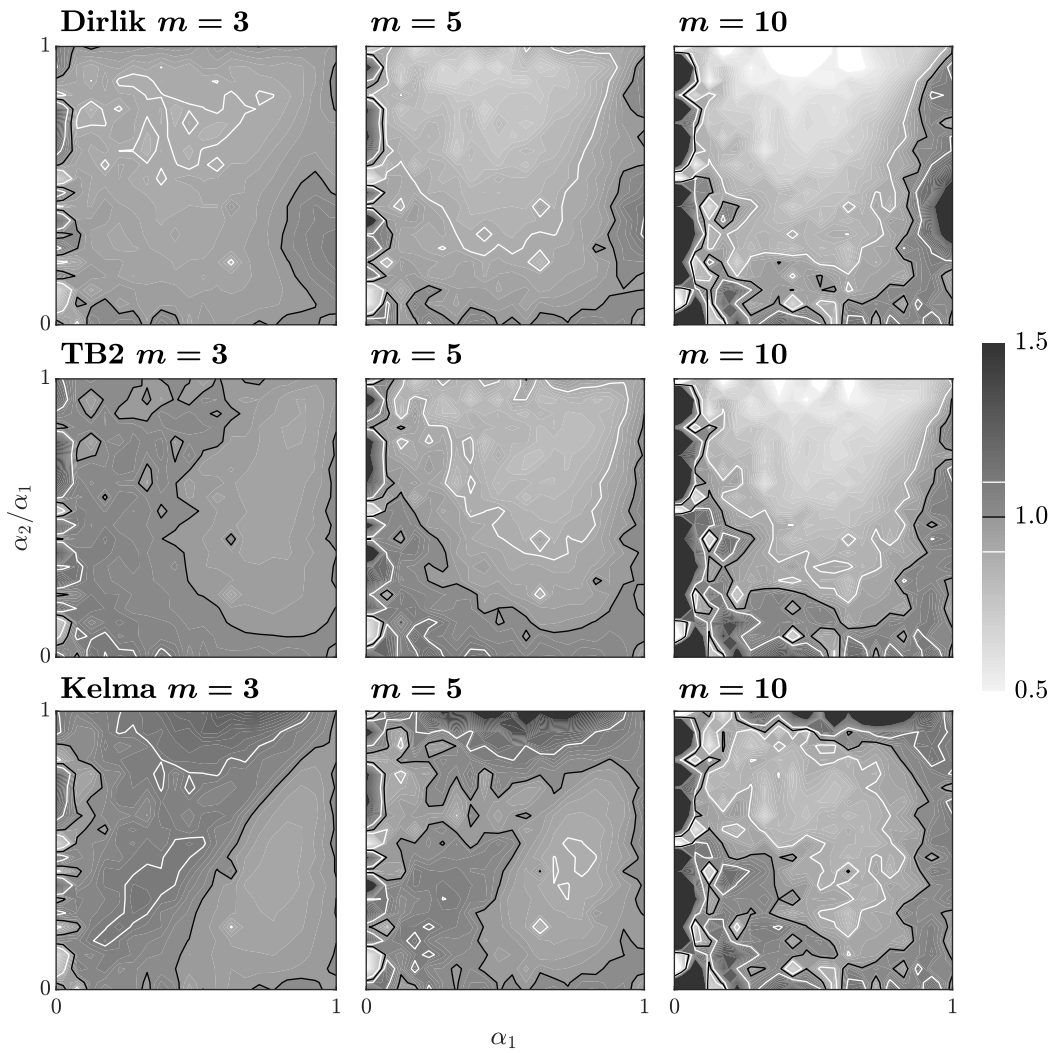


Figure 6.19: Ratio of analytical fatigue damage to simulated fatigue damage in dependence of α_1 and α_2 , with various values for the slope of the SN curve. Acronyms for analytical distribution functions: Dirlik (Dirlik, 1985), TB2 (Benasciutti and Tovo, 2005b), Kelma (Eq. (6.12))

modelled numerically or analytically. The fatigue analysis of random transient load is more complicated due to randomness of the amplitudes of the transient oscillations and the time lags. Due to the complexity of the counting algorithms to determine fatigue loads, a superposition of the fatigue loads of different load types generally does not result in the fatigue loads of the superposed load types. Hence, detailed analyses is required to quantify the impact of the superposition of different load types on the distribution function of fatigue loads.

The distribution functions of fatigue loads in frequency domain, which are introduced in Section 6.2, are only valid for random Gaussian signals. Hence, the signal must be transformed to a Gaussian signal first, as already introduced for non-Gaussian extreme loads in Section 5.2.3. The required spectral moments can be extracted from the transformed signal. The transformation to a Gaussian signal according to Winterstein (1985), referring to Section 5.2.3, is applied by Benasciutti and Tovo (2005a) for the fatigue loads derived from a non-Gaussian time series.

6.5 Findings

Fatigue loads are obtained from time series by means of counting algorithms. Here, the rainflow-counting algorithm is commonly applied.

Fatigue loads can also be extracted from power spectral densities. Different approaches exist which are solely based on spectral moments. These existing approaches are fitted to the simulation results determined in time domain which do not cover the possible values of the decisive spectral moments to a full extent. Hence, a new approach to determine distribution functions for fatigue loads in frequency domain is introduced by the author. This approach is derived from simulated time series, which cover the domain of the decisive spectral moments almost completely. During the development of this new approach, emphasis is put on the very high, rarely occurring fatigue loads which contribute strongly to the fatigue damage. In comparison to the previously existing approaches to determine distribution functions for fatigue loads on the basis of spectral moments, the new approach describes the distribution functions obtained from the time series better. The respective damage-equivalent loads and fatigue damages also match the respective values of the time series very well. It is also to be noted that the new approach to determine distribution functions for fatigue loads in frequency domain has an easier formulation. Therefore, it is easier to compute in comparison to the previously known approaches.

Similar to the extreme values, referring to Chapter 5, non-Gaussianity of signals is to be considered, which is also shown in Section 8.1.

7 Techniques for inverse Fourier transformation

Frequency-domain analysis does not yield sufficiently accurate results in all cases. This is especially true when non-linearities have a noticeable effect on the structural response. In this case, time-domain simulations may be required. Power spectral densities, which would be directly applied in frequency-domain analysis, are to be transferred into time domain, usually by applying the inverse Fourier transformation.

With the exception that aliasing and periodicity of the randomly generated time series are to be avoided, only a few recommendations on the inverse Fourier transformation are stated in literature and respective standards. With respect to sea states, DNV-RP-C205 (2019) states that a random sea state shall consist of at least 1,000 wavelets superposed. This recommendation is based on the findings of Elgar et al. (1985) who investigated the impact of discretisation on the run length of sea states. Additionally, since the theoretical power spectral densities to describe sea states have an unlimited domain, referring to Section 3.2.2, a frequency at which the power spectral density can be cut is defined for practical reasons (DNV-RP-C205, 2019).

In the following, power spectral densities of sea states are transferred into time domain by means of different approaches of discretisation. The impact on the statistics of the water-surface elevation as well as of the loads acting on a monopile substructure are investigated. Recommendations for the satisfying discretisation of power spectral densities are stated based on these analyses. Especially the number of wavelets are discussed in detail.

7.1 Techniques for inverse Fourier transformation

As shortly mentioned in Section 2.1.1, the inverse Fourier transformation is applied to transfer random signals given by power spectral densities into the time domain. This results in time series as given by Eq. (2.1) or Eq. (2.2). Power spectral densities are split in several partial areas, limited by their boundary wave frequencies. Based on these partial areas, the properties of the superposed wavelets are defined. Different techniques to determine the values for amplitudes and for wave frequencies exist, which are discussed in the following. Two methods to generate randomness of the resulting time series are shown.

7.1.1 Derivation of amplitudes

The wave frequency and the amplitude of the wavelets are given by the respective properties of each partial area, denoted with the index n . The wave frequency is usually chosen within the interval boundaries of the respective partial area.

The wavelet contains the energy E_n which is equal to the area of the partial area. The deterministic value of the amplitude a_n is given on the basis of the wave energy E_n ,

$$a_n = \sqrt{2 \cdot E_n} = \sqrt{2 \cdot \int_{I_n} S(\omega) \cdot d\omega}, \quad (7.1)$$

where I_n is the interval of the partial area. The integral within Eq. (7.1) is often solved numerically. Böker (2010) proposes to approximate the integral by means of the rectangle rule. Then, the amplitude is calculated as $a_n = \sqrt{2 \cdot S(\omega_n) \cdot \Delta\omega_n}$, with $\Delta\omega_n$ denoting the width of the interval of the respective partial area, and ω_n the associated wave frequency. The deterministic value of the amplitude can also be used in order to generate the randomness of the time series, as explained in the following.

7.1.2 Randomness in time domain

Two common approaches exist to generate a random time series on the basis of the inverse Fourier transformation, which are usually referred to as random-phase method and random-amplitude method.

For the random-phase method, the phase angles φ_n of each wavelet within Eq. (2.1) are considered to follow an uniform distribution with the interval $[0, 2\pi]$. The amplitudes are taken as deterministic values (Böker, 2010; Schaumann et al., 2011).

Instead of taking the amplitudes as deterministic values, Tucker et al. (1984) propose that the values of the amplitudes shall be selected randomly to generate a random time series. In addition to the phase angles being uniformly-distributed, the amplitudes a_n of each wavelet shall be taken as Rayleigh-distributed. The mode of the underlying Rayleigh distribution is the deterministic amplitude a_n of the respective wavelet, referring to Section 7.1.1. Taking the amplitudes of each wavelet within Eq. (2.2) as normal-distributed with the standard deviation equal to the respective deterministic amplitude is equivalent to consider the Rayleigh-distributed amplitudes and uniformly-distributed phase angles within Eq. (2.1) (Tucker et al., 1984).

Both Tucker et al. (1984) and Elgar et al. (1985) discuss the methods for generation of a random Gaussian process with respect to the simulation of sea states. Both groups of researchers analyse the impact of the methods on wave-group statistics within the generated seas state. A wave group consists of consecutive waves within a sea state whose wave heights exceed a certain value. The number of waves within a wave group is the run length.

Tucker et al. (1984) state that the random-phase method does not simulate a random Gaussian process and thus does not correctly simulate sea states. The random-phase method also affects the wave-group statistics; the mean run length may be underestimated. As an extension of these findings by Tucker et al. (1984), Elgar et al. (1985) describe that the wave-group statistics for both methods to generate a random time

series are almost identical in case that at least 1,000 wavelets are superposed to generate a random sea state. Mittendorf (2006) and DNV-RP-C205 (2019) recommend the random-amplitudes method for the discretisation of sea states.

7.1.3 Number of wavelets

A certain number of wavelets is required for the inverse Fourier transformation to generate a random signal in time domain. The more wavelets are superposed to generate the random time series, the power spectral density and its properties are more accurately represented in time domain. Especially the values of the signal follow a normal distribution to a greater degree, referring to e.g. Rice (1944). The computational effort increases with increasing number of wavelets. Hence, it is beneficial to keep the number of wavelets as small as possible without losing too much information of the power spectral density.

As stated before, DNV-RP-C205 (2019) recommends that a random sea state shall consist of at least 1,000 wavelets. This is based on a study on wave groups within sea states (Elgar et al., 1985). The authors investigated two measured power spectral densities of water-surface elevation, which are narrow- and broad-banded, respectively, and which are representative of a broad range of ocean conditions. They described that the wave-group statistics are almost identical for at least 1,000 wavelets, which are superposed to generate a random sea state.

7.1.4 Derivation of wave frequencies

Different techniques exist to divide the given power spectral density into the aforementioned partial areas. Most commonly the equidistant discretisation and the equienergetic discretisation (Webster and Trudell, 1981) are applied. When using the equidistant discretisation, the power spectral density is divided into such partial areas that the interval boundaries of the partial areas are set regularly. Hence, each interval has the same width. The wave frequencies are chosen within the respective intervals, usually as a whole multiple of the constant width between neighbouring wave frequencies. When applying the equienergetic discretisation, the power spectral density is divided into such partial areas that each partial area contains the same value of the area. Hence, the respective value of the amplitude is equal for all wavelets, and the difference between neighbouring wave frequencies is generally not equal.

The techniques of the equidistant discretisation and of the equienergetic discretisation are shown in Fig. 7.1. The respective partial areas of the discretised power spectral density are given at the top, and the amplitudes and wave frequencies consequently selected are given at the bottom. The power spectral density represents a JONSWAP spectrum of a sea state according to Eq. (3.17), with a significant wave height of $H_s = 2.0$ m, a peak period of $T_p = 5.0$ s, and a peak-enhancement factor of $\gamma = 3.3$.

The area below the power spectral density considered for the discretisation is limited such that the considered interval is finite. The integration limits at both tails of the power spectral density are chosen such that the area cut off at each tail is a fraction of the whole area, which is the zeroth-order spectral moment, referring to Eq. (2.7). Hence, the considered area for discretisation is reduced by twice the area cut off at each

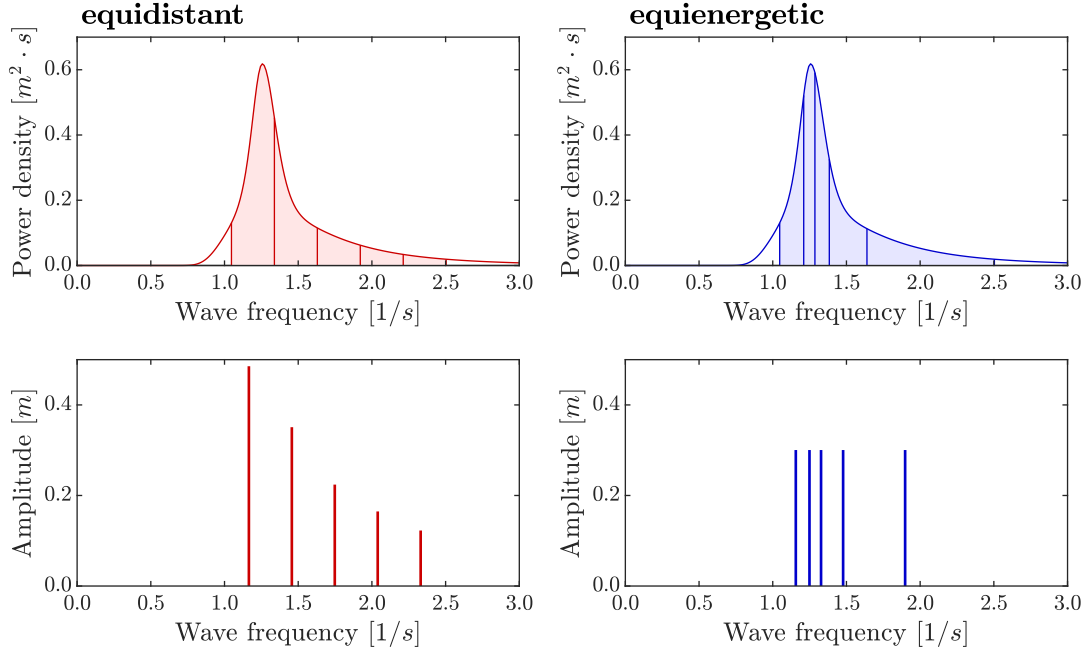


Figure 7.1: Equidistant and equienergetic discretisation of a power spectral density and the respective discrete amplitudes for the inverse Fourier transformation

tail. The area cut at each tail is equal to 5% of the zeroth-order spectral moment in Fig. 7.1.

Besides the equidistant and the equienergetic discretisation, the so-called irrational discretisation technique (Jiang, 1988) is proposed for the inverse Fourier transformation of wave-energy spectra (Mittendorf, 2006; Böker, 2010; Schaumann et al., 2011). The difference $\Delta\omega_n$ between consecutive wave frequencies ω_{n-1} and ω_n is calculated by using an irrational factor,

$$\Delta\omega_n = \frac{\sqrt{\frac{n}{n+1}}}{\sum_{j=1}^N \sqrt{\frac{j}{j+1}}} \cdot (\omega_N - \omega_1) , \quad n = 2 \dots N , \quad (7.2)$$

where ω_1 and ω_N denote the minimum and maximum wave frequency, respectively.

Properties of the methods to determine wave frequencies

The wave frequencies are easily found by dividing the considered interval of the power spectral density in equally sized intervals whilst applying the equienergetic discretisation. However, the determination of the respective amplitudes usually requires an increased numerical effort. Contrarily, the constant amplitudes are easily calculated whilst applying the equidistant discretisation, but the numerical determination of the wave frequencies is generally more elaborate.

A periodic behaviour of the autocorrelation function and thus of the respective time series can be noticed when applying the equidistant discretisation, referring to Eq. (2.19),

$$C(\tau) = \frac{1}{2 \cdot m_0^2} \cdot \cos(\omega_1 \cdot \tau) \cdot \sum_{n=1}^N a_n^2 \cdot \cos((n-1) \cdot \Delta\omega \cdot \tau) - \frac{1}{2 \cdot m_0^2} \cdot \sin(\omega_1 \cdot \tau) \cdot \sum_{n=1}^N a_n^2 \cdot \sin((n-1) \cdot \Delta\omega \cdot \tau), \quad (7.3)$$

where $\Delta\omega$ is the constant width between neighbouring wave frequencies. The derivation of Eq. (7.3) with $\omega_1 = 0 \text{ s}^{-1}$ is shown by e.g. Jiang (1988). The sinusoidal terms $\sum a_n^2 \cdot \cos((n-1) \cdot \Delta\omega \cdot \tau)$ and $\sum a_n^2 \cdot \sin((n-1) \cdot \Delta\omega \cdot \tau)$ in Eq. (7.3) are periodic with a period of $\tau = 2\pi/\Delta\omega$. If ω_1 is a whole multiple of $\Delta\omega$, the autocorrelation function and thus the respective time series are also periodic with this period of $\tau = 2\pi/\Delta\omega$. Even for ω_1 not being a whole multiple of $\Delta\omega$, the autocorrelation function and the time series show a certain periodic behaviour with a period of $2\pi/\Delta\omega$. When applying the equidistant discretisation, it is recommended to use time series with a duration equal to or less than the period $2\pi/\Delta\omega$. Thus, any periodic behaviour within the time series is excluded. Otherwise, any periodic behaviour has an impact on the statistical properties as shown in the following.

A periodic behaviour can also be observed when applying the irrational discretisation of the power spectral density (Jiang, 1988) despite the irrational determination of the wave frequencies. The term $\sqrt{n/(n+1)}$ in Eq. (7.2) approaches the limit of unity as n increases. Hence, the difference between consecutive wave frequencies approaches a constant value. This behaviour is shown in Jiang (1988, Fig. 3b) and is described as “non-decaying”. Figure 7.2 shows the autocorrelation functions for a JONSWAP spectrum according to Eq. (3.17) with $H_s = 2 \text{ m}$, $T_p = 5 \text{ s}$, and $\gamma = 3.3$, obtained with the discretisation of the wave-energy spectrum as described in the beginning of Section 7.2. The different aforementioned approaches of discretisation are applied. The autocorrelation function of the power spectral density according to Eq. (2.18) is shown for comparison (top, left). The time series are generated with 1,000 wavelets. The periodic behaviour is notable with a periodicity of $1,746.2 \text{ s}$ for the equidistant discretisation, due to the constant difference of consecutive wave frequencies of $\Delta\omega = 3.60 \cdot 10^{-3} \text{ s}^{-1}$. A similar periodicity is observed for the irrational discretisation.

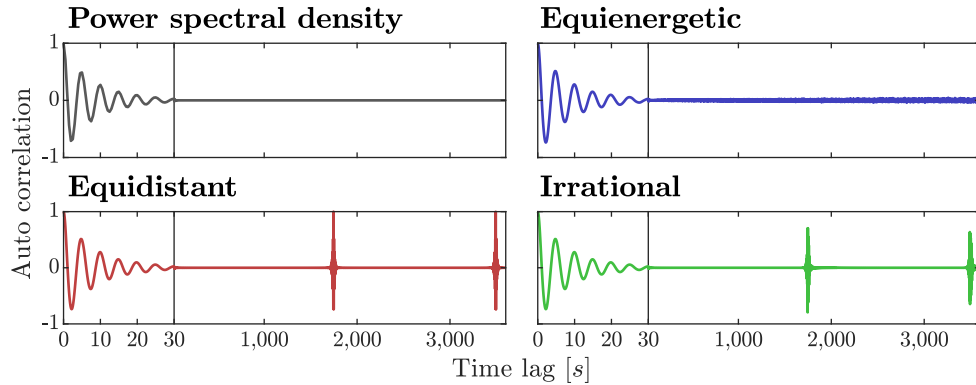


Figure 7.2: Autocorrelation function for different approaches of the inverse Fourier transformation

Impact of integration limits on spectral moments

The wave-energy spectra usually are defined for an unlimited domain of wave frequencies. Therefore, limits are to be set for the discretisation of the wave-energy spectra for practical reasons. The impact of the chosen limits on spectral properties of the signal are shown in the following. The impact of these chosen limits on extreme loads and fatigue loads of the respective signal are discussed in Section 5.2.1 and Section 7.2, respectively.

The impact of the right limit of a JONSWAP spectrum according to Eq. (3.17) on the zeroth-, second-, and fourth-order spectral moments as well as on the spectral width parameter, referring to Eq. (2.15), is shown in Fig. 7.3. The course of the values are plotted against the chosen right boundary ω of the adjusted spectral moment $m'_n = \int_0^\omega S(\omega') \cdot \omega'^n \cdot d\omega'$. The values of the spectral moments (left) are divided by the respective adjusted spectral moments for a wave frequency of $10 \cdot \omega_p$. The limits which are set to obtain a certain accuracy with respect to the target zeroth-order spectral moment are additionally shown in Fig. 7.3 (right). All courses shown are true for any value of the significant wave height and of the peak period but otherwise constant parameters of the JONSWAP spectrum.

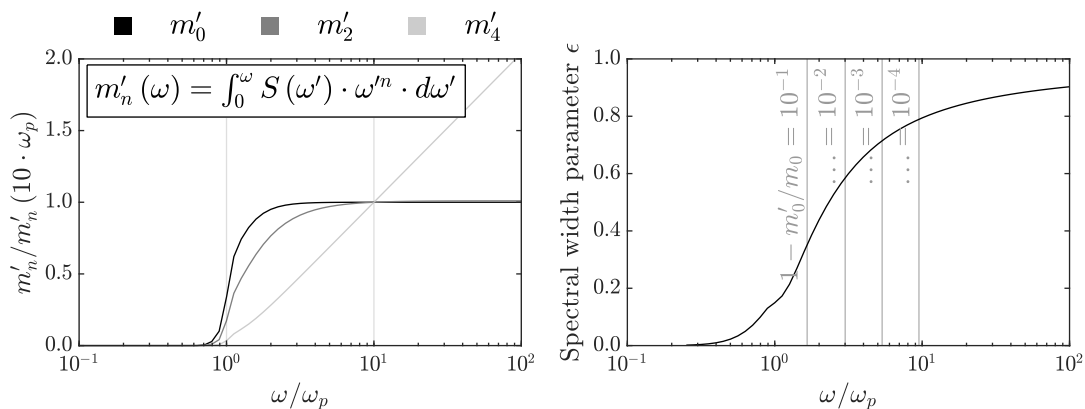


Figure 7.3: Spectral moments (left) and spectral width parameter (right) in dependence of the right integration limit of Eq. (2.7)

Evaluation of Eq. (2.7) for the JONSWAP spectrum indicates that the zeroth- and second-order spectral moments converge, and that the fourth-order spectral moment approaches infinity. The values of the zeroth- and second-order spectral moments are almost constant for wave frequencies greater than $10 \cdot \omega_p$. Contrarily, the value of the fourth-order spectral moment grows without bound for increasing wave frequency. This can also be noticed for the spectral width parameter. Its value is strictly increasing and converges to unity for increasing wave frequency.

The accuracy of discrete power spectral densities and of the resulting time series in comparison to the corresponding power spectral density is discussed in the following concerning the spectral properties. Considering a JONSWAP spectrum according to Eq. (3.17) with $H_s = 2 \text{ m}$, $T_p = 5 \text{ s}$, and $\gamma = 3.3$, the simulated time series of the resulting water-surface elevation consists of 1,000 wavelets. Both the equidistant as well as equienergetic discretisation are applied. Two specific kinds of integration limits are

investigated. The limits are chosen such that 0.5% as well as 0.0005% of the area are cut off at both tails of the power spectral density, respectively.

The second- and fourth-order spectral moments of the water-surface elevation, normalised by the zeroth-order spectral moments, according to Eq. (2.7) for the power spectral density, according to Eq. (2.8) for the discretised power spectral density, as well as on the basis of the time series are given in Tbl. 7.1. Additionally, the zero-up-crossing period T_z , the peak-to-peak period T_c , as well as the spectral width parameter are shown. The values of the spectral width parameter and the peak-to-peak period are already given in Tbl. 5.1. They are repeated here for reasons of clarity. The periods are calculated on the basis of the zeroth-, second-, and fourth-order spectral moments for the power spectral density and the discretised power spectral density, referring to Eq. (2.11) and Eq. (2.12), respectively. In order to determine these parameters from time series, 500 random time series of the water-surface elevation, each with a duration of 10,800 s, are analysed in order to determine the respective periods. Therefore, the temporal differences between consecutive zero-up-crossings and the temporal differences between consecutive maxima are extracted from each time series. The zero-up-crossing period and the peak-to-peak period are the mean values of those temporal differences.

Table 7.1: Spectral moments, specific periods and spectral width parameters of a power spectral density, of its discrete power spectral density, and of the respective time series for different integration limits of Eq. (2.7) and for the equidistant discretisation as well as equienergetic discretisation

	99.999% of PSD			99% of PSD		
	PSD	D-PSD	TS ^a	PSD	D-PSD	TS ^a
$m_2/m_0 [s^{-2}]$	2.6066	2.6297 <i>2.5851</i>		2.4315	2.4315 <i>2.4314</i>	
$m_4/m_0 [s^{-4}]$	23.8382	24.0222 <i>16.9716</i>		9.8213	9.8210 <i>9.8180</i>	
$T_z [s]$	3.8917 ^b	3.8746 ^b <i>3.9079^b</i>	3.8778 <i>3.9076</i>	4.0294 ^b	4.0294 ^b <i>4.0295^b</i>	4.0347 <i>4.0250</i>
$T_c [s]$	2.0777 ^c	2.0789 ^c <i>2.4522^c</i>	2.0782 <i>2.4368</i>	3.1263 ^c	3.1263 ^c <i>3.1268^c</i>	3.1226 <i>3.1210</i>
ϵ	0.8456 ^d	0.8439 ^d <i>0.7786^d</i>	0.8443 <i>0.7818</i>	0.6309 ^d	0.6309 ^d <i>0.6308^d</i>	0.6333 <i>0.6315</i>

PSD: power spectral density, D-PSD: discrete power spectral density,

TS: time series

Non-italic: equidistant discretisation, italic: equienergetic discretisation

^a Extracted from random time series

^b Zero-up-crossing period according to Eq. (2.11)

^c Peak-to-peak period according to Eq. (2.12)

^d Spectral width parameter according to Eq. (2.15)

As already observed in Fig. 7.3, the integration limits of the power spectral density have an impact on the respective spectral moments calculated for the power spectral density. Here, the second- and fourth-order spectral moments of the power spectral density for a utilised area of 99% of the power spectral density underestimate the respective values for a utilised area of 99.999% of the power spectral density by approximately 7% and 59%, respectively. Hence, the zero-up-crossing period and the peak-to-peak period also

differ noticeably. The values for a utilised area of 99% of the power spectral density differ from the respective values for a utilised area of 99.999% of the power spectral density by factors of approximately 1.04 and 1.50, respectively. The values of the spectral width parameter also differ in comparison.

For a relative utilised area of the power spectral density of 99%, only very small differences for the values calculated for the power spectral density, for the discrete power spectral density as well as for the time series are detected. The discretisation type almost has no impact on the respective values. Contrarily, greater deviations are observed for a relative utilised area of the power spectral density of 99.999%. The values for the equidistant discretisation nearly are equal to those for the power spectral density. The spectral moments for the equienergetic discretisation underestimate the respective values for the power spectral density. This affects especially the peak-to-peak period. The values exceed the respective values for the power spectral density and for the equidistant discretisation by approximately 17%. Hence, a smaller number of peaks are observed during a certain duration when applying the equienergetic discretisation. The spectral width parameter, which depends on the peak-to-peak period, is reduced for the equienergetic discretisation.

As shown in Fig. 7.3 and Tbl. 7.1, the selection of the integration limit as well as of the discretisation type has an impact on the properties of the water-surface elevation.

7.2 Comparison of different approaches of inverse Fourier transformation

As introduced above, different approaches with either equidistant or equienergetic discretisation and with either constant or Rayleigh-distributed amplitudes can be used for the inverse Fourier transformation of power spectral densities. The impact of these different approaches of the inverse Fourier transformation on the wave-induced loads acting on a monopile substructure is investigated in the following. Since the values of the spectral moments and of the spectral width parameter are of special importance for the estimation of extreme loads and fatigue loads, referring to Section 5.2 and Section 6.2, respectively, special attention is to be given to the selection of the integration limits of discretised power spectral densities and of the different approaches of the inverse Fourier transformation, considering both the number of wavelets as well as the discretisation type.

Exemplarily, the bending moment at the level of the seabed is investigated. The monopile is located at a water depth of 25 m, and the diameter of the monopile is 5 m. The wave-induced loads are calculated by Morison's equation, referring to Eq. (3.19), with the drag coefficient $C_d = 0.7$ and the inertia coefficient $C_m = 2.0$. A sea state given by the JONSWAP spectrum according to Eq. (3.17) with $H_s = 2$ m, $T_p = 5$ s, and $\gamma = 3.3$ is considered. The area cut at each end of the power spectral density has a value of 0.5% of the zeroth-order spectral moment. Hence, the area considered for the discretisation has a value of 99% of the zeroth-order spectral moment. For the discretisation of the power spectral density, the equidistant as well as the equienergetic discretisation as previously introduced are considered whilst the amplitudes are determined either as constant or as Rayleigh-distributed. The water-surface elevation as well as the result-

ing water kinematics are given by superposition of varying number of wavelets N , with $N = [50, 100, 200, 500, 1,000, 2,000, 5,000, 10,000]$, referring to Eq. (3.14). The periodicity for the equidistant discretisation is dependent on the number of wavelets, with a value of $(1.7426 \cdot N)$ s.

The impact of the utilised area of the power spectral densities is also analysed. The integration limits at both tails of the power spectral densities are set such that the area cut off at each tail is $5 \cdot 10^{-3}$, $5 \cdot 10^{-4}$, $5 \cdot 10^{-5}$, and $5 \cdot 10^{-6}$ of the zeroth-order spectral moment, which is the area below the power spectral density. This cut-off areas relate to relative utilised areas of 99%, 99.9%, 99.99%, and 99.999% of the power spectral density. Only time series composed of 1,000 wavelets are investigated. Here, the periodicities for the equidistant discretisation, which is dependent on the integration limits, have values of approximately 1,742.6 s, 874.7 s, 466.7 s, 255.7 s, respectively, for the relative utilised areas aforementioned.

In order to account for the randomness of the time series in the following analysis, a sufficient number of time series are generated for each combination of discretisation type, amplitude determination, number of wavelets, and relative utilised areas. Unless stated otherwise, the simulated time series have a duration of 600 s. In case of the equidistant discretisation and that the periodicity is less than 600 s, the time series have a duration of the respective periodicity. The time step is 0.05 s. The simulation of the random water-surface elevation and the load simulation are carried out with executable programs written by the author in the numeric computing environment *MATLAB*. The statistical evaluation is also done with *MATLAB*.

Due to the importance for the design of offshore wind turbines, the impact of the inverse Fourier transformation on the extreme loads and fatigue loads is investigated.

7.2.1 Impact on Gaussianity of time series

As stated by e.g. Rice (1944), time series obtained via inverse Fourier transformation tend to be normal-distributed for increasing number of wavelets.

The Kullback-Leibler divergence, referring to Eq. 2.27, is applied to assess whether the time series are normal-distributed. The Kullback-Leibler divergences for the different discretisation types and numbers of wavelets are compared to each other to determine which configuration provides the best fit with the normal distribution. The Kullback-Leibler divergences of bending moments acting on a monopile at seabed are shown in Fig. 7.4 for a duration of the signal of 10,800 s and in Fig. 7.5 for a duration of the signal of 150 s. Different approaches of the inverse Fourier transformation are considered. The values are presented in linear (left) and logarithmic scale (right) in Fig. 7.4.

For a duration of the signal of 10,800 s shown in Fig. 7.4, it is observed that the Kullback-Leibler divergence is almost constant for the equienergetic discretisation for the analysed numbers of wavelets. Hence, these signals are considered as Gaussian. For the equidistant discretisation, the mean value of the Kullback-Leibler divergence as well as the range of the 95% confidence interval also decrease for increasing number of wavelets. The range of the 95% confidence interval is greater for the discretisation with random amplitudes in comparison to the discretisation with constant amplitudes. At a number of wavelets of 10,000, the value of the equienergetic discretisation is reached.

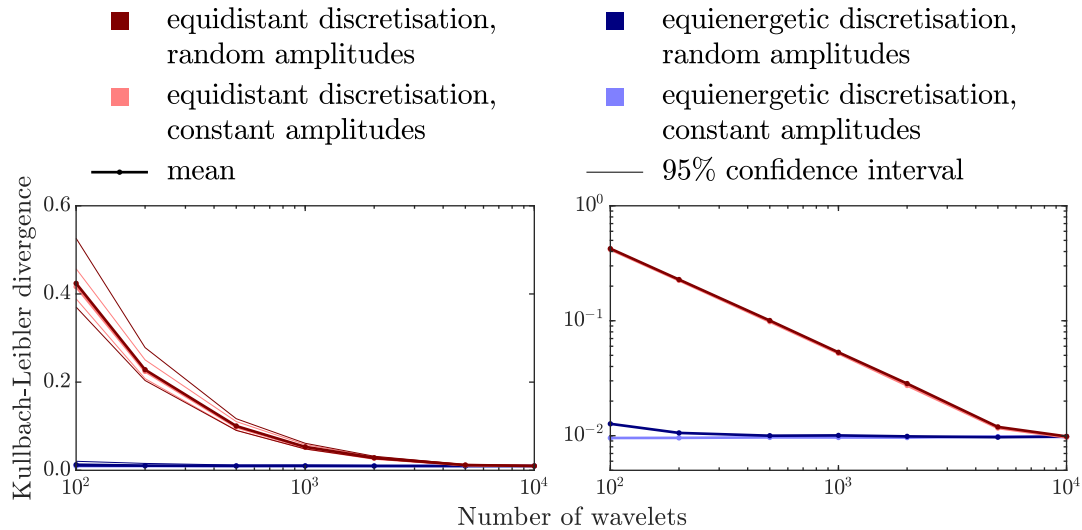


Figure 7.4: Kullback-Leibler divergences of bending moments acting on a monopile at seabed obtained by different approaches of the inverse Fourier transformation for a duration of 10,800 s

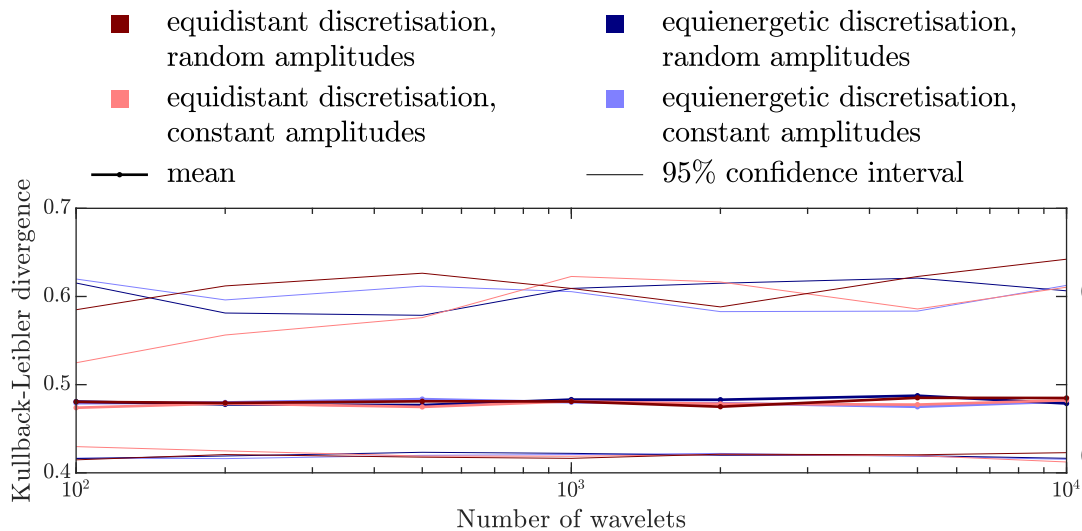


Figure 7.5: Kullback-Leibler divergences of bending moments acting on a monopile at seabed obtained by different approaches of the inverse Fourier transformation for a duration of 150 s

For a duration of the signal of 150 s, referring to Fig. 7.5, the Kullback-Leibler divergences for all different types of discretisations are almost identical. This is observed for both the mean values as well as for the 95% confidence intervals. Since the signals obtained with the equienergetic discretisation are considered as Gaussian for a duration of the signal of 10,800 s, signals with a shorter duration shall also be Gaussian. Hence, the signals obtained with the equidistant discretisation have this same property because of the same values of the Kullback-Leibler divergence. The differences between equienergetic discretisation and equidistant discretisation for a duration of the signal of 10,800 s result from the periodicity of the signals obtained with the equidistant discretisation. Here, repeating values are considered for the calculation of the Kullback-Leibler divergence, referring to Eq. (2.27), which directly results in greater values. For a duration of the signal of 150 s, the signals obtained with the equidistant discretisation

tion are not periodic such that similar values of the Kullback-Leibler divergence are obtained for the equienergetic discretisation and the equienergetic discretisation.

7.2.2 Impact on wave grouping

As stated above, consecutive waves within a sea state whose wave heights exceed a certain value are referred to as a wave group. The number of waves within a wave group is the run length. Here, the value of the significant wave height is the reference wave height. Elgar et al. (1985) investigated two measured power spectral densities of water-surface elevation, which are narrow- and broad-banded, respectively, and which are representative of a broad range of ocean conditions. The authors described that the wave-group statistics are almost identical for at least 1,000 wavelets, which are superposed to generate a random sea state. This finding of Elgar et al. (1985) is basis for the discretisation recommendations stated in DNV-RP-C205 (2019).

A reanalysis of the narrow-band- and broad-band power spectral densities as stated by Elgar et al. (1985) is carried out by the author, mostly to investigate the impact of number of wavelets in combination with the different approaches of the inverse Fourier transformation. The mean values of run length for both type of spectra are shown in Fig. 7.6 for different number of wavelets and different approaches of the inverse Fourier transformation. Both the mean values (left) as well as the mean values and the 95% confidence intervals (right) are presented. Additionally, the distributions of run lengths for both type of spectra are shown in Fig. 7.7 for different number of wavelets and different approaches of the inverse Fourier transformation.

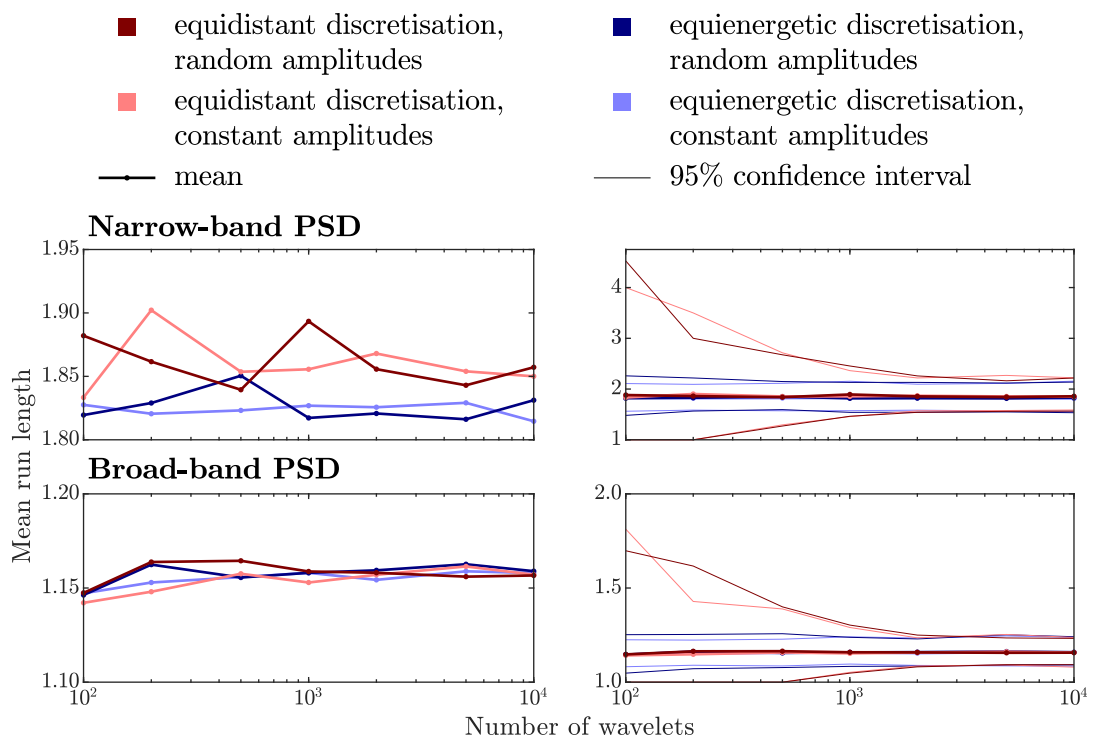


Figure 7.6: Mean run lengths for narrow-band power spectral density (PSD) (top) and for broad-band power spectral density (bottom) obtained by different approaches of the inverse Fourier transformation for a duration of 10,800 s

As can be observed, the mean run lengths are almost constant for the broad-band power spectral density and for the different approaches of the inverse Fourier transformation. The random scattering of the run lengths, here presented by the 95% confidence intervals, is also almost constant for the equienergetic discretisation. Up to a number of wavelets of approximately 2,000, the range of the 95% confidence intervals decreases for the equienergetic discretisation significantly. The greater range of 95% confidence intervals results from the periodicity of the signals due to the equidistant discretisation and of the respective run lengths within the signals. Here, the ranges of 95% confidence intervals are almost constant above a number of wavelets of 2,000. Similar results regarding the scattering of the mean run lengths are observed for the narrow-band power spectral density. However, the mean run length is slightly greater for the equidistant discretisation in comparison to the equienergetic discretisation even for very high numbers of wavelets. The mean run lengths for the equidistant discretisation also scatter noticeably for numbers of wavelets less than 1,000, which may result from the periodicity of the equidistant discretisation.

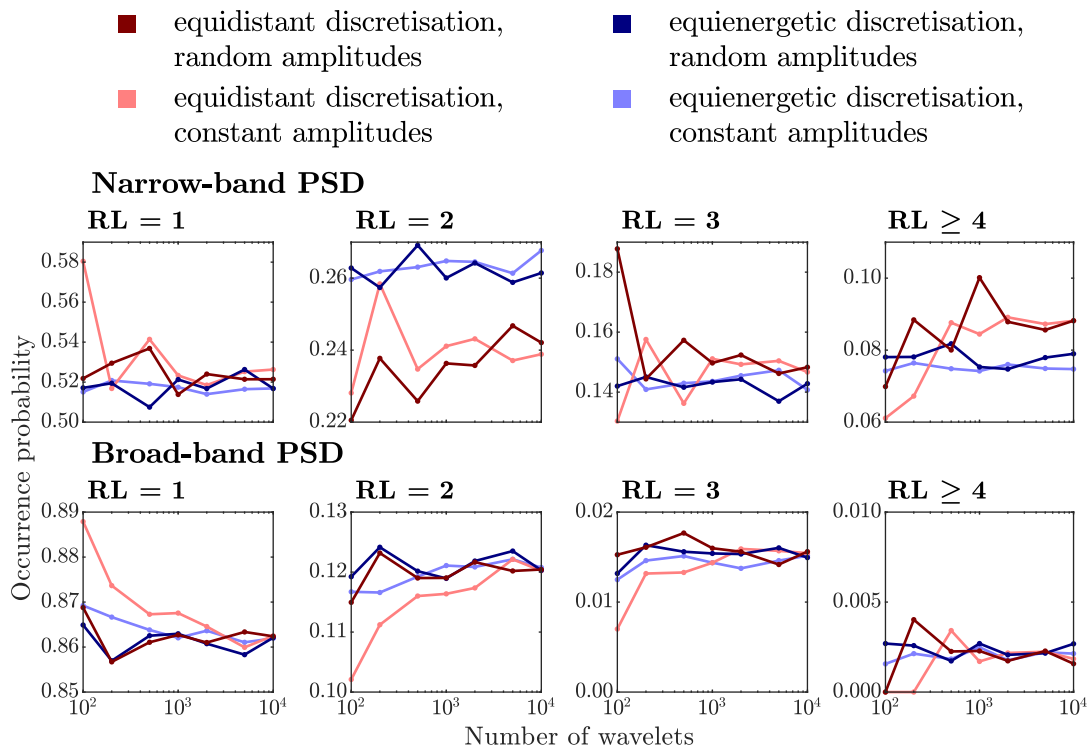


Figure 7.7: Distribution of run lengths (RL) for narrow-band power spectral density (PSD) (top) and for broad-band power spectral density (bottom) obtained by different approaches of the inverse Fourier transformation for a duration of 10,800 s

The reason for the slightly greater mean run lengths for the equidistant discretisation and for the narrow-band power spectral density can be seen in the occurrence probabilities of the run lengths. For a run length of 2, the occurrence probability for the equidistant discretisation is less in comparison the equienergetic discretisation, but it is increased for run lengths of 3 and greater 4. Again, the occurrence probabilities are scattering noticeably for the equidistant discretisation and numbers of wavelets less than 2,000, which is due to the already mentioned periodicity of the time series.

For the equienergetic discretisation, the occurrence probabilities are mostly constant. Contrarily, the occurrence probabilities for the broad-band power spectral density are mostly constant for the different approaches of the inverse Fourier transformation. The only exception is the occurrence probabilities for the equienergetic discretisation with constant amplitudes. For small numbers of wavelets, these occurrence probabilities for different run lengths differ noticeably, but they reach the values of the other discretisation approaches with increasing number of wavelets.

7.2.3 Impact on statistical properties of maximum loads acting on a monopile foundation

The extreme loads occurring during the lifetime are of importance for the design of structures. Due to the random generation of time series, the extreme loads occurring during a time series are random, too. According to the extreme value theory (Gumbel, 1958), the extreme loads can be described by the generalized extreme value distribution. It is assumed that the extreme loads are independent and identically distributed. In order to fit the generalized extreme value distribution to a data set of extreme loads, a sufficiently high number of independent and identically distributed extreme values are required.

The extreme values within each simulated time series of the wave-induced bending moments are extracted. For each discretisation type and number of wavelets considered, 500 time series with a duration of 600 s are analysed. In case of the equidistant discretisation and of the periodicity being less than 600 s, the time series have a duration of the respective periodicity. The underlying distribution type according to the extreme value theory and its respective parameters, referring to Eq. (2.28), are determined by means of the maximum-likelihood estimation, referring to Section 2.2.2. The parameters of the generalized extreme value distribution are adapted to a period of 600 s, applying Eq. (2.29). The parameters and their 95% confidence intervals are plotted against the number of wavelets in Fig. 7.8. The calculated values, marked with a dot, are linearly connected to visualise the course of the values.

The parameters can be considered as constant in dependence of the number of wavelets, with the scale parameter for the equidistant discretisation with constant amplitudes being the exception. This scale parameter increases for numbers of wavelets less than 1,000. It is considered as constant for greater numbers of wavelets.

Without the exception mentioned above, it is observed that the type of discretisation almost has no notable affect on the underlying generalized extreme value distribution and its parameters. The 95% confidence intervals shown in Fig. 7.8 indicate that the values of the parameters are scattering. In order to determine the parameters of the underlying generalized extreme value distribution more accurately, further goodness-of-fit tests are to be applied, or the data set of extreme values is to be extended. For example, a Gumbel distribution of the extreme wave-induced bending moments may also be assumed by evaluating the respective Q-Q plot, referring to Section 2.2.2.

The impact of the utilised area of the power spectral densities on the distribution of the extreme wave-induced bending moments is analysed in the following. Again, the extreme values within each simulated time series of the wave-induced bending

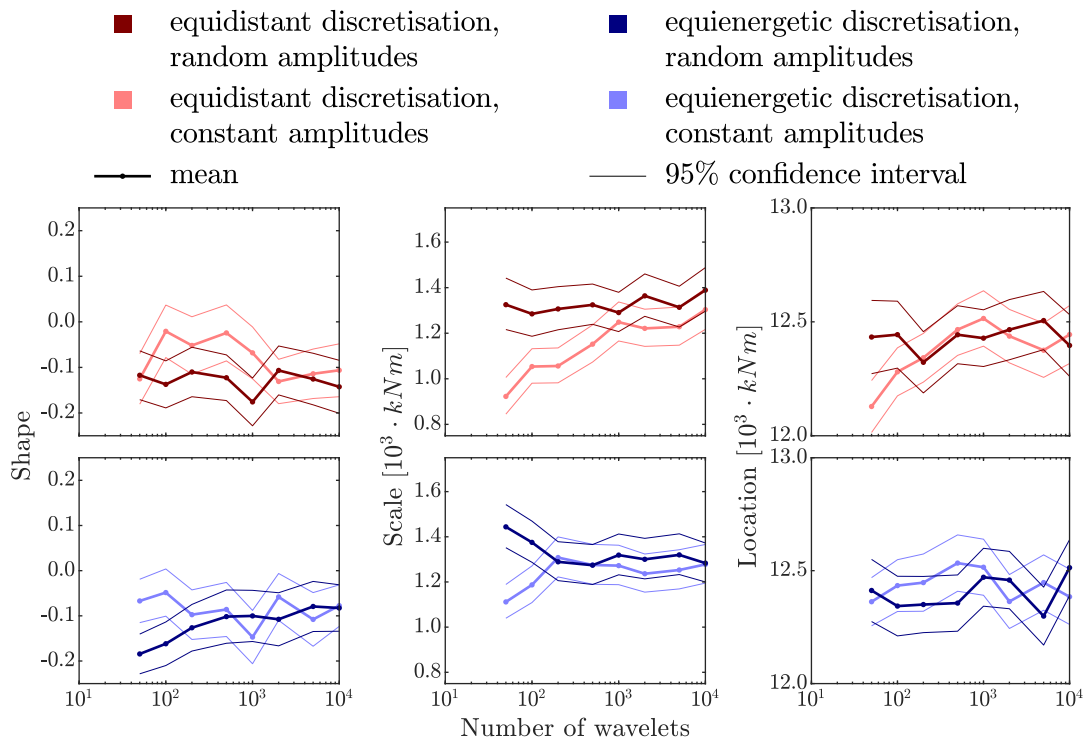


Figure 7.8: Shape-, scale-, and location parameters for the generalized extreme value distribution of maximum bending moments acting on a monopile at seabed obtained by different approaches of the inverse Fourier transformation for a duration of 600 s

moments are extracted. For each discretisation type and cut-off area considered, 500 time series with a duration of 600 s are analysed. The time series of the water-surface elevation consist of 1,000 wavelets. The procedure to determine the parameters of the underlying generalized extreme value distribution is the same as described above for the analysis regarding the impact of discretisation types and numbers of wavelets. Utilised areas of 99%, 99.9%, 99.99%, and 99.999% of the power spectral density are analysed, with the specifications as described above. The parameters and their 95% confidence intervals are plotted against the relative utilised area of the power spectral density in Fig. 7.9. The calculated values, marked with a dot, are linearly connected to visualise the course of the values. Here, only the results for the inverse Fourier transformation with constant amplitudes are shown. No additional findings are obtained for the inverse Fourier transformation with random amplitudes.

In comparison, the scale parameter obtained by the equidistant discretisation with constant amplitudes is underestimated for relative utilised areas of 99.999%. Here, the duration of the time series is equal to the periodicity of 255.7 s. Similar to the observation described for the dependency of the number of wavelets, the duration of the time series may be too short in order to accurately detect the parameters of the generalized extreme value distribution on the basis of the data set. Otherwise, the parameters of the underlying generalized extreme value distribution are almost constant with respect to the utilised area of the power spectral density. Therefore, it can be assumed that the value of the cut-off areas almost has no notable affect on the underlying generalized extreme value distribution and its parameters. As mentioned above, more accurate determined parameters of the underlying generalized extreme value distribution are to

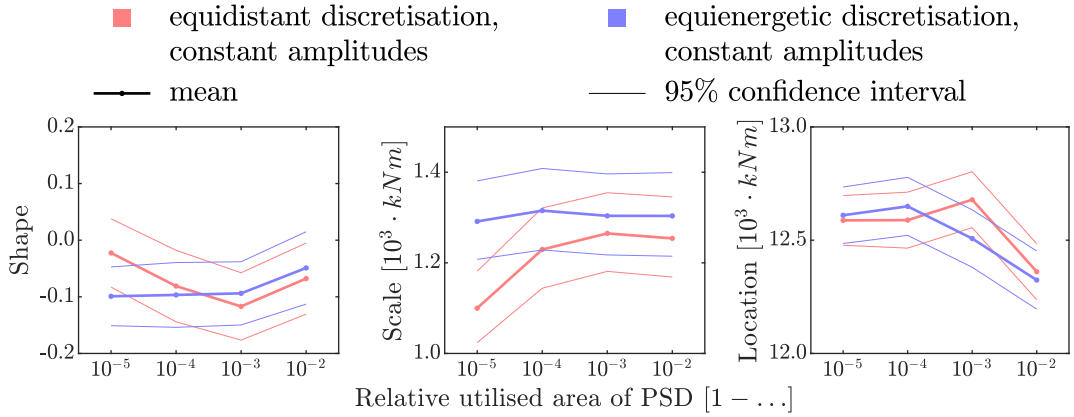


Figure 7.9: Shape-, scale-, and location parameters for the generalized extreme value distribution of maximum bending moments acting on a monopile at seabed obtained by different integration limits of the power spectral density (PSD) for a duration of 600 s

be obtained by applying further goodness-of-fit tests or by an increased data set of extreme values.

7.2.4 Impact on statistical properties of fatigue loads

Especially for the fatigue design of dynamically-loaded structures, it is of importance to determine the frequency distribution of fatigue loads during a certain period accurately. Besides the distribution of the fatigue loads, the scattering of the number of fatigue loads during a certain period as well as the distribution of the very high, rarely occurring fatigue loads are investigated.

Impact on probabilistic distribution of fatigue loads

The fatigue bending moments acting on the monopile at the seabed are derived from time series with a duration of 600 s by applying the rainflow-count algorithm. In case of the equidistant discretisation and that the periodicity is less than 600 s, duration of the time series is set as the respective periodicity. Both full cycles as well as half cycles are considered. The occurrence probability of one half cycle is set as half the occurrence probability of one full cycle.

The fatigue bending moments of each respective time series are analysed for each approach of the inverse Fourier transformation and number of wavelets. The empirical cumulative distribution function of each data set is obtained by allocating the fatigue bending moments sorted in ascending order to the respective non-exceeding probability. The non-exceeding probability of the n -th data point in the sorted data set is modelled as $P_n = (-0.5 \cdot p_1 + \sum_{i=1}^n p_i) / \sum_{i=1}^N p_i$, with the total number of data points N and the probability p of the data points sorted in ascending order. Here, the mean of all cumulative distribution functions derived from the respective time series is evaluated for each approach of the inverse Fourier transformation and number of wavelets. The respective probability density functions are derived from the empirical cumulative distribution functions by numerical differentiation. Multiplying the probability density function with the number of occurrences during a certain period yields the frequency

density. The frequency densities of the fatigue bending moments for a period of 600 s are shown in Fig. 7.10 for 100, 1,000, and 10,000 wavelets. The frequency densities are shown for fatigue loads up to $30 \cdot 10^3 \text{ kNm}$.

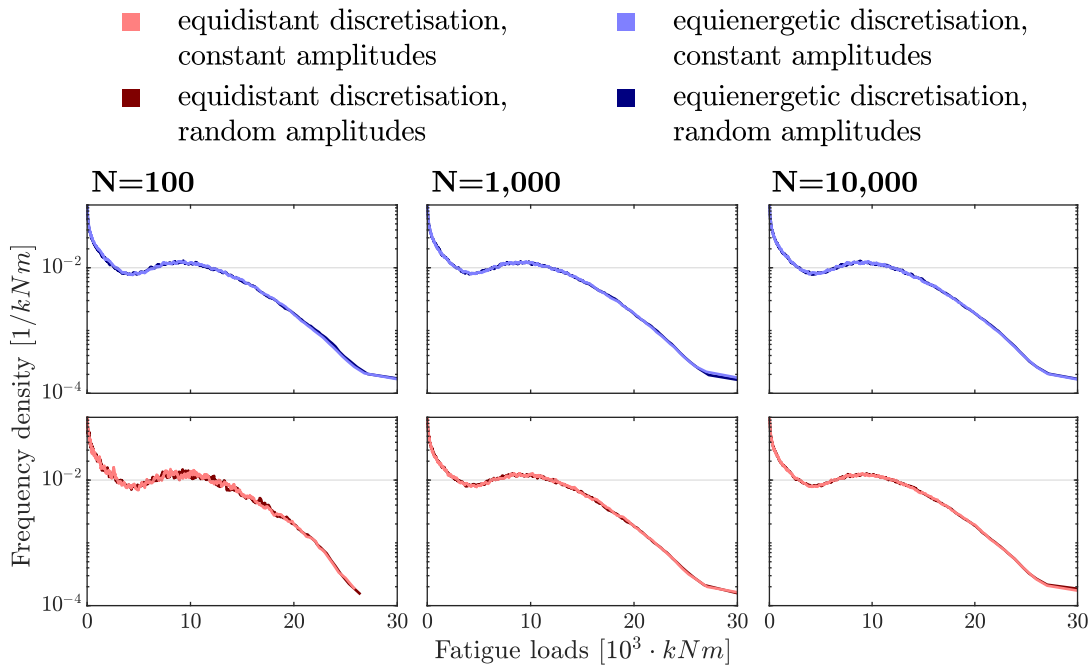


Figure 7.10: Frequency densities of fatigue bending moments obtained by different approaches of the inverse Fourier transformation for numbers of wavelets N

As can be seen, the frequency densities are almost independent of the number of wavelets and of the discretisation type. It is noted that no fatigue loads greater than $28 \cdot 10^3 \text{ kNm}$ occur for the equidistant discretisation of the power spectral density with 100 wavelets. Further analysis of the very high, rarely occurring fatigue loads is given in the following.

Besides the underlying distribution of the fatigue loads, the number of load cycles is important for the calculation of the fatigue damage. The total numbers of cycles as well as the number of cycles exceeding the fatigue loads of $10 \cdot 10^3 \text{ kNm}$ and $20 \cdot 10^3 \text{ kNm}$ occurring within 600 s as well as the 95% confidence intervals are plotted against the number of wavelets in Fig. 7.11 (from left to right). Both the mean of all time series as well as 95% confidence intervals are shown.

The courses of the mean number of cycles are almost equal independent of the type of discretisation and of the determination of amplitudes. The mean number of cycles is approximately constant for more than or equal to 1,000 wavelets. For the equidistant discretisation and less than 1,000 wavelets, the courses of the mean number of cycles increase slightly. For the equienergetic discretisation, the number of cycles exceeding the fatigue loads of $10 \cdot 10^3 \text{ kNm}$ and $20 \cdot 10^3 \text{ kNm}$ is nearly constant independent of the number of wavelets. The 95% confidence intervals are almost constant for more than and equal to 1,000 wavelets independent of the discretisation type and determination of amplitudes. Considering the equidistant discretisation, the 95% confidence intervals decrease for less than 500 wavelets. This is due to the fact that the periodicity of the

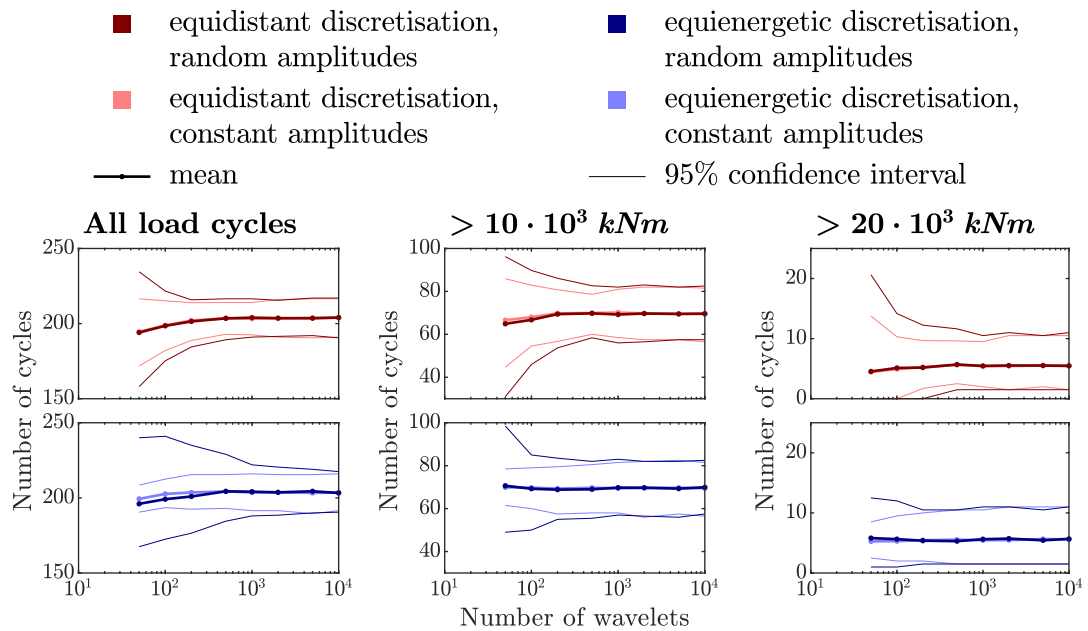


Figure 7.11: Number of cycles of fatigue bending moments obtained by different approaches of the inverse Fourier transformation

equidistant discretisation is less than the duration of the time series of 600 s. It is noticeable that the 95% confidence intervals also decrease for less than 100 wavelets when applying the equienergetic discretisation with random amplitudes. The 95% confidence interval is nearly constant for the equienergetic discretisation with constant amplitudes. In general, applying Rayleigh-distributed amplitudes results in greater scattering of the number of cycles than constant amplitudes for less than 1,000 wavelets of the inverse Fourier transformation.

The impact of the utilised area of the power spectral densities on the distribution of the wave-induced fatigue bending moments is analysed in the following. The fatigue loads are determined for time series with a duration of 600 s as described above for the analysis regarding the impact of discretisation types and numbers of wavelets. All simulated time series of the water-surface elevation consist of 1,000 wavelets. The frequency densities (left) and the cumulative distribution functions (right) of the fatigue loads are shown in Fig. 7.12. Discretisations with utilised areas of 99% and 99.999% of the power spectral density are analysed, with the specifications as described above. Only the results for the inverse Fourier transformation with constant amplitudes are shown, since no additional findings are obtained for the inverse Fourier transformation with random amplitudes.

As already noticed in Fig. 7.10, the frequency densities as well as the cumulative distribution functions for a relative utilised area of 99% (dashed line) are almost identical. The frequency densities for a relative utilised area of 99.999% (solid line) have noticeably greater values for fatigue loads less than $3 \cdot 10^3 \text{ kNm}$ in comparison to a relative utilised area of 99%. For greater fatigue loads the courses of the frequency densities are nearly equal. The differences can also be seen at the respective cumulative distribution functions. Additionally, the cumulative distribution functions in dependence of the discretisation types notably differ for a relative utilised area of 99.999%. Smaller fatigue loads are more probable to occur for the equidistant discretisation.

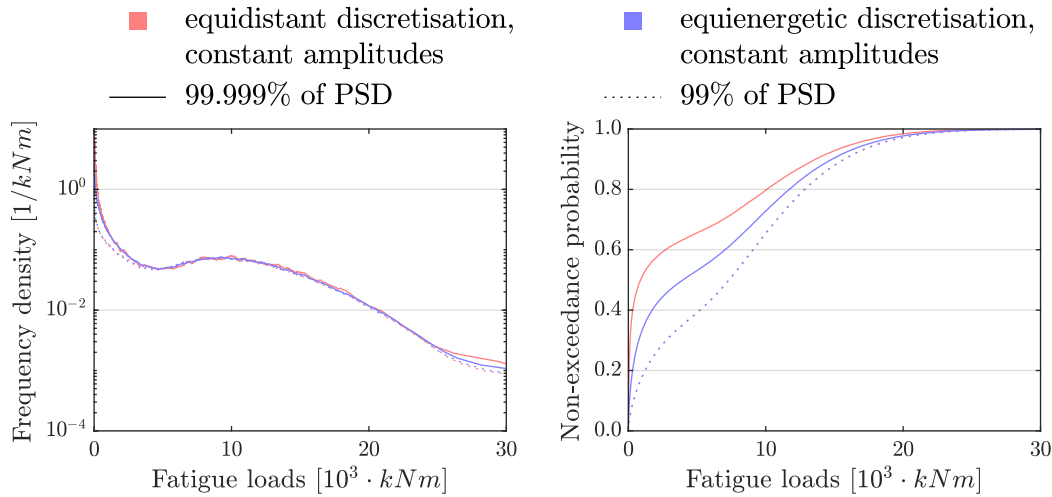


Figure 7.12: Frequency densities (left) and cumulative distribution functions (right) of fatigue bending moments obtained by different integration limits of the power spectral density (PSD) for a duration of 600 s

The total numbers of cycles as well as the number of cycles exceeding the fatigue loads of $10 \cdot 10^3 kNm$ and $20 \cdot 10^3 kNm$ occurring within 600 s as well as the 95% confidence intervals are shown in dependence of the utilised area of the power spectral density in Fig. 7.13 (from left to right). Only the mean values as well as the 95% confidence intervals of all time series for the inverse Fourier transformation with constant amplitudes are shown, since no additional findings are obtained for the inverse Fourier transformation with Rayleigh-distributed amplitudes.

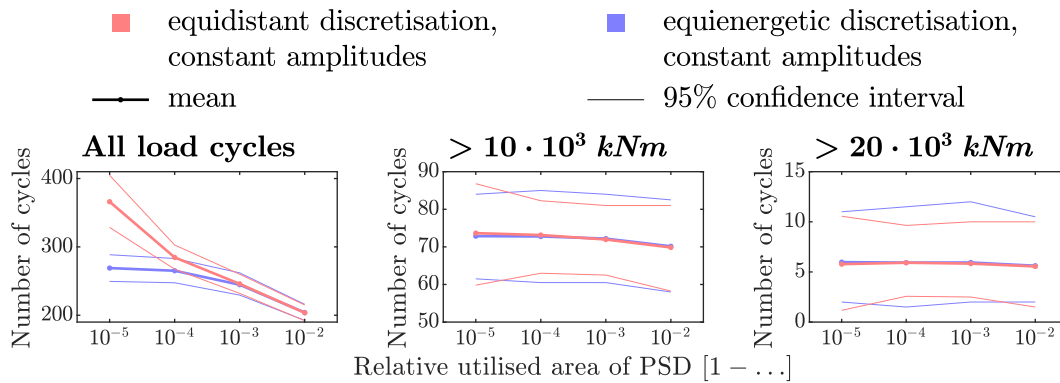


Figure 7.13: Number of cycles of fatigue bending moments obtained by different integration limits of the power spectral density (PSD) for a duration of 600 s

For both discretisation types considered, the numbers of all loads cycles increase with increasing relative utilised area of the power spectral density. The number of all load cycles for the equidistant discretisation is significantly greater compared to the equienergetic discretisation, especially for a relative utilised area of 99.999%. Mean numbers of cycles of approximately 365 for the equidistant discretisation and of approximately 270 for the equienergetic discretisation are observed. This can also be derived from the findings of Fig. 7.12. The mean number of cycles is nearly constant for fatigue loads greater $20 \cdot 10^3 kNm$ independent of discretisation type and utilised area of the power spectral density. For fatigue loads greater $10 \cdot 10^3 kNm$, the mean numbers of

cycles during 600 s slightly increase with increasing relative utilised area of the power spectral density. It can almost be considered as constant. Here, the number of cycles increases from ~ 70 for 99.9% to ~ 74 for 99.999% of the power spectral density. As can be seen, the 95% confidence intervals are almost constant for both discretisation types. Increased 95% confidence intervals are noted for relative utilised areas of the power spectral density of 99.99% and 99.999%. These values again can be explained by the periodicities of the respective equidistant discretisation which are less than the analysed duration of the time series of 600 s.

Impact on probabilistic distribution of the fatigue loads exceeding a certain threshold

As stated in Kelma and Schaumann (2015), especially the very high but rarely occurring fatigue loads contribute significantly to the fatigue damage. Hence, the probability distribution of the fatigue loads exceeding a certain threshold is investigated in the following. Again, the impact of the number of wavelets and approaches of the inverse Fourier transformation as well as of different integration limits are analysed separately.

It is assumed that the fatigue bending moments exceeding a certain threshold follow the generalised Pareto distribution (Eq. (2.31)), referring to Section 2.2.4. Therefore, the fatigue bending moments of all respective time series with a duration of 600 s are taken as data sets, which are analysed separately for different discretisation types and numbers of wavelets. In case that the periodicity is less than 600 s, the duration of the respective time series is equal to the periodicity. The fatigue loads of all time series are considered due to the otherwise very small data set of very high fatigue loads. In case that the fatigue loads of a single time series with a duration of 600 s are analysed, the number of fatigue loads exceeding the very high thresholds are too small. This can be seen in Figs. 7.11 and 7.13 for fatigue loads greater $20 \cdot 10^3 \text{ kNm}$, here with a mean number of ~ 5 cycles. As described in Section 2.2.2, the parameters defining the generalised Pareto distribution are numerically calculated by applying the maximum-likelihood estimation. The p -value is applied to test the hypothesis whether the data sets fit the generalised Pareto distribution with the calculated parameters.

The shape parameters (top) and the scale parameters (middle), which are numerically calculated, as well as the respective 95% confidence intervals are plotted against the threshold in Fig. 7.14 for 100, 1,000, and 10,000 wavelets. Additionally, the p -values are plotted (bottom). The mean values of the 95%-, 99%-, and 99.9%-quantiles are shown for both discretisation types. Only the values for the inverse Fourier transformation with random amplitudes are shown, since no additional findings are obtained for the inverse Fourier transformation with constant amplitudes.

As can be seen, the courses of the shape- and scale parameters are very similar independent of the discretisation type and the number of wavelets, with the exception of the equidistant discretisation with 100 wavelets. The mean of the shape parameter has a value of approximately -0.15 for thresholds between $15 \cdot 10^3 \text{ kNm}$ and $28 \cdot 10^3 \text{ kNm}$. The inclinations of the linear mean courses of the scale parameter have approximately the same value as the respective shape parameters. Both the facts that the shape parameter is constant as well as that the course of the scale parameter is equal to the shape parameter are in very good accordance to the theoretical requirements for fitting data

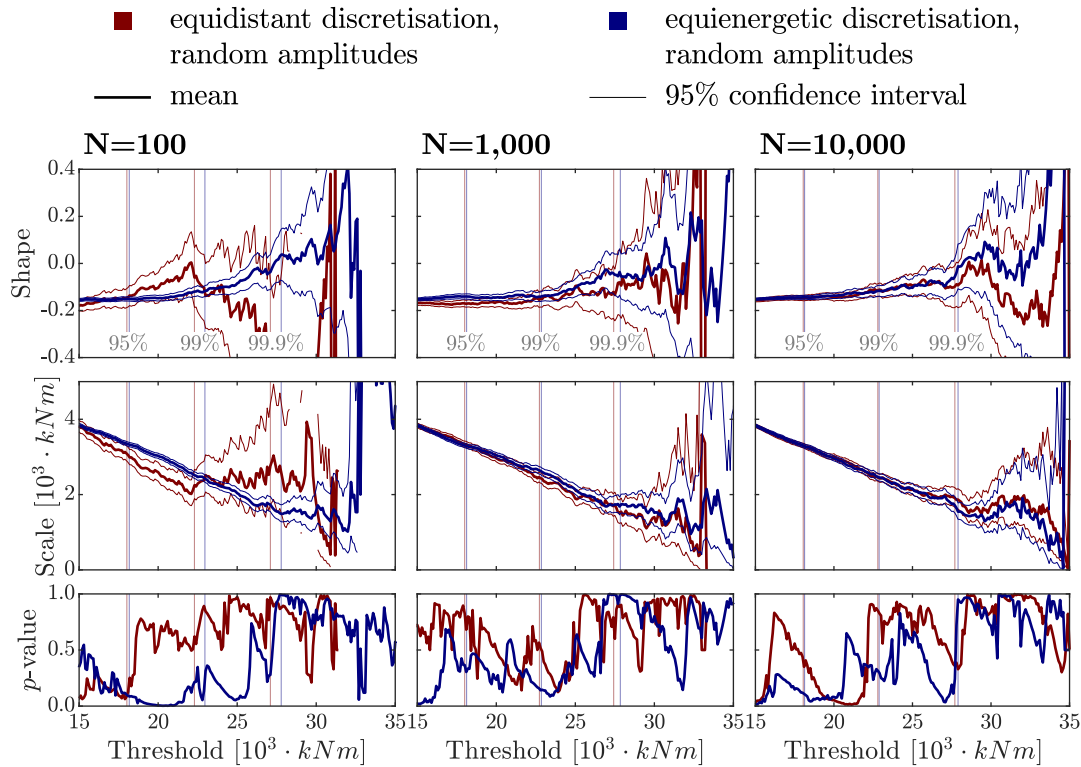


Figure 7.14: Parameters for the generalised Pareto distribution of the fatigue bending moments and the respective p -values obtained by different approaches of the inverse Fourier transformation for a duration of 600 s

to the generalised Pareto distribution, as explained in e.g. Embrechts et al. (1997). The parameters for thresholds greater $28 \cdot 10^3 \text{ kNm}$ do not follow the previous courses and have obviously greater 95% confidence intervals, which is due to the very limited data set for great thresholds. The courses of the p -value exceed the typical significance level of 0.05 for almost each threshold. This is especially noted for discretisations with 1,000 and 10,000 wavelets. Hence, the hypothesis that the fatigue bending moments exceeding a certain threshold can be described by a generalised Pareto distribution with the respective parameters is not to reject.

The parameters determined for the equidistant discretisation with 100 wavelets differ noticeably from the other respective courses. The 95% confidence intervals are also greater in comparison which may be due to the reduced duration of the times series with the value of the periodicity. The mean shape parameter is not constant in dependence of the threshold, and the inclination of the scale parameter is not equal to the respective shape parameter. Both aspects contradict to the theory regarding the generalised Pareto distribution (Embrechts et al., 1997). Hence, it is doubtful to assume a generalised Pareto distribution for the fatigue bending moments exceeding a certain threshold obtained by the equidistant discretisation with 100 wavelets, even though the course of the p -value suggests to reject this hypothesis.

As described above for the analysis regarding the impact of discretisation types and numbers of wavelets, the parameters of the underlying generalised Pareto distribution are determined numerically for different utilised areas of the power spectral density by applying the maximum-likelihood estimation. The simulated time series of the water-surface elevation consist of 1,000 wavelets. Again, the duration of the time series is the

minimum of their periodicity and 600 s. The numerically determined shape parameter (left) and the scale parameter (right) are plotted against the threshold in Fig. 7.15 for relative utilised areas of 99% and 99.999%. Only the values for the discretisation of the power spectral density with random amplitudes are shown, since no additional findings are obtained for the inverse Fourier transformation with constant amplitudes.

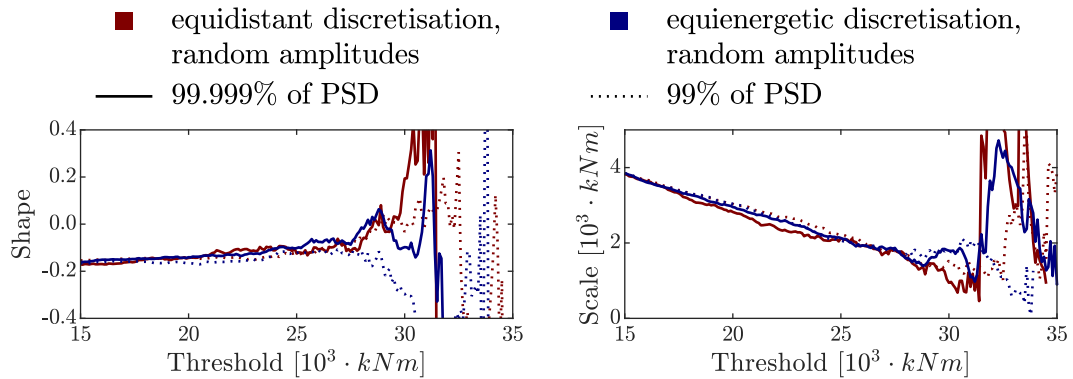


Figure 7.15: Parameters for the generalised Pareto distribution of the fatigue bending moments obtained by different integration limits of the power spectral density (PSD) for a duration of 600 s

The courses of the shape- and scale parameters are very similar independent of the discretisation type and number of wavelets for thresholds between $15 \cdot 10^3 \text{ kNm}$ and approximately $28 \cdot 10^3 \text{ kNm}$. The inclinations of the linear mean courses of the scale parameters have approximately the same value as the respective shape parameters which are nearly constant with an approximate value -0.15 . This is in accordance to the theoretical requirements for fitting data to the generalised Pareto distribution (Embrechts et al., 1997). The parameters for thresholds greater $28 \cdot 10^3 \text{ kNm}$ do not follow the previous courses, which is due to the very limited data set for great thresholds. The courses of the p -value, which are not shown here, exceed the typical significance level of 0.05 for each threshold.

7.3 Findings

Only limited information on how to carry out inverse Fourier transformation is provided in standards and guidelines. DNV-RP-C205 (2019) recommends at least 1,000 wavelets to be superposed.

Within the extensive study, different approaches for the discretisation of power spectral densities are analysed. Inter alia different numbers of wavelets are considered. The respective time series are investigated regarding different properties. Besides periodicity and Gaussianity of the time series, the extreme loads and fatigue loads occurring within the time series are evaluated. It can be concluded that the time series must not be periodic. Considering the results presented in Chapter 5 and Chapter 6, the spectral moments which are decisive for the estimation of the distribution functions for extreme loads and fatigue loads shall be represented well by the simulated time series.

For structural-dynamic load simulations, both the input power spectral densities, such as wave-energy spectra, as well as the power spectral densities of the expected response

shall be represented appropriately by the discretised spectra. Otherwise, inaccurate spectral moments may lead to erroneous results. This suggestion is in line with the proposal by Kleineidam (2005) who states that the power spectral density is discretised finer within the domain close to the Eigen frequencies of the structure in comparison to the power spectral density outside of this domain.

8 Studies on analyses of load simulations for offshore wind turbines

Within this chapter, two studies are carried out to evaluate certain aspects of the load simulations. Different methods to determine spectral moments from time series, as they are described in Section 2.1.2, are analysed, and their impact on extreme loads and fatigue loads are evaluated. Additionally, the effect of currents within sea states on fatigue loads is investigated. The impact of currents on the wave-induced loads and their respective power spectral densities is shown in theory in Section 3.2.5.

The studies are carried out for an offshore wind turbine with a rated power capacity of 5 MW.

8.1 Spectral properties from load simulations in time domain

Within the following study, the methods to determine the spectral properties of signals as well as their effect on the fatigue loads and on the extreme loads are investigated. These results are compared to the respective values obtained from time series.

Load time series for an offshore wind turbine during production, which is to be simulated for the design load case DLC 1.2, referring to IEC 61400-3-1 (2019) and DNV-ST-0437 (2016), are analysed. Only one load scenario is considered, which has the same characteristic parameters for the wind field and the sea state. Several time series of this load scenario with different realisations of wind fields and of sea states are simulated such that characteristic values within the time series, such as extreme values, can be considered as independent and identically distributed. Hence, a statistical analysis can be carried out.

8.1.1 Load simulations

The loads acting on an offshore wind turbine during production are simulated in time domain. The offshore wind turbine consists of the NREL 5 MW wind turbine (Jonkman et al., 2009) and of the jacket substructure defined within the OC4 project (Vorpahl et al., 2011). The foundation piles are modelled as rigid at mudline such that no soil-structure interaction is considered. The water depth is 50 m.

Different seeds of turbulent wind fields with mean wind velocity of 12 m/s and a turbulence intensity of 14% at hub height of the offshore wind turbine are applied. The exponential wind shear factor is 0.14. The irregular sea state follows a JONSWAP spectrum according to Eq. (3.17) with $H_s = 2.5$ m, $T_p = 7.5$ s, and $\gamma = 3.3$. This set-up is

previously used for a study on probabilistic fatigue design carried out by Kelma and Schaumann (2015).

Fully-coupled simulations of the offshore wind turbine with jacket substructure are carried out. The wind-induced loads are computed by using the widely-used wind-energy simulation program *Flex5*, which is coupled with the finite-element software *Poseidon* (Böker, 2010). Fifty-two random time series with different wind seeds and irregular sea states are simulated, each with a duration of 3,600 s.

The stresses at upper brace of the tubular K-joint (I) are analysed in the study, as it is marked at the jacket substructure in Fig. 8.1 (left). The structural stress approach is applied for calculation of the stresses acting at the K-joints of the jacket structure. The stress due to the branched geometry of the tubular K-joints is given by multiplying the occurring nominal stress with stress concentration factors. Stress concentration factors for crown and saddle according to Efthymiou (1988) are calculated for each brace of the considered K-joints. The positions of the stress concentration factors are visualised in Fig. 8.1 (right). The stresses at the bottom crown are exemplarily investigated within the study.

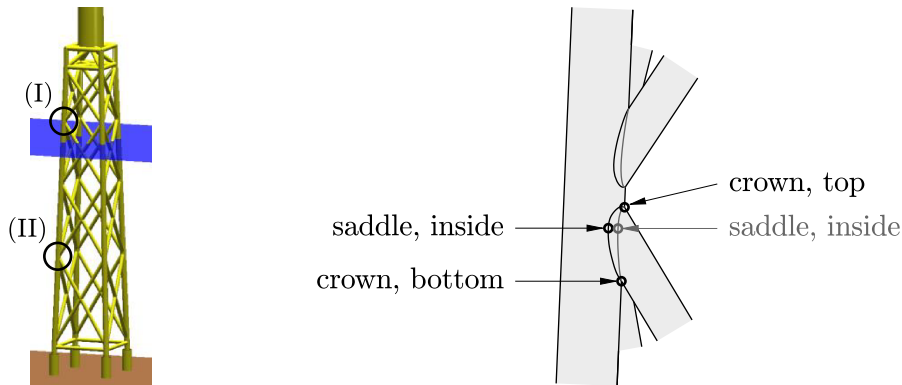


Figure 8.1: Jacket substructure with tubular K-joints analysed (left), tubular K-joint (right)

8.1.2 Gaussianity of the signal

It is checked by means of Q-Q plots whether the analysed time series follow a Gaussian distribution. The Q-Q plots of the time series are shown in Fig. 8.2. The original time series (left) as well as the time series transferred to Gaussian signal as described in Section 5.2.3 (right) are analysed. The time series are shown as zero-mean signal. The respective 1%-, 5%-, 95%-, and 99%-quantiles are marked as well.

One can observe that the original signal shown in Fig. 8.2 (left) does not follow the assumed Gaussian distribution. The skewness of the original signals is greater than zero. After transferring the signal to a Gaussian signal as described in Section 5.2.3, the Q-Q plot shows a very good agreement between simulated and theoretical signals (right). The skewness and the kurtosis of the signal transferred to a Gaussian signal have values of close to zero and 3, respectively, which are the theoretical values for a Gaussian distribution. For both Q-Q plots, the quantiles lie close to each other. Below the 1%-quantiles and above the 99%-quantiles, the curves for the different random time series differ significantly. This is due to the very high and very low values which occur

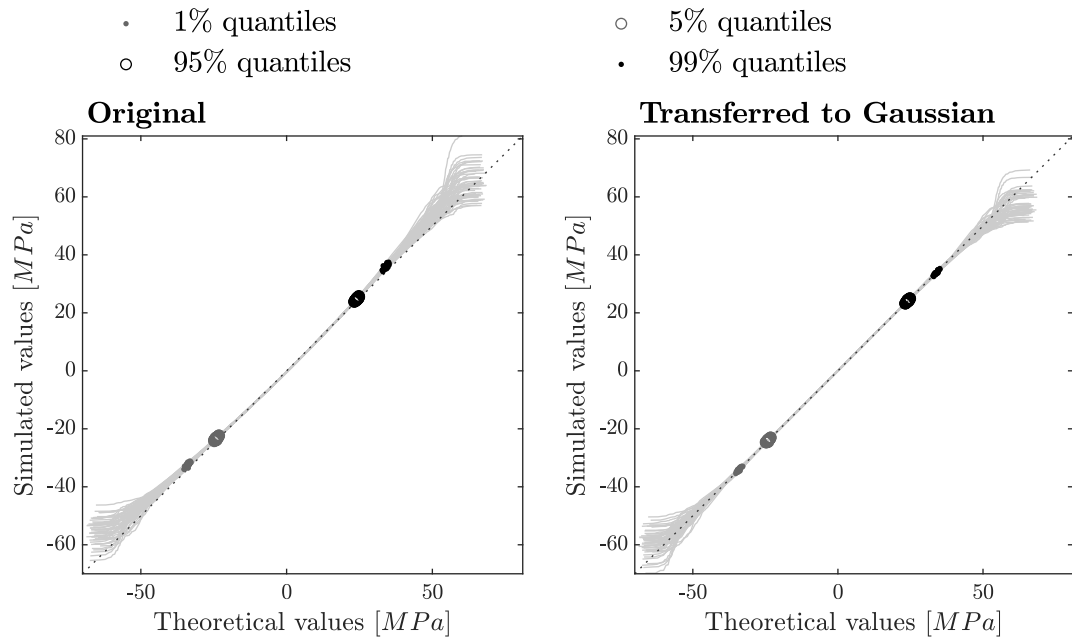


Figure 8.2: Q-Q plots of stresses at the analysed tubular K-joint, assuming a Gaussian distribution: original data (left) as well as transferred to Gaussian signal (right)

rarely and are subject to scatter. It is noticed that maximum values of each time series are reduced for the signals transferred to Gaussian signals in comparison to the original signals. The minimum values are almost the same for both signals. This is equivalent to the positive value of the skewness, which indicates that the right tail of the probability density function of the signal is stronger. The skewness of the original signal has an average value of ~ 0.16 and is greater zero for all time series. The kurtosis of the original signal is greater than 3 for all 52 time series, with an average value of ~ 3.06 .

The results for the extreme values and the fatigue loads are separately presented for signals transferred to Gaussian signals in Section 8.1.5 and Section 8.1.6, respectively. In order to evaluate the impact of this transfer on the respective loads, the original signals and the signals transferred to Gaussian signals are compared in Fig. 8.3 for all time series. Both the extremes values (left) as well as the damage-equivalent load (right) are shown. The damage-equivalent loads are calculated according to Eq. (6.5) for a slope of the SN curve of $m = 4$ and with a reference number of load cycles equal to number of load cycles within the analysed time series.

As already stated above, the extreme loads of the original signal are greater than those of the Gaussian signal for the analysed tubular K-joint. The fatigue loads of the original signal are also slightly greater than those of the Gaussian signal. It is generally concluded that the transfer of original, non-Gaussian signals to Gaussian signals and vice versa after the analysis in frequency domain are to be carried out in order to determine the distribution functions of extreme loads and of fatigue loads on the basis of power spectral densities accurately.

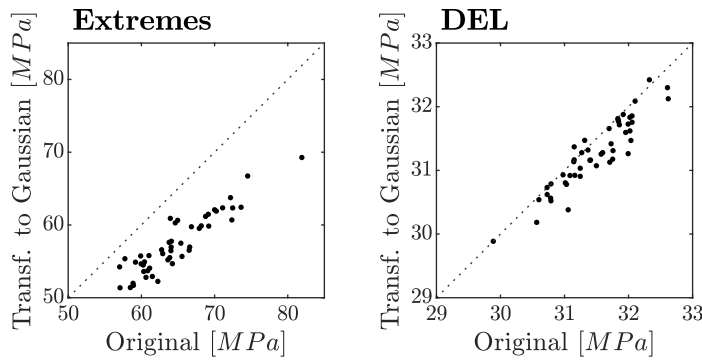


Figure 8.3: Comparison of spectral parameters α_1 and α_2 as well as of the resulting damage-equivalent load, obtained with different approaches, for the analysed tubular K-joint

8.1.3 Power spectral densities

The power spectral densities are determined via Fourier transformation as described in Section 2.1.1. The power spectral densities for all time series transferred to Gaussian signals are shown in logarithmic scale in Fig. 8.4. Additionally, the average of all power spectral densities as well as the 5%- and 95%-quantiles are shown. The general characteristics of the power spectral densities such as the general course of the power spectral densities and the locations of peaks are comparable for all time series. It is observed that the power spectral densities for all 52 time series differ locally. These differences are also notable in the findings derived in the following.

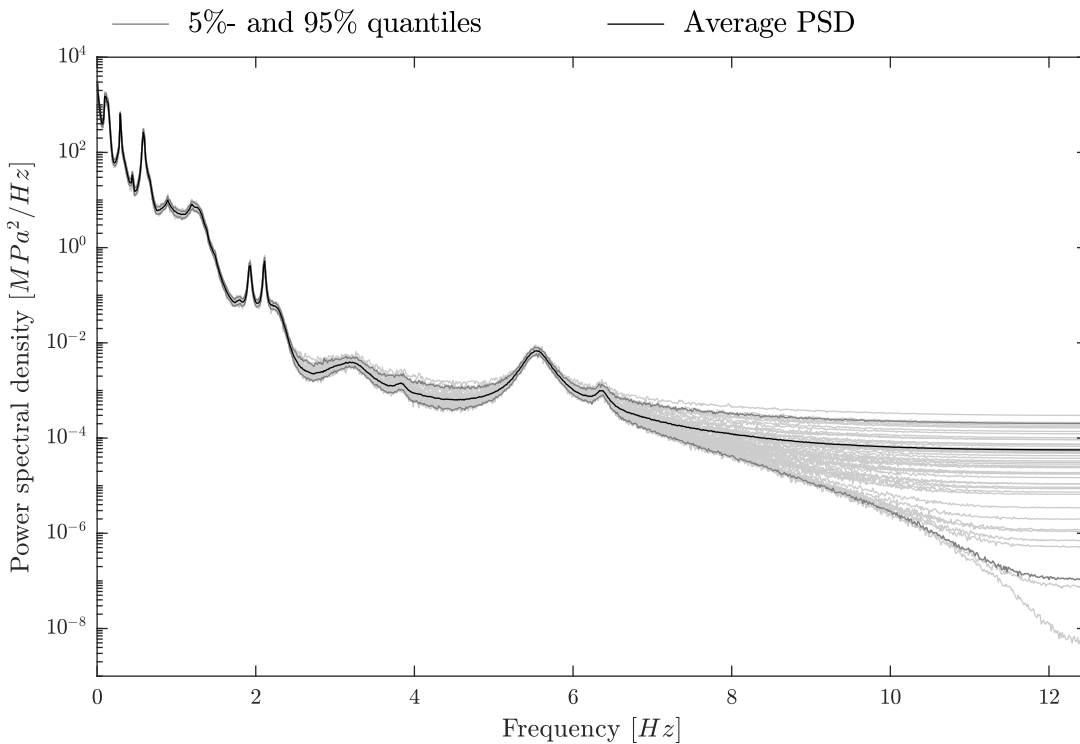


Figure 8.4: Power spectral densities (PSD) of all time series transferred to Gaussian signals for the analysed tubular K-joint

8.1.4 Spectral properties

Special attention is given to the calculation of spectral moments due to their importance for the determination of extreme loads and of fatigue loads. As described in Section 2.1.1, different approaches are identified for the calculation of spectral moments. They can either be determined on the basis of power spectral densities or amplitude spectra, referring to Eq. (2.7) and Eq. (2.8), or on the basis of the derivatives of the signals. For the latter approach, spectral moments of even order are calculated by means of Eq. (2.9), and spectral moments of odd order are determined via finding the absolute maximum value of Eq. (2.21). The respective zero-up-crossing periods and the peak-to-peak periods are calculated according to Eq. (2.11) and Eq. (2.12), respectively. Only the signals transferred to a Gaussian signal are considered in the analysis, since the respective distribution functions of extreme loads and of fatigue loads are based on Gaussian signals, referring to Section 5.2.1 and Section 6.2.1.

The zeroth-, first-, second-, and fourth-order spectral moments for the different approaches are shown in Fig. 8.5. Additionally, the zero-up-crossing periods and the peak-to-peak periods on the basis of the spectral moments are plotted against the respective values which are extracted from the time series via calculating the average time between consecutive zero-up-crossings and via calculating the average time between consecutive local maxima, respectively.

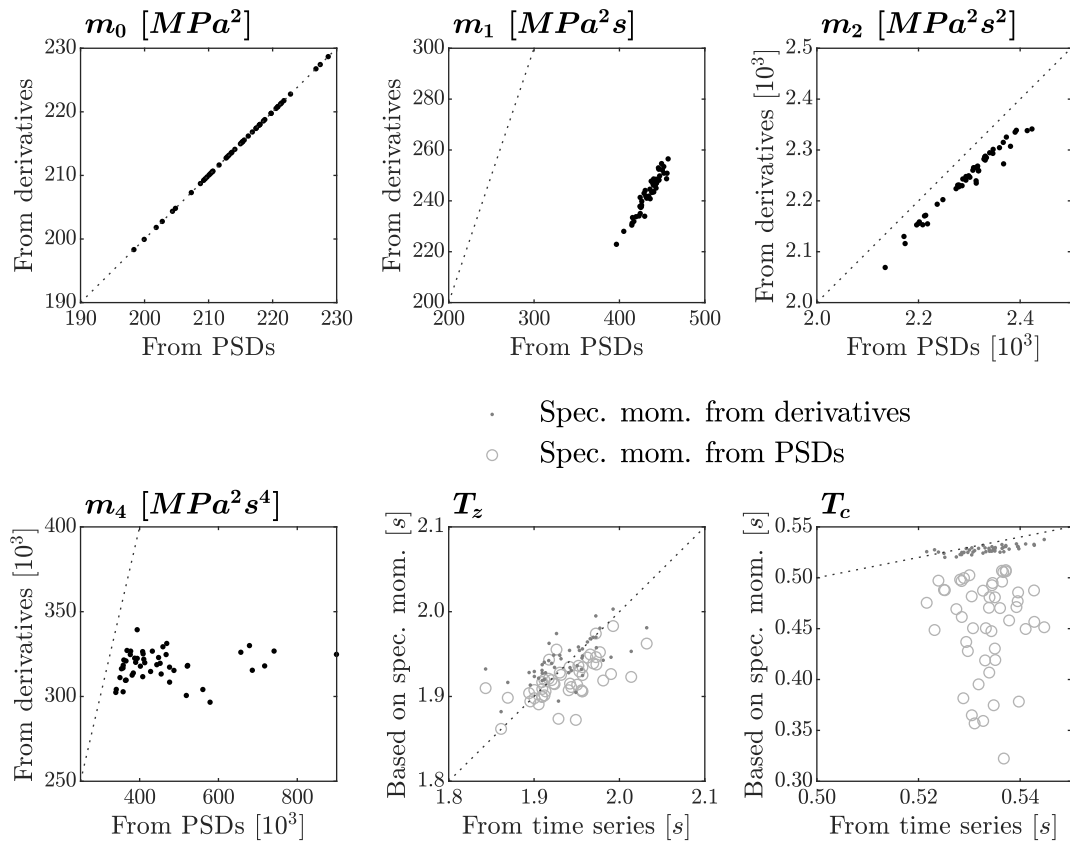


Figure 8.5: Comparison of spectral moments m_n of order n as well as of the zero-up-crossing periods T_z and the peak-to-peak periods T_c , obtained by means of different approaches, for the analysed tubular K-joint

It is noticeable for all spectral moments that the values are subject of scattering. For example, 90% of the zeroth-order spectral moments lie within the range of $\sim -5.9\%$ to $\sim +5.8\%$ relative to the average value. This corresponds to a range for the standard deviations of $\sim -3.0\%$ to $\sim +2.9\%$ relative to the average value.

As for the zeroth-order spectral moment, the values determined from the power spectral densities match the variances of the time series. The second-order spectral moment determined from power spectral densities overestimate the second-order spectral moment calculated on the basis of the first derivative of the signal by $\sim 2\%$. The fourth-order spectral moment determined from power spectral densities scatter extensively. The values exceed the fourth-order spectral moment calculated on the basis of the second derivative of the signal significantly. The scattering of the fourth-order spectral moments determined from power spectral densities is due to the differences between the single power spectral densities of the signals shown in Fig. 8.4. The power spectral densities of very high wave frequencies contribute significantly to the fourth-order spectral moments, referring to Eq. (2.7), where the wave frequency to the power of four is evaluated. This effect is minor for spectral moments of lower order, but it is also noticeable for the second-order spectral moments. Following this argumentation, it is to be expected that first-order spectral moments determined from the power spectral densities match the theoretical first-order spectral moment very well. In comparison, the first-order spectral moments determined via finding the absolute maximum value of Eq. (2.21) underestimate the first-order spectral moments determined from the power spectral densities significantly by $\sim 35\%$. It is to be concluded that the approach to determine spectral moments of odd order by means of Eq. (2.21) might cause misleading and underestimated values.

Referring to Fig. 8.5 (bottom, middle and right), both the zero-up-crossing periods and the peak-to-peak periods extracted from the time series are subject of scatter. They differ from the respective average value by approximately $\pm 5\%$. The zero-up-crossing periods determined by means of spectral moments according to Eq. (2.11) match the values from the time series very well. The zero-up-crossing periods on the basis of power spectral densities (grey circles) slightly underestimate the values from the time series due to the small overestimation of the second-order spectral moment. As for the peak-to-peak periods, the values on the basis of power spectral densities (grey circles) scatter significantly. The values constantly underestimate the values extracted from the time series. This is also due to the scattering and overestimation of the fourth-order spectral moments, which is used for the calculation of the peak-to-peak period, referring to Eq. (2.12). The peak-to-peak periods determined on the basis of the derivatives of the signals (grey dots) match the values from the time series very well.

It is concluded that the calculation of spectral moments of even order on the basis of the derivatives of the signals leads to accurate results. The first-order spectral moments are underestimated to an unknown degree in case that they are determined by means of finding the absolute maximum value of Eq. (2.21). The determination of the first-order spectral moments on the basis of power spectral densities yields more accurate values. However, spectral moments of higher order determined on the basis of power spectral densities are overestimated, and they are subject of increased scatter.

8.1.5 Distribution functions of extreme loads

The distribution functions of extreme loads based on power spectral densities depend on the first-order spectral moment and on the spectral width parameter, referring to Section 5.2. The spectral moments determined by means of different approaches are already presented in Fig. 8.5.

In Fig. 8.6 (left), the spectral width parameters which are calculated on the basis of spectral moments are compared to the values derived from the peak-to-peak periods and zero-up-crossing periods derived from the time series, referring to Section 2.1.2. The spectral width parameters based on spectral moments are determined from power spectral densities (circles) as well as from the derivatives of the time series (dots). Based on the spectral width parameter, the distribution functions of extreme loads are obtained. The mean values and standard deviations of the distribution functions of extreme values derived for each time series are shown in Fig. 8.6 (right). Additionally, the mean value and the standard deviation of the extreme values of all 52 time series are marked (black dot). The extreme values are determined for the zero-mean signal transferred to Gaussian signals for the analysed tubular K-joint. Only the results for maximum values are shown here. The analysis of the minimum values can be carried out with the same approach as for the maximum values.

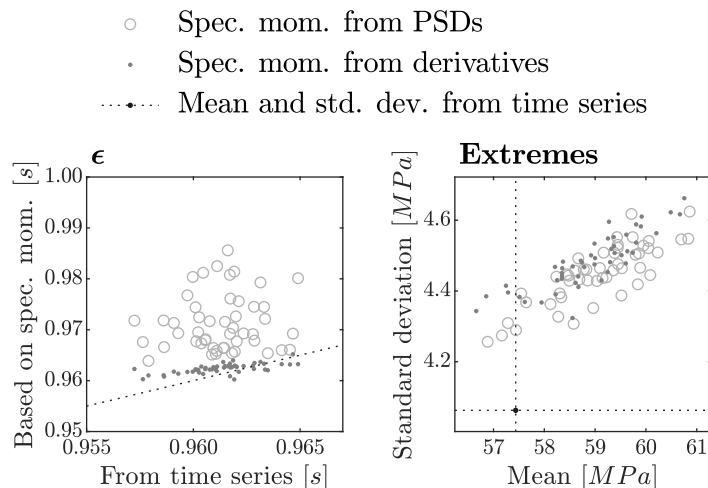


Figure 8.6: Comparison of (left) spectral width parameters ϵ as well as of (right) the resulting mean values and standard deviations of the distribution functions of extreme values, obtained with different approaches, for the analysed tubular K-joint

Very high values for the spectral width parameters are observed for all analysed time series, here with an average value of 0.9613. Approximately 90% of the simulated values lie within the range of 0.9579 to 0.9645. The spectral width parameters based on spectral moments calculated from derivatives are almost constant. They are considerably linear to the values obtained from the time series. The spectral width parameters based on spectral moments calculated from power spectral densities are greater than the values from the time series, and they scatter significantly. This results from the scattering of the fourth-order spectral moment, as described in Section 8.1.4, on which the spectral width parameter depends. The values lie in the range of 0.9640 to 0.9850.

As can be seen in Fig. 8.6 (right), almost all mean values calculated on the basis of the spectral moments are greater than the mean value of the time series. The standard deviations are also greater than the respective value of the time series. In general, an approximately linear relation between mean values and standard deviations is observed for both approaches to determine the spectral moments. The ranges of the mean extreme values are very similar for both approaches to determine the spectral moments. The standard deviations of extreme values based on spectral moments calculated from power spectral densities have a greater range in comparison to the standard deviations of extreme values based on spectral moments calculated from derivatives. This is due to the scattering of the spectral width parameter.

The distribution function of the extreme values are further analysed by means of Q-Q plots. The Q-Q plots of the extreme values are shown in Fig. 8.7. The extremes derived from the 52 time series are plotted against all respective quantiles obtained from the distribution functions of extreme values which are determined on the basis of spectral moments calculated from the derivatives of the time series. The respective mean as well as the 10%- and 90%-quantiles of the distribution functions of extreme values are also shown for reasons of clarity.

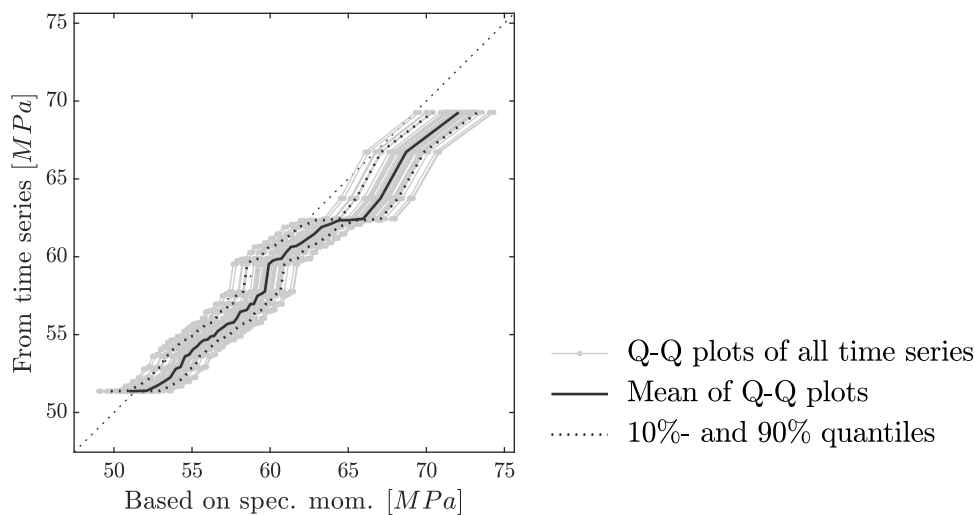


Figure 8.7: Q-Q plot for the distribution functions of extreme values determined on the basis of spectral moments calculated from the derivatives for the analysed tubular K-joint

In general, the Q-Q plots can be considered as linear which confirms that the derived type of distribution function of extreme values is applicable. However, the parameters of the distribution function are mostly overestimated, here shown for the mean value and standard deviation. Almost all of the 52 Q-Q plots for the distribution functions of extreme values determined on the basis of spectral moments calculated from the derivatives lie below the bisection line. This is especially true for the mean curve of the Q-Q plots. The slopes of the Q-Q plots are also smaller than unity, which is the slope of the bisection line. Hence, scattering of the extremes determined on the basis of spectral moments is greater, which is equivalent to increased standard deviations. These findings confirm the conclusion from Fig. 8.6 (right) that the mean values and the standard deviations of extreme values overestimate the respective values obtained from simulated time series.

It is already noted in Section 5.2.2 that extreme values in signals derived via inverse Fourier transformation are less than the values obtained from the theoretical distribution function of extreme values. This is also concluded here from the findings shown above.

8.1.6 Distribution functions of fatigue loads

As described in Section 6.2.1, the different models of distribution functions of fatigue loads based on power spectral densities depend on several spectral moments or on spectral parameters α_1 and α_2 , referring to Eq. (2.14), respectively. The spectral moments can be determined by means of different approaches, referring to Section 8.1.4. Due to the described scattering of the values of the spectral moments, the spectral parameters are also subject of scattering.

The spectral parameters α_1 and α_2 are compared to each other in Fig. 8.8 (left and middle). The spectral parameters compared to each other are calculated on the basis of the spectral moments determined from power spectral densities, on the basis of the spectral moments calculated on the basis of derivatives, as well as on the basis of spectral moments of even order calculated on the basis of derivatives and the first-order spectral moment determined from power spectral densities. The latter is the optimised approach as suggested in Section 8.1.4. The spectral parameter α_2 can also be calculated as ratio of peak-to-peak period to zero-up-crossing period. The resulting damage-equivalent loads for a slope of the SN curve of $m = 4$ are shown in Fig. 8.8 (right). The damage-equivalent loads according to the newly-developed approach to determine the distribution functions of fatigue loads based on power spectral densities, referring to Eq. (6.12), are compared to the damage-equivalent loads extracted from the time series. The damage-equivalent loads are calculated according to Eq. (6.5) with a reference number of load cycles equal to the number of load cycles within the analysed time series. Just as for the spectral parameters, the damage-equivalent loads are determined on the basis of the spectral moments calculated from power spectral densities, on the basis of the spectral moments calculated on the basis of derivatives, as well as on the basis of spectral moments of even order calculated on the basis of derivatives and the first-order spectral moment determined from power spectral densities. Only the results of the signals transferred to a Gaussian signal are presented.

The spectral parameters α_1 based on spectral moments calculated from power spectral densities and those for the optimised approach agree very well. The spectral parameters α_1 based on spectral moments calculated from derivatives underestimate the respective values based on spectral moments calculated from power spectral densities significantly. This is due to the underestimation of the first-order spectral moment which is calculated by means of Eq. (2.9). This effect is already reported in Section 8.1.4. The spectral parameters α_2 on the basis of the peak-to-peak periods and the zero-up-crossing periods is almost constant for all time series. The respective spectral parameters based on spectral moments from derivatives match those values from the time series very well. The spectral parameters α_2 for the optimised approach are not shown here, since they match the values based on spectral moments from derivatives. The spectral parameters α_2 based on spectral moments obtained from power spectral densities scatter signific-

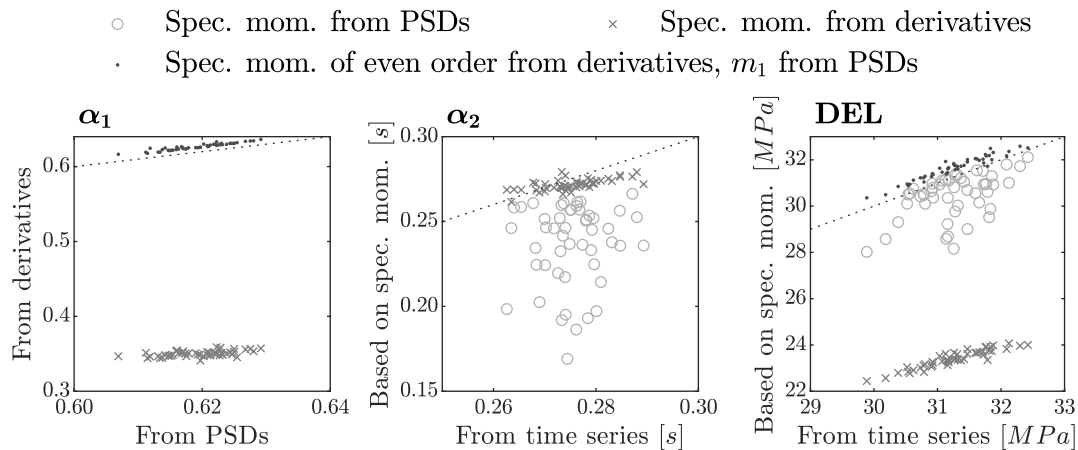


Figure 8.8: Comparison of spectral parameters α_1 and α_2 as well as of the resulting damage-equivalent load (DEL), obtained with different approaches, for the analysed tubular K-joint

antly due to the scattering of the fourth-order spectral moments, which is explained in Section 8.1.4.

The damage-equivalent loads of the simulated time series have an average value of 31.26 MPa , and 90% of all damage-equivalent loads lie within the range of 30.37 MPa to 32.13 MPa . The damage-equivalent loads determined on the basis of spectral moments calculated from power spectral densities are less than the respective values of the simulated time series, and they scatter noticeably. This is due to the scattering of the fourth-order spectral moment and of the spectral parameter α_2 . The damage-equivalent loads determined on the basis of spectral moments calculated from derivatives underestimate the damage-equivalent loads of the simulated time series significantly, here by $\sim 25\%$. The reason for this deviation is the underestimation of the first-order spectral moment and hence of the spectral parameter α_1 . Both damage-equivalent loads are approximately proportional to each other. The damage-equivalent loads for the optimised approach match the damage-equivalent loads of the simulated time series very well. They slightly overestimate the simulated damage-equivalent loads, here by $\sim 1\%$. According to Fig. 6.18, a very small underestimation of the damage-equivalent load of the simulated time series is expected, but a greater damage-equivalent load according to the newly-developed approach to determine the distribution functions of fatigue loads based on power spectral densities is observed here. One reason may be small deviations for the calculated spectral parameters. Additionally, it is observed that the simulated maximum values and the very high peak values are less than the values which are theoretically expected, as already noted for the extreme values, referring to Section 8.1.5. Hence, the ranges of the very high fatigue loads are also underestimated which causes a reduction of the damage-equivalent loads of the simulated time series.

8.1.7 Conclusion

Referring to Section 2.1.2, spectral moments can be obtained from time series. However, some difficulties exist for the calculation. Spectral moments of odd order calculated on the basis of derivatives are underestimated, and spectral moments of high order determined from power spectral densities are subject of scatter. In general, the resulting

extreme loads and fatigue loads are slightly greater than the values of the time series. Reasons for the overestimation may be due to the calculation of the spectral moments and in particular due to the general overestimation of peak values by the models in comparison to simulated peak values within time series.

Scattering of the fatigue loads, as it is described by Zwick and Muskulus (2015) for time-domain simulations with a duration of 600 s, is also observed for the fatigue loads based on spectral moments. The relation between the fatigue loads obtained from time series and from spectral moments is almost linear. In general, increasing the lengths of the time series results in less scattering values of the spectral moments and thus in more constant characteristics of the extreme loads and fatigue loads.

8.2 Impact of currents on the simulation of wave-induced loads

As noted in Section 4.2.3, the simulations of wave-induced loads are carried out without considering any current for the fatigue design of offshore wind turbines (IEC 61400-3-1, 2019; DNV-ST-0437, 2016). However, currents have a significant impact on the drag term of Morison's equation, referring to Eq. (3.19), and on the power spectral densities of the drag term of Morison's equation, as it is described to Section 3.2.5. The power spectral density of the drag term can be modelled as superposition of several power spectral densities which depend on the original power spectral density of the water-particle velocity. Due to currents, the coefficients of the superposed power spectral densities vary such that the energy density at different wave frequencies are of different magnitude. These energy densities may be amplified due to the structural-dynamic behaviour of the structure.

Within the following study, wave-load simulations for an offshore wind turbine with jacket substructure are carried out for different current velocities. The resulting time series are analysed with respect to their contribution to fatigue damage.

8.2.1 Load simulations

The offshore wind turbine as modelled for the study on spectral properties in Section 8.1 is also applied for this study, consisting of the NREL 5 MW wind turbine (Jonkman et al., 2009) and of the jacket substructure described by Vorpahl et al. (2011). The first bending Eigen frequency of the modelled offshore wind turbine has a value of 0.3230 Hz. Both static and structural-dynamic simulations of the offshore wind turbine are carried with the finite-element software *Poseidon* (Böker, 2010). Rayleigh damping with damping of 1% at frequencies of 0.30 Hz and 0.20 Hz is considered for the structural-dynamic simulations.

Only the loadings caused by the sea state are simulated to emphasize the impact of the currents. A JONSWAP spectrum according to Eq. (3.17) with $H_s = 1.75$ m, $T_p = 6.19$ s, and $\gamma = 3.3$ is applied for modelling of the irregular sea state. The peak period is chosen such that the peak frequency with a value of 0.1615 Hz is half of the first bending Eigen frequency. Since the second-order term of the drag term of Morison's equation has a local maximum close to twice of the peak period, referring to Fig. 3.8, it is expected

that the amplification at the first bending Eigen frequency causes increased loads during structural-dynamic load simulations in case of currents. The value of significant wave height is selected from the H_s - T_p scatter table given in Appendix A1 as the mean of the class which has the highest occurrence frequency for the class of the selected peak period. Current velocities of zero and 1 m/s are considered in the load simulation. The hydrodynamic coefficients for Morison's equation are set as $C_d = 1.0$ and $C_m = 2.0$. Six different realisations of the sea states are simulated.

The stresses at lower brace of the tubular K-joint (II) are analysed in the study, as marked in Fig. 8.1 (left). As already described for the previous study in Section 8.1, the structural stress approach is applied for calculation of the stresses acting at the K-joints of the jacket structure. Here, the stresses at the bottom crown are exemplarily investigated within the study.

8.2.2 Impact of currents on power spectral densities of loads

Power spectral densities of the stresses at the considered tubular K-joint are derived via Fourier transformation of the simulated time series. The power spectral densities for the static load simulations are shown in Fig. 8.9. They are plotted for current velocities with values of zero (grey lines) and of 1.0 m/s (black lines) and for the total wave-induced stresses (dashed lines) and for the drag term of Morison's equation only (solid lines). The first bending Eigen frequency is marked.

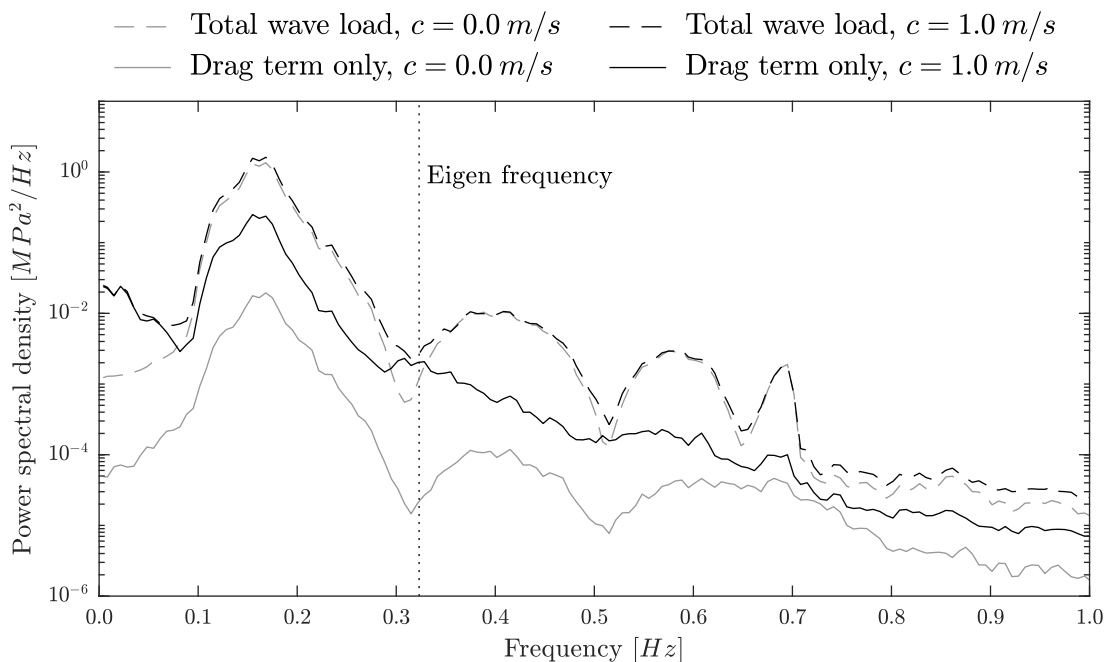


Figure 8.9: Power spectral densities of the wave-induced stresses at the analysed tubular K-joint for different current velocities, obtained from static load simulations

It is generally noted that the energy of the power spectral density for the drag term of Morison's equation including current is significantly greater in comparison to the power spectral density without current. Referring to Fig. 3.8, the different n -fold convolutions are identified in the power spectral densities for the drag term of Morison's equation. For a current velocity of zero, the power spectral density of the horizontal

water-particle velocity with its peak close to the peak frequency and the 3-fold convolution with its peak close to trice of the peak frequency can clearly be detected. As for the power spectral density for the drag term of Morison's equation including current velocity of 1.0 m/s , the power spectral density of the horizontal water-particle velocity is still dominant. The 3-fold convolution is almost distinguished because its coefficient according to Eq. (3.21) and Fig. 3.9 tends to zero for increasing current velocities. The 2-fold convolution with its peaks close to zero and close to half of the peak frequency is clearly notable, since its coefficient increases for increasing current velocities. Its coefficient is zero for a current velocity of zero. Hence, it is not observed within the power spectral density for a current velocity of zero.

The impact of the current is also observed for the total wave-induced stresses. In comparison to the power spectral density with no current, the impact of the 2-fold convolution of the power spectral densities for the drag term on the power spectral density is noticed for frequencies in the range of zero to 0.1 Hz and in the range of 0.28 Hz to 0.35 Hz where the first bending Eigen frequency lies. Besides from these ranges mentioned, the curves of the power spectral densities for current velocities of zero and 1.0 m/s are almost identical.

The power spectral densities for the structural-dynamic load simulations are shown in Fig. 8.9 as solid lines. Additionally, the power spectral densities for the structural-dynamic load simulations (dashed lines) are shown. They are plotted for current velocities with values of zero (grey line) and of 1.0 m/s (black line). Again, the first bending Eigen frequency is marked.

Since the power spectral density close to the first bending Eigen frequency is increased due to the existence of current, a significant increase at the first bending Eigen frequency is seen for the structural-dynamic load simulations.

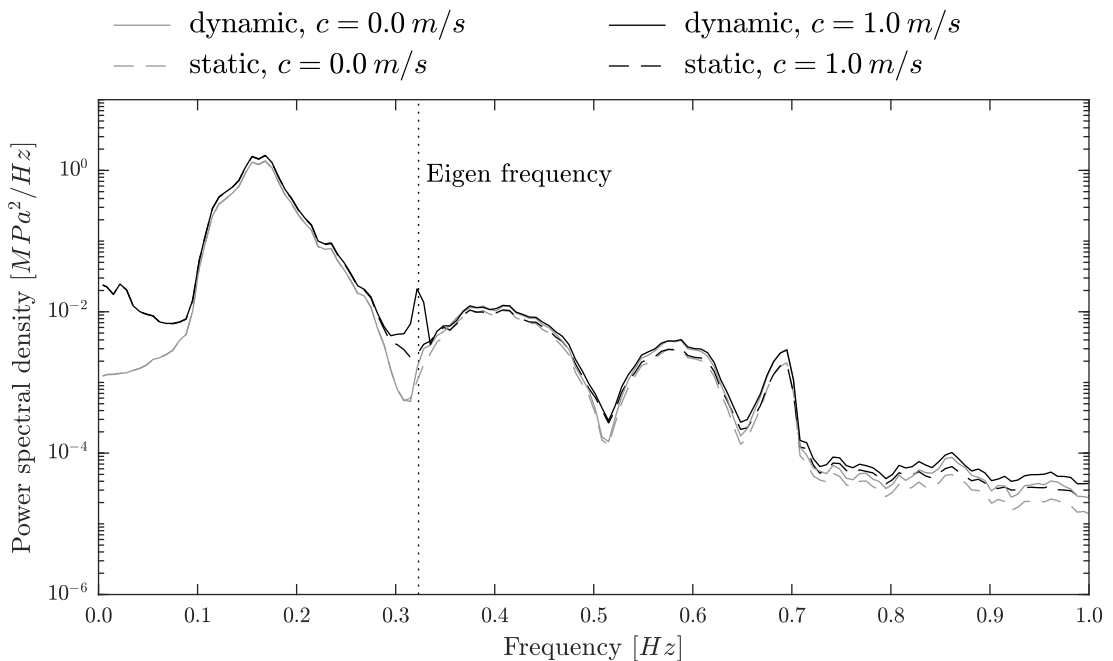


Figure 8.10: Power spectral densities of the wave-induced stresses at the analysed tubular K-joint for different current velocities, obtained from structural-dynamic load simulations

Almost no increase at the first bending Eigen frequency of the power spectral density for the structural-dynamic load simulation is observed for no currents in comparison to the static load simulation. As for the power spectral density for the structural-dynamic load simulation, the power spectral density close to the first bending Eigen frequency is significantly greater at the first bending Eigen frequency due to the dynamic amplification.

8.2.3 Impact of currents on fatigue loads

Due to the quadratic term of the water-particle velocity within the drag term of Morison's equation, the range of fatigue loads is greater for increased current velocities. Hence, greater damage-equivalent loads and greater fatigue damage occur. The effect of currents on the fatigue loads is analysed shortly below for both static and structural-dynamic load simulations.

The zeroth-order spectral moments as well as the damage-equivalent loads for the analysed tubular K-joint are listed in Tbl. 8.1 for current velocities with values of zero and of 1.0 m/s . The results for both static and structural-dynamic load simulations are shown.

Table 8.1: Impact of currents on the zeroth-order spectral moments and on the damage-equivalent loads (DEL) for the analysed tubular K-joint for static and structural-dynamic load simulations

	Simulation parameters			from time series	
	c [m/s]	C_d	C_m	m_0 [MPa ²]	DEL [MPa]
static	0.0	0.0	2.0	0.0689	4.3840
	0.0	1.0	2.0	0.0701	4.4361
	1.0	1.0	2.0	0.0852 +21.6% ^a	4.8790 +10.0% ^a
dynamic	0.0	0.0	2.0	0.0699	4.4410
	0.0	1.0	2.0	0.0711	4.4994
	1.0	1.0	2.0	0.0868 +22.0% ^a	4.9655 +10.4% ^a

^a Relative to no current, $C_d = 1.0$, and $C_m = 2.0$

Besides the zeroth-order spectral moments as well as the damage-equivalent loads for the total wave-induced loads, the respective values for only the inertia term of Morison's equation are stated. Both values almost match the values for the total wave-induced loads. The ratios are greater 98% for the zeroth-order spectral moments and the damage-equivalent load as well as for the static and structural-dynamic simulation. Hence, the inertia term of Morison's equation is dominant for the total wave-induced stresses. This is in line with the findings stated in Section 3.2.6.

Considering a current velocity of 1.0 m/s for the analysed set-up instead of no current, the zeroth-order spectral moments are increased by more than 20%. The damage-equivalent loads are increased by more than 10%. This is found for both the static and structural-dynamic simulations. This increase of the damage-equivalent load may contribute significantly to the fatigue damage for the selected sea state without considered the wind-induced loads simultaneously acting on the offshore wind turbine.

The comparison of the static and structural-dynamic simulations shows only small differences for the zeroth-order spectral moments as well as the damage-equivalent loads. Even in case of simulations with high damping values, which may be modelled as static process, the increase of the damage-equivalent load due to currents is significant for the selected set-ups of the structural model and the sea state.

8.2.4 Conclusion

Currents have a significant impact on the wave-induced fatigue loads. An increase of the damage-equivalent load of 10% is calculated for the analysed tubular K-joint for both static and structural-dynamic load simulations. Approximately the same percentages of increase are observed for other structural details of the analysed jacket substructure.

The analyses are carried out for offshore wind turbine with a rated power capacity of 5 MW. For offshore wind turbines of the new generation with rated power capacities of at least 15 MW, the Eigen frequencies are lower such that greater peak frequencies of the sea states, and their multiples match these Eigen frequencies. Considering the H_s - T_p scatter table, referring to Appendix A1, higher significant wave heights occur for these peak periods. These sea states contain more energy, which is approximately proportional to the squared significant wave height. Hence, they cause greater wave-induced loads. This also leads to greater damage-equivalent loads when not considering the occurrence probability of the respective sea states. However, the occurrence frequencies of these more severe sea states are usually smaller which causes a reduction of the total damage-equivalent load. In combination, no exclusive statement can be made regarding the impact on the fatigue loads for offshore wind turbines with greater rated power capacity, but this is to be analysed for each specific offshore wind turbine.

9 Summary and outlook

9.1 Summary

Offshore wind energy is one of the cornerstones in order to meet the goals to produce climate-neutral energy. Therefore, the further installation of offshore wind turbines is decisive in order to meet this aim.

The structural design of offshore wind turbines shall be safe with respect to standard and guidelines as well as economic. It is usually carried out by means of the semi-probabilistic safety concept. Here, partial factors are applied on characteristic values of the resistance of the structural components and of the effects of actions in order to consider scattering of these values. The level of safety is implicitly included in the characteristic values and the partial factors. Contrarily, the probabilistic safety concept considers the distribution functions of resistance and of the effects of actions. No partial factors are applied. A great number of evaluations of these distribution functions is required to calculate the probability of failure, which is the probability that the scattering effects of actions exceed the scattering resistance of the structural components. Probabilistic design methods are considered to provide a more economic design in comparison to the semi-probabilistic safety concept.

Therefore, probabilistic models are required which describe the structural model and its structural-dynamic variations, the long-term weather conditions, as well as the short-term statistics of the loads which are to occur during short windows of constant environmental conditions. The load simulations are to be carried out for constant structural properties and constant weather conditions. Load simulation can either be carried out in time- or frequency domain. Different aspects of the structural-dynamic changes over the lifetime of offshore wind turbines are described. Exemplarily, these are due to marine growth, soil and scour development, corrosion, and deterioration of structural components due to the harsh condition offshore. Long-term weather conditions, which are based on measurements at the research platform FINO1, are also summarised. In general, they form the basis for the weather conditions to be simulated. Here, the seasonal dependence as well as the data availability are shortly analysed for the mean wind velocity and the decisive sea-state parameters, namely significant wave height and peak period.

Several thousands of load simulation in time domain are already required for the structural design of offshore wind turbines when applying the semi-probabilistic safety concept. Even more time-domain simulations are necessary for the probabilistic safety concept in order to determine the probability of failure accurately. For example, especially the derivation of the distribution function of extreme loads is very time-consuming. Since only one extreme value from a time series can be used, a sufficient number of random time-domain simulations is essential to generate a data set of ex-

treme values for the derivation of the respective distribution function. In comparison to time-domain simulations, the computational effort to carry out simulations in frequency domain is reduced significantly. Additionally, only one simulation in frequency domain is required in order to determine the distribution function of extreme loads and the fatigue loads. However, non-linearities within the equations of motions to be solved to describe the structural-response of an offshore wind turbine cannot be described well by the simulation in frequency domain. These non-linearities are due to temporarily changing structural properties of the structural model of the offshore wind turbine, which is i.a. caused by the controller of the rotor-nacelle assembly. Hence, frequency-domain simulations are only applied for the early design stages of an offshore-wind project for an approximate load estimation. Besides these limitations, frequency-domain simulations would be very beneficial for the structural design of offshore wind turbines, especially by means of the probabilistic safety concept.

Advanced approaches are introduced within this thesis to determine the distribution functions of extreme loads as well as of fatigue loads on the basis of frequency-domain analysis. These distribution functions only depend on a few properties of the power spectral densities of the structural response. Additionally, the potentially-existing non-Gaussianity of the signal is considered. The respective distribution function of extreme loads is based on theoretical background and is well established. Different empirical approaches to determine the distribution function of fatigue loads in frequency domain exist. The already existing approaches are defined for a limited range of possible values of the relevant spectral properties. Hence, a new approach is developed within this thesis which covers the domains of the relevant spectral properties. Since especially the high, rarely occurring fatigue loads contribute significantly to the fatigue damage, the new approach is developed with an emphasis on these high loads. In comparison to the already existing approaches, the newly-developed approach yields better agreement between the simulated and modelled distribution functions of fatigue loads. The modelled fatigue damages also match the simulated values for SN curves with different slopes very well. This approach is not only applicable for the estimation of fatigue loads for offshore wind turbines, but it can also be applied for other fields of engineering which are concerned with fatigue due to random loads.

Since load simulations in frequency domain are not always suitable, inverse Fourier transformation of power spectral densities of the acting loads is applied to generate random time series. Only limited information on the discretisation of power spectral densities is provided within standards and guidelines which are considered as too conservative. An extensive analysis is carried out in order to evaluate the impact of different types of discretisation on the generated time series. Again, special attention is paid to the extreme loads and fatigue loads. It is concluded from the analysis that the discretisation must not generate a signal which is periodic within the considered duration. In combination with the findings for the determination of the distribution functions for extreme loads and fatigue loads, the spectral moments of the discretised signal shall also match those of the expected power spectral densities of the structural response.

The accurate determination of spectral moments is decisive in order to obtain the distribution functions of extreme loads and of fatigue loads in frequency domain. Different methods exist which allow to determine the spectral moments in frequency domain as well as in time domain. Within a study, the extraction of spectral moments from time

series is investigated for time series derived from a load simulation of an offshore wind turbine. Especially the calculation of spectral moments of odd order on the basis of time series is erroneous, and the determination of spectral moments becomes more inaccurate for increasing order. Additionally, the non-Gaussianity of the signal is evaluated for the extreme loads and fatigue loads in particular.

Morison's equation is usually applied for the calculation of wave-induced loads acting on bottom-fixed substructures of offshore wind turbines. The inertia term of wave-induced loads is dominant. In general, the significance of the drag term increases for more severe sea states and smaller pile diameters. Increased current velocities also lead to a more significant drag term. A study carried within this thesis shows the significant impact which currents have on the fatigue loads. This finding is especially relevant, since no currents are to be modelled for the design load cases which are to be considered for the fatigue design within the respective standards and guidelines. Additionally, common presentations of the predominance of drag term and inertia term of Morison's equation in dependence of wave height and wave length of a periodic wave as well as of pile diameter are extended for current velocities. For the first time, a similar presentation is introduced for sea states in order to evaluate the impact on fatigue loads. This presentation shows the dominance of drag term and inertia term of Morison's equation on the fatigue loads in dependence of significant wave height and wave length representative for the sea state as well as of pile diameter. The impact of currents is also shown.

9.2 Outlook

Different load types, denoted as constant, periodic, transient, random, and random-transient, are introduced and described. They commonly occur during the lifetime of offshore wind turbines. Hence, they are to be considered during the load simulations. These load types are simulated simultaneously within load simulation in time domain. Since load simulations in frequency domain are especially suited for the simulation of random loads, the combination of different load types in frequency domain is to be further analysed with respect to the load analysis of offshore wind turbines.

In comparison to time domain, load simulation in frequency domain are computationally very efficient. They are especially suitable for the probabilistic design. On basis of the resulting power spectral densities of the responses, the distribution functions of the extreme loads and fatigue loads can easily be extracted on basis of the spectral moments, as it is described within the thesis. Contrarily, time series of sufficiently long duration or many time series of shorter duration must exist such that the distribution functions of the extreme loads and fatigue loads can be determined with acceptable accuracy. This is very time-consuming. However, load simulations in time domain are still state-of-the-art for the design of offshore wind turbines. In comparison to frequency domain, the load simulations in time domain are capable of modelling the time-variant behaviour of the structural model and non-linearities. This random behaviour mostly results from the controller of the offshore wind turbine. Until now, no model in frequency domain is given which describes the behaviour of the controller appropriately.

Load simulations in frequency domain which also cover non-linear behaviour and non-Gaussian loads would improve the accuracy of the resulting loads.

The newly-developed distribution function for fatigue loads on the basis of power spectral densities only describes the distribution of the ranges of fatigue loads. The mean values of each load cycle is not considered. Both the ranges and mean values of fatigue loads are required for the structural design of certain structural components, such as prestressed bolts of ring-flange connections. Hence, the distribution function for fatigue loads on the basis of power spectral densities can be extended in order to include the mean values. This may be done on the basis of the time series already used to develop the new approach. During the development of the new approach to describe the distribution function of fatigue loads on the basis of power spectral densities, it is noticed that the different distribution functions for the same spectral parameters are not congruent, but small differences exist. It is suggested that the distribution function of fatigue loads may depend on other parameters than the spectral parameters used for the previously- and the newly-developed approach. Further analyses of the time series are required to identify these parameters for an even more accurate model of the fatigue loads.

Bibliography

- Adedipe, O.; Brennan, F.; Kolios, A. (2015): „Corrosion fatigue load frequency sensitivity analysis“. *Marine Structures*, **42**:115–136.
- Al Shamaa, D. (2015): *Probabilistische Betrachtung der Schadensakkumulation für stählerne Schweißverbindungen*. Dissertation, Technische Universität Berlin, Berlin.
- API RP 2A-WSD (2014): „Recommended Practice for Planning, Designing and Constructing Fixed Offshore Platforms—Working Stress Design“. Recommended Practice, American Petroleum Institute, Washington, D.C.
- API RP 2GEO (2014): „Geotechnical and Foundation Design Considerations“. Recommended Practice, American Petroleum Institute, Washington, D.C.
- ASTM E1049-85 (2017): „Standard Practices for Cycle Counting in Fatigue Analysis“. Standard, ASTM International, West Conshohocken.
- ASTM E1823-13 (2013): „Standard Terminology Relating to Fatigue and Fracture Testing“. Standard, ASTM International, West Conshohocken.
- Barltrop, N. D. P.; Adams, A. J. (1991): *Dynamics of fixed marine structures*. Butterworth-Heinemann, Oxford, 3rd edition.
- Benasciutti, D. (2005): *Fatigue analysis of random loadings*. Dissertation, Università degli Studi di Ferrara, Ferrara.
- Benasciutti, D.; Tovo, R. (2005a): „Cycle distribution and fatigue damage assessment in broad-band non-Gaussian random processes“. *Probabilistic Engineering Mechanics*, **20**(2):115–127.
- Benasciutti, D.; Tovo, R. (2005b): „Spectral methods for lifetime prediction under wide-band stationary random processes“. *International Journal of Fatigue*, **27**(8):867–877.
- Benasciutti, D.; Tovo, R. (2006): „Comparison of spectral methods for fatigue analysis of broad-band Gaussian random processes“. *Probabilistic Engineering Mechanics*, **21**(4):287–299.
- Bergmann, W. (2013): *Werkstofftechnik 1*. Carl Hanser Verlag, München, 7th edition.
- Blackwood, D. J. (2018): „An Electrochemist Perspective of Microbiologically Influenced Corrosion“. *Corrosion and Materials Degradation*, **1**(1):59–76.
- Bohm, G.; Zech, G. (2010): *Introduction to Statistics and Data Analysis for Physicists*. Verlag Deutsches Elektronen-Synchrotron, Hamburg.
- Böhm, M.; Schaumann, P. (2022): „Shell buckling simulations of suction buckets with stochastic and deterministic imperfection forms“. *Journal of Physics: Conference Series*, **2265**(4):042031.
- Böker, C. (2010): *Load simulation and local dynamics of support structures for offshore wind turbines*. Dissertation, Leibniz Universität Hannover, Hannover.

- Bonnefoy, F.; Ducrozet, G.; Le Touzé, D.; Ferrant, P. (2010): „Time Domain Simulation of Nonlinear Water Waves Using Spectral Methods“. In Ma, Q. (ed.): *Advances in Coastal and Ocean Engineering*, vol. 11, chap. 4, pp. 129–164. World Scientific, Singapore.
- Borgman, L. E. (1965): „The Spectral Density for Ocean Wave Forces“. In *Coastal Engineering : Santa Barbara Specialty Conferences*, Santa Barbara, pp. 147–182.
- Bouma, S.; Lengkeek, W. (2012): „Benthic communities on hard substrates of the offshore wind farm Egmond aan Zee (OWEZ)“. Technical report 11-205, Bureau Waardenburg, Culemborg.
- Bruijs, M. C. M. (2010): „Survey of marine fouling on turbine support structures of the Offshore Windfarm Egmond aan Zee“. Technical report 50863231-TOS/MEC 08-9096, KEMA Nederland B.V., Arnhem.
- BSH (2015): „Mindestanforderungen an die konstruktive Ausführung von Offshore-Bauwerken in der ausschließlichen Wirtschaftszone (AWZ)“. Standard Konstruktion, Bundesamt für Seeschifffahrt und Hydrographie, Hamburg/Rostock.
- Burton, T.; Sharpe, D.; Jenkins, N.; Bossanyi, E. (2001): *Wind Energy Handbook*. John Wiley & Sons, Ltd, Chichester.
- Butz, T. (2011): *Fouriertransformation für Fußgänger*. Vieweg+Teubner Verlag, Wiesbaden, 7th edition.
- Cartwright, D. E.; Longuet-Higgins, M. S. (1956): „The Statistical Distribution of the Maxima of a Random Function“. *Proceedings of the Royal Society of London A: Mathematical, Physical and Engineering Sciences*, **237**(1209):212–232.
- Chakrabarti, S. K. (1981): „Impact of analytical, model and field studies on the design of offshore structures“. In Thulin, S. (ed.): *International Symposium on Ocean Engineering - Ship Handling*, Swedish Maritime Research Centre (SSPA: Statens Skeppsprovingsanstalt), Gothenburg, pp. 6:1–6:79.
- Clauss, G.; Lehmann, E.; Östergaard, C. (1992): *Offshore Structures*, vol. I. Springer, London.
- Coles, S. (2001): *An Introduction to Statistical Modeling of Extreme Values*. Springer series in statistics. Springer, London.
- Collmann, M. (2021): *Ermüdungsfestigkeit von Stumpfnahverbindungen größerer Blechdicke gefügt mit Hochleistungsschweißverfahren*. Dissertation, Leibniz Universität Hannover, Hannover.
- Collmann, M.; Wefer, M. (2017): „Aging and Fatigue – Combined Testing of Welded Joints under Offshore Conditions“. In *Proceedings of the Twenty-seventh (2017) International Ocean and Polar Engineering Conference*, ISOPE, San Francisco, pp. 369–375.
- Couch, A. T.; Conte, J. P. (1997): „Field Verification of Linear and Nonlinear Hybrid Wave Models for Offshore Tower Response Prediction“. *Journal of Offshore Mechanics and Arctic Engineering*, **119**(3):158–165.
- Crandall, S. H.; Mark, W. D. (1967): *Random vibration in mechanical systems*. Academic Press, New York.

- de Haan, L.; Ferreira, A. (2006): *Extreme Value Theory*. Springer Series in Operations Research and Financial Engineering. Springer, New York.
- Dean, R. G. (1965): „Stream function representation of nonlinear ocean waves“. *Journal of Geophysical Research*, **70**(18):4561–4572.
- Dean, R. G.; Dalrymple, R. A. (1984): *Water wave mechanics for engineers and scientists*, vol. 2 of *Advanced Series on Ocean Engineering*. World Scientific, Singapore.
- Desmars, N. (2020): *Real-Time Reconstruction and Prediction of Ocean Wave Fields from Remote Optical Measurements*. Dissertation, École Centrale de Nantes, Nantes.
- Deutsche WindGuard GmbH (2023): „Status des Offshore-Windenergieausbaus in Deutschland – Jahr 2022“. Online, last accessed on April 15th, 2023.
URL https://www.windguard.de/veroeffentlichungen.html?file=files/cto_layout/img/unternehmen/veroeffentlichungen/2023/Status%20des%20ffshore-Windenergieausbaus_Jahr%202022.pdf
- DIN 18088-3 (2019): „Tragstrukturen für Windenergieanlagen und Plattformen - Teil 3: Stahlbauten“. Deutsche Norm, DIN Deutsches Institut für Normung e. V., Berlin.
- DIN EN 10025-1 (2005): „Warmgewalzte Erzeugnisse aus Baustählen - Teil 1: Allgemeine technische Lieferbedingungen“. Deutsche Norm, DIN Deutsches Institut für Normung e. V., Berlin.
- DIN EN 1990 (2010): „Eurocode: Grundlagen der Tragwerksplanung“. Deutsche Norm, DIN Deutsches Institut für Normung e. V., Berlin.
- DIN EN 1993-1-1 (2010): „Eurocode 3: Bemessung und Konstruktion von Stahlbauten - Teil 1-11: Bemessung und Konstruktion von Tragwerken mit Zuggliedern aus Stahl“. Deutsche Norm, DIN Deutsches Institut für Normung e. V., Berlin.
- DIN EN 1993-1-6 (2017): „Eurocode 3 - Bemessung und Konstruktion von Stahlbauten - Teil 1-6: Festigkeit und Stabilität von Schalen“. Deutsche Norm, DIN Deutsches Institut für Normung e. V., Berlin.
- DIN EN 1993-1-9 (2010): „Eurocode 3: Bemessung und Konstruktion von Stahlbauten - Teil 1-9: Ermüdung“. Deutsche Norm, DIN Deutsches Institut für Normung e. V., Berlin.
- DIN EN 1993-1-9 (2023): „Eurocode 3: Bemessung und Konstruktion von Stahlbauten - Teil 1-9: Ermüdung“. Deutsche Norm (draft), DIN Deutsches Institut für Normung e. V., Berlin.
- DIN EN ISO 19902 (2014): „Erdöl- und Erdgasindustrie – Gegründete Stahlplattformen (ISO 19902:2007 + Amd 1:2013); Englische Fassung EN ISO 19902:2007 + A1:2013, nur auf CD-ROM“. Deutsche Norm, DIN Deutsches Institut für Normung e. V., Berlin.
- Dirlik, T. (1985): *Application of computers in fatigue analysis*. Dissertation, University of Warwick, Coventry.
- DNV-OS-C101 (2019): „Design of offshore steel structures, general - LRFD method“. Offshore Standard, DNV AS, Høvik.
- DNV-RP-0416 (2016): „Corrosion protection for wind turbines“. Recommended Practice, DNV GL, Høvik. Amended November 2021.

- DNV-RP-C203 (2019): „Fatigue design of offshore steel structures“. Recommended Practice, DNV AS, Høvik. Amended September 2021.
- DNV-RP-C205 (2019): „Environmental conditions and environmental loads“. Recommended Practice, DNV AS, Høvik.
- DNV-ST-0126 (2021): „Support structures for wind turbines“. Standard, DNV AS, Høvik.
- DNV-ST-0437 (2016): „Loads and site conditions for wind turbines“. Standard, DNV AS, Høvik. Amended November 2021.
- EEG (2023): „Gesetz für den Ausbau erneuerbarer Energien (Erneuerbare-Energien-Gesetz - EEG 2023)“. Bundesgesetz, Federal Republic of Germany.
- Efthymiou, M. (1988): „Development of SCF formulae and generalised influence functions for use in fatigue analysis“. In *OTC'88: Proceedings of the Conference OTJ'88 on Recent Developments in Tubular Joints Technology*, Surrey.
- Eichstädt, R. (2019): *Fatigue Assessment of Large-Size Bolting Assemblies for Wind Turbine Support Structures*. Dissertation, Leibniz Universität Hannover, Hannover.
- Elgar, S.; Guza, R. T.; Seymour, R. J. (1985): „Wave group statistics from numerical simulations of a random sea“. *Applied Ocean Research*, **7**(2):93–96.
- Embrechts, P.; Klüppelberg, C.; Mikosch, T. (1997): *Modelling Extremal Events*, vol. 33 of *Stochastic Modelling and Applied Probability*. Springer, Berlin, Heidelberg.
- Emeis, S.; Türk, M. (2008): „Offshore wind and turbulence characteristics – New insights from the FINO1 data“. In *DEWEK 2008*, DEWI, Bremen.
- Ernst, B.; Seume, J. R. (2012): „Investigation of Site-Specific Wind Field Parameters and Their Effect on Loads of Offshore Wind Turbines“. *Energies*, **5**(10):3835–3855.
- Gasch, R.; Twele, J. (Eds.) (2012): *Wind Power Plants*. Springer, Berlin, Heidelberg.
- Gkatzogiannis, S.; Weinert, J.; Engelhardt, I.; Knoedel, P.; Ummenhofer, T. (2019): „Correlation of laboratory and real marine corrosion for the investigation of corrosion fatigue behaviour of steel components“. *International Journal of Fatigue*, **126**:90–102.
- Goda, Y. (2000): *Random Seas and Design of Maritime Structures*, vol. 15 of *Advanced Series on Ocean Engineering*. World Scientific, Singapore, 2nd edition.
- Gottschalk, M. (2017): *Zur Beultragfähigkeit von Suction Buckets*. Dissertation, Leibniz Universität Hannover, Hannover.
- Gudehus, H.; Zenner, H. (1999): *Leitfaden für eine Betriebsfestigkeitsrechnung*. Verlag Stahleisen GmbH, Düsseldorf, 4th edition.
- Gudmestad, O. T.; Connor, J. J. (1983): „Linearization methods and the influence of current on the nonlinear hydrodynamic drag force“. *Applied Ocean Research*, **5**(4):184–194.
- Gumbel, E. J. (1958): *Statistics of Extremes*. Columbia University Press, New York.
- Halfpenny, A. (1998): *Dynamic Analysis of Both On and Offshore Wind Turbines in the Frequency Domain*. Dissertation, University College London, London.

- Hapel, K.-H. (1990): *Festigkeitsanalyse dynamisch beanspruchter Offshore-Konstruktionen*. Grundlagen und Fortschritte der Ingenieurwissenschaften. Vieweg+Teubner Verlag, Wiesbaden.
- Haselsteiner, A. F. (2022): *Offshore structures under extreme loads: A methodology to determine design loads*. Dissertation, Universität Bremen, Bremen.
- Haselsteiner, A. F.; Coe, R. G.; Manuel, L.; Chai, W.; Leira, B.; Clarindo, G.; Guedes Soares, C.; Hannesdóttir, A.; Dimitrov, N.; Sander, A.; Ohlendorf, J.-H.; Thoben, K.-D.; de Hauteclocque, G.; Mackay, E.; Jonathan, P.; Qiao, C.; Myers, A.; Rode, A.; Hildebrandt, A.; Schmidt, B.; Vanem, E.; Huseby, A. B. (2021): „A benchmarking exercise for environmental contours“. *Ocean Engineering*, **236**:109504.
- Hasselmann, K.; Barnett, T. P.; Bouws, E.; Carlson, H.; Cartwright, D. E.; Enke, K.; Ewing, J. A.; Gienapp, H.; Hasselmann, D. E.; Kruseman, P.; Meerhurg, A.; Müller, P.; Olhers, D. J.; Richter, K.; Seil, W.; Walden, H. (1973): „Measurements of Wind-Wave Growth and Swell Decay during the Joint North Sea Wave Project (JONSWAP)“. *Ergänzungsheft zur Deutschen Hydrographischen Zeitschrift*, **A(8)**(12).
- Hau, E. (2013): *Wind Turbines*. Springer, Berlin, Heidelberg, 3rd edition.
- Herklotz, K. (2007): „Oceanographic Results of Two Years Operation of the First Offshore Wind Research Platform in the German Bight - FINO1“. *DEWI Magazin*, **30**:47–51.
- Hilbert, L. R.; Black, A. R.; Mathiesen, T.; Osvoll, H. (2012): „Corrosion control inside offshore wind farm monopile foundations“. In *EUROCORR 2012*, Istanbul, ID 1301.
- Hübler, C. J. (2019): *Efficient probabilistic analysis of offshore wind turbines based on time-domain simulations*. Dissertation, Leibniz Universität Hannover, Hannover.
- IEC 61400-1 (2005): „Wind turbines – Part 1: Design requirements“. International Standard, International Electrotechnical Commission, Geneva.
- IEC 61400-3-1 (2019): „Wind energy generation systems – Part 3-1: Design requirements for fixed offshore wind turbines“. International Standard, International Electrotechnical Commission, Geneva.
- JCSS (2001): „Static Properties of Structural Steel (Rolled Sections)“. In *Probabilistic Model Code*, chap. 3.02. Joint Committee on Structural Safety.
- JCSS (2013): „Fatigue“. In *Probabilistic Model Code*, chap. 3.12. Joint Committee on Structural Safety.
- Jiang, T. (1988): „Rationale Beschreibung des Seegangs in der Zeitebene“. Technical report BMFT FB MTK 0325 8, Germanischer Lloyd, Hamburg.
- Jonkman, J.; Butterfield, S.; Musial, W.; Scott, G. (2009): „Definition of a 5-MW Reference Wind Turbine for Offshore System Development“. Technical report NREL/TP-500-38060, National Renewable Energy Laboratory, Golden.
- Katsikogiannis, G.; Hegseth, J. M.; Bachynski-Polić, E. E. (2022): „Application of a lumping method for fatigue design of monopile-based wind turbines using fully coupled and simplified models“. *Applied Ocean Research*, **120**:102998.

- Katsikogiannis, G.; Sørum, S. H.; Bachynski, E. E.; Amdahl, J. (2021): „Environmental lumping for efficient fatigue assessment of large-diameter monopile wind turbines“. *Marine Structures*, **77**:102939.
- Kazmierczak, F.; Laudien, J.; Fürst, R.; Bönsch, R. (2010): „Benthosbiologische Erhebungen während der Bauphase des Offshore-Windparks „alpha ventus““. Survey, Institut für Angewandte Ökosystemforschung GmbH, Neu Broderstorf.
- Kazmierczak, F.; Preuß, S.; Breyer, S.; Kern, K.; Fürst, R.; Bönsch, R. (2011): „Fachgutachten „Benthos“ zum Offshore-Windpark „alpha ventus“ – 1. Betriebsjahr“. Survey, Institut für Angewandte Ökosystemforschung GmbH, Neu Broderstorf.
- Kelma, S.; Schaumann, P. (2015): „Probabilistic Fatigue Analysis of Jacket Support Structures for Offshore Wind Turbines Exemplified on Tubular Joints“. *Energy Procedia*, **80**:151–158.
- Kettle, A. J. (2014): „Unexpected vertical wind speed profiles in the boundary layer over the southern North Sea“. *Journal of Wind Engineering and Industrial Aerodynamics*, **134**:149–162.
- Kirchner, J. W. (2005): „Aliasing in $1/f^\alpha$ noise spectra: Origins, consequences, and remedies“. *Physical Review E*, **71**(6):066110.
- Kleineidam, P. (2005): *Zur Bemessung der Tragstrukturen von Offshore-Windenergieanlagen gegen Ermüdung*. Dissertation, Leibniz Universität Hannover, Hannover.
- Krone, R.; Gutow, L.; Joschko, T. J.; Schröder, A. (2013): „Epifauna dynamics at an offshore foundation – Implications of future wind power farming in the North Sea“. *Marine Environmental Research*, **85**:1–12.
- Kühn, M. J. (2001): *Dynamics and Design Optimisation of Offshore Wind Energy Conversion Systems*. Dissertation, Technische Universiteit Delft, Delft.
- Kullback, S.; Leibler, R. A. (1951): „On Information and Sufficiency“. *The Annals of Mathematical Statistics*, **22**(1):79–86.
- Leiding, T.; Tinz, B.; Gates, L.; Rosenhagen, G.; Herklotz, K.; Senet, C.; Outzen, O.; Lindenthal, A.; Neumann, T.; Frühmann, R.; Wilts, F.; Bégué, F.; Schwenk, P.; Stein, D.; Bastigkeit, I.; Lange, B.; Hagemann, S.; Müller, S.; Schwabe, J. (2016): „Standardisierung und vergleichende Analyse der meteorologischen FINO-Messdaten (FINO123)“. Final report, Deutscher Wetterdienst, Hamburg.
- Leimeister, M. (2020): *Reliability-based optimization of floating wind turbine support structures*. Dissertation, University of Strathclyde, Glasgow.
- Lohaus, L.; Cotardo, D.; Werner, M.; Schaumann, P.; Kelma, S. (2015): „Experimental and Numerical Investigations of Grouted Joints in Monopiles Subjected to Early-age Cycling“. *Journal of Ocean and Wind Energy*, **2**(4):193–201.
- Lupton, R. (2014): *Frequency-domain modelling of floating wind turbines*. Dissertation, University of Cambridge, Cambridge.
- Ma, H.; Yang, J.; Chen, L. (2018): „Effect of scour on the structural response of an offshore wind turbine supported on tripod foundation“. *Applied Ocean Research*, **73**:179–189.

- MacCamy, R. C.; Fuchs, R. A. (1954): „Wave forces on piles: a diffraction theory“. Technical Memorandum 69, Corps of Engineers, Washington, D.C.
- Melcher, J.; Kala, Z.; Holický, M.; Fajkus, M.; Rozlívka, L. (2004): „Design characteristics of structural steels based on statistical analysis of metallurgical products“. *Journal of Constructional Steel Research*, **60**(3):795–808.
- Mittendorf, K. E. (2006): *Hydromechanical Design Parameters and Design Loads for Offshore Wind Energy Converters*. Dissertation, Leibniz Universität Hannover, Hannover.
- Momber, A. (2011): „Corrosion and corrosion protection of support structures for offshore wind energy devices (OWEA)“. *Materials and Corrosion*, **62**(5):391–404.
- Momber, A.; Schaumann, P.; Mund, M.; Kelma, S.; Nattkemper, T.; Langenkamper, D.; van Kevelaer, R. (2019): „Monitoring und Zustandsbewertung von Oberflächenschutzsystemen an Offshore-Windenergieanlagen“. In *Korrosionsschutz in der maritimen Technik: Tagungsband zur 18. Tagung*, Hamburg, pp. 59–79.
- Momber, A. W.; Marquardt, T. (2018): „Protective coatings for offshore wind energy devices (OWEAs): a review“. *Journal of Coatings Technology and Research*, **15**(1):13–40.
- Morison, J. R.; O’Brien, M. P.; Johnson, J. W.; Schaaf, S. A. (1950): „The Force Exerted by Surface Waves on Piles“. *Petroleum Transactions*, **189**:149–154.
- Naess, A.; Moan, T. (2012): *Stochastic Dynamics of Marine Structures*. Cambridge University Press, New York.
- Passon, P. (2015): *Offshore Wind Turbine Foundation Design*. Dissertation, Technical University of Denmark.
- Paulsen, B. T.; de Sonnevile, B.; van der Meulen, M.; Jacobsen, N. G. (2019): „Probability of wave slamming and the magnitude of slamming loads on offshore wind turbine foundations“. *Coastal Engineering*, **143**:76–95.
- Pierson, W. J. J.; Moskowitz, L. (1964): „A proposed spectral form for fully developed wind seas based on the similarity theory of S. A. Kitaigorodskii“. *Journal of Geophysical Research*, **69**(24):5181–5190.
- Popko, W. (2020): *Impact of Sea Ice Loads on Global Dynamics of Offshore Wind Turbines*. Dissertation, Leibniz Universität Hannover, Hannover.
- Prendergast, L. J.; Gavin, K.; Doherty, P. (2015): „An investigation into the effect of scour on the natural frequency of an offshore wind turbine“. *Ocean Engineering*, **101**:1–11.
- Preumont, A. (1994): *Random Vibration and Spectral Analysis*. Springer, Dordrecht.
- Preuß, S.; Breyer, S.; Fürst, R.; Bönsch, R. (2012): „Fachgutachten „Benthos“ zum Offshore-Windpark „alpha ventus“ – 2. Betriebsjahr“. Survey, Institut für Angewandte Ökosystemforschung GmbH, Neu Broderstorf.
- Preuß, S.; von Allwörden, S.; Nestler, S.; Kazmierczak, F.; Fuchs, A.; Gloede, F.; Breyer, S.; Fürst, R.; Bönsch, R. (2013): „Fachgutachten „Benthos“ zum Offshore-Windpark „alpha ventus“ – Bericht über das 3. Betriebsjahr“. Survey, Institut für Angewandte Ökosystemforschung GmbH, Neu Broderstorf.

- Puente León, F.; Kiencke, U.; Jäkel, H. (2011): *Signale und Systeme*. Oldenbourg Wissenschaftsverlag GmbH, München, 5th edition.
- Raba, A. (2018): *Fatigue Behaviour of Submerged Axially Loaded Grouted Connections*. Dissertation, Leibniz Universität Hannover, Hannover.
- Radaj, D.; Sonsino, C. M.; Fricke, W. (2006): *Fatigue assessment of welded joints by local concepts*. Woodhead Publishing, Cambridge, 2nd edition.
- Radaj, D.; Vormwald, M. (2007): *Ermüdungsfestigkeit*. Springer, Berlin, Heidelberg, 3rd edition.
- Rice, S. O. (1944): „Mathematical analysis of random noise“. *Bell System Technical Journal*, **23**(3):282–332.
- Rice, S. O. (1945): „Mathematical analysis of random noise“. *Bell System Technical Journal*, **24**(1):46–156.
- Roberts, J. B.; Spanos, P. (2003): *Random vibration and statistical linearization*. Dover Publications, Mineola (NY, USA).
- Rolfes, R. et al. (2018): „Lebensdauer-Forschung an den OWEA-Tragstrukturen im Offshore-Testfeld alpha ventus – GIGAWIND life – Teilvorhaben: Validierte Methoden und Strukturmodelle für ein integrales und wirtschaftliches Design von OWEA-Tragstrukturen“. Technical report, Leibniz Universität Hannover, Hannover.
- Sadowski, A. J.; Rotter, J. M.; Reinke, T.; Ummenhofer, T. (2015): „Statistical analysis of the material properties of selected structural carbon steels“. *Structural Safety*, **53**:26–35.
- Schaumann, P.; Böker, C.; Bechtel, A.; Lochte-Holtgreven, S. (2011): „Support Structures of Wind Energy Converters“. In Baniotopoulos, C. C.; Borri, C.; Stathopoulos, T. (eds.): *Environmental Wind Engineering and Design of Wind Energy Structures*, vol. 531 of *CISM Courses and Lectures*, pp. 191–253. Springer, Vienna.
- Schaumann, P.; Lochte-Holtgreven, S.; Lohaus, L.; Lindschulte, N. (2010): „Durchdruchende Grout-Verbindungen in OWEA – Tragverhalten, Instandsetzung und Optimierung“. *Stahlbau*, **79**(9):637–647.
- Schendel, A. (2018): *Wave-current-induced scouring processes and protection by widely graded material*. Dissertation, Leibniz Universität Hannover, Hannover.
- Schmidt, B. (2017): *Kombinierte extreme Einwirkungen für Offshore-Windenergieanlagen*. Dissertation, Leibniz Universität Hannover, Hannover.
- Schmoor, K. A. (2017): *Probabilistische Analyse zum Sicherheitsniveau von Offshore-Gründungspfählen*. Dissertation, Leibniz Universität Hannover, Hannover.
- Schürmann, K. W. (2021): *Fatigue Behavior of Automatically Welded Tubular Joints for Offshore Wind Energy Substructures*. Dissertation, Leibniz Universität Hannover, Hannover.
- Seidel, M. (2014a): „Substructures for offshore wind turbines – Current trends and developments“. In Schaumann, P. (ed.): *Festschrift Peter Schaumann*, pp. 363–368. Institut für Stahlbau, Hannover.
- Seidel, M. (2014b): „Wave induced fatigue loads“. *Stahlbau*, **83**(8):535–541.

- Seidel, M.; Kelma, S. (2012): „Stochastic modelling of wind and wave induced loads on jacket piles“. *Stahlbau*, **81**(9):705–710.
- Seidel, M.; von Mutius, M.; Steudel, D. (2004): „Design and load calculations for offshore foundations of a 5 MW turbine“. In *DEWEK 2004*, DEWI, Wilhelmshaven.
- Seidel, M.; Voormeeren, S.; van der Steen, J.-B. (2016): „State-of-the-art design processes for offshore wind turbine support structures“. *Stahlbau*, **85**(9):583–590.
- Sharma, J. N.; Dean, R. G. (1979): „Development and evaluation of a procedure for simulating a random directional second order sea surface and associated wave forces“. Ocean Engineering Report No. 20, University of Delaware, Newark (DE, USA).
- Sharma, J. N.; Dean, R. G. (1981): „Second-Order Directional Seas and Associated Wave Forces“. *Society of Petroleum Engineers Journal*, **21**(1):129–140.
- Shojai, S.; Schaumann, P.; Braun, M.; Ehlers, S. (2022a): „Influence of pitting corrosion on the fatigue strength of offshore steel structures based on 3D surface scans“. *International Journal of Fatigue*, **164**:107128.
- Shojai, S.; Schaumann, P.; Brömer, T. (2022b): „Probabilistic modelling of pitting corrosion and its impact on stress concentrations in steel structures in the offshore wind energy“. *Marine Structures*, **84**:103232.
- Sonsino, C. M.; Maddox, S. J.; Haagenen, P. (2005): „A Short Study on the Form of the SN-Curves for Weld Details in the High-Cycle-Fatigue Regime“. Technical report IIW-Doc. no. XIII-2045-05, International Institute of Welding.
- Sørensen, J. D.; Toft, H. S. (2010): „Probabilistic Design of Wind Turbines“. *Energies*, **3**(2):241–257.
- Stahlmann, A. (2014): *Experimental and numerical modeling of scour at offshore wind turbines*. Dissertation, Leibniz Universität Hannover, Hannover.
- Stahlmann, A.; Schlurmann, T. (2012): „Numerical and Experimental Modeling of Scour at Tripod Foundations for Offshore Wind Turbines“. In *Sixth International Conference on Scour and Erosion*, ISSMGE, Paris, ID ICSE6-235.
- Teixeira, A. P.; Guedes Soares, C.; Wang, G. (2013): „Probabilistic modelling of the ultimate strength of ship plates with non-uniform corrosion“. *Journal of Marine Science and Technology*, **18**(1):115–132.
- Thieken, K. G. (2015): *Geotechnical design aspects of foundations for offshore wind energy converters*. Dissertation, Leibniz Universität Hannover, Hannover.
- Tovo, R. (2002): „Cycle distribution and fatigue damage under broad-band random loading“. *International Journal of Fatigue*, **24**(11):1137–1147.
- Tucker, M. J.; Challenor, P. G.; Carter, D. J. T. (1984): „Numerical simulation of a random sea: a common error and its effect upon wave group statistics“. *Applied Ocean Research*, **6**(2):118–122.
- Türk, M.; Grigutsch, K.; Emeis, S. (2008): „The Wind Profile Above the Sea – Investigations Basing on Four Years of FINO 1 Data“. *DEWI Magazin*, **33**:12–15.
- Turkstra, C. J.; Madsen, H. O. (1980): „Load Combinations in Codified Structural Design“. *Journal of the Structural Division*, **106**(12):2527–2543.

- Ummenhofer, T.; Gkatzogiannis, S.; Weidner, P. (2017): „Einfluss der Korrosion auf die Ermüdungsfestigkeit von Konstruktionen des Stahlwasserbaus“. In *Kolloquium Korrosionsschutz und Tragfähigkeit bestehender Stahlwasserbauverschlüsse*, Bundesanstalt für Wasserbau, Karlsruhe, pp. 80–87.
- van der Tempel, J. (2006): *Design of Support Structures for Offshore Wind Turbines*. Dissertation, Technische Universiteit Delft, Delft.
- van der Tempel, J.; Zaaijer, M. B.; Subroto, H. (2004): „The effects of Scour on the design of Offshore Wind Turbines“. In *MAREC 2004: 3rd International Conference on Marine Renewable Energy*, Blyth, pp. 27–35.
- Videla, H. A.; Characklis, W. G. (1992): „Biofouling and microbially influenced corrosion“. *International Biodeterioration & Biodegradation*, **29**(3):195–212.
- Vorpahl, F.; Popko, W.; Kaufer, D. (2011): „Description of a basic model of the "Up-Wind reference jacket" for code comparison in the OC4 project under IEA Wind Annex XXX“. Technical report, Fraunhofer Institute for Wind Energy and Energy System Technology, Bremerhaven.
- Wasserstein, R. L.; Lazar, N. A. (2016): „The ASA’s Statement on p-Values: Context, Process, and Purpose“. *The American Statistician*, **70**(2):129–133.
- Webster, W. C.; Trudell, R. W. (1981): „Statistics of local motions on a ship“. In *Proceedings of Conference on Directional Wave Spectra Applications*, ASCE, Berkeley, pp. 461–482.
- Welzel, M. (2021): *Wave-current-induced scouring processes around complex offshore structures*. Dissertation, Leibniz Universität Hannover, Hannover.
- Wheeler, J. D. (1969): „Methods for Calculating Forces Produced by Irregular Waves“. In *Offshore Technology Conference*, Houston, ID OTC 1006.
- WindSeeG (2023): „Gesetz zur Entwicklung und Förderung der Windenergie auf See“. Bundesgesetz, Federal Republic of Germany.
- Winterstein, S. R. (1985): „Non-Normal Resonances and Fatigue Damage“. *Journal of Engineering Mechanics*, **111**(10):1291–1295.
- Wirsching, P. H.; Light, M. C. (1980): „Fatigue under Wide Band Random Stresses“. *Journal of the Structural Division*, **106**(7):1593–1607.
- Yang, R.-Y.; Chen, H.-H.; Hwung, H.-H.; Jiang, W.-P.; Wu, N.-T. (2010): „Scour around the Jacket Type Offshore Wind Turbine Foundation in Shallow Water“. In *Proceedings of the Twentieth (2010) International Offshore and Polar Engineering Conference*, ISOPE, Beijing, pp. 688–692.
- Zaaijer, M.; Subroto, T.; Speet, L.; Vugts, J.; van Rooij, R.; van der Kraan, M.; Kay, S.; Smith, B.; Mirza, U.; Heywood, P. (2002): „Design Methods for Offshore Wind Turbines at Exposed Sites (OWTES) – Sensitivity Analysis for Foundations of Offshore Wind Turbines“. OWTES Task 4.1, OWEC Tools Task B.1 - B.2, Delft University of Technology, Delft.

- Zhao, W.; Baker, M. J. (1990): „A New Stress-Range Distribution Model For Fatigue Analysis Under Wave Loading“. In *Environmental Forces on Offshore Structures and their Prediction*, vol. 26 of *Advances in Underwater Technology, Ocean Science and Offshore Engineering*, Society for Underwater Technology, Kluwer Academic Publishers, Dordrecht, pp. 271–291.
- Zhao, W.; Baker, M. J. (1992): „On the probability density function of rainflow stress range for stationary Gaussian processes“. *International Journal of Fatigue*, **14**(2):121–135.
- Zwick, D.; Muskulus, M. (2015): „The simulation error caused by input loading variability in offshore wind turbine structural analysis“. *Wind Energy*, **18**(8):1421–1432.

List of symbols

Roman symbols

a	Amplitude
$a_n, a_{c,n}, a_{s,n}$	Fourier coefficients
A	Cross-section area
A	Scale parameter of the Weibull distribution function
c	Current velocity
c_n	Complex Fourier coefficients
C	Autocorrelation function, cross-correlation function
C	Material parameter of SN curve
C_d	Drag coefficient of Morison's equation
C_m	Inertia coefficient of Morison's equation
\underline{C}	Damping matrix
$\underline{\hat{C}}$	Modal damping matrix
d	Water depth
D	Damping ratio
D	Fatigue damage
D	Pile diameter
D_{KL}	Kullback-Leibler divergence
E	Effects of actions
E	Wave energy
$E[g(x)]$	Expected value of the function $g(x)$
$\text{erf}((\bullet))$	Error function
f	Frequency
f, g	Functions, signals
f	Load
f_u	Ultimate strength
f_y	Yield strength
\underline{f}	Vector of loads
g	Earth's acceleration
g	Limit-state function
H	Wave height
H_b	Wave-breaking limit
H_s	Significant wave height
\underline{H}	Transfer function
i	Imaginary unit
k	Shape parameter of the Weibull distribution function
k	Wave number
\underline{K}	Stiffness matrix
$\underline{\hat{K}}$	Modal stiffness matrix

L	Wave length
\mathcal{L}	Log-likelihood function
m	Slope of SN curve
m_j	Spectral moment of order j
me	Mean-excess function
\underline{M}	Mass matrix
$\underline{\underline{M}}$	Modal mass matrix
N	Endurable number of fatigue loads
N_c	Number of peaks within a certain duration
N_z	Number of zero-up-crossings within a certain duration
p	Probability density function
p	Static pressure
P	Cumulative distribution function
P_f	Probability of failure
P_s	Survival probability
$\text{Prob}[(\bullet)]$	Occurrence probability of a certain event (\bullet)
R	Exceedance probability function
R	Resistance
s	Fatigue load
S	Power spectral density (general)
S_{ff}	Power spectral density of the function f
S_{JS}	JONSWAP spectrum
S_{PM}	Pierson-Moskowitz spectrum
\underline{S}	Matrix of power spectral densities
T	Duration, period
T	Wave period
T_c	Peak-to-peak period
T_m	Mean period
T_p	Peak period
T_z	Zero-up-crossing period
u	Threshold of the generalized extreme value distribution
u, v, w	Velocity along axes of Cartesian coordinate system x, y, z
\underline{u}	Vector of modal deformation
\underline{u}_n	Eigen vector
v	Velocity (general)
V	Dynamic amplification factor
Var_X	Variance of data set X
x, y, z	Axes of Cartesian coordinate system
X_n	Coefficients of the stream function wave theory
\underline{y}	Vector of deformation

Greek symbols

α	Power-law coefficient, wind-shear coefficient
α_j	Spectral parameter
β	Scale parameter of the generalised Pareto distribution
γ	Euler-Mascheroni constant

γ	Peak-enhancement factor of the JONSWAP spectrum
γ_3	Skewness of a data set
γ_4	Kurtosis of a data set
$\Gamma((\bullet))$	Gamma function
$\delta((\bullet))$	Dirac function
ϵ	Spectral width parameter
η	Water-surface elevation
μ	Location parameter of the generalized extreme value distribution
μ_X	Mean value of data set X
ξ	Shape parameter of the generalized extreme value distribution
ξ	Shape parameter of the generalised Pareto distribution
ρ	Density of a medium or material
σ	Scale parameter of the generalized extreme value distribution
σ_X	Standard deviation of data set X
τ	Time lag
φ	Phase angles
Φ	Velocity potential
Ψ	Stream function
ω	Wave frequency
ω_n	Eigen frequency
ω_p	Peak frequency

Abbreviations

CoV	Coefficient of variance
DEL	Damage-equivalent load
DLC	Design load case
GEV	Generalized extreme value distribution
GPD	Generalised Pareto distribution
LCC	Level-crossing counting
MSL	Mean sea level
NB	Narrow-band process
PC	Peak counting
PSD	Power spectral density
RC	Range counting
RFC	Rainflow counting
RL	Run length

List of Figures

1.1	Offshore wind turbines with monopile substructure and jacket substructure	2
1.2	Offshore wind turbines of the offshore wind park alpha ventus ©FuE-Zentrum FH Kiel GmbH	2
2.1	Aliasing effect of a sinusoidal wave	10
2.2	Graphical methods for estimation of distribution functions, here for normal-distributed values with mean of zero and standard deviation of unity: histogram, Q-Q plot, P-P plot, Kolmogorov-Smirnov test	16
3.1	Wind field consisting of a vertical wind-shear profile and turbulence (adapted from Hau (2013))	24
3.2	Definition of wave properties	26
3.3	Selection of the applicable wave theory for regular waves (DNV-RP-C205, 2019)	27
3.4	Wheeler stretching of water-particle kinematics (Wheeler, 1969)	28
3.5	Pierson-Moskowitz spectrum and JONSWAP spectrum with $H_s = 2\text{ m}$ and $T_p = 5\text{ s}$	31
3.6	Periodic function $u \cdot u $ with $u = c + a_u \cdot \cos(-\omega \cdot t)$ and corresponding Fourier coefficients normalised by the respective value for the base wave frequency ω for different ratios of constant current c to amplitude of sinusoidal wave a_u	33
3.7	Fourier coefficients of the function $u \cdot u $ with $u = c + a_u \cdot \cos(-\omega \cdot t)$ in dependence of the ratio of constant current c to amplitude of sinusoidal wave a_u , here with $a_u = 1$, referring to Eq. (A3.5)	34
3.8	Normalised power spectral density of the horizontal water-particle velocity as well as its n -fold convolutions and the normalised power spectral density of the drag force according to Eq. (3.21) for different current velocities	36
3.9	Coefficients of n -fold convolutions of the horizontal water-particle velocity for the power spectral density of the drag force according to Eq. (3.21)	36
3.10	Load regimes of horizontal load at water-surface elevation of regular Airy waves in deep water for different current velocities	38
3.11	Load regimes of horizontal load at water-surface elevation of linear sea states in deep water for different current velocities	39
3.12	Monthly statistical properties at the research platform FINO1 for wind velocity at 90 m above mean sea level and significant wave height summarised for the years 2004 to 2016	41

3.13	Monthly data availability at the research platform FINO1 for wind velocity at 90 m above mean sea level, significant wave height, and peak period for the years 2003 to 2017	42
3.14	Daily data availabilities at the research platform FINO1 for wind velocity at 90 m above mean sea level, significant wave height, and peak period summarised for the years 2004 to 2016	43
3.15	Scatter tables of significant wave height and wind velocity at 90 m above mean sea level and of significant wave height and peak period	44
3.16	Thicknesses of marine growth at the research platform FINO1 and at offshore wind turbines R1, R6, M7, and M12 of the offshore wind park alpha ventus for different depths below mean sea level as well as respective photographs of marine growth, observed at alpha ventus, adapted from Preuß et al. (2012)	46
3.17	Scour at jacket and monopile substructures (van der Tempel et al., 2004) and overburden reduction depth determination for global and local scour according to API RP 2GEO (2014)	48
3.18	Uniform corrosion, irregular corrosion, and pitting corrosion	50
3.19	Corroded steel specimen covered by calcareous remains of the barnacles and the measured profile of its surface after removal of the calcareous remains of the barnacles and of the corrosion products	51
4.1	Classification of load types: constant, periodic, random, transient, and random transient	56
4.2	Campbell diagram for a three-bladed wind turbine, with an exemplary range of first bending Eigen frequencies for offshore wind turbines and of rotor speeds	58
4.3	Dynamic amplification factor for different damping ratios	69
5.1	Idealised stress-strain curve for a steel probe	72
5.2	Probability density functions of peak values and Q-Q plots of extreme peaks obtained by different integration limits of the power spectral density for a duration of 600 s	77
6.1	Influencing factors on SN curves of steel (adapted from Gudehus and Zenner (1999))	84
6.2	SN curve with detail category of 90 MPa and probability density function of the detail category	85
6.3	Stress-strain relationship for a single load cycle and for a random load time series	85
6.4	Example of rainflow-counting algorithm	86
6.5	Scheme for the verification against fatigue damage by means of SN curves	90
6.6	Weightings and parameters for the distribution function of fatigue loads according to Eq. (6.7) (Dirlik, 1985) in dependence of α_1 and α_2	94
6.7	Weightings for the distribution function of fatigue loads according to Eq. (6.9) and Eq. (6.11) (Benasciutti and Tovo, 2005b) in dependence of α_1 and α_2	95

6.8	Coefficients for the newly-developed distribution function of fatigue loads according to Eq. (6.12) in dependence of α_1 and α_2 : weightings of Rayleigh distribution functions and scale parameter of the second Rayleigh distribution function	96
6.9	Types of power spectral densities used for derivation of distribution functions of fatigue loads	98
6.10	Pairings of α_1 and α_2/α_1 and pairings of $\alpha_{0.75}$ and $\alpha_2/\alpha_{0.75}$ used for the derivation of different theoretical distribution functions of fatigue loads .	100
6.11	Examples of time series for different pairings of α_1 and α_2/α_1	102
6.12	Simulated reverse cumulative distribution functions of fatigue loads for various pairings of α_1 and α_2	103
6.13	Relative minima and relative maxima as well as coefficients of variance of the fatigue damage of the five time series simulated for each pairing of α_1 and α_2 , with the slope of the SN curve of $m = 4$	104
6.14	Relative minima and relative maxima as well as coefficients of variance of the fatigue damage of the five time series simulated for each pairing of α_1 and α_2 , with the slope of the SN curve of $m = 4$, for the fatigue loads up to the 99.9%-quantile	105
6.15	Simulated and analytical reverse cumulative distribution functions of fatigue loads for various pairings of α_1 and α_2	107
6.16	Error of different analytical reverse cumulative distribution functions according to Eq. (6.16) in dependence of α_1 and α_2	108
6.17	Error of different analytical reverse cumulative distribution functions according to Eq. (6.16) with a non-exceedance probability less than 0.01 in dependence of α_1 and α_2	109
6.18	Ratio of analytical fatigue damage to simulated fatigue damage in dependence of α_1 and α_2 , with the slope of the SN curve of $m = 4$	110
6.19	Ratio of analytical fatigue damage to simulated fatigue damage in dependence of α_1 and α_2 , with various values for the slope of the SN curve	112
7.1	Equidistant and equienergetic discretisation of a power spectral density and the respective discrete amplitudes for the inverse Fourier transformation	118
7.2	Autocorrelation function for different approaches of the inverse Fourier transformation	119
7.3	Spectral moments and spectral width parameter in dependence of the right integration limit of Eq. (2.7)	120
7.4	Kullback-Leibler divergences of bending moments acting on a monopile at seabed obtained by different approaches of the inverse Fourier transformation for a duration of 10,800 s	124
7.5	Kullback-Leibler divergences of bending moments acting on a monopile at seabed obtained by different approaches of the inverse Fourier transformation for a duration of 150 s	124
7.6	Mean run lengths for narrow-band power spectral density and for broadband power spectral density obtained by different approaches of the inverse Fourier transformation for a duration of 10,800 s	125

7.7	Distribution of run lengths for narrow-band power spectral density and for broad-band power spectral density obtained by different approaches of the inverse Fourier transformation for a duration of 10,800 s	126
7.8	Parameters for the generalized extreme value distribution of maximum bending moments acting on a monopile at seabed obtained by different approaches of the inverse Fourier transformation	128
7.9	Parameters for the generalized extreme value distribution of maximum bending moments acting on a monopile at seabed obtained by different integration limits of the power spectral density	129
7.10	Frequency densities of fatigue bending moments obtained by different approaches of the inverse Fourier transformation	130
7.11	Number of cycles of fatigue bending moments obtained by different approaches of the inverse Fourier transformation	131
7.12	Frequency densities and cumulative distribution functions of fatigue bending moments obtained by different integration limits of the power spectral density	132
7.13	Number of cycles of fatigue bending moments obtained by different integration limits of the power spectral density	132
7.14	Parameters for the generalised Pareto distribution of the fatigue bending moments and the respective p -values obtained by different approaches of the inverse Fourier transformation	134
7.15	Parameters for the generalised Pareto distribution of the fatigue bending moments and the respective p -values obtained by different approaches of the inverse Fourier transformation	135
8.1	Jacket substructure with tubular K-joints analysed and tubular K-joint	138
8.2	Q-Q plots of stresses at the analysed tubular K-joint, assuming a Gaussian distribution: original data as well as transferred to Gaussian signal	139
8.3	Comparison of spectral parameters α_1 and α_2 as well as of the resulting damage-equivalent load, obtained with different approaches, for the analysed tubular K-joint	140
8.4	Power spectral densities of all time series transferred to Gaussian signals for the analysed tubular K-joint	140
8.5	Comparison of spectral moments m_n of order n as well as of the zero-upcrossing periods T_z and the peak-to-peak periods T_c , obtained by means of different approaches, for the analysed tubular K-joint	141
8.6	Comparison of spectral width parameters ϵ as well as of the resulting mean values and standard deviations of the distribution functions of extreme values, obtained with different approaches, for the analysed tubular K-joint	143
8.7	Q-Q plot for the distribution functions of extreme values determined on the basis of spectral moments calculated from the derivatives for the analysed tubular K-joint	144
8.8	Comparison of spectral parameters α_1 and α_2 as well as of the resulting damage-equivalent load, obtained with different approaches, for the analysed tubular K-joint	146

8.9	Power spectral densities of the wave-induced stresses at the analysed tubular K-joint for different current velocities, obtained from static load simulations	148
8.10	Power spectral densities of the wave-induced stresses at the analysed tubular K-joint for different current velocities, obtained from structural-dynamic load simulations	149
A2.1	Scheme of electrolytic bath for removal of corrosion products	188
A2.2	Surface of the steel specimen before removal of the adhesive corrosion products	188
A2.3	Surface of the steel specimen before and after applying different methods for removal of adhesive corrosion products according to Tbl. A2.1	189
A2.4	Sections measured at the surface of the steel specimen	190
A2.5	Measured surface topologies at the surface of the steel specimen	190
A2.6	Power spectral densities of the measured surface topologies at the surface of the steel specimen	191
A2.7	Measured surface topologies and the respective power spectral densities at the surface of the steel specimen for different measurement methods .	192
A3.1	Pulse wave with $\Theta = \frac{T}{3}$ and the respective Fourier coefficients	195
A3.2	Periodic function according to Eq. (A3.3) with $a = \frac{1}{2}$ and $b = 1$ and the respective Fourier coefficients	197

List of Tables

3.1	Yearly data availability at the research platform FINO1 for wind velocity at 90 m above mean sea level, significant wave height, and peak period for the years 2003 to 2017	42
4.1	Definition of consequences classes and their associated probabilities of failures according to DIN EN 1990 (2010)	54
4.2	Design load cases for the design of support structures of offshore wind turbines according to IEC 61400-3-1 (2019) and associated load types	60
5.1	Statistical properties of the extreme values of a power spectral density, of its discrete power spectral density, and of respective time series for different discretisation types	78
6.1	Mean fatigue damage per load cycle of various distribution functions of fatigue loads for linear SN curve according to Eq. (6.1)	96
7.1	Spectral properties of a power spectral density, of its discrete power spectral density, and of respective time series for different integration limits	121
8.1	Impact of currents on the zeroth-order spectral moments and on the damage-equivalent loads for the analysed tubular K-joint for static and structural-dynamic load simulations	150
A1.1	Joint probability of significant wave height and peak period for the year 2013, measured at the research platform FINO1	184
A1.2	Joint probability of significant wave height and wind velocity for the year 2013, measured at the research platform FINO1	185
A2.1	Overview of methods consecutively applied in order to remove corrosion products from the steel specimen as well as the respective periods of exposure	189
A4.1	Coefficients of the power spectral densities according to Eq. (6.15) and Fig. 6.9(h) applied for analysis of distribution functions of fatigue loads	199

A1 Reference design basis: environmental data

The research platform FINO1 was erected about 40 *km* north of the East Frisian island Borkum in the North Sea. The local water depth at the considered site is about 28 *m*. Today, it is located close to several German offshore wind parks, including the first German offshore wind park alpha ventus. Data are measured since autumn 2003.

Environmental data measured at the research platform FINO1 are used as reference environmental conditions for the analysis carried out within this thesis. These environmental conditions include parameters of wind conditions and of sea-state conditions. Data series for the years 2003 to 2017 are evaluated. The environmental data measured at the research platform FINO1 are kindly provided by the Bundesamt für Seeschifffahrt und Hydrographie (BSH, Federal Maritime and Hydrographic Agency). The research project FINO is funded by the German Federal Ministry for the Environment, Nature Conservation and Nuclear Safety (BMU) and the Project Management Jülich (PtJ).

The levels of technical availability of the various measurement sensors and thus the completeness of measurement data differ due to various reasons. An overview of the data completeness of wind velocity at a height of 90 *m* above mean sea level, significant wave height, peak period as well as their joint availabilities for the years 2003 to 2017 are shown in Tbl. 3.1.

A1.1 H_s - T_p scatter diagram

Only the year with the greatest level of completeness is analysed to ensure an accurate representation of seasonal effects which may be biased by additionally considering years with smaller level of completeness. Hence, the year 2013 is analysed for the derivation of the scatter diagram of significant wave height and peak period. The combined completeness rate is 97.3%, referring to Tbl. 3.1.

A1.2 v - H_s scatter diagram

Just as for the H_s - T_p scatter diagram, stated in Tbl. A1.1, only the year with the greatest level of completeness is analysed to ensure an accurate representation of seasonal effects. Hence, the year 2013 is analysed for the derivation of the scatter diagram of significant wave height and wind velocity at a height of 90 *m* above mean sea level. The combined completeness rate is 88.4%, referring to Tbl. 3.1.

Table A1.1: Joint probability of significant wave height and peak period (H_s - T_p scatter diagram) for the year 2013, measured at the research platform FINO1

Significant wave height [m]	Peak period [s]																			Σ	
	2.0...3.0	3.0...4.0	4.0...5.0	5.0...6.0	6.0...7.0	7.0...8.0	8.0...9.0	9.0...10.0	10.0...11.0	11.0...12.0	12.0...13.0	13.0...14.0	14.0...15.0	15.0...16.0	16.0...17.0	17.0...18.0	18.0...19.0	19.0...20.0	20.0...21.0		21.0...22.0
0.0...0.5	103	222	254	177	101	67	57	82	117	98	52	32	17	13	5						1,397
0.5...1.0	40	586	1,169	1,008	906	400	222	153	269	164	150	63	55	41	29						5,255
1.0...1.5		44	742	1,258	712	502	170	105	111	75	64	25	27	17	7	2					3,861
1.5...2.0			88	728	1,019	600	318	78	71	40	20	5	1								2,968
2.0...2.5			1	90	639	506	331	89	39	12	8			2	1	2	1				1,721
2.5...3.0				7	237	395	222	70	31	21	15			1	1						1,000
3.0...3.5					61	223	112	75	27	6	2										506
3.5...4.0					4	39	33	27	32	6	5	1	1			1					149
4.0...4.5							15	12	26	6	4										63
4.5...5.0						1	4	10	8	2				1							27
5.0...5.5							1	2	5	2	4										14
5.5...6.0							1		3	4	1										9
6.0...6.5								3	3	4	3	1									14
6.5...7.0									2	3	8	1									14
7.0...7.5										1	1	2	2	3	2						11
7.5...8.0											2	1		5							8
8.0...8.5											4	2	6	4							16
8.5...9.0												3	3	2							8
9.0...9.5																					
9.5...10.0												1									1
Σ	143	852	2,254	3,268	3,679	2,733	1,486	706	744	444	343	137	112	89	45	5	1				1

Table A1.2: Joint probability of significant wave height and wind velocity at a height of 90 m above mean sea level ($v-H_s$ scatter diagram) for the year 2013, measured at the research platform FINO1

Significant wave height [m]	Wind velocity at 90 m above mean sea level [m/s]												Σ		
	4.0...6.0	6.0...8.0	8.0...10.0	10.0...12.0	12.0...14.0	14.0...16.0	16.0...18.0	18.0...20.0	20.0...22.0	22.0...24.0	24.0...26.0	26.0...28.0		28.0...30.0	30.0...32.0
0.0...0.5	371	221	127	37	30	7	1								1,375
0.5...1.0	1,287	1,265	719	353	182	78	31	11	2						4,998
1.0...1.5	579	709	816	648	294	92	24	11	1						3,456
1.5...2.0	238	366	389	546	611	321	53	14	3						2,664
2.0...2.5	36	158	192	200	324	301	147	39	12	3					1,438
2.5...3.0	14	18	67	81	108	217	186	95	46	12	1				849
3.0...3.5	1	7	13	22	26	67	127	98	45	18	4				428
3.5...4.0		6	2	9	11	9	20	24	16	15	7				119
4.0...4.5		3	4	14	5	5	7	4	4	4	3	1			54
4.5...5.0			1	4		2	1		2	6	2	2			20
5.0...5.5				2		1	2	1	1	1	4		2		13
5.5...6.0				1	2		1		1	1				1	7
6.0...6.5				1	3	1			1	1	2			4	13
6.5...7.0					5	1		4	1	2	1				14
7.0...7.5					4	5	1		1						11
7.5...8.0					2		5		1						8
8.0...8.5						4	6	3	2		1				16
8.5...9.0							2	3	2	1					8
9.0...9.5															
9.5...10.0									1						1
Σ	2,526	2,753	2,330	1,918	1,607	1,111	614	307	142	63	25	3	2	5	

A2 Removal of corrosion products from small steel specimens

Due to the environmental conditions, corrosion of material may occur. For steel specimens or steel structures, corrosion products such as iron oxid are produced within the chemical corrosion process. Iron oxid or rust is usually attached to the steel surface. In order to analyse the steel surface hidden by the rust, the iron oxid has to be removed. Different methods exist which are described in the following for a small steel specimen. Iron oxid does not contribute to the load-bearing capacity of the steel specimen.

A2.1 Methods for removal of corrosion products from steel

Three methods to remove corrosion products from steel specimens are shortly listed in the following. They are suitable for small-scale specimens such that the procedure can be completed in laboratory. The required amount of time for removal depends on the size of the specimen and on the severity of corrosion.

A2.1.1 Removal with paraffine

Oils, such as paraffine, penetrate between the steel surface and the adhesive corrosion products due to their comparably small interfacial surface tension. Thus, the corrosion products can be removed more easily with cloth and brushes. No hard tools shall be used for cleaning, which might cause damage to the steel surface. The corroded specimen is wetted with paraffine up to several days. The specimen is occasionally cleaned. Several repetitions of the procedure might be necessary.

A2.1.2 Removal with acids

A faster method to remove corrosion products is the usage of acid instead of paraffine. The rate of the removal depends on the acidity of the acid. For example, placing a corroded specimen in 10% hydrochloride acid requires up to 30 minutes for removal. Using customary 10% acetic acid instead, several hours up to a day may be necessary. One shall consider that acid may not only remove the corrosion products, but it may also attack the uncorroded steel surface, resulting in its alteration.

A2.1.3 Removal with electrolytic bath

Another method to remove corrosion products from steel specimen is the electrolysis. Here, the specimen as well as an anode are placed in water with dissolved sodium hydrogen carbonate. A battery is connected to the steel specimen and the anode, with the specimen being the cathode. The specimen and the anode shall not be directly in contact. The battery assembly and the sodium hydrogen carbonate solution form a closed circuit. Due to the current, the corrosion products are removed and accumulate at the anode. The electrolysis takes several hours to a day for removal, depending on the size of the specimen. The principle of the electrolytic bath is sketched in Fig. A2.1.

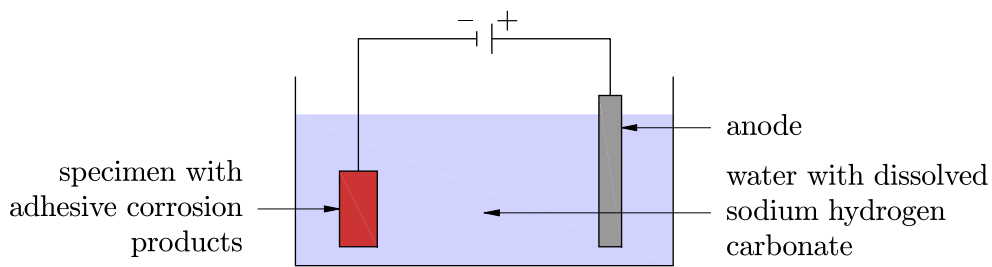


Figure A2.1: Scheme of electrolytic bath for removal of corrosion products

A2.2 Removal of corrosion products from a steel specimen

The adhesive corrosion products at a corroded steel specimen shall be removed. The cuboid specimen has the dimensions of $50\text{ mm} \times 25\text{ mm} \times 10\text{ mm}$. It was exposed to the weather for an indefinite period in 30167 Hannover. Then it was stored in dry conditions at room temperature. The steel grade is also unknown. The surface of the corroded steel specimen is shown in Fig. A2.2.

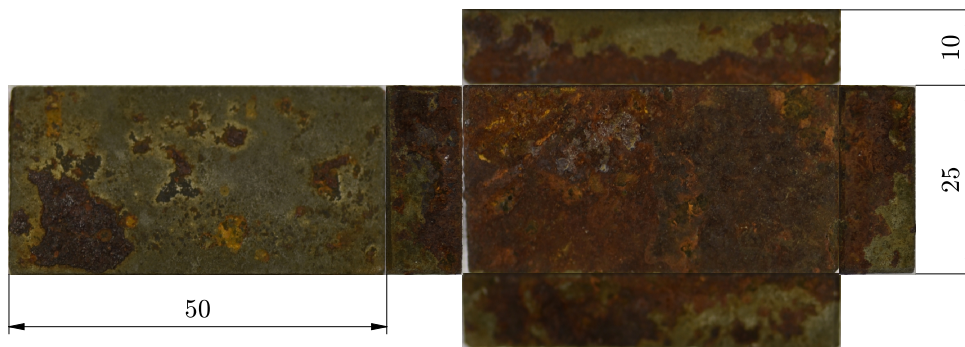


Figure A2.2: Surface of the steel specimen before removal of the adhesive corrosion products

The methods described above were applied to remove the corrosion products from the steel specimen. The order, applied methods, and the respective periods of exposure are listed in Tbl. A2.1

During the wetting with paraffine (stage 1), each side of the cuboid specimen was wetted during the period of two weeks. The specimen was cleaned every two to three days to remove detached corrosion products. Afterwards, the specimen was exposed

Table A2.1: Overview of methods consecutively applied in order to remove corrosion products from the steel specimen as well as the respective periods of exposure

Stage	Method for corrosion removal	Duration of exposure
1	Paraffine	Two weeks
2	10% acetic acid	19 hours
3	10% acetic acid	Two weeks
4	Electrolytical bath	Two days
5	Electrolytical bath	19 hours
6	Electrolytical bath	24 hours

to 10% acetic acid for 19 hours (stage 2) and two weeks (stage 3), respectively. For stage 1 to 3, the steel specimen was placed in a closed glass container. Further removal of the corrosion products was done via electrolysis (stage 4 to 6). Approximately 3 g of sodium hydrogen carbonate was dissolved in 0.2 l water. The steel specimen and the anode were connected to a 9-volt block battery. They were placed in the electrolytical bath for two days, 19 hours, and 24 hours, respectively. The electrolysis was carried out in an aerated room at room temperature.

The surface of the steel specimen before removal of corrosion products, after exposure to paraffine and 10% acetic acid (stage 3), and after the subsequent electrolysis (stage 6) are shown in Fig. A2.3. Only the surface investigated in the following are shown.

**Before removal of
corrosion products**

After stage 3

After stage 6

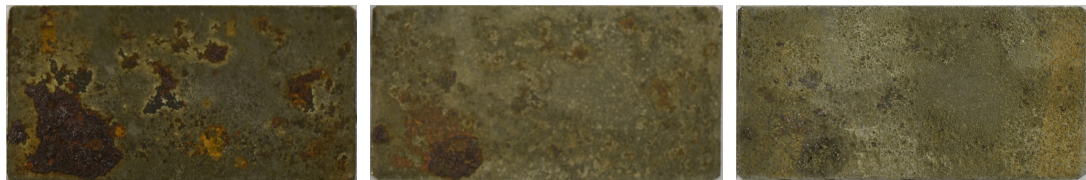


Figure A2.3: Surface of the steel specimen before and after applying different methods for removal of adhesive corrosion products according to Tbl. A2.1

A2.2.1 Surface topology of the steel specimen

In order to evaluate the possible impact of the methods to remove corrosion products on the steel specimen, the surface topology of the steel specimen was measured after each stage listed in Tbl. A2.1. Here, the roughness-measurement device *HOMMEL TESTER 1000* by *JENOPTIC* is used. A needle is moved over the surface along a defined section, whilst the vertical deflection of the needle is piezoelectrically recorded. Here, the sampling rate along the measured sections is 0.6 1/ μm . The measured sections, each with a length of 16 mm, are shown in Fig. A2.4. The distance from horizontal edges to the measured section, here 8.3 mm, is complied for each measurement. However, the distance from vertical edges to the starting point of the measured section cannot be assured. A possible deviation of a few tenth millimeters is expected.

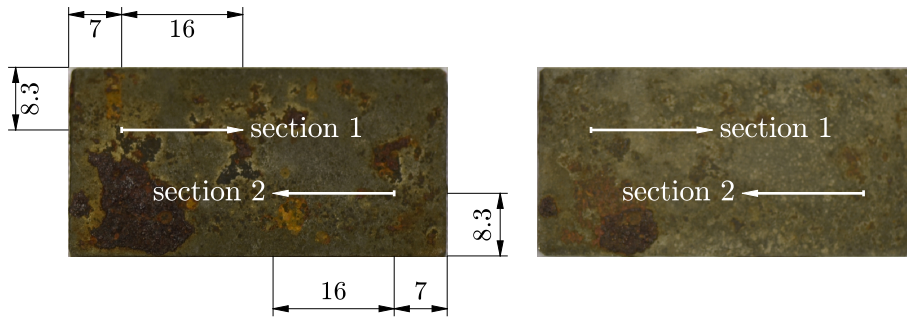


Figure A2.4: Sections measured at the surface of the steel specimen

Each section as shown in Fig. A2.4 is measured thrice after each applied method for removal of corrosion products (stage 1 to 6) in order to detect potential errors. Here, no significant differences or errors are found for the repeated measurements.

The measured surface topologies were processed such that they are almost congruent. This is necessary, since the horizontal position of the starting point of the measured section cannot be assured as explained above. Therefore, the cross-correlation of the measured surface topology of stage 1 and each measured surface topology (stage 2 to 6) are evaluated for an offset between the measured surface topologies of up to 1.6 mm. The measured profiles are shifted by the value at which the cross-correlation factor is maximal. Thus, it is assumed that the spatial positions of the measured sections are approximately congruent. The measured surface topologies, shifted as described above, are shown in Fig. A2.5 for both measurement sections and all stages as listed in Tbl. A2.1.

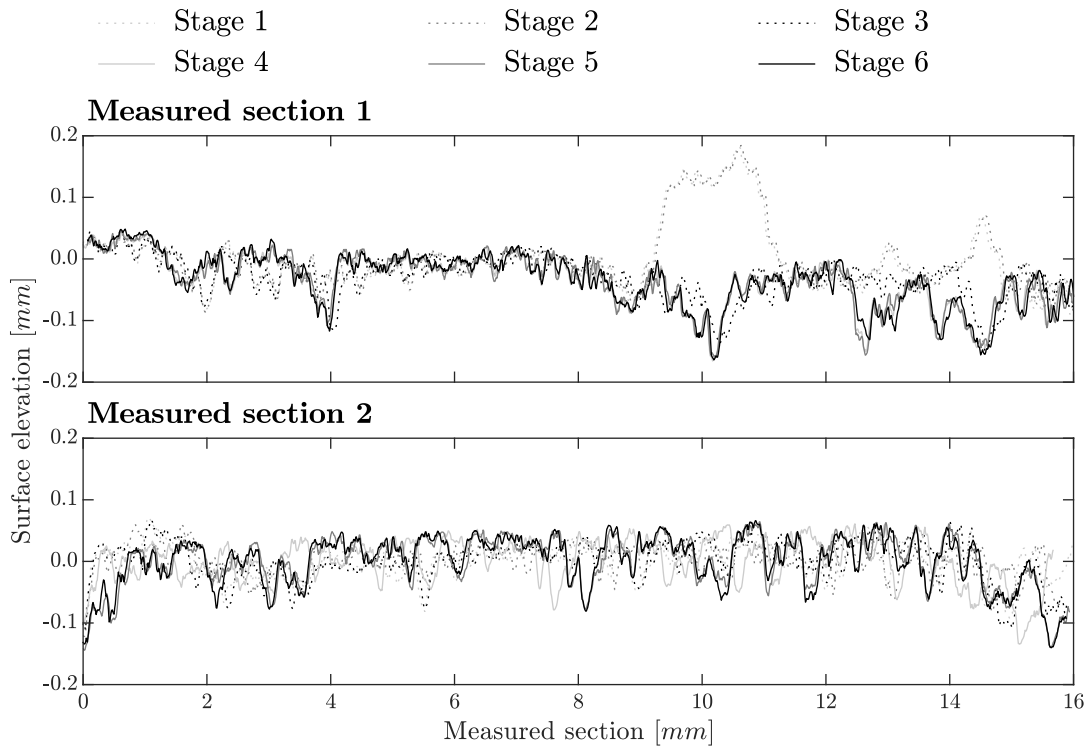


Figure A2.5: Measured surface topologies at the surface of the steel specimen (section 1 and section 2)

Almost no differences between the surface topologies are observed for the measured section 1. For the measured section 2, no differences are observed for stage 1 and 2, either. In comparison to stage 3 to 6, major differences are detected between 9 mm and 11 mm as well as between 14 mm and 15 mm. Smaller differences are noticed at approximately 4 mm and 13 mm. These differences stem from corrosion products which are detached from the steel surface after stage 3. This can be noted by comparing the steel surfaces in Fig. A2.5. Otherwise, the surface topologies of all stages are almost congruent.

A2.2.2 Power spectral densities of the surface topology of the steel specimen

Fourier transformation of the measured signals are carried out according to Section 2.1.1. The resulting power spectral densities were adapted such that the integral of each power spectral density with respect to the wave number equals the respective variance. Due to the sampling rate of $0.6 \text{ 1}/\mu\text{m}$, the power spectral densities of the surface topologies are given for wave numbers smaller than the corresponding Nyquist wave number of approximately $1.885 \text{ 1}/\mu\text{m}$.

The resulting power spectral densities of the sections measured after each stage are shown in Fig. A2.6.

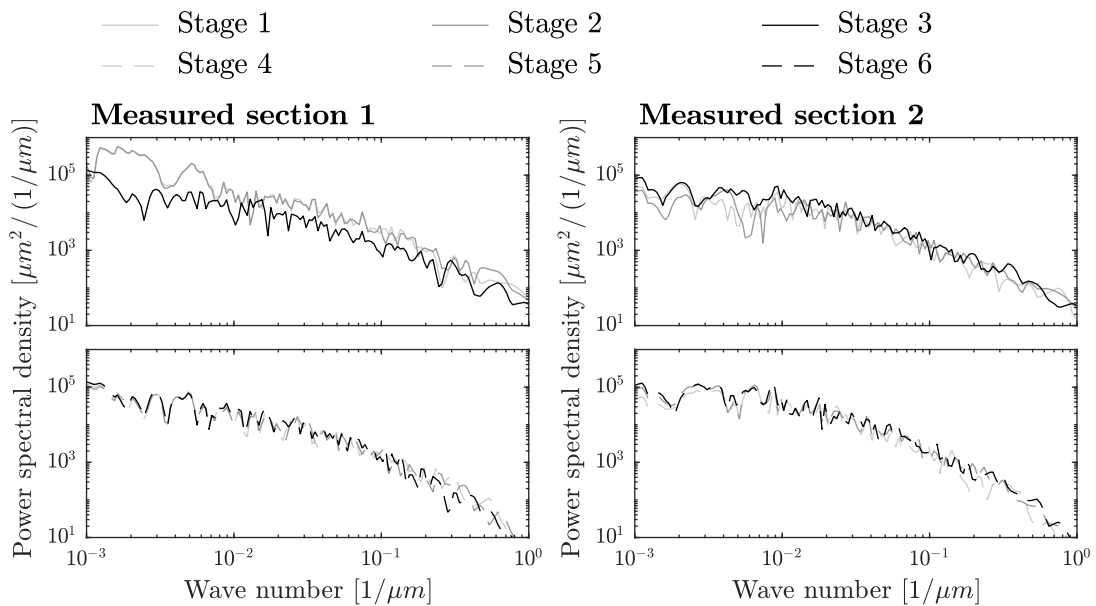


Figure A2.6: Power spectral densities of the measured surface topologies at the surface of the steel specimen (section 1 and section 2)

For the measured section 1, discrepancies are observed for stage 1 and 2 in comparison to the stages 3 to 6. Otherwise, the curves do not have noticeable differences. Noticeably greater values of the power spectral densities for stage 1 and 2 exist for wave numbers of $1 \text{ 1}/\text{mm}$ up to $3 \text{ 1}/\text{mm}$ as well as for wave numbers of $4 \text{ 1}/\text{mm}$ up to $7 \text{ 1}/\text{mm}$. These wave numbers are approximately equivalent to the ranges of adhesive corrosion products which were removed only after completion of stage 3. These adhesive corrosion products

were located in the ranges of 9 mm and 11 mm as well as of 14 mm and 15 mm, referring to Fig. A2.5.

No significant differences are noticed when comparing the power spectral densities after each stage for the measured section 2.

In comparison, the power spectral densities after completion of stage 6 are almost congruent for both measured sections.

A2.2.3 Impact of different measurement methods

For a comparison of different measurement devices, the surface of the specimen is additionally measured and analysed with an optical 3D-measuring system after the last stage of corrosion removal. Here, the 3D-profilometer *VR-3200* by *KEYENCE* is used, which measures the complete surface optically. The surface is measured with a sampling rate of approximately $31.8 \text{ 1}/\mu\text{m}$. The surface topologies for the measured sections as shown in Fig. A2.5 are extracted from the three-dimensional data by interpolation. The surface topologies (right) as well as the respective power spectral densities (right) are shown in Fig. A2.7 for both measured sections.

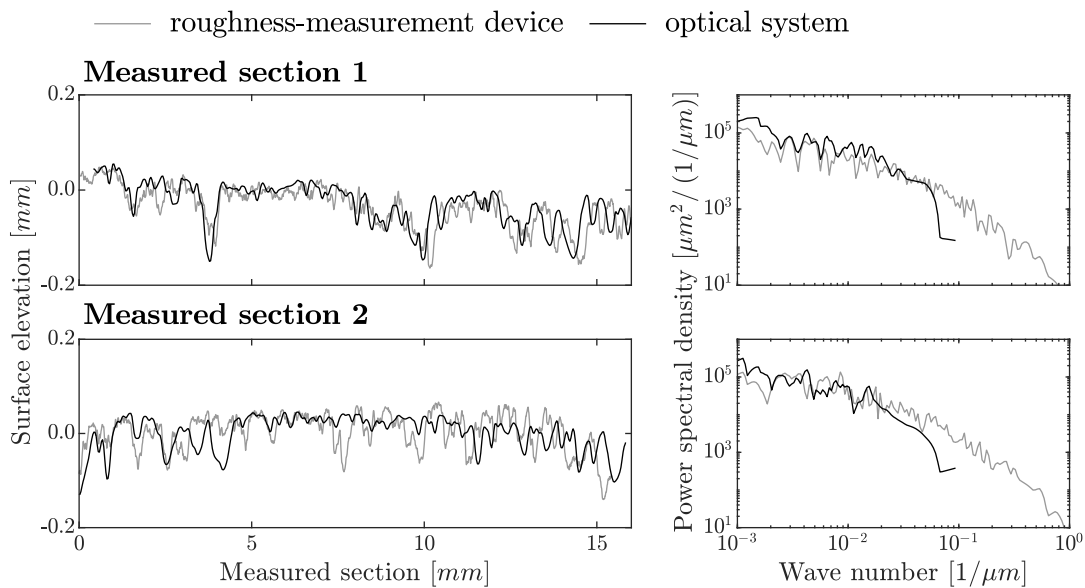


Figure A2.7: Measured surface topologies (left) and the respective power spectral densities (right) at the surface of the steel specimen (section 1 and section 2) for different measurement methods

The surface topologies measured by either roughness-measurement device or optical system are almost congruent for both measured sections. Due to the greater sampling rate of the optical system, the inverse Fourier transformation of the surface topologies and the respective power spectral density only are valid for wave numbers smaller than the corresponding Nyquist wave number of approximately $99.8 \mu\text{m}$. Otherwise, a good agreement of the power spectral densities with respect to the measurement method is observed for both measured sections.

A2.3 Conclusion

In order to evaluate the surface of a corroded steel specimen, the removal of adhesive corrosion products is necessary. Different methods for corrosion removal exist. Tests show that placing the corroded steel specimen in acid or in an electrolytical bath is an effective method. The measurement of the surface after removal of corrosion products with a roughness-measurement device indicates that these methods only remove the corrosion products, but they do not impair the steel surface. The measuring methods provide similar results.

A3 Fourier series of relevant functions

Relevant Fourier series are presented here. Fourier transformation of the signals are carried out according to Section 2.1.1.

A3.1 Fourier coefficients of a pulse wave

The pulse wave denotes a periodic signal which alternates between two values (here 1 and -1) periodically,

$$f_{\Theta}(t) = \begin{cases} 1 & , t \in \left[\left(z - \frac{1}{2} \right) \cdot T + \Theta/2, \left(z + \frac{1}{2} \right) \cdot T - \Theta/2 \right] \\ -1 & , t \in \left(\left(z + \frac{1}{2} \right) \cdot T - \Theta/2, \left(z + \frac{1}{2} \right) \cdot T + \Theta/2 \right) \end{cases}, z \in \mathbb{Z}, \quad (\text{A3.1})$$

with period T . The parameter $\Theta \in [0, T]$ is the length for which the function $f_{\Theta}(t)$ has a value -1 during one period. For $\Theta = \frac{T}{2}$, the lengths are equal. This form of Eq. (A3.1) is usually denoted as square wave. The coefficients of the double-sided Fourier series are obtained by the Fourier transformation of $f_{\Theta}(t)$,

$$\begin{aligned} a_0 &= 1 - 2 \cdot \frac{\Theta}{T} \\ a_n &= \frac{2}{n \cdot \pi} \cdot (-1)^{n+1} \cdot \sin \left(\frac{1}{2} \cdot \omega \cdot \Theta \right), \\ b_n &= 0 \end{aligned} \quad (\text{A3.2})$$

with wave frequency $\omega = \frac{2\pi}{T}$. The pulse function with $\Theta = \frac{1}{3} \cdot T$ and the respective Fourier coefficients are shown in Fig. A3.1.

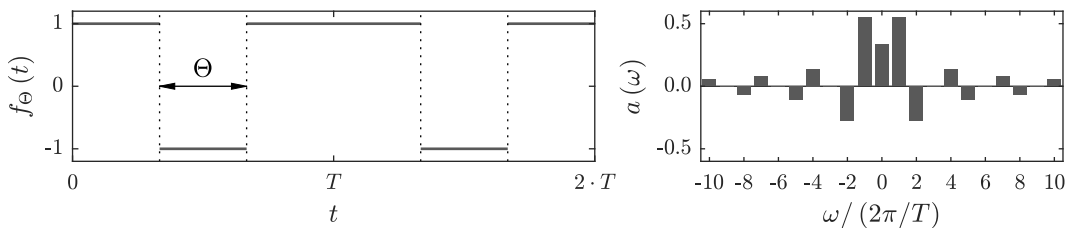


Figure A3.1: Pulse wave with $\Theta = \frac{T}{3}$ (left) and the respective Fourier coefficients (right)

A3.2 Fourier coefficients of non-linear drag term of Morison's equation for regular Airy waves

The function $f_{u|u|}(t)$ stated in Eq. (A3.3) is a term of the drag term of Morison's equation according to Eq. (3.19) for regular Airy waves,

$$\begin{aligned} f_{u|u|}(t) &= (a + b \cdot \cos(\omega \cdot t)) \cdot |a + b \cdot \cos(\omega \cdot t)| \\ &= (a + b \cdot \cos(\omega \cdot t))^2 \cdot f_{\Theta}(t) \end{aligned} \quad (\text{A3.3})$$

with wave frequency $\omega = \frac{2\pi}{T}$, wave period T , and the pulse wave $f_{\Theta}(t)$ according to Eq. (A3.1). The value of Θ is set such that the change of sign for both functions $f_{u|u|}(t)$ and $f_{\Theta}(t)$ occurs simultaneously. Hence, $\Theta = T - \frac{T}{\pi} \cdot \arccos(-\frac{a}{b})$ for $|a| < |b|$. For $|a| \geq |b|$, no change of sign occurs. Hence, $f_{\Theta}(t) = -1$ with $\Theta = T$ for $|a| \geq |b| \wedge a < 0$, and $f_{\Theta}(t) = 1$ with $\Theta = 0$ for $|a| \geq |b| \wedge a > 0$. The coefficients of the Fourier series are obtained either by Fourier transformation of $f_{u|u|}(t)$ or by convolution of the Fourier coefficients of $(a + b \cdot \cos(t))^2$ and of $f_{\Theta}(t)$,

$$\begin{aligned} a_0 &= \left(a^2 + \frac{b^2}{2}\right) \cdot \left(1 - 2 \cdot \frac{\Theta}{T}\right) + a \cdot b \cdot \frac{4}{\pi} \cdot \sin\left(\pi \cdot \frac{\Theta}{T}\right) - \frac{b^2}{2\pi} \cdot \sin\left(2\pi \cdot \frac{\Theta}{T}\right) \\ a_1 &= \frac{2}{\pi} \cdot \left(a^2 + \frac{b^2}{2}\right) \cdot \sin\left(\pi \cdot \frac{\Theta}{T}\right) + a \cdot b \cdot \left(1 - 2 \cdot \frac{\Theta}{T} - \frac{\sin\left(2\pi \cdot \frac{\Theta}{T}\right)}{\pi}\right) + \\ &\quad \frac{b^2}{2} \cdot \left(\frac{\sin\left(\pi \cdot \frac{\Theta}{T}\right)}{\pi} + \frac{\sin\left(3\pi \cdot \frac{\Theta}{T}\right)}{3\pi}\right) \\ a_2 &= -\left(a^2 + \frac{b^2}{2}\right) \cdot \frac{\sin\left(2\pi \cdot \frac{\Theta}{T}\right)}{\pi} - 2 \cdot a \cdot b \cdot \left(\frac{\sin\left(\pi \cdot \frac{\Theta}{T}\right)}{\pi} + \frac{\sin\left(3\pi \cdot \frac{\Theta}{T}\right)}{3\pi}\right) + \\ &\quad \frac{b^2}{4} \cdot \left(1 - 2 \cdot \frac{\Theta}{T} - \frac{\sin\left(4\pi \cdot \frac{\Theta}{T}\right)}{2\pi}\right) \\ a_n &= \frac{2 \cdot (-1)^{n+1}}{\pi} \cdot \left(\left(a^2 + \frac{b^2}{2}\right) \cdot \frac{\sin\left(n \cdot \pi \cdot \frac{\Theta}{T}\right)}{n} - \right. \\ &\quad \left. a \cdot b \cdot \left(\frac{\sin\left((n-1) \cdot \pi \cdot \frac{\Theta}{T}\right)}{n-1} + \frac{\sin\left((n+1) \cdot \pi \cdot \frac{\Theta}{T}\right)}{n+1}\right) + \right. \\ &\quad \left. \frac{b^2}{4} \cdot \left(\frac{\sin\left((n-2) \cdot \pi \cdot \frac{\Theta}{T}\right)}{n-2} + \frac{\sin\left((n+2) \cdot \pi \cdot \frac{\Theta}{T}\right)}{n+2}\right)\right), \quad n \geq 3 \\ a_{-n} &= a_n \\ b_n &= 0 \end{aligned} \quad (\text{A3.4})$$

for $|a| < |b|$, and

$$\begin{aligned}
 a_0 &= \text{sign } a \cdot \left(a^2 + \frac{b^2}{2} \right), \quad a_1 = a \cdot b, \quad a_2 = \frac{b^2}{4} \\
 a_n &= 0, \quad n \geq 3 \\
 a_{-n} &= a_n \\
 b_n &= 0
 \end{aligned}
 \tag{A3.5}$$

for $|a| \geq |b|$, with the sign function sign . For $a = 0$, the Fourier coefficients read as follows,

$$\begin{aligned}
 a_n &= \begin{cases} \frac{4 \cdot (-1)^{\frac{n+1}{2}}}{\pi} \cdot \frac{b^2}{n \cdot (n^2 - 4)} & , n \geq 2 \cdot m + 1, m \in \mathbb{N} \\ 0 & , \text{otherwise} \end{cases} \\
 a_{-n} &= a_n \\
 b_n &= 0
 \end{aligned}
 \tag{A3.6}$$

The non-linear term of Morison's equation for regular Airy waves according to Eq. (A3.3) with $a = \frac{1}{2}$ and $b = 1$ and the respective Fourier coefficients are shown in Fig. A3.2.

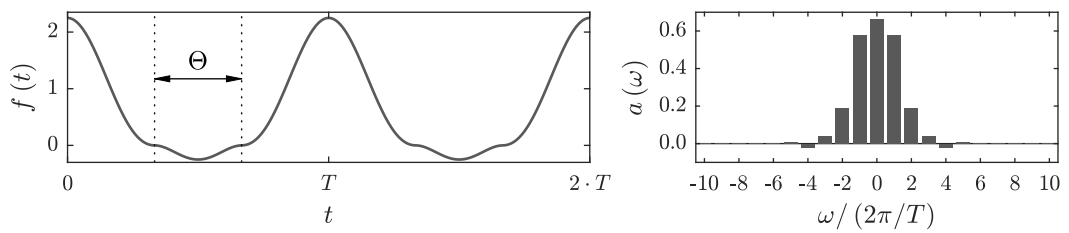


Figure A3.2: Periodic function according to Eq. (A3.3) with $a = \frac{1}{2}$ and $b = 1$ (left) and the respective Fourier coefficients (right)

A4 Power spectral densities applied for analysis of distribution functions of fatigue loads

The values of the coefficients and wave frequencies of the power spectral densities according to Eq. (6.15) and Fig. 6.9(h) which are used for the analysis of distribution functions of fatigue loads in Section 6.3 are listed in Tbl. A4.1. The values are set such that the first-order spectral moment of all power spectral densities is unity. The upper wave frequency $\omega_{2,1}$ is equal to unity.

Table A4.1: Coefficients of the power spectral densities according to Eq. (6.15) and Fig. 6.9(h) applied for analysis of distribution functions of fatigue loads

α_1	α_2/α_1	Term 1			Term 2	
		A_1	$\omega_{1,0}$	$\omega_{1,1}$	A_2	$\omega_{2,0}$
0.025	0.025	1.728E+05	5.570E-06	1.714E-05	1.739E-06	0.4781
		9.874E+04	5.576E-07	2.081E-05	3.286E-06	0.8439
		1.048E+05	8.702E-06	2.779E-05	3.283E-06	0.6029
		7.062E+04	3.269E-06	3.159E-05	2.721E-06	0.4961
		1.209E+05	4.388E-06	2.093E-05	6.593E-06	0.9089
	0.075	5.266E+04	1.804E-05	5.601E-05	5.208E-05	0.8760
		1.661E+05	3.456E-05	4.660E-05	2.880E-05	0.7287
		3.739E+04	2.057E-05	7.406E-05	1.529E-04	0.9493
		2.595E+04	6.871E-06	8.393E-05	7.902E-05	0.9046
		2.928E+04	3.436E-06	7.174E-05	1.400E-05	0.2627
	0.125	3.914E+04	3.512E-05	8.622E-05	6.152E-05	0.6574
		1.593E+04	1.163E-05	1.372E-04	4.909E-04	0.9557
		3.587E+04	3.132E-05	8.708E-05	6.429E-05	0.6909
		4.621E+04	3.824E-05	8.152E-05	4.437E-05	0.4665
		6.663E+04	4.604E-05	7.606E-05	1.265E-04	0.8545
	0.175	2.038E+04	1.057E-05	1.087E-04	5.712E-05	0.1513
		1.452E+05	5.676E-05	7.054E-05	6.055E-05	0.1611
		3.548E+04	5.405E-05	1.104E-04	6.162E-04	0.9414
		2.500E+04	4.847E-05	1.285E-04	3.194E-04	0.8756
		2.294E+04	4.753E-05	1.347E-04	2.053E-04	0.7881
0.225	3.130E+04	6.472E-05	1.286E-04	2.617E-04	0.7547	
	1.856E+04	2.976E-05	1.375E-04	1.464E-04	0.5692	
	1.158E+04	2.492E-05	1.976E-04	1.454E-03	0.9547	
	1.529E+04	2.034E-05	1.511E-04	1.249E-04	0.4131	
	2.467E+04	6.438E-05	1.454E-04	3.455E-04	0.8045	

α_1	α_2/α_1	Term 1			Term 2	
		A_1	$\omega_{1,0}$	$\omega_{1,1}$	A_2	$\omega_{2,0}$
0.025	0.275	1.526E+04	5.731E-05	1.884E-04	1.218E-03	0.9203
		1.498E+04	2.730E-05	1.608E-04	2.042E-04	0.5347
		1.074E+04	7.918E-06	1.940E-04	2.739E-04	0.6583
		2.701E+04	8.525E-05	1.593E-04	6.698E-04	0.8501
		9.493E+03	2.653E-05	2.372E-04	0.1730	0.9994
	0.325	1.660E+04	2.915E-05	1.496E-04	1.997E-04	0.2399
		2.258E+04	9.267E-05	1.812E-04	3.456E-03	0.9612
		1.546E+04	5.722E-05	1.866E-04	4.433E-04	0.6822
		7.984E+03	6.949E-06	2.574E-04	2.376E-02	0.9947
		6.631E+04	7.774E-05	1.079E-04	2.097E-04	0.2698
	0.375	1.328E+06	1.386E-04	1.401E-04	1.969E-03	0.9111
		3.281E+04	8.136E-05	1.423E-04	3.652E-04	0.4879
		8.028E+04	8.120E-05	1.061E-04	2.626E-04	0.2397
		1.045E+04	1.273E-05	2.041E-04	3.153E-04	0.3466
		1.022E+05	7.739E-05	9.695E-05	2.440E-04	0.1399
	0.425	4.246E+04	1.140E-04	1.611E-04	1.154E-03	0.8042
		2.577E+04	8.869E-05	1.663E-04	6.828E-04	0.6633
		8.770E+03	2.538E-05	2.534E-04	1.086E-03	0.7872
		1.187E+04	5.708E-05	2.256E-04	1.541E-03	0.8531
		1.305E+04	2.773E-05	1.809E-04	3.892E-04	0.4035
	0.475	2.260E+04	8.719E-05	1.757E-04	9.753E-04	0.7120
		1.849E+04	9.255E-05	2.007E-04	2.197E-03	0.8710
		9.587E+03	2.096E-05	2.295E-04	6.356E-04	0.5111
		7.969E+03	2.100E-05	2.719E-04	1.864E-02	0.9857
		5.200E+04	1.132E-04	1.516E-04	8.818E-04	0.6715
	0.525	7.654E+03	1.649E-05	2.777E-04	2.703E-03	0.8713
		1.085E+04	2.502E-05	2.094E-04	7.079E-04	0.4839
		1.042E+04	5.193E-05	2.439E-04	8.478E-03	0.9607
		1.758E+04	5.993E-05	1.737E-04	7.013E-04	0.4789
		6.508E+04	1.266E-04	1.573E-04	1.686E-03	0.7917
	0.575	1.033E+04	4.567E-05	2.392E-04	3.152E-03	0.8691
		1.322E+04	5.723E-05	2.085E-04	1.437E-03	0.7018
		2.008E+04	9.723E-05	1.968E-04	2.680E-02	0.9851
		1.019E+04	4.560E-05	2.418E-04	3.042E-03	0.8621
		1.415E+04	5.964E-05	2.010E-04	1.595E-03	0.7433
	0.625	1.182E+04	1.950E-07	1.694E-04	7.146E-04	0.1945
		1.056E+04	4.578E-06	1.939E-04	8.500E-04	0.3811
		1.034E+04	3.016E-05	2.235E-04	1.860E-03	0.7356
		1.744E+04	6.576E-05	1.804E-04	1.760E-03	0.7273
		7.808E+03	2.591E-05	2.820E-04	7.689E-02	0.9933

α_1	α_2/α_1	Term 1			Term 2	
		A_1	$\omega_{1,0}$	$\omega_{1,1}$	A_2	$\omega_{2,0}$
0.025	0.675	1.237E+04	8.810E-07	1.625E-04	8.802E-04	0.2172
		9.241E+03	2.351E-05	2.399E-04	1.228E-02	0.9544
		6.321E+04	7.080E-05	1.024E-04	9.215E-04	0.2797
		2.956E+04	9.658E-05	1.642E-04	5.433E-03	0.8949
		1.382E+04	4.106E-05	1.857E-04	1.692E-03	0.6564
	0.725	1.338E+04	4.125E-05	1.907E-04	3.947E-03	0.8298
		2.431E+04	5.832E-05	1.406E-04	1.853E-03	0.6456
		1.731E+04	4.407E-05	1.595E-04	1.742E-03	0.5977
		1.616E+04	6.570E-06	1.303E-04	9.881E-04	0.2037
		1.266E+04	2.705E-05	1.849E-04	3.122E-03	0.7996
	0.775	2.191E+04	4.747E-05	1.387E-04	2.569E-03	0.6979
		2.676E+04	1.617E-05	9.088E-05	1.088E-03	0.1935
		1.216E+04	3.616E-06	1.680E-04	2.116E-03	0.6485
		2.442E+04	2.344E-05	1.053E-04	1.244E-03	0.2760
		1.633E+04	1.958E-05	1.420E-04	1.655E-03	0.5132
	0.825	2.183E+04	2.787E-05	1.195E-04	2.707E-03	0.6811
		1.408E+04	1.445E-05	1.564E-04	4.842E-03	0.8143
		1.323E+04	7.541E-06	1.587E-04	8.062E-03	0.8978
		2.790E+04	4.353E-05	1.152E-04	3.417E-03	0.7448
		1.120E+04	8.083E-06	1.866E-04	0.2190	0.9958
0.875	3.105E+04	1.081E-05	7.520E-05	1.910E-03	0.4122	
	1.878E+04	6.480E-06	1.129E-04	8.198E-03	0.8922	
	2.086E+04	3.874E-06	9.970E-05	2.973E-03	0.7000	
	1.818E+04	1.190E-05	1.219E-04	4.875E-03	0.7797	
	2.225E+04	2.614E-05	1.160E-04	1.690E-02	0.9386	
0.925	3.901E+04	4.127E-06	5.537E-05	2.730E-03	0.6055	
	2.941E+04	1.003E-05	7.799E-05	1.635E-02	0.9321	
	4.958E+04	1.562E-05	5.593E-05	3.769E-03	0.7096	
	2.318E+04	1.663E-06	8.790E-05	1.471E-02	0.9200	
	3.842E+04	1.797E-05	7.000E-05	8.218E-03	0.8525	
0.975	1.292E+05	2.109E-07	1.568E-05	3.140E-03	0.6755	
	1.645E+05	3.418E-06	1.557E-05	3.299E-03	0.6548	
	3.538E+05	1.205E-05	1.769E-05	2.127E-02	0.9357	
	1.401E+05	4.719E-06	1.899E-05	1.481E-02	0.9404	
	7.163E+04	2.746E-07	2.818E-05	0.2567	0.9948	
0.075	0.025	1.803E+04	7.969E-05	1.906E-04	4.414E-03	0.9984
		1.499E+05	1.226E-04	1.359E-04	9.352E-05	0.9286
		8.921E+03	2.263E-05	2.468E-04	3.122E-04	0.9774
		1.082E+04	4.215E-05	2.271E-04	1.160E-04	0.9372
		1.350E+04	3.035E-05	1.785E-04	1.375E-05	0.4828

α_1	α_2/α_1	Term 1			Term 2	
		A_1	$\omega_{1,0}$	$\omega_{1,1}$	A_2	$\omega_{2,0}$
0.075	0.075	5.231E+03	8.832E-05	4.707E-04	1.062E-04	0.3406
		3.189E+03	5.929E-05	6.864E-04	7.703E-04	0.9190
		3.665E+03	3.384E-05	5.795E-04	1.388E-04	0.5257
		1.716E+04	2.256E-04	3.422E-04	1.096E-04	0.3599
		3.343E+03	1.810E-05	6.164E-04	1.618E-04	0.6034
0.125	0.125	3.555E+03	2.594E-04	8.220E-04	7.019E-04	0.7492
		7.547E+03	4.724E-04	7.374E-04	5.305E-03	0.9671
		3.523E+03	2.047E-04	7.724E-04	4.091E-04	0.5579
		4.729E+03	1.885E-04	6.114E-04	2.541E-04	0.1265
		1.103E+04	4.235E-04	6.048E-04	5.155E-04	0.6555
0.175	0.175	2.126E+03	1.518E-04	1.092E-03	6.985E-04	0.4797
		3.486E+03	4.352E-04	1.009E-03	1.443E-03	0.7592
		1.534E+03	3.639E-07	1.304E-03	8.452E-04	0.5827
		1.436E+03	2.711E-06	1.395E-03	1.194E-03	0.7104
		2.249E+03	3.158E-04	1.205E-03	2.941E-03	0.8844
0.225	0.225	1.929E+03	2.714E-04	1.308E-03	1.397E-03	0.5807
		8.986E+03	8.535E-04	1.076E-03	1.956E-02	0.9711
		7.793E+03	8.225E-04	1.079E-03	9.753E-03	0.9421
		2.211E+04	7.378E-04	8.282E-04	1.344E-03	0.5608
		4.949E+03	7.522E-04	1.156E-03	1.049E-02	0.9461
0.275	0.275	3.312E+03	4.456E-04	1.049E-03	1.310E-03	0.1661
		8.226E+03	6.942E-04	9.373E-04	1.520E-03	0.3903
		3.418E+03	4.227E-04	1.008E-03	1.234E-03	0.1213
		3.066E+03	5.102E-04	1.162E-03	1.621E-03	0.4387
		4.656E+03	5.939E-04	1.023E-03	1.489E-03	0.3739
0.325	0.325	3.745E+03	4.747E-04	1.008E-03	1.652E-03	0.1770
		2.726E+04	7.867E-04	8.601E-04	1.823E-03	0.2231
		4.729E+03	9.599E-04	1.383E-03	1.066E-02	0.8886
		2.278E+03	6.450E-04	1.522E-03	4.548E-03	0.7356
		2.832E+03	6.868E-04	1.393E-03	3.654E-03	0.6708
0.375	0.375	8.938E+02	3.814E-05	2.274E-03	1.140E-02	0.8703
		2.041E+03	6.251E-04	1.604E-03	4.877E-03	0.6694
		1.396E+04	7.779E-04	9.210E-04	2.356E-03	0.1812
		2.164E+04	7.905E-04	8.829E-04	2.323E-03	0.1611
		2.952E+03	8.106E-04	1.487E-03	5.717E-03	0.7186
0.425	0.425	5.703E+04	1.329E-03	1.364E-03	1.481E-02	0.8559
		2.037E+03	4.548E-04	1.436E-03	3.338E-03	0.3133
		1.936E+03	4.959E-04	1.528E-03	3.835E-03	0.4291
		2.702E+03	5.098E-04	1.249E-03	3.041E-03	0.1714
		1.703E+03	7.772E-04	1.950E-03	0.4022	0.9950

α_1	α_2/α_1	Term 1			Term 2	
		A_1	$\omega_{1,0}$	$\omega_{1,1}$	A_2	$\omega_{2,0}$
0.075	0.475	1.958E+03	7.342E-04	1.755E-03	3.456E-02	0.9338
		9.942E+03	8.640E-04	1.065E-03	4.226E-03	0.3239
		1.853E+04	9.629E-04	1.071E-03	4.648E-03	0.4030
		1.758E+03	7.897E-04	1.926E-03	3.680E-02	0.9312
		4.756E+03	1.033E-03	1.453E-03	1.058E-02	0.7579
	0.525	2.504E+03	6.231E-04	1.420E-03	5.761E-03	0.4041
		2.617E+03	6.099E-04	1.373E-03	6.265E-03	0.5234
		1.937E+03	7.071E-04	1.738E-03	1.302E-02	0.7591
		1.523E+04	8.232E-04	9.543E-04	4.720E-03	0.2198
		1.568E+04	8.115E-04	9.389E-04	4.650E-03	0.1869
	0.575	1.107E+03	9.430E-06	1.813E-03	6.521E-03	0.4542
		2.219E+03	4.934E-04	1.393E-03	6.346E-03	0.3414
		2.300E+04	1.124E-03	1.211E-03	1.243E-02	0.6979
		1.479E+03	2.361E-04	1.586E-03	6.040E-03	0.2923
		1.353E+03	4.468E-04	1.922E-03	1.275E-02	0.7021
	0.625	1.728E+03	4.907E-04	1.645E-03	1.179E-02	0.6183
		3.898E+03	5.170E-04	1.029E-03	6.541E-03	0.1634
		9.296E+03	6.214E-04	8.360E-04	6.345E-03	0.1029
		2.260E+03	3.570E-04	1.240E-03	6.678E-03	0.2054
		1.100E+04	1.052E-03	1.233E-03	1.586E-02	0.7180
	0.675	1.583E+03	2.675E-04	1.528E-03	1.034E-02	0.4879
		4.742E+03	7.931E-04	1.214E-03	1.352E-02	0.6144
		2.081E+03	7.091E-04	1.668E-03	6.076E-02	0.9155
		1.030E+04	8.790E-04	1.073E-03	1.264E-02	0.5787
		9.250E+03	7.371E-04	9.527E-04	9.151E-03	0.3838
	0.725	1.963E+03	4.661E-04	1.482E-03	2.082E-02	0.7051
		4.121E+03	2.676E-04	7.512E-04	7.705E-03	0.1270
		7.716E+04	8.259E-04	8.517E-04	1.285E-02	0.5153
		1.114E+03	1.017E-04	1.891E-03	2.617E-02	0.7721
		1.059E+03	8.367E-05	1.967E-03	3.292E-02	0.8193
	0.775	2.092E+03	8.976E-05	1.042E-03	1.074E-02	0.3310
		5.981E+03	7.395E-04	1.073E-03	4.292E-02	0.8420
		4.635E+03	3.899E-04	8.197E-04	1.143E-02	0.3337
		4.428E+03	7.560E-04	1.206E-03	1.812	0.9963
		3.061E+04	9.337E-04	9.989E-04	0.1881	0.9641
	0.825	6.788E+03	5.504E-04	8.439E-04	2.898E-02	0.7325
2.275E+03		2.993E-04	1.175E-03	4.263E-02	0.8198	
2.914E+03		3.500E-04	1.034E-03	2.790E-02	0.7221	
3.074E+03		5.103E-05	6.987E-04	1.162E-02	0.2059	
2.032E+03		2.994E-04	1.280E-03	0.1120	0.9315	

α_1	α_2/α_1	Term 1			Term 2	
		A_1	$\omega_{1,0}$	$\omega_{1,1}$	A_2	$\omega_{2,0}$
0.075	0.875	2.515E+03	1.925E-04	9.843E-04	9.421E-02	0.9086
		2.119E+03	6.433E-05	1.004E-03	3.652E-02	0.7624
		2.608E+03	7.820E-05	8.417E-04	2.182E-02	0.5904
		3.310E+03	3.091E-04	9.108E-04	0.4049	0.9788
		2.346E+03	1.836E-04	1.032E-03	0.2435	0.9645
	0.925	1.337E+04	3.195E-04	4.683E-04	12.384	0.9992
		2.857E+03	4.268E-05	7.393E-04	0.8255	0.9883
		5.296E+03	1.482E-04	5.240E-04	4.211E-02	0.7683
		3.653E+03	7.096E-05	6.158E-04	4.714E-02	0.7944
		5.500E+03	9.747E-05	4.593E-04	2.566E-02	0.6133
	0.975	1.140E+04	4.509E-05	2.196E-04	0.1549	0.9308
		1.439E+04	5.473E-05	1.930E-04	7.635E-02	0.8588
		2.795E+04	9.175E-05	1.629E-04	9.815E-02	0.8902
		2.117E+04	8.887E-05	1.828E-04	13.440	0.9992
		1.097E+04	4.538E-05	2.267E-04	0.3992	0.9730
0.125	0.025	2.638E+04	3.345E-04	4.103E-04	1.431E-03	0.9870
		1.034E+04	2.731E-04	4.665E-04	3.346E-04	0.9428
		3.833E+03	2.612E-05	5.479E-04	3.723E-05	0.4527
		1.117E+05	3.269E-04	3.448E-04	7.733E-05	0.7471
		3.524E+03	6.952E-05	6.371E-04	1.377E-04	0.8624
	0.075	4.532E+03	4.718E-04	9.130E-04	2.460E-04	0.1431
		2.809E+03	4.549E-04	1.167E-03	3.601E-04	0.5162
		5.202E+03	5.166E-04	9.010E-04	2.506E-04	0.1328
		3.798E+03	8.055E-04	1.332E-03	1.244E-02	0.9863
		2.563E+03	4.443E-04	1.225E-03	3.563E-04	0.4894
	0.125	7.476E+02	3.640E-04	3.038E-03	1.540E-02	0.9689
		1.561E+03	7.915E-04	2.072E-03	1.265E-03	0.6131
		2.259E+03	7.993E-04	1.684E-03	8.495E-04	0.3185
		6.303E+03	9.999E-04	1.317E-03	7.314E-04	0.2227
		7.924E+03	1.455E-03	1.708E-03	3.435E-03	0.8612
	0.175	1.723E+03	1.585E-03	2.745E-03	1.106E-02	0.9139
		8.496E+02	6.529E-04	3.006E-03	2.928E-03	0.6978
		1.446E+03	1.274E-03	2.657E-03	3.518E-03	0.7312
		1.004E+03	1.222E-03	3.213E-03	3.671E-02	0.9747
		9.070E+02	5.748E-04	2.779E-03	1.759E-03	0.4284
0.225	9.902E+02	1.495E-03	3.513E-03	6.354E-03	0.7430	
	6.477E+03	2.399E-03	2.707E-03	4.104E-02	0.9635	
	4.587E+02	3.439E-04	4.701E-03	4.147E-02	0.9651	
	5.319E+03	2.677E-03	3.053E-03	0.2753	0.9941	
	5.785E+02	4.085E-05	3.494E-03	2.344E-03	9.981E-02	

α_1	α_2/α_1	Term 1			Term 2	
		A_1	$\omega_{1,0}$	$\omega_{1,1}$	A_2	$\omega_{2,0}$
0.125	0.275	6.968E+02	4.030E-04	3.269E-03	3.220E-03	1.601E-02
		1.168E+03	1.194E-03	2.905E-03	3.624E-03	0.3115
		3.693E+03	1.695E-03	2.236E-03	3.346E-03	0.2418
		6.540E+02	1.225E-03	4.279E-03	6.782E-03	0.6188
		7.500E+02	1.711E-03	4.375E-03	2.322E-02	0.8944
	0.325	3.939E+02	4.228E-04	5.492E-03	1.087E-02	0.6937
		4.748E+02	1.915E-04	4.396E-03	5.045E-03	0.2412
		3.230E+03	2.991E-03	3.609E-03	2.873E-02	0.8856
		3.029E+02	1.212E-05	6.604E-03	3.408	0.9991
		1.007E+03	1.582E-03	3.565E-03	6.844E-03	0.5227
0.375	5.734E+03	3.302E-03	3.650E-03	6.085E-02	0.9292	
	9.710E+02	1.842E-03	3.897E-03	9.537E-03	0.5057	
	3.643E+02	2.446E-04	5.724E-03	1.447E-02	0.7159	
	3.473E+02	1.013E-03	6.758E-03	0.4695	0.9901	
	8.788E+02	2.787E-03	5.057E-03	0.3709	0.9875	
0.425	3.441E+02	3.561E-04	6.151E-03	1.710E-02	0.6662	
	1.538E+03	2.563E-03	3.860E-03	1.744E-02	0.6735	
	5.327E+02	1.777E-03	5.521E-03	0.1559	0.9652	
	8.820E+02	1.950E-03	4.211E-03	1.262E-02	0.5228	
	8.612E+02	1.285E-03	3.600E-03	8.239E-03	0.2157	
0.475	1.626E+03	2.462E-03	3.687E-03	1.552E-02	0.5131	
	1.782E+04	3.849E-03	3.961E-03	7.535	0.9991	
	3.589E+02	1.164E-03	6.715E-03	8.254E-02	0.9116	
	4.438E+02	9.944E-04	5.484E-03	1.652E-02	0.5291	
	7.168E+03	2.803E-03	3.081E-03	1.437E-02	0.4739	
0.525	3.818E+03	3.593E-03	4.114E-03	0.1234	0.9293	
	3.442E+02	1.150E-03	6.935E-03	1.759	0.9950	
	4.097E+02	8.801E-04	5.739E-03	2.369E-02	0.6102	
	8.418E+02	1.183E-03	3.546E-03	1.245E-02	0.1150	
	9.516E+02	1.913E-03	4.006E-03	2.025E-02	0.5848	
0.575	3.362E+02	7.765E-04	6.693E-03	8.822E-02	0.8800	
	3.274E+02	1.889E-04	6.264E-03	2.894E-02	0.6297	
	2.978E+02	8.557E-05	6.769E-03	6.394E-02	0.8445	
	3.750E+02	3.080E-05	5.334E-03	1.789E-02	0.3770	
	4.747E+02	1.302E-03	5.494E-03	7.100E-02	0.8620	
0.625	9.925E+02	1.154E-03	3.155E-03	1.785E-02	0.1855	
	3.986E+02	8.210E-04	5.807E-03	5.621E-02	0.7770	
	5.583E+02	1.249E-03	4.809E-03	3.284E-02	0.6228	
	4.161E+02	5.950E-04	5.370E-03	3.176E-02	0.5936	
	7.258E+02	1.501E-03	4.239E-03	2.668E-02	0.5203	

α_1	α_2/α_1	Term 1			Term 2	
		A_1	$\omega_{1,0}$	$\omega_{1,1}$	A_2	$\omega_{2,0}$
0.125	0.675	4.423E+02	4.440E-04	4.933E-03	3.327E-02	0.5574
		3.224E+02	3.490E-04	6.508E-03	0.2615	0.9446
		5.324E+02	1.297E-03	5.027E-03	0.1211	0.8860
		5.656E+02	6.038E-04	4.113E-03	2.584E-02	0.4096
		8.982E+02	1.427E-03	3.637E-03	2.944E-02	0.5071
	0.725	1.248E+03	7.694E-04	2.356E-03	2.385E-02	0.1127
		4.314E+02	6.180E-04	5.215E-03	8.656E-02	0.8043
		7.293E+02	1.285E-03	4.005E-03	5.172E-02	0.6794
		3.912E+02	1.664E-04	5.233E-03	4.836E-02	0.6324
		1.339E+03	1.893E-03	3.374E-03	4.823E-02	0.6527
	0.775	4.235E+02	5.256E-04	5.203E-03	29.768	0.9994
		7.417E+02	1.026E-03	3.698E-03	8.903E-02	0.7941
		6.285E+02	5.021E-04	3.651E-03	3.998E-02	0.4784
		5.157E+03	2.309E-03	2.693E-03	7.288E-02	0.7298
		6.605E+02	4.742E-04	3.469E-03	3.725E-02	0.4106
	0.825	4.619E+02	1.159E-04	4.399E-03	0.9951	0.9784
		4.443E+02	7.385E-05	4.526E-03	0.4867	0.9548
		1.210E+03	1.128E-03	2.763E-03	9.611E-02	0.7797
		2.226E+03	1.676E-03	2.564E-03	0.1795	0.8796
		4.905E+02	3.662E-04	4.398E-03	0.5300	0.9580
	0.875	2.786E+03	8.041E-04	1.513E-03	5.155E-02	0.5010
		8.352E+02	2.493E-04	2.613E-03	7.040E-02	0.6338
		2.231E+03	7.226E-04	1.608E-03	5.439E-02	0.5414
		1.372E+04	8.265E-04	9.703E-04	4.106E-02	0.3490
		8.788E+02	5.293E-04	2.778E-03	0.2639	0.9091
	0.925	2.705E+04	1.039E-03	1.112E-03	44.757	0.9994
		2.046E+03	1.155E-04	1.079E-03	5.342E-02	0.4516
		1.438E+04	7.980E-04	9.352E-04	9.967E-02	0.7229
		1.149E+03	1.818E-04	1.897E-03	0.1533	0.8137
		1.898E+03	1.245E-04	1.164E-03	5.699E-02	0.5039
	0.975	2.568E+03	9.217E-06	7.765E-04	2.568	0.9884
		5.962E+03	1.051E-04	4.356E-04	0.1082	0.7217
		4.465E+03	7.139E-05	5.126E-04	0.1238	0.7576
		5.222E+03	1.852E-05	3.957E-04	8.465E-02	0.6400
		8.834E+03	1.358E-04	3.588E-04	9.769E-02	0.6901
0.175	0.025	2.301E+03	1.218E-04	9.909E-04	8.528E-05	0.6081
		4.728E+03	4.444E-04	8.674E-04	1.575E-04	0.7677
		1.818E+04	4.761E-04	5.861E-04	6.146E-05	0.3384
		3.206E+03	3.955E-04	1.019E-03	5.021E-04	0.9288
		2.246E+03	5.466E-05	9.453E-04	5.461E-05	0.2073

α_1	α_2/α_1	Term 1			Term 2	
		A_1	$\omega_{1,0}$	$\omega_{1,1}$	A_2	$\omega_{2,0}$
0.175	0.075	6.570E+03	1.810E-03	2.114E-03	1.688E-03	0.7953
		1.504E+03	7.326E-04	2.062E-03	5.109E-04	9.314E-02
		3.984E+03	1.113E-03	1.615E-03	4.722E-04	0.2641
		1.249E+03	1.163E-03	2.764E-03	2.701E-03	0.8740
		9.239E+02	9.178E-04	3.082E-03	3.085E-03	0.8935
0.125	0.125	7.158E+02	1.362E-03	4.155E-03	2.657E-03	0.6548
		1.013E+03	1.476E-03	3.450E-03	1.694E-03	0.4025
		4.817E+03	2.732E-03	3.147E-03	4.066E-03	0.7730
		4.415E+02	8.152E-05	4.609E-03	1.482E-03	0.2382
		2.559E+03	3.009E-03	3.790E-03	7.882E-02	0.9882
0.175	0.175	1.250E+03	3.330E-03	4.929E-03	1.110E-02	0.8336
		3.218E+02	3.117E-04	6.521E-03	3.934E-03	0.5101
		3.316E+02	1.156E-03	7.181E-03	3.720E-02	0.9544
		2.798E+02	9.325E-06	7.151E-03	5.373E-03	0.6829
		3.147E+02	4.565E-04	6.805E-03	5.506E-03	0.6687
0.225	0.225	3.682E+02	2.276E-03	7.699E-03	2.307E-02	0.8699
		3.071E+02	1.364E-03	7.866E-03	9.554E-03	0.6726
		9.331E+02	3.707E-03	5.847E-03	1.495E-02	0.8041
		4.868E+02	2.601E-03	6.703E-03	1.324E-02	0.7811
		2.503E+03	3.001E-03	3.798E-03	4.353E-03	2.603E-02
0.275	0.275	3.047E+02	1.786E-03	8.334E-03	1.197E-02	0.6152
		1.619E+03	4.104E-03	5.336E-03	9.834E-03	0.5241
		2.653E+02	5.703E-04	8.091E-03	7.672E-03	0.3780
		3.577E+02	1.058E-03	6.634E-03	6.390E-03	0.1501
		6.401E+02	4.128E-03	7.245E-03	2.355E-02	0.8054
0.325	0.325	2.687E+02	1.183E-03	8.601E-03	1.118E-02	0.3795
		1.649E+02	5.690E-04	1.266E-02	0.1307	0.9517
		4.551E+02	3.851E-03	8.231E-03	2.653E-02	0.7586
		9.071E+02	4.112E-03	6.310E-03	1.380E-02	0.5297
		3.619E+02	3.235E-03	8.743E-03	2.446E-02	0.7343
0.375	0.375	4.381E+02	4.865E-03	9.410E-03	1.918	0.9957
		2.540E+02	3.190E-03	1.103E-02	0.1901	0.9559
		2.002E+02	1.296E-03	1.124E-02	3.194E-02	0.7348
		3.116E+02	3.831E-03	1.022E-02	0.1438	0.9420
		5.760E+02	3.720E-03	7.177E-03	1.674E-02	0.4569
0.425	0.425	1.311E+03	6.710E-03	8.228E-03	0.4661	0.9767
		1.710E+02	9.307E-04	1.256E-02	5.480E-02	0.8044
		4.378E+02	5.304E-03	9.847E-03	0.8906	0.9877
		1.459E+02	5.173E-04	1.415E-02	0.1234	0.9117
		1.299E+03	5.771E-03	7.302E-03	4.399E-02	0.7566

α_1	α_2/α_1	Term 1			Term 2	
		A_1	$\omega_{1,0}$	$\omega_{1,1}$	A_2	$\omega_{2,0}$
0.175	0.475	1.674E+02	6.985E-04	1.257E-02	4.767E-02	0.7116
		2.370E+02	3.289E-03	1.167E-02	0.2673	0.9495
		2.917E+02	2.548E-03	9.356E-03	2.965E-02	0.5172
		2.125E+02	3.036E-03	1.239E-02	0.6668	0.9796
		4.622E+02	4.922E-03	9.219E-03	7.897E-02	0.8267
	0.525	4.651E+03	7.503E-03	7.929E-03	2.255	0.9926
		2.570E+02	3.723E-03	1.144E-02	0.2270	0.9256
		1.657E+02	4.013E-04	1.237E-02	4.625E-02	0.6279
		2.432E+02	1.348E-03	9.496E-03	2.935E-02	0.3775
		2.405E+02	2.521E-03	1.077E-02	5.391E-02	0.6807
	0.575	1.896E+02	1.304E-03	1.174E-02	7.131E-02	0.7180
		3.122E+02	3.362E-03	9.701E-03	6.847E-02	0.7001
		1.888E+02	8.424E-04	1.132E-02	4.815E-02	0.5632
		6.610E+03	6.527E-03	6.827E-03	8.074E-02	0.7475
		6.653E+02	3.283E-03	6.254E-03	3.059E-02	0.2414
	0.625	2.766E+02	1.241E-03	8.374E-03	3.925E-02	0.3069
		3.194E+02	4.290E-03	1.048E-02	3.310	0.9928
		2.134E+02	9.747E-04	1.023E-02	5.152E-02	0.5075
		2.946E+02	3.429E-03	1.014E-02	0.1977	0.8814
		1.865E+02	2.021E-03	1.262E-02	0.6519	0.9630
	0.675	1.772E+02	3.819E-04	1.151E-02	0.1064	0.7364
		6.733E+02	2.375E-03	5.294E-03	4.137E-02	0.1592
		1.872E+02	7.566E-04	1.129E-02	0.1178	0.7657
		4.229E+02	2.528E-03	7.184E-03	5.153E-02	0.4040
		3.659E+02	3.783E-03	9.175E-03	0.4114	0.9342
	0.725	6.055E+02	2.838E-03	6.083E-03	6.298E-02	0.4503
		2.482E+02	1.670E-03	9.600E-03	0.1700	0.8120
		6.020E+02	4.078E-03	7.348E-03	0.2017	0.8423
		1.242E+03	3.421E-03	5.002E-03	5.835E-02	0.3947
		3.475E+02	1.164E-03	6.818E-03	5.397E-02	0.3469
	0.775	2.074E+02	4.360E-04	9.901E-03	0.3336	0.8901
		4.377E+02	1.123E-03	5.599E-03	6.172E-02	0.3293
		3.211E+02	1.835E-03	7.949E-03	0.1892	0.8052
		2.222E+02	1.054E-03	9.893E-03	7.204	0.9949
		4.142E+02	2.807E-03	7.545E-03	0.2511	0.8502
	0.825	6.009E+02	2.301E-03	5.559E-03	0.1695	0.7500
		9.863E+02	3.370E-03	5.356E-03	0.9883	0.9585
		3.794E+02	1.047E-03	6.209E-03	0.1232	0.6624
		3.734E+02	1.171E-04	5.353E-03	7.207E-02	0.3745
		1.991E+03	1.621E-03	2.601E-03	6.240E-02	0.2202

α_1	α_2/α_1	Term 1			Term 2	
		A_1	$\omega_{1,0}$	$\omega_{1,1}$	A_2	$\omega_{2,0}$
0.175	0.875	8.770E+02	5.435E-04	2.763E-03	7.823E-02	0.3175
		1.522E+03	2.621E-04	1.537E-03	7.021E-02	0.1333
		6.788E+02	1.473E-03	4.351E-03	0.2014	0.7689
		4.716E+02	1.069E-03	5.208E-03	0.2260	0.7893
		5.547E+02	1.682E-03	5.200E-03	1.927	0.9749
	0.925	1.672E+03	1.099E-03	2.263E-03	0.1541	0.6487
		5.972E+02	4.742E-04	3.735E-03	2.798	0.9812
		4.323E+03	1.326E-03	1.776E-03	0.1451	0.6206
		1.548E+03	4.429E-04	1.697E-03	0.1028	0.4265
		6.773E+02	8.750E-04	3.749E-03	5.609	0.9905
	0.975	1.462E+03	1.188E-04	1.447E-03	2.865	0.9797
		1.524E+04	4.478E-04	5.753E-04	0.2649	0.7821
		3.637E+03	5.324E-04	1.067E-03	0.5238	0.8913
		8.640E+03	4.573E-04	6.819E-04	0.2337	0.7482
		1.240E+04	2.847E-05	1.848E-04	0.1222	0.4956
0.225	0.025	7.612E+03	9.208E-04	1.184E-03	1.927E-04	0.6801
		3.640E+03	9.136E-04	1.463E-03	2.964E-04	0.7663
		4.628E+03	7.154E-04	1.148E-03	1.193E-04	0.4947
		3.064E+03	6.571E-04	1.310E-03	1.474E-04	0.5972
		6.021E+03	6.172E-04	9.493E-04	8.209E-05	9.988E-02
	0.075	4.548E+02	3.701E-04	4.767E-03	9.294E-04	0.3324
		1.868E+03	2.400E-03	3.470E-03	2.064E-03	0.7658
		5.802E+02	1.745E-03	5.191E-03	8.640E-02	0.9941
		9.025E+02	2.522E-03	4.738E-03	0.1196	0.9953
		6.204E+02	1.934E-03	5.157E-03	1.468E-02	0.9626
	0.125	2.137E+02	7.335E-04	1.009E-02	8.283E-02	0.9825
		3.194E+02	1.941E-03	8.198E-03	9.754E-03	0.8489
		2.565E+02	1.496E-03	9.287E-03	0.2197	0.9936
		4.354E+02	2.817E-03	7.407E-03	1.318E-02	0.8903
		3.955E+02	1.263E-03	6.315E-03	2.341E-03	0.2934
	0.175	2.228E+03	6.139E-03	7.035E-03	1.512E-02	0.8088
		2.144E+02	2.499E-03	1.182E-02	6.380E-02	0.9542
		2.897E+02	3.360E-03	1.025E-02	2.503E-02	0.8849
		1.560E+02	5.580E-04	1.336E-02	2.954E-02	0.9013
		2.416E+02	9.614E-04	9.227E-03	4.748E-03	0.3037
	0.225	4.682E+02	4.064E-03	8.325E-03	7.989E-03	0.3306
		8.115E+02	6.052E-03	8.511E-03	1.383E-02	0.6469
		2.762E+04	5.997E-03	6.069E-03	7.649E-03	0.2782
		2.182E+02	3.391E-03	1.253E-02	2.530E-02	0.8092
3.185E+02		2.502E-03	8.760E-03	7.078E-03	7.166E-02	

α_1	α_2/α_1	Term 1			Term 2	
		A_1	$\omega_{1,0}$	$\omega_{1,1}$	A_2	$\omega_{2,0}$
0.225	0.275	3.749E+02	4.654E-03	9.967E-03	1.272E-02	0.3675
		1.236E+02	8.247E-04	1.694E-02	2.786E-02	0.7374
		1.967E+02	4.280E-03	1.441E-02	4.797E-02	0.8499
		3.059E+02	3.396E-03	9.904E-03	1.085E-02	0.1588
		1.655E+02	8.604E-04	1.289E-02	1.122E-02	0.2487
	0.325	1.040E+02	1.294E-03	2.043E-02	0.1764	0.9426
		3.821E+02	4.987E-03	1.019E-02	1.605E-02	0.2684
		2.074E+02	3.960E-03	1.355E-02	2.246E-02	0.5197
		1.859E+02	3.813E-03	1.451E-02	2.643E-02	0.5982
		1.575E+02	1.313E-03	1.394E-02	1.617E-02	0.2576
	0.375	84.290	3.028E-04	2.387E-02	39.736	0.9997
		1.154E+02	7.915E-04	1.800E-02	3.060E-02	0.5339
1.010E+02		9.857E-04	2.064E-02	6.355E-02	0.7848	
2.831E+02		6.642E-03	1.366E-02	4.193E-02	0.6694	
1.045E+02		1.467E-03	2.048E-02	7.192E-02	0.8103	
0.425	1.103E+02	3.525E-03	2.149E-02	1.228	0.9857	
	3.164E+02	7.138E-03	1.340E-02	4.656E-02	0.6083	
	1.028E+02	2.736E-03	2.202E-02	0.4665	0.9624	
	92.405	1.836E-03	2.329E-02	0.7413	0.9761	
	1.572E+02	2.443E-03	1.504E-02	2.960E-02	0.3382	
0.475	2.095E+02	4.431E-03	1.386E-02	3.886E-02	0.3670	
	95.878	1.862E-03	2.249E-02	0.2092	0.8946	
	1.023E+02	1.366E-03	2.070E-02	7.392E-02	0.6971	
	1.843E+02	5.853E-03	1.658E-02	8.044E-02	0.7182	
	1.194E+02	2.009E-03	1.857E-02	5.485E-02	0.5865	
0.525	1.207E+02	4.490E-03	2.083E-02	0.6483	0.9582	
	1.249E+02	3.334E-03	1.913E-02	0.1003	0.7245	
	1.471E+02	6.164E-04	1.396E-02	3.887E-02	2.965E-02	
	2.612E+02	9.081E-03	1.663E-02	1.059	0.9741	
	76.323	8.586E-05	2.593E-02	3.417	0.9920	
0.575	90.227	8.411E-04	2.265E-02	0.2158	0.8486	
	1.156E+02	3.986E-03	2.100E-02	0.5880	0.9440	
	4.124E+02	4.490E-03	9.227E-03	4.690E-02	1.336E-02	
	85.116	1.171E-03	2.428E-02	1.805	0.9818	
	1.446E+02	6.050E-03	1.965E-02	13.948	0.9976	
0.625	1.264E+02	4.298E-03	1.981E-02	0.9181	0.9575	
	1.637E+02	3.238E-03	1.520E-02	8.192E-02	0.4954	
	2.062E+02	5.643E-03	1.515E-02	0.1298	0.6949	
	1.186E+02	1.487E-03	1.800E-02	9.545E-02	0.5748	
	3.137E+02	3.746E-03	9.961E-03	5.665E-02	0.1150	

α_1	α_2/α_1	Term 1			Term 2	
		A_1	$\omega_{1,0}$	$\omega_{1,1}$	A_2	$\omega_{2,0}$
0.225	0.675	1.482E+02	4.773E-03	1.796E-02	1.845	0.9754
		5.968E+02	9.359E-03	1.263E-02	0.5044	0.9094
		1.883E+02	6.360E-03	1.674E-02	31.318	0.9985
		1.246E+03	5.020E-03	6.576E-03	6.597E-02	4.948E-02
		1.804E+03	9.138E-03	1.022E-02	0.1491	0.6903
	0.725	2.214E+02	4.920E-03	1.371E-02	0.2350	0.7736
		3.577E+02	7.610E-03	1.305E-02	1.676	0.9686
		1.853E+02	3.622E-03	1.412E-02	0.1776	0.6968
		2.013E+02	5.583E-03	1.525E-02	2.233	0.9762
		2.937E+02	7.007E-03	1.364E-02	1.893	0.9721
	0.775	7.713E+02	6.866E-03	9.379E-03	0.2677	0.7722
		1.801E+02	2.146E-03	1.291E-02	0.1823	0.6623
		3.234E+02	4.767E-03	1.076E-02	0.2102	0.7087
		2.031E+02	3.791E-03	1.334E-02	0.4107	0.8515
		1.544E+02	2.163E-03	1.472E-02	0.3800	0.8403
	0.825	4.701E+02	3.840E-03	7.944E-03	0.1779	0.6015
		2.130E+02	2.349E-03	1.141E-02	0.3445	0.7985
		2.167E+02	3.045E-03	1.196E-02	2.225	0.9690
		2.366E+02	3.308E-03	1.147E-02	1.265	0.9456
		7.287E+02	1.922E-03	4.551E-03	0.1017	0.1714
0.875	2.504E+02	1.283E-03	8.958E-03	0.3879	0.7987	
	2.205E+02	5.817E-04	9.294E-03	0.3082	0.7438	
	2.125E+02	8.820E-04	9.926E-03	0.4989	0.8424	
	4.737E+02	2.643E-03	6.701E-03	0.2400	0.6754	
	2.880E+02	2.303E-03	8.976E-03	0.8325	0.9062	
0.925	3.285E+03	2.958E-03	3.541E-03	0.4268	0.7977	
	4.588E+02	3.495E-04	4.512E-03	0.2006	0.5513	
	3.568E+02	9.174E-04	6.278E-03	5.779	0.9849	
	5.614E+02	1.385E-03	4.793E-03	0.3814	0.7735	
	1.376E+03	2.539E-04	1.634E-03	0.1385	0.2763	
0.975	4.129E+03	2.829E-04	7.435E-04	0.2348	0.5818	
	2.023E+03	7.765E-04	1.718E-03	0.6963	0.8639	
	1.390E+03	5.248E-04	1.897E-03	1.622	0.9427	
	1.098E+03	3.291E-04	2.059E-03	3.624	0.9724	
	9.750E+02	4.237E-04	2.379E-03	1.435	0.9350	
0.275	0.025	3.624E+03	7.999E-04	1.352E-03	1.007E-04	0.1384
		2.101E+03	7.646E-04	1.716E-03	1.290E-04	0.2494
		1.482E+03	8.678E-04	2.218E-03	3.053E-04	0.7359
		1.031E+03	4.811E-04	2.422E-03	2.060E-04	0.5889
		1.322E+03	7.839E-04	2.297E-03	3.005E-04	0.7303

α_1	α_2/α_1	Term 1			Term 2	
		A_1	$\omega_{1,0}$	$\omega_{1,1}$	A_2	$\omega_{2,0}$
0.275	0.075	1.441E+03	3.018E-03	4.405E-03	1.325E-03	0.4186
		3.601E+02	8.866E-04	6.438E-03	1.266E-03	0.3239
		7.387E+02	3.050E-03	5.757E-03	2.586E-03	0.7183
		2.442E+02	6.208E-04	8.807E-03	3.913E-03	0.8096
		6.803E+02	2.607E-03	5.546E-03	1.979E-03	0.6429
	0.125	1.982E+02	2.945E-03	1.303E-02	0.2561	0.9921
		1.552E+02	1.674E-03	1.454E-02	5.186E-02	0.9587
		2.370E+02	3.663E-03	1.209E-02	4.678E-02	0.9568
		2.528E+02	1.155E-03	9.055E-03	2.997E-03	3.142E-02
		3.810E+02	3.411E-03	8.654E-03	3.935E-03	0.4557
	0.175	1.505E+02	1.850E-03	1.511E-02	8.981E-03	0.5161
		3.431E+02	4.626E-03	1.044E-02	6.687E-03	0.2688
		2.508E+02	5.678E-03	1.364E-02	1.771E-02	0.7596
		1.618E+02	9.214E-04	1.325E-02	6.132E-03	0.1211
		2.935E+02	4.465E-03	1.126E-02	7.390E-03	0.4006
	0.225	2.075E+02	7.186E-03	1.679E-02	3.763E-02	0.8151
		1.566E+03	9.319E-03	1.059E-02	1.375E-02	0.4628
		1.170E+02	1.325E-03	1.836E-02	1.327E-02	0.4448
		2.194E+02	5.590E-03	1.467E-02	1.440E-02	0.4849
		1.025E+02	3.195E-03	2.264E-02	0.1364	0.9492
0.275	6.962E+02	9.646E-03	1.250E-02	1.891E-02	0.3888	
	94.875	1.950E-03	2.292E-02	2.802E-02	0.6174	
	3.761E+02	8.681E-03	1.397E-02	1.990E-02	0.4268	
	1.395E+02	7.823E-03	2.209E-02	0.5943	0.9825	
	8.684E+02	1.181E-02	1.410E-02	3.366E-02	0.6785	
0.325	2.169E+02	1.111E-02	2.026E-02	0.1053	0.8588	
	1.703E+02	1.078E-02	2.244E-02	0.6705	0.9780	
	1.022E+02	1.292E-03	2.069E-02	2.223E-02	0.1823	
	2.128E+02	1.050E-02	1.983E-02	7.664E-02	0.8063	
	71.181	2.703E-03	3.059E-02	0.9659	0.9848	
0.375	58.465	5.937E-04	3.446E-02	0.3001	0.9341	
	1.001E+02	8.156E-03	2.793E-02	15.983	0.9988	
	74.753	4.146E-03	3.063E-02	0.2279	0.9128	
	1.947E+02	9.629E-03	1.980E-02	5.266E-02	0.6119	
	58.882	4.126E-05	3.367E-02	0.1299	0.8468	
0.425	82.974	6.712E-03	3.051E-02	0.5890	0.9563	
	1.230E+02	9.676E-03	2.572E-02	0.1852	0.8599	
	1.728E+02	7.005E-03	1.841E-02	4.068E-02	0.2507	
	1.073E+02	3.699E-03	2.207E-02	4.138E-02	0.2801	
	2.757E+02	1.392E-02	2.108E-02	0.1547	0.8322	

α_1	α_2/α_1	Term 1			Term 2	
		A_1	$\omega_{1,0}$	$\omega_{1,1}$	A_2	$\omega_{2,0}$
0.275	0.475	83.163	3.733E-03	2.738E-02	7.861E-02	0.5706
		89.198	6.804E-03	2.886E-02	0.1896	0.8283
		84.633	7.956E-03	3.120E-02	19.698	0.9983
		1.052E+02	9.491E-03	2.819E-02	0.4250	0.9229
		2.243E+02	7.293E-03	1.601E-02	4.721E-02	7.938E-02
0.525	0.525	7.197E+02	1.247E-02	1.519E-02	7.114E-02	0.3751
		84.081	4.526E-03	2.783E-02	0.1131	0.6380
		72.866	3.177E-04	2.716E-02	6.956E-02	0.3642
		1.351E+02	1.021E-02	2.471E-02	0.1805	0.7754
		91.260	8.949E-03	3.042E-02	6.609	0.9939
0.575	0.575	5.421E+02	1.187E-02	1.546E-02	8.769E-02	0.3918
		67.067	3.758E-03	3.285E-02	0.4196	0.8841
		53.424	4.579E-04	3.699E-02	0.7229	0.9332
		1.359E+02	1.168E-02	2.604E-02	1.007	0.9519
		6.249E+02	1.653E-02	1.965E-02	0.3565	0.8630
0.625	0.625	75.349	1.030E-03	2.676E-02	0.1180	0.4802
		1.331E+02	7.431E-03	2.201E-02	0.1409	0.5742
		54.409	7.161E-04	3.642E-02	5.982	0.9904
		1.027E+02	2.990E-03	2.183E-02	9.611E-02	0.3181
		55.164	8.004E-04	3.601E-02	1.633	0.9646
0.675	0.675	93.183	5.682E-03	2.642E-02	0.3866	0.8241
		59.658	1.083E-04	3.249E-02	0.4468	0.8480
		1.309E+02	9.908E-03	2.467E-02	2.229	0.9696
		5.428E+02	1.491E-02	1.847E-02	0.7214	0.9064
		1.771E+02	8.217E-03	1.911E-02	0.1606	0.5588
0.725	0.725	66.737	2.206E-04	2.901E-02	0.4499	0.8252
		97.265	5.381E-03	2.514E-02	0.8331	0.9057
		65.364	1.009E-03	3.041E-02	1.675	0.9533
		3.677E+02	1.351E-02	1.873E-02	1.094E+02	0.9993
		3.513E+02	9.188E-03	1.465E-02	0.1723	0.5213
0.775	0.775	5.668E+02	5.169E-03	8.497E-03	0.1339	0.1518
		4.610E+02	1.193E-02	1.607E-02	11.846	0.9924
		1.024E+02	4.783E-03	2.344E-02	9.531	0.9905
		3.501E+02	5.307E-03	1.072E-02	0.1440	0.2761
		1.065E+02	4.907E-03	2.283E-02	1.927	0.9530
0.825	0.825	1.373E+02	4.475E-03	1.829E-02	1.838	0.9442
		3.030E+02	7.411E-03	1.367E-02	0.5610	0.8168
		1.525E+02	3.156E-03	1.558E-02	0.2897	0.6373
		1.392E+02	4.339E-03	1.797E-02	0.9946	0.8967
		1.173E+02	3.502E-03	1.967E-02	3.813	0.9730

α_1	α_2/α_1	Term 1			Term 2	
		A_1	$\omega_{1,0}$	$\omega_{1,1}$	A_2	$\omega_{2,0}$
0.275	0.875	4.013E+03	7.403E-03	7.872E-03	0.4766	0.7547
		1.910E+02	1.783E-04	9.986E-03	0.2101	0.3962
		4.023E+02	4.568E-03	9.243E-03	0.3235	0.6320
		2.265E+02	1.826E-03	1.011E-02	0.2486	0.5081
		1.467E+02	2.172E-03	1.503E-02	2.058	0.9442
	0.925	3.207E+02	2.477E-03	8.309E-03	1.635	0.9206
		2.015E+02	6.421E-04	9.925E-03	0.9576	0.8647
		6.506E+03	4.977E-03	5.265E-03	0.7621	0.8303
		5.043E+02	2.056E-03	5.758E-03	0.3358	0.6036
		4.485E+02	3.143E-03	7.314E-03	1.147	0.8870
	0.975	6.828E+03	1.844E-04	4.549E-04	0.3065	0.5012
		8.391E+02	4.090E-04	2.619E-03	0.5523	0.7361
		2.921E+03	1.841E-03	2.476E-03	14.132	0.9898
		1.153E+03	1.250E-03	2.862E-03	2.299	0.9385
		5.607E+02	5.106E-04	3.818E-03	7.613	0.9809
0.325	0.025	4.783E+02	2.907E-04	4.472E-03	5.637E-04	0.7769
		5.777E+02	5.701E-04	4.032E-03	9.174E-04	0.8831
		6.201E+02	6.498E-04	3.875E-03	1.621E-03	0.9422
		1.081E+03	1.052E-03	2.902E-03	2.260E-04	0.3905
		1.742E+03	8.831E-04	2.031E-03	1.211E-04	0.2621
	0.075	8.118E+02	4.874E-03	7.337E-03	3.500E-03	0.7147
		3.240E+03	4.899E-03	5.516E-03	1.750E-03	0.3706
		4.612E+02	5.002E-03	9.336E-03	0.1515	0.9933
		2.411E+02	2.317E-03	1.061E-02	7.181E-03	0.8719
		2.354E+02	2.101E-03	1.059E-02	4.115E-03	0.7484
	0.125	96.095	3.832E-05	2.082E-02	1.969E-02	0.8631
		1.010E+02	6.048E-04	2.038E-02	2.108E-02	0.8713
		2.064E+02	2.776E-03	1.245E-02	4.183E-03	0.1801
		96.878	9.719E-04	2.159E-02	0.5610	0.9952
		3.573E+02	6.957E-03	1.255E-02	1.017E-02	0.7229
	0.175	1.328E+02	2.384E-03	1.739E-02	8.106E-03	0.1486
		1.180E+02	6.324E-03	2.322E-02	0.1509	0.9636
		1.202E+02	6.293E-03	2.288E-02	9.000E-02	0.9391
		1.397E+02	4.883E-03	1.916E-02	1.284E-02	0.5516
		1.363E+02	5.222E-03	1.985E-02	1.560E-02	0.6342
0.225	1.064E+02	4.021E-03	2.271E-02	1.642E-02	0.3761	
	74.572	4.304E-03	3.100E-02	0.1107	0.9170	
	5.458E+02	1.429E-02	1.793E-02	3.755E-02	0.7508	
	81.077	4.855E-03	2.941E-02	6.375E-02	0.8549	
	2.084E+02	9.903E-03	1.945E-02	2.192E-02	0.5534	

α_1	α_2/α_1	Term 1			Term 2	
		A_1	$\omega_{1,0}$	$\omega_{1,1}$	A_2	$\omega_{2,0}$
0.325	0.275	65.549	2.015E-03	3.231E-02	3.494E-02	0.5862
		65.896	5.479E-03	3.562E-02	0.2016	0.9304
		60.903	1.435E-03	3.404E-02	4.049E-02	0.6482
		1.256E+02	9.258E-03	2.507E-02	3.504E-02	0.5821
		86.368	9.051E-03	3.204E-02	0.1956	0.9279
	0.325	46.805	2.297E-03	4.461E-02	1.617	0.9878
		2.462E+02	1.450E-02	2.254E-02	4.486E-02	0.5290
		89.088	6.198E-03	2.840E-02	3.665E-02	0.4099
		84.827	1.190E-02	3.524E-02	4.913	0.9959
		76.225	5.025E-03	3.099E-02	4.097E-02	0.4837
	0.375	75.008	6.279E-03	3.256E-02	5.523E-02	0.4808
		1.927E+02	1.842E-02	2.866E-02	0.1706	0.8407
		1.182E+02	9.485E-03	2.615E-02	4.530E-02	0.3227
		75.470	1.149E-02	3.764E-02	0.3454	0.9218
		47.605	1.036E-03	4.248E-02	8.715E-02	0.6871
	0.425	67.930	1.041E-02	3.933E-02	0.2305	0.8468
		37.929	2.556E-04	5.207E-02	0.5926	0.9411
		67.095	2.341E-03	3.149E-02	5.194E-02	0.1434
		61.262	1.076E-02	4.283E-02	6.640	0.9947
		2.940E+03	2.594E-02	2.661E-02	0.7532	0.9531
	0.475	88.914	1.268E-02	3.466E-02	0.1529	0.7040
		1.235E+02	1.190E-02	2.769E-02	7.980E-02	0.3814
		1.665E+02	2.088E-02	3.263E-02	0.6157	0.9273
		51.348	6.615E-03	4.470E-02	0.2992	0.8508
		66.769	4.143E-03	3.332E-02	7.209E-02	0.2835
	0.525	49.844	8.334E-03	4.736E-02	7.080	0.9922
		69.263	6.444E-03	3.446E-02	0.1052	0.4346
		46.097	6.021E-03	4.821E-02	0.8806	0.9375
		2.238E+02	1.702E-02	2.569E-02	0.1193	0.5127
		44.645	6.073E-03	4.964E-02	4.620	0.9881
	0.575	1.171E+02	1.440E-02	3.090E-02	0.1875	0.6340
		1.839E+02	1.477E-02	2.525E-02	0.1278	0.4353
		53.915	9.109E-03	4.497E-02	1.864	0.9643
		1.454E+02	1.878E-02	3.207E-02	0.4205	0.8405
		1.216E+02	9.486E-03	2.526E-02	0.1033	0.2167
	0.625	1.595E+03	1.885E-02	2.005E-02	0.1579	0.4578
		2.029E+03	2.083E-02	2.178E-02	0.2063	0.6011
		66.766	1.934E-03	3.043E-02	0.1214	0.1973
		62.518	5.819E-03	3.649E-02	0.1975	0.5828
		2.071E+02	1.292E-02	2.214E-02	0.1320	0.3124

α_1	α_2/α_1	Term 1			Term 2	
		A_1	$\omega_{1,0}$	$\omega_{1,1}$	A_2	$\omega_{2,0}$
0.325	0.675	1.069E+02	3.582E-03	2.104E-02	0.1355	1.500E-02
		9.347E+02	1.785E-02	1.988E-02	0.2031	0.5133
		77.167	7.952E-03	3.262E-02	0.2529	0.6177
		2.845E+03	1.971E-02	2.038E-02	0.2451	0.6051
		49.897	1.852E-03	4.001E-02	0.2834	0.6620
	0.725	90.971	1.020E-02	3.098E-02	0.5348	0.7947
		1.271E+02	1.281E-02	2.768E-02	0.4707	0.7661
		9.377E+02	1.836E-02	2.037E-02	0.3664	0.6975
		99.206	9.973E-04	1.960E-02	0.1572	1.615E-02
		59.129	4.052E-03	3.601E-02	0.4322	0.7448
	0.775	1.822E+02	1.483E-02	2.512E-02	5.122	0.9755
		1.075E+02	4.470E-03	2.179E-02	0.2237	0.3817
		2.031E+02	1.539E-02	2.462E-02	5.061	0.9752
		1.406E+02	8.929E-03	2.223E-02	0.3057	0.5732
		54.763	2.072E-03	3.631E-02	1.210	0.8967
	0.825	83.454	8.192E-04	2.298E-02	0.3032	0.5021
		1.834E+02	1.134E-02	2.147E-02	3.165	0.9549
		1.285E+02	7.338E-03	2.177E-02	0.5827	0.7522
		64.035	3.458E-04	2.933E-02	0.6504	0.7787
		1.146E+02	6.788E-03	2.298E-02	0.6651	0.7843
	0.875	1.538E+02	6.059E-03	1.802E-02	1.461	0.8894
		86.763	5.602E-04	2.174E-02	0.7085	0.7713
		1.889E+02	6.326E-03	1.605E-02	0.7319	0.7774
		2.854E+02	6.089E-03	1.251E-02	0.3943	0.5763
		1.967E+02	5.582E-03	1.491E-02	0.4859	0.6601
	0.925	2.633E+02	4.032E-03	1.094E-02	1.260	0.8558
		1.580E+02	7.512E-04	1.225E-02	0.6257	0.7063
		1.355E+02	1.421E-03	1.485E-02	12.443	0.9855
2.544E+02		4.456E-03	1.161E-02	8.646	0.9792	
1.909E+02		2.313E-03	1.184E-02	0.8822	0.7948	
0.975	1.730E+03	5.889E-04	1.624E-03	0.5085	0.5888	
	9.543E+02	2.961E-04	2.177E-03	0.5108	0.5976	
	3.530E+02	4.840E-04	5.580E-03	71.981	0.9972	
	3.196E+02	1.794E-04	5.808E-03	5.453	0.9631	
	6.024E+02	6.477E-04	3.632E-03	0.9658	0.7905	
0.375	0.025	1.154E+03	1.892E-03	3.625E-03	4.565E-04	0.7144
		4.861E+03	2.404E-03	2.815E-03	4.098E-04	0.7142
		2.031E+03	2.406E-03	3.391E-03	4.411E-04	0.6494
		6.991E+02	5.262E-04	3.387E-03	1.626E-04	0.4267
		1.998E+03	2.278E-03	3.279E-03	7.562E-04	0.8524

α_1	α_2/α_1	Term 1			Term 2	
		A_1	$\omega_{1,0}$	$\omega_{1,1}$	A_2	$\omega_{2,0}$
0.375	0.075	1.801E+02	2.149E-03	1.325E-02	3.442E-03	0.6485
		1.464E+02	2.267E-03	1.592E-02	2.918E-02	0.9588
		4.025E+02	3.783E-03	8.748E-03	1.840E-03	0.1819
		2.293E+02	1.834E-03	1.055E-02	1.805E-03	0.1600
		3.828E+02	5.165E-03	1.039E-02	3.730E-03	0.6783
	0.125	1.102E+02	4.032E-03	2.215E-02	1.443E-02	0.7629
		86.697	1.448E-03	2.448E-02	1.368E-02	0.7557
		1.530E+02	7.845E-03	2.089E-02	4.991E-02	0.9313
		1.426E+02	6.905E-03	2.091E-02	3.037E-02	0.8882
		3.323E+02	6.928E-03	1.293E-02	5.190E-03	0.1602
	0.175	70.447	4.297E-03	3.259E-02	4.669E-02	0.8538
		70.608	2.921E-03	3.115E-02	2.274E-02	0.6954
		2.694E+02	8.682E-03	1.607E-02	9.912E-03	1.628E-03
		61.527	7.414E-04	3.314E-02	2.177E-02	0.6830
		1.063E+02	1.008E-02	2.883E-02	0.1997	0.9658
	0.225	49.203	3.046E-03	4.346E-02	0.1223	0.9059
		56.574	6.717E-03	4.186E-02	1.266	0.9908
		1.107E+02	1.329E-02	3.125E-02	6.379E-02	0.8152
		1.643E+02	1.620E-02	2.830E-02	6.295E-02	0.8118
		45.612	1.524E-03	4.512E-02	0.1229	0.9061
	0.275	1.646E+02	1.143E-02	2.343E-02	2.596E-02	9.041E-03
		1.981E+02	1.344E-02	2.342E-02	2.666E-02	0.1493
		41.266	1.503E-04	4.819E-02	5.787E-02	0.6921
		60.817	9.484E-03	4.208E-02	9.529E-02	0.8126
		2.026E+02	1.927E-02	2.904E-02	5.910E-02	0.6913
	0.325	1.027E+02	1.058E-02	2.973E-02	3.763E-02	0.1173
		94.480	1.577E-02	3.666E-02	7.190E-02	0.6352
		46.739	9.070E-03	5.132E-02	0.2717	0.9066
		35.825	1.354E-03	5.647E-02	0.1398	0.8192
		49.381	4.988E-03	4.495E-02	5.769E-02	0.5400
	0.375	41.355	3.546E-03	5.104E-02	8.166E-02	0.5628
		1.417E+02	1.429E-02	2.807E-02	5.080E-02	7.617E-02
		97.639	1.701E-02	3.712E-02	8.030E-02	0.5472
		52.774	8.516E-03	4.573E-02	8.018E-02	0.5495
		90.656	2.315E-02	4.483E-02	2.454	0.9859
	0.425	64.228	1.305E-02	4.344E-02	0.1011	0.5283
43.837		3.290E-03	4.776E-02	7.720E-02	0.3442	
49.122		3.138E-03	4.268E-02	6.713E-02	0.1407	
57.284		1.909E-02	5.321E-02	25.190	0.9982	
62.510		1.577E-02	4.703E-02	0.1677	0.7264	

α_1	α_2/α_1	Term 1			Term 2	
		A_1	$\omega_{1,0}$	$\omega_{1,1}$	A_2	$\omega_{2,0}$
0.375	0.475	45.234	5.028E-03	4.782E-02	9.978E-02	0.3559
		32.741	5.645E-03	6.498E-02	0.4864	0.8820
		50.394	1.597E-02	5.451E-02	0.4881	0.8819
		35.094	6.577E-03	6.193E-02	0.3312	0.8263
		66.475	8.832E-03	3.780E-02	8.600E-02	0.1388
	0.525	1.210E+02	1.564E-02	3.143E-02	0.1083	0.1698
		59.719	2.109E-02	5.338E-02	2.208	0.9675
		51.690	1.100E-02	4.825E-02	0.1650	0.5470
		53.489	5.414E-03	4.110E-02	0.1068	0.1479
		57.291	9.007E-03	4.248E-02	0.1186	0.3052
	0.575	80.598	2.522E-02	4.894E-02	3.282	0.9733
		83.067	2.130E-02	4.431E-02	0.3479	0.7460
		33.279	4.276E-03	6.173E-02	0.3471	0.7463
		1.014E+02	1.850E-02	3.729E-02	0.1767	0.4703
		47.037	4.871E-03	4.527E-02	0.1433	0.3022
0.625	94.091	2.588E-02	4.602E-02	4.533	0.9769	
	61.268	5.001E-03	3.535E-02	0.1531	8.334E-02	
	36.139	9.608E-03	6.206E-02	2.707	0.9614	
	2.301E+02	2.921E-02	3.745E-02	0.6174	0.8294	
	92.896	2.294E-02	4.333E-02	0.5792	0.8179	
0.675	1.305E+02	2.614E-02	4.051E-02	1.981	0.9375	
	1.075E+03	3.322E-02	3.496E-02	9.205	0.9866	
	2.026E+02	1.218E-02	2.116E-02	0.1794	1.786E-03	
	38.007	6.716E-03	5.608E-02	0.7061	0.8247	
	47.691	5.290E-03	4.444E-02	0.2421	0.4504	
0.725	5.450E+02	2.840E-02	3.181E-02	1.591	0.9093	
	1.064E+02	1.713E-02	3.454E-02	0.4214	0.6501	
	1.077E+02	1.935E-02	3.657E-02	0.6585	0.7796	
	43.291	6.688E-03	4.954E-02	0.6716	0.7842	
	31.987	2.269E-03	6.031E-02	7.024	0.9796	
0.775	46.689	6.926E-03	4.620E-02	1.791	0.9072	
	95.711	1.821E-02	3.737E-02	49.893	0.9967	
	45.242	4.196E-03	4.471E-02	0.7088	0.7640	
	49.203	4.817E-03	4.203E-02	0.5578	0.6973	
	69.766	1.286E-02	3.915E-02	1.310	0.8731	
0.825	54.517	2.575E-04	3.329E-02	0.4199	0.5259	
	1.932E+02	1.387E-02	2.322E-02	0.5440	0.6421	
	67.012	6.460E-03	3.344E-02	0.7283	0.7363	
	46.503	2.425E-03	4.136E-02	1.751	0.8918	
	49.607	4.136E-03	4.064E-02	2.833	0.9333	

α_1	α_2/α_1	Term 1			Term 2	
		A_1	$\omega_{1,0}$	$\omega_{1,1}$	A_2	$\omega_{2,0}$
0.375	0.875	4.299E+02	5.345E-03	9.412E-03	0.3379	0.2550
		2.781E+02	1.206E-02	1.848E-02	0.8987	0.7589
		1.232E+02	1.035E-02	2.485E-02	22.148	0.9903
		1.638E+02	9.600E-03	2.049E-02	0.8480	0.7448
		71.144	4.764E-03	2.986E-02	5.730	0.9626
	0.925	1.337E+02	1.135E-03	1.424E-02	0.5967	0.5836
		1.932E+02	6.135E-03	1.524E-02	2.648	0.9091
		1.496E+02	3.331E-03	1.507E-02	0.8892	0.7257
		1.030E+02	1.122E-03	1.818E-02	1.059	0.7705
		3.985E+02	4.210E-03	8.589E-03	0.4942	0.4835
	0.975	2.167E+02	6.411E-05	8.061E-03	21.940	0.9878
		4.371E+02	1.158E-03	5.118E-03	1.123	0.7607
		3.447E+02	9.665E-04	5.994E-03	1.827	0.8539
		6.060E+02	1.971E-03	4.826E-03	1.820	0.8518
		2.629E+02	6.654E-04	7.247E-03	30.546	0.9912
0.425	0.025	3.954E+02	2.518E-04	5.310E-03	2.332E-04	0.2994
		7.390E+02	2.300E-03	5.006E-03	1.222E-03	0.8837
		3.382E+02	3.979E-04	6.312E-03	5.182E-04	0.7334
		6.237E+02	1.095E-03	4.302E-03	2.266E-04	0.3487
		4.936E+02	2.288E-03	6.339E-03	3.655E-03	0.9491
	0.075	1.957E+02	5.415E-03	1.563E-02	6.843E-03	0.7917
		1.589E+02	5.320E-03	1.790E-02	0.4544	0.9969
		1.638E+02	5.107E-03	1.731E-02	1.547E-02	0.9069
		3.274E+02	6.661E-03	1.277E-02	4.021E-03	0.6413
		4.818E+02	7.113E-03	1.126E-02	3.069E-03	0.4930
	0.125	62.094	1.099E-03	3.324E-02	2.382E-02	0.8347
		2.244E+02	1.377E-02	2.267E-02	6.161E-02	0.9336
		1.324E+02	4.269E-03	1.933E-02	5.759E-03	1.366E-02
		2.484E+02	1.459E-02	2.263E-02	0.2351	0.9827
		2.236E+02	1.208E-02	2.100E-02	1.662E-02	0.7519
	0.175	56.125	1.405E-03	3.689E-02	1.580E-02	0.4591
		4.656E+02	1.625E-02	2.052E-02	1.451E-02	0.3593
		47.776	5.411E-04	4.223E-02	2.522E-02	0.6775
		1.079E+02	1.511E-02	3.356E-02	9.350E-02	0.9109
		1.929E+02	1.485E-02	2.517E-02	1.887E-02	0.5401
	0.225	77.090	8.976E-03	3.471E-02	2.282E-02	0.2949
		1.748E+02	2.293E-02	3.429E-02	8.074E-02	0.8242
		41.752	6.772E-03	5.434E-02	0.3520	0.9609
		52.269	2.804E-03	4.077E-02	2.239E-02	0.2958
1.035E+02		1.087E-02	3.002E-02	2.090E-02	0.1476	

α_1	α_2/α_1	Term 1			Term 2	
		A_1	$\omega_{1,0}$	$\omega_{1,1}$	A_2	$\omega_{2,0}$
0.425	0.275	1.200E+02	2.585E-02	4.234E-02	0.1672	0.8699
		69.048	1.659E-02	4.524E-02	6.907E-02	0.6813
		62.220	1.182E-02	4.359E-02	4.352E-02	0.4719
		1.704E+02	2.845E-02	4.006E-02	0.1768	0.8769
		3.675E+02	2.127E-02	2.664E-02	3.276E-02	0.1651
0.325	0.325	1.399E+02	2.950E-02	4.357E-02	0.1443	0.7819
		32.958	9.227E-03	6.898E-02	0.3498	0.9121
		51.837	2.036E-02	5.834E-02	0.4065	0.9237
		27.564	4.299E-03	7.575E-02	0.6674	0.9542
		25.930	2.748E-03	7.871E-02	7.209	0.9958
0.375	0.375	45.016	2.207E-02	6.555E-02	1.361	0.9688
		30.747	1.106E-02	7.473E-02	0.5682	0.9258
		45.024	1.643E-02	5.989E-02	0.1457	0.7048
		5.400E+02	2.919E-02	3.281E-02	7.121E-02	0.3141
		26.302	4.455E-03	7.890E-02	0.3205	0.8691
0.425	0.425	63.664	1.502E-02	4.532E-02	8.441E-02	0.1612
		36.850	5.045E-03	5.750E-02	8.640E-02	0.2258
		21.972	2.902E-04	8.881E-02	0.4637	0.8813
		31.576	8.169E-03	6.970E-02	0.1530	0.6268
		1.094E+02	2.993E-02	4.769E-02	0.1559	0.6294
0.475	0.475	24.357	2.923E-03	8.208E-02	0.2562	0.7196
		57.599	2.092E-02	5.432E-02	0.1539	0.5061
		25.840	7.710E-05	7.456E-02	0.1460	0.4846
		21.704	2.336E-03	9.122E-02	0.7122	0.9006
		1.257E+02	3.557E-02	5.090E-02	0.3053	0.7619
0.525	0.525	8.813E+02	4.316E-02	4.533E-02	0.4024	0.7745
		65.079	2.540E-02	5.470E-02	0.2294	0.5949
		40.559	1.669E-02	6.371E-02	0.2300	0.5972
		32.080	1.655E-02	7.610E-02	0.6193	0.8552
		46.869	2.760E-02	6.836E-02	1.256	0.9286
0.575	0.575	75.391	3.558E-02	6.065E-02	1.967	0.9441
		40.052	2.103E-02	6.820E-02	0.5450	0.7973
		43.834	8.264E-03	5.064E-02	0.1628	0.1250
		43.541	2.040E-02	6.377E-02	0.3634	0.6930
		4.075E+02	3.152E-02	3.612E-02	0.1874	0.3346
0.625	0.625	39.684	2.254E-02	6.961E-02	1.495	0.9116
		33.746	4.782E-05	5.407E-02	0.1935	8.611E-02
		33.162	9.952E-03	6.613E-02	0.3187	0.5698
		38.314	1.246E-02	6.102E-02	0.2874	0.5152
		85.608	3.059E-02	5.238E-02	0.4811	0.7209

α_1	α_2/α_1	Term 1			Term 2	
		A_1	$\omega_{1,0}$	$\omega_{1,1}$	A_2	$\omega_{2,0}$
0.425	0.675	31.515	7.642E-04	5.854E-02	0.2581	0.3053
		25.119	2.609E-03	7.592E-02	0.5452	0.7092
		1.496E+03	2.515E-02	2.636E-02	0.2349	0.1516
		51.616	2.764E-02	6.336E-02	31.973	0.9951
		25.934	6.553E-03	7.763E-02	0.9672	0.8381
	0.725	52.048	1.524E-02	5.000E-02	0.4434	0.5698
		56.791	4.037E-03	3.468E-02	0.2664	2.521E-02
		34.012	1.484E-02	6.827E-02	7.997	0.9771
		1.928E+02	2.438E-02	3.371E-02	0.3431	0.4159
		60.149	8.725E-03	3.821E-02	0.2795	0.1893
	0.775	66.506	1.335E-02	4.004E-02	0.4414	0.4892
		92.838	8.340E-03	2.694E-02	0.3140	0.1305
		87.385	1.416E-02	3.436E-02	0.3813	0.3857
		50.729	1.313E-02	4.830E-02	0.6624	0.6738
		43.391	6.223E-03	4.712E-02	0.4386	0.4856
	0.825	41.388	9.180E-03	5.165E-02	5.533	0.9562
		1.536E+02	2.435E-02	3.579E-02	3.849	0.9369
		6.781E+02	9.068E-03	1.153E-02	0.3523	5.976E-02
		49.522	9.991E-04	3.591E-02	0.4182	0.3520
		3.911E+02	2.576E-02	3.025E-02	1.345	0.8189
	0.875	1.200E+02	2.146E-03	1.608E-02	0.4247	0.2263
		47.466	9.520E-04	3.719E-02	0.8384	0.6660
		46.298	3.332E-03	4.058E-02	1.863	0.8521
		75.199	2.147E-03	2.472E-02	0.4965	0.3910
		45.668	4.599E-03	4.237E-02	9.516	0.9711
	0.925	1.352E+02	8.440E-03	2.095E-02	5.107	0.9396
		5.221E+02	3.700E-03	6.867E-03	0.5244	0.3393
		92.823	8.701E-04	1.896E-02	0.7297	0.5603
89.079		2.635E-03	2.157E-02	1.055	0.7028	
4.890E+02		1.335E-02	1.681E-02	2.866E+02	0.9989	
0.975	2.544E+02	2.086E-03	8.600E-03	29.376	0.9883	
	1.312E+03	1.095E-03	2.346E-03	0.7982	0.5511	
	2.977E+02	2.107E-03	7.672E-03	2.650	0.8705	
	2.215E+02	1.733E-03	9.217E-03	97.879	0.9965	
	2.107E+02	1.170E-03	9.031E-03	9.117	0.9623	
0.475	0.025	2.756E+02	9.204E-04	8.176E-03	5.247E-03	0.9716
		2.569E+02	1.151E-03	8.936E-03	5.318E-03	0.9649
		2.652E+02	8.800E-04	8.422E-03	8.744E-04	0.7798
		3.264E+02	3.217E-04	6.449E-03	2.678E-04	0.1035
		4.627E+02	1.161E-03	5.483E-03	2.552E-04	0.1601

α_1	α_2/α_1	Term 1			Term 2	
		A_1	$\omega_{1,0}$	$\omega_{1,1}$	A_2	$\omega_{2,0}$
0.475	0.075	1.200E+02	1.937E-03	1.859E-02	2.662E-03	0.3539
		1.026E+02	4.110E-03	2.358E-02	4.309E-02	0.9644
		1.174E+02	5.077E-03	2.210E-02	1.542E-02	0.8972
		74.516	9.302E-05	2.691E-02	1.378E-02	0.8876
		1.393E+02	6.923E-03	2.127E-02	0.1011	0.9846
	0.125	2.166E+02	1.532E-02	2.453E-02	1.603E-02	0.7057
		1.221E+02	8.785E-03	2.512E-02	8.241E-03	0.3841
		50.204	3.355E-04	4.008E-02	1.781E-02	0.7501
		1.136E+02	5.793E-03	2.334E-02	6.574E-03	1.775E-02
	0.175	2.559E+02	1.103E-02	1.882E-02	6.799E-03	6.464E-02
		69.852	1.540E-02	4.390E-02	8.574E-02	0.8902
		60.501	9.463E-03	4.236E-02	2.583E-02	0.6299
		73.083	1.444E-02	4.168E-02	4.478E-02	0.7901
		74.766	8.625E-03	3.523E-02	1.520E-02	0.2880
	0.225	49.515	6.294E-03	4.650E-02	2.856E-02	0.6727
		28.400	2.118E-03	7.199E-02	0.1892	0.9178
		50.493	9.956E-03	4.923E-02	3.245E-02	0.4763
		36.964	7.767E-04	5.441E-02	2.645E-02	0.3379
		44.395	1.129E-02	5.598E-02	5.856E-02	0.7237
	0.275	30.908	5.594E-03	6.979E-02	0.2894	0.9456
40.552		1.027E-02	5.894E-02	4.996E-02	0.4706	
28.813		8.715E-03	7.728E-02	0.2257	0.8912	
32.807		7.485E-03	6.768E-02	6.851E-02	0.6321	
61.231		2.720E-02	5.946E-02	0.2642	0.9048	
0.325	29.593	1.588E-04	6.685E-02	4.465E-02	0.4096	
	22.109	4.862E-03	9.372E-02	0.4480	0.9211	
	27.039	7.117E-03	7.974E-02	0.1121	0.6766	
	40.921	7.591E-03	5.519E-02	5.247E-02	2.446E-03	
	1.289E+02	3.439E-02	4.962E-02	9.749E-02	0.6124	
0.375	23.665	8.328E-03	9.134E-02	0.6284	0.9434	
	8.570E+02	3.878E-02	4.105E-02	8.756E-02	0.3514	
	28.260	1.703E-02	8.604E-02	0.2975	0.8326	
	34.140	7.289E-03	6.397E-02	7.343E-02	0.1161	
	53.196	3.227E-02	6.891E-02	0.2476	0.7954	
0.425	21.780	6.767E-03	9.633E-02	0.2927	0.8316	
	28.859	1.013E-02	7.691E-02	0.1199	0.3940	
	18.742	1.674E-04	0.1034	0.2286	0.7120	
	67.380	4.402E-02	7.271E-02	1.367	0.9511	
	69.467	4.505E-02	7.288E-02	2.274	0.9706	
67.787	2.748E-02	5.585E-02	0.1120	0.3155		

α_1	α_2/α_1	Term 1			Term 2	
		A_1	$\omega_{1,0}$	$\omega_{1,1}$	A_2	$\omega_{2,0}$
0.475	0.475	59.975	3.426E-02	6.612E-02	0.2169	0.5879
		31.667	7.579E-03	6.692E-02	0.1255	3.718E-02
		64.920	3.128E-02	6.064E-02	0.1645	0.4297
		24.378	9.403E-03	8.777E-02	0.1870	0.5208
		22.390	1.631E-02	0.1018	0.7558	0.8873
	0.525	19.947	1.292E-02	0.1078	0.9287	0.8845
		26.277	2.736E-02	9.937E-02	6.845	0.9843
		21.843	1.760E-02	0.1042	1.113	0.9034
		17.987	5.077E-03	0.1103	0.5261	0.7961
		20.545	8.845E-03	0.1009	0.3697	0.7063
	0.575	16.052	3.894E-04	0.1168	0.7372	0.8209
		20.438	1.456E-04	9.088E-02	0.2378	0.3876
		37.237	1.287E-02	6.177E-02	0.1973	9.062E-02
		70.071	2.583E-02	5.195E-02	0.2023	0.1590
		84.410	4.102E-02	6.308E-02	0.3663	0.6239
	0.625	30.827	1.324E-02	7.224E-02	0.2797	0.3524
		43.646	1.630E-02	5.740E-02	0.2433	0.1515
		19.747	4.221E-03	9.714E-02	0.4255	0.6117
		22.768	5.509E-03	8.574E-02	0.3126	0.4457
		55.418	1.763E-02	4.957E-02	0.2376	3.248E-02
	0.675	54.475	3.999E-02	7.316E-02	2.138	0.9098
		1.408E+03	3.916E-02	4.042E-02	0.3350	0.3526
		47.917	3.838E-02	7.610E-02	2.796	0.9310
		60.304	2.893E-02	5.869E-02	0.3977	0.4832
		33.551	1.622E-02	6.966E-02	0.3776	0.4510
	0.725	75.061	4.195E-02	6.558E-02	6.676	0.9661
		3.623E+02	5.189E-02	5.678E-02	18.226	0.9876
		27.736	1.119E-02	7.485E-02	0.5601	0.5815
		26.335	2.100E-02	8.838E-02	39.752	0.9943
		35.604	2.725E-02	7.707E-02	2.381	0.9050
	0.775	24.222	1.048E-02	8.221E-02	2.700	0.9028
		28.266	1.500E-02	7.645E-02	2.187	0.8798
		25.759	8.714E-03	7.607E-02	1.058	0.7496
		55.555	1.198E-02	4.235E-02	0.4139	0.2440
		27.946	5.444E-03	6.715E-02	0.5856	0.5296
	0.825	59.822	8.925E-03	3.658E-02	0.4985	0.3062
		23.294	3.496E-03	7.644E-02	6.738	0.9554
		41.079	9.678E-04	4.098E-02	0.4764	0.2516
		65.662	2.558E-02	5.144E-02	2.961	0.8981
		67.368	2.586E-02	5.106E-02	2.907	0.8961

α_1	α_2/α_1	Term 1			Term 2	
		A_1	$\omega_{1,0}$	$\omega_{1,1}$	A_2	$\omega_{2,0}$
0.475	0.875	87.616	2.155E-02	4.047E-02	37.415	0.9909
		50.442	3.797E-03	3.618E-02	0.6868	0.4666
		3.334E+03	2.994E-02	3.044E-02	5.813	0.9411
		41.847	1.076E-02	5.038E-02	8.680	0.9606
		2.445E+02	1.192E-02	1.851E-02	0.5684	0.3133
	0.925	1.096E+02	2.652E-03	1.711E-02	0.7350	0.4341
		1.267E+02	1.033E-02	2.305E-02	1.525	0.7453
		2.734E+02	1.461E-02	2.052E-02	1.940	0.8008
		92.661	2.587E-03	1.975E-02	0.7939	0.4840
		1.249E+03	1.727E-02	1.856E-02	2.215	0.8250
	0.975	2.050E+02	2.906E-03	1.056E-02	8.386	0.9488
		2.276E+02	3.668E-03	1.057E-02	44.830	0.9905
		3.599E+02	3.943E-03	8.306E-03	2.814	0.8473
		4.916E+02	4.541E-03	7.731E-03	2.733	0.8421
		4.607E+02	4.855E-03	8.266E-03	4.789	0.9105
0.525	0.025	4.862E+02	1.821E-03	5.933E-03	2.682E-04	0.2097
		4.412E+02	2.502E-03	7.035E-03	4.688E-04	0.5793
		2.535E+02	1.416E-03	9.306E-03	4.038E-03	0.9603
		3.988E+02	2.291E-03	7.306E-03	6.549E-04	0.7505
		2.530E+02	1.806E-03	9.709E-03	1.669E-03	0.8803
	0.075	1.078E+02	4.217E-03	2.275E-02	3.949E-03	0.5600
		1.083E+02	7.094E-03	2.555E-02	2.608E-02	0.9356
		6.647E+02	1.504E-02	1.805E-02	3.670E-02	0.9531
		95.865	4.670E-03	2.552E-02	7.653E-03	0.7813
		1.814E+02	1.039E-02	2.140E-02	1.415E-02	0.8792
	0.125	63.948	1.871E-03	3.304E-02	6.880E-03	3.479E-02
		66.372	7.495E-03	3.755E-02	1.284E-02	0.6074
		2.984E+02	2.437E-02	3.106E-02	1.630	0.9969
		71.099	1.073E-02	3.879E-02	2.385E-02	0.7921
		50.009	4.597E-03	4.449E-02	2.171E-02	0.7758
	0.175	67.484	2.036E-02	4.985E-02	7.424E-02	0.8609
		1.038E+02	2.280E-02	4.196E-02	3.534E-02	0.7022
		33.772	4.748E-03	6.368E-02	5.564E-02	0.8224
		60.969	1.964E-02	5.228E-02	0.1156	0.9111
		31.342	5.208E-03	6.871E-02	0.4680	0.9790
0.225	52.745	1.371E-02	5.124E-02	2.833E-02	0.2660	
	54.184	2.009E-02	5.666E-02	4.669E-02	0.6062	
	1.625E+02	3.173E-02	4.392E-02	4.426E-02	0.5762	
	28.548	1.141E-02	8.086E-02	0.5686	0.9695	
	36.594	1.923E-02	7.341E-02	0.6844	0.9742	

α_1	α_2/α_1	Term 1			Term 2	
		A_1	$\omega_{1,0}$	$\omega_{1,1}$	A_2	$\omega_{2,0}$
0.525	0.275	70.490	2.638E-02	5.431E-02	5.025E-02	0.3799
		32.421	7.238E-03	6.792E-02	4.259E-02	0.2333
		27.310	6.796E-04	7.270E-02	4.047E-02	0.1815
		33.365	1.620E-02	7.530E-02	7.652E-02	0.6305
		25.861	1.587E-02	9.215E-02	0.5835	0.9531
	0.325	59.532	2.768E-02	6.048E-02	6.835E-02	0.3089
		1.278E+02	5.456E-02	6.989E-02	1.952	0.9788
		43.962	3.522E-02	7.978E-02	0.2350	0.8246
		4.975E+02	4.352E-02	4.745E-02	7.344E-02	0.3725
		32.636	1.125E-02	7.096E-02	6.073E-02	0.1557
	0.375	1.453E+02	4.202E-02	5.534E-02	9.720E-02	0.3239
		27.609	2.956E-02	9.995E-02	0.4298	0.8679
		28.195	3.463E-02	0.1036	20.805	0.9973
		19.233	1.898E-03	0.1028	0.1094	0.4611
		56.338	3.961E-02	7.406E-02	0.1551	0.6193
	0.425	39.277	3.659E-02	8.550E-02	0.2093	0.6233
		29.058	2.299E-02	8.901E-02	0.1515	0.4603
		27.719	1.368E-02	8.236E-02	0.1149	0.1615
		22.345	1.464E-02	0.1006	0.1630	0.5112
		26.916	3.050E-02	0.1020	0.3413	0.7754
	0.475	1.151E+03	6.278E-02	6.443E-02	0.2686	0.6150
		51.924	4.990E-02	8.647E-02	0.3915	0.7416
		48.282	5.594E-02	9.529E-02	1.709	0.9416
		28.114	4.151E-02	0.1091	1.421	0.9300
		34.681	2.555E-02	7.983E-02	0.1606	0.2691
	0.525	24.334	3.255E-02	0.1095	0.5432	0.7660
		19.379	2.525E-02	0.1220	0.7373	0.8292
		79.744	5.526E-02	7.871E-02	0.3857	0.6630
		23.407	2.812E-02	0.1081	0.4110	0.6884
		26.383	1.345E-02	8.271E-02	0.1870	7.632E-02
	0.575	63.540	4.863E-02	7.751E-02	0.3684	0.5518
		15.564	9.194E-03	0.1276	0.4923	0.6792
		28.036	3.493E-02	0.1006	0.4915	0.6741
		30.372	2.235E-02	8.196E-02	0.2482	0.2362
		65.453	6.619E-02	9.434E-02	87.358	0.9982
	0.625	33.235	3.684E-02	9.106E-02	0.5089	0.6109
		19.282	1.504E-02	0.1084	0.4378	0.5435
		90.663	3.698E-02	5.628E-02	0.2907	0.1394
		76.496	6.655E-02	9.018E-02	12.009	0.9840
		27.529	4.323E-02	0.1089	2.446	0.9216

α_1	α_2/α_1	Term 1			Term 2	
		A_1	$\omega_{1,0}$	$\omega_{1,1}$	A_2	$\omega_{2,0}$
0.525	0.675	72.521	4.876E-02	7.305E-02	0.6148	0.6126
		22.141	1.101E-02	8.949E-02	0.3876	0.3231
		67.047	3.274E-02	5.834E-02	0.3587	0.2094
		28.297	2.130E-02	8.293E-02	0.4108	0.3767
		27.962	1.628E-02	7.795E-02	0.3653	0.2454
	0.725	22.540	1.068E-02	8.615E-02	0.4987	0.4004
		46.963	2.447E-02	6.014E-02	0.4347	0.2534
		57.237	4.235E-02	7.240E-02	0.7869	0.6446
		12.940	3.114E-03	0.1368	9.701	0.9722
		64.896	4.337E-02	6.986E-02	0.7491	0.6250
	0.775	67.880	2.505E-02	4.906E-02	0.5200	0.2883
		15.759	4.231E-03	0.1110	1.877	0.8308
		27.059	1.215E-02	7.328E-02	0.5992	0.4226
		43.741	4.278E-02	8.125E-02	20.945	0.9848
		44.175	4.091E-02	7.899E-02	3.979	0.9201
	0.825	19.192	1.456E-03	8.628E-02	1.177	0.6839
		25.744	2.077E-02	8.425E-02	37.770	0.9903
		18.725	5.154E-03	9.239E-02	2.392	0.8468
		1.592E+02	3.523E-02	4.541E-02	0.9212	0.5876
		30.297	1.938E-02	7.320E-02	1.617	0.7717
0.875	22.437	5.111E-03	7.569E-02	31.210	0.9867	
	56.492	8.320E-03	3.549E-02	0.7289	0.3623	
	29.280	7.961E-03	6.188E-02	1.694	0.7513	
	30.266	1.434E-02	6.667E-02	8.186E+02	0.9995	
	57.688	1.468E-02	4.176E-02	0.9355	0.5322	
0.925	1.277E+02	1.966E-02	3.164E-02	17.992	0.9739	
	82.803	1.183E-02	3.023E-02	1.676	0.7154	
	35.670	3.489E-03	4.637E-02	6.012	0.9218	
	1.393E+02	1.883E-02	2.981E-02	4.018	0.8830	
	32.541	1.380E-03	4.840E-02	5.199	0.9096	
0.975	3.821E+02	4.727E-03	8.573E-03	2.033	0.7392	
	1.649E+02	4.283E-03	1.323E-02	5.558	0.9056	
	1.906E+02	4.380E-03	1.212E-02	3.466	0.8485	
	1.172E+02	1.663E-03	1.425E-02	3.311	0.8414	
	1.817E+02	3.231E-03	1.133E-02	2.252	0.7654	
0.575	0.025	5.072E+02	4.556E-03	8.499E-03	3.078E-03	0.9382
		3.117E+02	2.394E-03	8.811E-03	5.457E-04	0.6534
		1.732E+02	8.128E-04	1.236E-02	5.361E-03	0.9664
		1.785E+02	1.124E-04	1.132E-02	6.046E-04	0.7092
		7.258E+02	3.606E-03	6.361E-03	3.432E-04	0.3793

α_1	α_2/α_1	Term 1			Term 2	
		A_1	$\omega_{1,0}$	$\omega_{1,1}$	A_2	$\omega_{2,0}$
0.575	0.075	2.827E+02	1.145E-02	1.852E-02	3.511E-03	0.4491
		1.258E+03	1.821E-02	1.980E-02	2.336E-02	0.9229
		4.532E+02	1.050E-02	1.491E-02	2.589E-03	5.590E-02
		95.705	7.565E-03	2.844E-02	1.032E-02	0.8313
		78.855	6.784E-03	3.213E-02	0.3089	0.9945
	0.125	55.299	1.368E-02	4.976E-02	0.1794	0.9715
		43.783	1.980E-03	4.754E-02	1.028E-02	0.5045
		84.899	1.283E-02	3.633E-02	1.033E-02	0.4641
		36.211	1.848E-03	5.695E-02	3.162E-02	0.8486
		39.559	5.304E-03	5.574E-02	5.523E-02	0.9111
	0.175	1.443E+02	3.417E-02	4.795E-02	7.182E-02	0.8469
		27.303	4.772E-03	7.765E-02	8.387E-02	0.8792
		44.639	1.848E-02	6.304E-02	6.679E-02	0.8398
		1.267E+02	3.467E-02	5.037E-02	0.1296	0.9155
		87.762	2.224E-02	4.489E-02	2.136E-02	0.4529
	0.225	68.790	4.089E-02	6.969E-02	1.421	0.9865
		26.527	1.641E-02	9.111E-02	0.3159	0.9419
		39.495	2.956E-02	7.973E-02	0.5556	0.9660
		30.674	3.249E-03	6.766E-02	2.620E-02	7.854E-02
		1.493E+02	3.505E-02	4.830E-02	3.660E-02	0.4288
	0.275	2.622E+02	5.426E-02	6.177E-02	0.1201	0.7437
		27.429	1.855E-02	9.037E-02	8.094E-02	0.6284
		32.953	3.252E-02	9.231E-02	0.2687	0.8888
		17.769	7.548E-03	0.1185	0.3423	0.9173
		48.410	3.014E-02	7.079E-02	6.121E-02	0.4760
	0.325	36.294	2.298E-02	7.654E-02	6.710E-02	0.1682
		14.026	5.246E-04	0.1402	0.3133	0.8679
		23.945	2.473E-02	0.1064	0.1614	0.7264
		38.429	4.997E-02	0.1009	32.403	0.9986
		14.710	2.203E-03	0.1353	0.2385	0.8254
	0.375	28.683	3.348E-02	0.1010	0.1522	0.5754
		48.585	6.363E-02	0.1035	58.159	0.9989
2.817E+02		6.074E-02	6.760E-02	0.1316	0.4868	
17.660		1.071E-02	0.1204	0.1340	0.5268	
25.432		1.509E-02	9.039E-02	9.135E-02	7.069E-02	
0.425	1.365E+02	6.086E-02	7.484E-02	0.1688	0.4518	
	30.340	3.266E-02	9.541E-02	0.1453	0.3383	
	16.326	1.937E-02	0.1367	0.2886	0.7094	
	18.202	1.508E-02	0.1200	0.1591	0.4356	
	1.349E+02	4.873E-02	6.265E-02	0.1279	4.968E-02	

α_1	α_2/α_1	Term 1			Term 2	
		A_1	$\omega_{1,0}$	$\omega_{1,1}$	A_2	$\omega_{2,0}$
0.575	0.475	13.524	2.190E-02	0.1617	1.229	0.9113
		21.360	1.714E-02	0.1040	0.1666	0.1268
		29.217	3.700E-02	0.1012	0.2017	0.3852
		15.006	2.525E-02	0.1512	0.6642	0.8348
		80.848	8.327E-02	0.1066	8.429	0.9867
	0.525	52.561	7.176E-02	0.1071	0.7393	0.8043
		26.352	4.537E-02	0.1157	0.3781	0.6090
		28.529	4.544E-02	0.1103	0.3317	0.5471
		23.030	5.586E-02	0.1365	2.523	0.9434
		17.138	1.090E-02	0.1173	0.2179	0.1914
	0.575	21.818	1.843E-02	9.841E-02	0.2683	4.979E-02
		3.019E+02	6.250E-02	6.840E-02	0.2902	0.2485
		56.838	4.498E-02	7.592E-02	0.2738	0.1177
		38.251	3.524E-02	8.078E-02	0.2707	4.649E-02
		16.818	8.786E-03	0.1136	0.2688	0.1202
	0.625	12.678	2.686E-02	0.1673	4.141	0.9471
		27.414	4.628E-02	0.1108	0.5419	0.5733
		49.572	7.569E-02	0.1115	2.059	0.8919
		36.843	5.284E-02	0.1008	0.5069	0.5390
		13.460	1.946E-02	0.1515	0.7600	0.7072
0.675	3.785E+02	5.488E-02	5.927E-02	0.4183	0.1933	
	38.411	4.576E-02	9.015E-02	0.5102	0.4223	
	42.189	4.167E-02	8.158E-02	0.4433	0.2873	
	32.045	3.916E-02	9.216E-02	0.4796	0.3712	
	68.547	5.923E-02	8.423E-02	0.5760	0.5025	
0.725	18.111	1.845E-02	0.1098	0.6282	0.4499	
	55.991	2.930E-02	5.681E-02	0.4774	3.680E-02	
	28.883	1.653E-02	6.988E-02	0.4762	3.643E-02	
	1.271E+02	8.135E-02	9.456E-02	15.158	0.9788	
	39.797	3.263E-02	7.310E-02	0.5061	0.2305	
0.775	92.360	6.802E-02	8.560E-02	5.388	0.9301	
	1.285E+02	5.885E-02	7.141E-02	1.111	0.6526	
	26.258	2.196E-02	8.212E-02	0.6676	0.3704	
	24.448	3.914E-02	0.1055	2.035	0.8141	
	18.731	3.322E-02	0.1199	4.344	0.9135	
0.825	1.694E+02	4.875E-02	5.790E-02	1.200	0.6259	
	13.527	5.558E-03	0.1212	3.247	0.8659	
	40.570	3.088E-02	6.890E-02	1.001	0.5429	
	15.126	1.323E-02	0.1167	5.051	0.9140	
	20.210	2.749E-02	0.1049	9.810	0.9557	

α_1	α_2/α_1	Term 1			Term 2	
		A_1	$\omega_{1,0}$	$\omega_{1,1}$	A_2	$\omega_{2,0}$
0.575	0.875	1.875E+02	4.336E-02	5.136E-02	3.039	0.8354
		68.618	2.595E-02	4.748E-02	1.133	0.5382
		59.771	1.953E-02	4.394E-02	0.9480	0.4292
		19.996	1.463E-02	8.978E-02	1.982E+02	0.9975
		40.985	8.440E-03	4.334E-02	0.8330	0.3164
	0.925	26.685	5.252E-03	5.911E-02	6.623	0.9150
		26.712	5.899E-03	5.971E-02	11.415	0.9507
		28.631	3.734E-03	5.376E-02	2.410	0.7644
		28.428	5.441E-03	5.595E-02	3.677	0.8466
		2.051E+02	2.706E-02	3.406E-02	3.677	0.8463
	0.975	62.968	4.846E-05	2.182E-02	5.137	0.8775
		87.504	4.069E-03	1.974E-02	2.307E+02	0.9973
		97.917	5.024E-03	1.904E-02	9.013E+02	0.9993
		2.427E+02	9.160E-03	1.481E-02	59.472	0.9894
		58.928	2.344E-04	2.351E-02	1.050E+02	0.9940
0.625	0.025	1.912E+02	2.141E-04	1.067E-02	2.967E-04	0.4252
		1.459E+02	5.252E-04	1.423E-02	3.515E-03	0.9508
		1.506E+02	9.277E-04	1.421E-02	4.866E-03	0.9629
		1.853E+02	1.017E-03	1.181E-02	7.881E-04	0.8031
		2.522E+02	2.804E-03	1.074E-02	8.003E-04	0.7667
	0.075	58.574	4.488E-03	3.861E-02	3.342E-02	0.9514
		1.654E+02	9.095E-03	2.117E-02	2.650E-03	0.1865
		66.748	3.935E-03	3.387E-02	5.556E-03	0.7059
		3.088E+02	1.222E-02	1.869E-02	2.756E-03	0.2312
		61.077	4.976E-03	3.770E-02	2.862E-02	0.9437
	0.125	60.335	8.582E-03	4.163E-02	7.730E-03	0.2295
		84.204	1.783E-02	4.151E-02	1.253E-02	0.5700
		1.211E+03	2.525E-02	2.690E-02	8.641E-03	0.2873
		82.573	2.480E-02	4.896E-02	1.918	0.9973
		34.321	1.807E-03	5.994E-02	1.540E-02	0.6965
	0.175	5.406E+02	3.384E-02	3.751E-02	1.788E-02	0.2720
		21.444	3.309E-03	9.612E-02	0.8249	0.9882
		35.736	1.472E-02	7.039E-02	3.132E-02	0.6592
		54.967	1.779E-02	5.396E-02	1.763E-02	0.2992
		28.760	9.302E-03	7.849E-02	3.809E-02	0.7309
0.225	20.285	1.467E-02	0.1124	2.050	0.9912	
	29.953	1.137E-02	7.742E-02	2.931E-02	0.2666	
	52.998	2.934E-02	6.668E-02	3.624E-02	0.4201	
	30.410	1.779E-02	8.291E-02	4.118E-02	0.5259	
	1.080E+04	5.485E-02	5.503E-02	6.276E-02	0.6814	

α_1	α_2/α_1	Term 1			Term 2	
		A_1	$\omega_{1,0}$	$\omega_{1,1}$	A_2	$\omega_{2,0}$
0.625	0.275	27.676	3.816E-02	0.1093	0.3545	0.9142
		15.454	5.837E-03	0.1334	0.1561	0.8191
		23.797	3.009E-02	0.1129	0.2076	0.8549
		25.790	2.696E-02	0.1033	9.419E-02	0.6749
		81.460	6.357E-02	8.774E-02	0.7502	0.9584
	0.325	16.292	1.673E-02	0.1368	0.1591	0.7220
		34.367	5.603E-02	0.1129	0.4605	0.8996
		40.137	5.000E-02	9.865E-02	0.1364	0.6525
		51.655	4.357E-02	8.124E-02	7.723E-02	0.3027
		3.084E+02	7.686E-02	8.320E-02	0.2276	0.7932
0.375	21.558	3.952E-02	0.1292	0.2079	0.6824	
	49.637	7.899E-02	0.1179	3.844	0.9828	
	54.078	7.367E-02	0.1094	0.4113	0.8380	
	26.392	4.496E-02	0.1182	0.1766	0.6182	
	28.282	4.005E-02	0.1083	0.1255	0.4332	
0.425	58.129	7.815E-02	0.1110	0.3483	0.7348	
	12.773	2.360E-02	0.1734	0.4597	0.8107	
	37.665	6.645E-02	0.1171	0.2875	0.6772	
	1.227E+04	9.413E-02	9.429E-02	0.3429	0.7298	
	46.976	5.511E-02	9.542E-02	0.1515	0.2973	
0.475	17.429	1.977E-02	0.1252	0.1787	8.791E-02	
	34.763	8.599E-02	0.1400	2.797	0.9567	
	82.489	8.679E-02	0.1095	0.3950	0.6856	
	17.059	3.240E-02	0.1421	0.2365	0.4591	
	24.881	4.698E-02	0.1220	0.2231	0.4043	
0.525	10.305	3.032E-02	0.2096	6.755	0.9775	
	19.743	5.481E-02	0.1480	0.4777	0.6656	
	14.781	1.511E-02	0.1364	0.2338	0.1158	
	47.583	6.877E-02	0.1071	0.2959	0.4101	
	30.358	7.362E-02	0.1342	0.5570	0.7129	
0.575	65.230	6.938E-02	9.639E-02	0.3332	0.2854	
	28.371	8.218E-02	0.1456	1.326	0.8487	
	25.837	5.172E-02	0.1203	0.3485	0.3447	
	41.214	7.524E-02	0.1187	0.4721	0.5540	
	31.169	8.883E-02	0.1466	2.296	0.9128	
0.625	38.228	6.282E-02	0.1077	0.4413	0.3554	
	20.724	2.965E-02	0.1083	0.3784	2.340E-02	
	15.278	6.351E-02	0.1782	6.313	0.9607	
	49.775	9.719E-02	0.1323	1.904	0.8683	
	25.795	4.171E-02	0.1064	0.3840	0.1373	

α_1	α_2/α_1	Term 1			Term 2	
		A_1	$\omega_{1,0}$	$\omega_{1,1}$	A_2	$\omega_{2,0}$
0.625	0.675	10.913	9.594E-03	0.1624	0.5638	0.4106
		31.645	8.657E-02	0.1401	3.100	0.9011
		52.061	5.252E-02	8.295E-02	0.4683	0.1127
		30.432	8.731E-02	0.1430	4.538	0.9326
		19.924	7.625E-02	0.1613	30.455	0.9900
	0.725	20.129	2.557E-02	0.1014	0.5673	0.1645
		34.584	4.867E-02	9.399E-02	0.6149	0.2967
		13.875	6.980E-03	0.1159	0.5571	0.1221
		1.341E+02	9.270E-02	0.1048	1.600	0.7668
		3.325E+02	6.121E-02	6.581E-02	0.5715	0.1730
	0.775	18.921	9.880E-03	8.366E-02	0.6534	7.546E-02
		14.659	2.838E-02	0.1341	1.168	0.6151
		11.087	5.793E-03	0.1446	0.9220	0.4994
		2.549E+02	5.887E-02	6.472E-02	0.7317	0.3043
		10.661	1.220E-02	0.1583	1.364	0.6755
	0.825	1.498E+02	6.123E-02	7.104E-02	1.284	0.5874
		2.360E+02	8.129E-02	8.761E-02	14.204	0.9641
		18.135	8.491E-03	8.565E-02	0.8252	0.2721
		13.271	3.057E-03	0.1120	0.9649	0.4252
		85.454	5.838E-02	7.561E-02	1.331	0.6031
	0.875	29.625	3.686E-02	8.451E-02	3.434	0.8287
		1.518E+02	5.371E-02	6.300E-02	2.612	0.7738
		17.286	1.630E-02	9.772E-02	2.211	0.7319
		41.585	3.326E-02	6.675E-02	1.481	0.5899
		15.331	2.047E-02	0.1128	30.314	0.9807
	0.925	48.219	2.125E-02	4.875E-02	2.333	0.7111
		35.537	2.435E-02	6.197E-02	64.814	0.9898
		38.767	9.927E-03	4.349E-02	1.465	0.5228
		1.704E+02	9.523E-03	1.680E-02	1.099	0.3090
		55.057	1.770E-02	4.151E-02	1.640	0.5799
	0.975	1.519E+02	8.224E-03	1.646E-02	3.442	0.7827
		1.799E+02	1.062E-02	1.760E-02	6.393	0.8837
		76.094	1.379E-03	1.771E-02	2.338	0.6762
		79.847	4.134E-04	1.592E-02	2.071	0.6323
		44.135	1.181E-03	2.968E-02	32.469	0.9771
	0.675	0.025	1.975E+02	1.491E-03	1.162E-02	3.619E-04
5.050E+02			6.116E-03	1.008E-02	9.531E-03	0.9828
3.743E+02			4.981E-03	1.032E-02	8.933E-04	0.8020
1.478E+02			1.090E-03	1.463E-02	2.350E-03	0.9366
5.481E+03			5.355E-03	5.719E-03	2.653E-04	4.551E-02

α_1	α_2/α_1	Term 1			Term 2	
		A_1	$\omega_{1,0}$	$\omega_{1,1}$	A_2	$\omega_{2,0}$
0.675	0.075	88.762	5.188E-03	2.770E-02	2.291E-03	0.1634
		93.408	4.845E-03	2.623E-02	2.195E-03	5.339E-03
		61.604	7.044E-04	3.314E-02	2.248E-03	0.3041
		72.980	1.069E-02	3.807E-02	5.536E-02	0.9714
		1.416E+02	1.292E-02	2.703E-02	3.899E-03	0.5600
	0.125	1.773E+02	3.185E-02	4.310E-02	2.543E-02	0.8020
		54.430	1.058E-02	4.722E-02	7.636E-03	0.3064
		28.765	5.264E-03	7.464E-02	0.7301	0.9942
		1.513E+02	2.119E-02	3.436E-02	7.520E-03	0.1711
		99.505	2.938E-02	4.943E-02	4.959E-02	0.8996
	0.175	37.560	2.527E-02	7.824E-02	5.225E-02	0.8055
		51.994	2.118E-02	5.942E-02	1.672E-02	0.2916
		2.778E+02	5.097E-02	5.813E-02	9.544E-02	0.8883
		73.986	2.820E-02	5.508E-02	1.814E-02	0.3544
		2.099E+02	3.302E-02	4.248E-02	1.576E-02	0.1107
	0.225	28.681	2.436E-02	9.345E-02	4.488E-02	0.5884
		17.625	3.687E-03	0.1162	4.810E-02	0.6608
		17.658	1.581E-02	0.1281	48.544	0.9997
		29.610	2.191E-02	8.881E-02	3.565E-02	0.4644
		40.988	2.878E-02	7.708E-02	3.213E-02	0.3628
	0.275	16.504	2.203E-02	0.1415	0.2138	0.8694
		23.321	2.605E-02	0.1105	6.190E-02	0.5083
		43.252	5.814E-02	0.1037	0.1758	0.8271
		16.517	1.403E-02	0.1334	8.512E-02	0.6727
		50.071	5.962E-02	9.895E-02	0.1445	0.7887
	0.325	12.146	1.053E-03	0.1624	9.844E-02	0.5847
		17.538	4.315E-02	0.1547	0.6874	0.9359
		1.364E+02	7.767E-02	9.198E-02	0.1277	0.6253
		38.501	7.225E-02	0.1230	0.4647	0.9011
		28.821	3.765E-02	0.1052	7.370E-02	0.2823
	0.375	11.726	3.007E-03	0.1681	0.1105	0.4226
		29.857	5.062E-02	0.1151	0.1140	0.3423
		30.158	5.281E-02	0.1167	0.1200	0.3890
		14.084	5.727E-03	0.1418	9.011E-02	7.837E-02
		37.677	5.247E-02	0.1034	0.1040	0.2066
	0.425	9.638	2.621E-02	0.2249	2.805	0.9695
18.143		3.465E-02	0.1389	0.1438	0.2385	
35.015		5.314E-02	0.1064	0.1411	3.846E-02	
87.973		7.373E-02	9.511E-02	0.1458	0.1806	
20.940		6.726E-02	0.1584	0.3836	0.7592	

α_1	α_2/α_1	Term 1			Term 2	
		A_1	$\omega_{1,0}$	$\omega_{1,1}$	A_2	$\omega_{2,0}$
0.675	0.475	1.797E+02	0.1293	0.1397	2.937	0.9571
		20.000	4.222E-02	0.1339	0.1901	0.1198
		33.714	6.219E-02	0.1166	0.1953	0.1596
		25.770	6.845E-02	0.1408	0.2564	0.4758
		3.309E+02	0.1338	0.1395	11.247	0.9888
	0.525	14.468	4.008E-02	0.1655	0.2815	0.3390
		31.506	0.1098	0.1680	1.946	0.9146
		1.198E+02	0.1092	0.1245	0.4215	0.5871
		20.359	8.089E-02	0.1709	0.6093	0.7254
		36.247	8.512E-02	0.1354	0.3432	0.4783
	0.575	13.113	3.282E-02	0.1654	0.3371	0.2238
		29.022	6.046E-02	0.1185	0.3323	4.679E-02
		60.324	0.1129	0.1424	0.7227	0.6963
		29.491	7.443E-02	0.1338	0.3713	0.3274
		9.846	2.946E-02	0.2106	0.4960	0.5627
	0.625	13.370	4.156E-02	0.1679	0.4656	0.3313
		47.492	6.947E-02	0.1029	0.4233	2.571E-02
		9.504	4.449E-02	0.2267	1.196	0.7757
		20.935	5.368E-02	0.1318	0.4243	0.1421
		47.203	7.672E-02	0.1116	0.4309	0.1741
	0.675	98.954	0.1041	0.1206	0.7371	0.5067
		28.096	6.446E-02	0.1205	0.5427	0.2155
		21.300	8.568E-02	0.1633	1.064	0.6742
		11.636	4.297E-02	0.1841	0.7269	0.5083
		53.792	9.110E-02	0.1213	0.6477	0.4183
	0.725	11.583	5.551E-02	0.1922	1.651	0.7477
		30.587	0.1005	0.1523	2.066	0.7979
		20.267	5.413E-02	0.1289	0.7023	0.3085
		25.744	8.752E-02	0.1487	1.324	0.6797
		7.087	2.663E-02	0.2515	6.921	0.9413
	0.775	9.719	3.025E-02	0.1840	1.502	0.6635
		13.720	3.560E-02	0.1415	0.9362	0.4154
		18.754	3.525E-02	0.1089	0.7859	0.2118
		14.380	1.437E-02	0.1041	0.7518	5.643E-02
		12.703	6.224E-02	0.1806	4.386	0.8869
	0.825	23.842	6.637E-02	0.1254	2.424	0.7556
		11.308	1.390E-02	0.1342	1.116	0.4268
		23.370	6.807E-02	0.1284	2.864	0.7940
		25.818	6.953E-02	0.1241	2.585	0.7711
		67.615	8.822E-02	0.1091	3.015	0.8043

α_1	α_2/α_1	Term 1			Term 2	
		A_1	$\omega_{1,0}$	$\omega_{1,1}$	A_2	$\omega_{2,0}$
0.675	0.875	78.840	6.993E-02	8.666E-02	4.122	0.8347
		22.831	3.733E-02	9.420E-02	1.792	0.6085
		16.407	1.367E-02	9.019E-02	1.265	0.4116
		57.274	6.658E-02	8.959E-02	3.997	0.8295
		30.531	2.953E-03	3.870E-02	1.007	9.792E-02
	0.925	31.457	1.520E-02	5.282E-02	1.672	0.5116
		18.337	1.332E-02	7.974E-02	2.911	0.7314
		19.759	5.917E-03	6.614E-02	1.759	0.5394
		90.370	4.840E-02	6.199E-02	26.979	0.9714
		29.647	1.962E-02	6.015E-02	2.015	0.6038
	0.975	42.744	5.819E-03	3.235E-02	9.664	0.9104
		1.318E+02	1.362E-02	2.221E-02	6.013	0.8556
		32.879	1.532E-04	3.454E-02	4.936	0.8238
		3.581E+02	1.799E-02	2.116E-02	17.511	0.9506
		66.175	1.026E-02	2.739E-02	8.618	0.8994
0.725	0.025	7.475E+02	7.515E-03	1.019E-02	1.267E-03	0.8676
		1.805E+02	3.760E-03	1.484E-02	3.033E-02	0.9949
		4.427E+02	4.749E-03	9.267E-03	3.332E-04	0.5492
		8.653E+02	4.665E-03	6.976E-03	2.056E-04	0.2018
		5.744E+02	6.367E-03	9.848E-03	1.344E-03	0.8988
	0.075	2.065E+02	2.072E-02	3.039E-02	1.220E-02	0.8790
		67.774	3.871E-03	3.336E-02	2.064E-03	0.3110
		88.878	1.016E-02	3.264E-02	3.252E-03	0.5571
		92.231	8.459E-03	3.013E-02	2.343E-03	0.3560
		63.157	2.694E-03	3.434E-02	2.008E-03	0.3338
	0.125	27.770	7.390E-03	7.928E-02	1.460	0.9975
		56.227	2.034E-02	5.584E-02	1.350E-02	0.6821
		1.932E+02	3.100E-02	4.133E-02	1.051E-02	0.5589
		51.868	8.949E-03	4.740E-02	5.720E-03	2.587E-02
		50.958	2.332E-02	6.248E-02	4.773E-02	0.9110
	0.175	17.998	1.635E-03	0.1124	6.938E-02	0.8952
		24.368	1.159E-02	9.333E-02	2.656E-02	0.6906
		34.728	2.991E-02	8.725E-02	6.712E-02	0.8665
		2.133E+02	3.615E-02	4.546E-02	1.402E-02	5.059E-02
		47.917	3.964E-02	8.119E-02	0.1107	0.9165
	0.225	89.529	5.965E-02	8.180E-02	6.335E-02	0.7259
		35.633	4.431E-02	9.997E-02	7.435E-02	0.7748
		26.790	2.790E-02	0.1019	3.959E-02	0.5841
		31.405	2.815E-02	9.127E-02	2.980E-02	0.4071
38.392		3.995E-02	9.159E-02	4.245E-02	0.5959	

α_1	α_2/α_1	Term 1			Term 2	
		A_1	$\omega_{1,0}$	$\omega_{1,1}$	A_2	$\omega_{2,0}$
0.725	0.275	75.818	5.156E-02	7.744E-02	4.219E-02	9.655E-02
		44.727	7.623E-02	0.1203	2.500	0.9889
		91.032	8.326E-02	0.1049	0.2829	0.9009
		14.269	2.029E-02	0.1588	0.1588	0.8473
		1.500E+02	8.790E-02	0.1010	0.3037	0.9075
	0.325	25.629	7.660E-02	0.1530	2.673	0.9843
		39.449	7.265E-02	0.1222	0.1285	0.6606
		44.353	7.733E-02	0.1214	0.1439	0.6981
		21.909	4.340E-02	0.1327	8.256E-02	0.4681
		82.847	6.719E-02	9.068E-02	6.801E-02	0.2159
	0.375	11.445	3.931E-02	0.2091	0.5332	0.8929
		13.342	2.771E-02	0.1730	0.1163	0.4768
		27.213	6.323E-02	0.1342	0.1184	0.4280
		26.902	5.849E-02	0.1302	0.1061	0.3321
		61.835	7.093E-02	0.1019	9.707E-02	0.1183
	0.425	9.881	3.687E-05	0.1926	0.1148	0.1485
		33.977	6.917E-02	0.1246	0.1382	0.1459
		8.014	1.252E-02	0.2526	0.4011	0.8109
		13.022	6.032E-02	0.2074	0.4622	0.8164
		9.225	4.153E-02	0.2496	5.051	0.9840
	0.475	17.186	6.595E-02	0.1747	0.2335	0.4356
		14.717	6.490E-02	0.1923	0.2869	0.5657
		8.975	1.816E-02	0.2279	0.2252	0.4777
		14.827	4.448E-02	0.1691	0.1863	0.1814
		9.247	2.982E-02	0.2336	0.2963	0.6103
	0.525	31.538	0.1009	0.1586	0.3348	0.4587
		2.538E+02	0.1211	0.1282	0.3067	0.3824
		32.895	8.509E-02	0.1392	0.2636	0.1631
		2.074E+02	0.1463	0.1552	0.6635	0.7454
		6.586	2.993E-02	0.3109	4.696	0.9681
	0.575	38.931	0.1376	0.1832	0.9935	0.7764
		1.343E+02	0.1073	0.1199	0.3497	0.1260
		14.585	9.842E-02	0.2205	0.9141	0.7599
		10.476	3.189E-02	0.1939	0.3309	8.542E-02
		9.573	3.717E-02	0.2209	0.3715	0.3511
	0.625	63.810	0.1101	0.1360	0.4782	0.2673
		16.805	6.810E-02	0.1646	0.4514	0.1604
		7.739	5.556E-02	0.2783	1.301	0.7876
		7.222	4.004E-03	0.2298	0.4216	0.1239
		36.227	9.088E-02	0.1351	0.4525	0.1165

α_1	α_2/α_1	Term 1			Term 2	
		A_1	$\omega_{1,0}$	$\omega_{1,1}$	A_2	$\omega_{2,0}$
0.725	0.675	63.578	9.083E-02	0.1134	0.5765	2.148E-02
		1.056E+02	9.900E-02	0.1129	0.5748	8.025E-02
		8.610	4.640E-02	0.2344	0.7490	0.4905
		9.739	4.791E-02	0.2114	0.6423	0.3658
		43.993	9.635E-02	0.1310	0.5842	0.1855
	0.725	17.363	7.875E-02	0.1642	0.8186	0.3695
		32.494	0.1014	0.1473	0.8548	0.4056
		23.175	8.674E-02	0.1503	0.7964	0.3382
		15.351	0.1043	0.2048	1.801	0.7458
		15.356	5.211E-02	0.1397	0.7075	7.352E-02
	0.775	29.715	8.045E-02	0.1259	0.9516	0.3167
		17.148	4.115E-02	0.1096	0.8557	3.439E-02
		39.841	0.1214	0.1575	2.005	0.7189
		23.087	5.957E-02	0.1143	0.8683	0.1509
		32.130	0.1228	0.1676	2.623	0.7872
	0.825	18.864	4.437E-02	0.1075	1.070	0.2440
		6.408	1.845E-02	0.2266	2.330	0.7142
		13.894	1.371E-02	8.789E-02	1.004	3.460E-02
		8.295	2.453E-02	0.1805	1.389	0.4920
		27.759	6.596E-02	0.1109	1.180	0.3629
0.875	8.257E+02	0.1045	0.1060	7.119	0.8910	
	11.137	3.136E-02	0.1388	1.983	0.5948	
	8.881	3.517E-03	0.1325	1.433	0.4039	
	20.986	3.488E-02	8.836E-02	1.357	0.3534	
	16.166	7.015E-02	0.1460	11.479	0.9325	
0.925	35.352	4.448E-02	7.556E-02	3.200	0.7183	
	26.743	1.886E-02	5.768E-02	1.723	0.4419	
	17.753	4.141E-02	0.1041	36.103	0.9754	
	9.783	2.600E-03	0.1146	2.872	0.6851	
	19.273	3.388E-02	9.112E-02	3.734	0.7598	
0.975	22.185	4.023E-03	4.920E-02	86.867	0.9885	
	46.572	1.275E-02	3.419E-02	6.490	0.8457	
	1.032E+02	1.855E-02	2.823E-02	6.664	0.8497	
	26.788	6.627E-03	4.399E-02	12.749	0.9216	
	19.949	1.158E-03	5.140E-02	39.059	0.9745	
0.775	0.025	1.807E+02	3.191E-03	1.426E-02	9.474E-04	0.8861
		2.156E+02	4.953E-03	1.423E-02	9.314E-02	0.9987
		1.711E+02	1.034E-03	1.272E-02	1.882E-04	0.4289
		2.368E+02	2.221E-03	1.067E-02	1.687E-04	0.3141
		2.466E+02	3.945E-03	1.206E-02	5.431E-04	0.8143

α_1	α_2/α_1	Term 1			Term 2	
		A_1	$\omega_{1,0}$	$\omega_{1,1}$	A_2	$\omega_{2,0}$
0.775	0.075	56.990	3.353E-03	3.843E-02	1.939E-03	0.5093
		76.216	7.276E-03	3.350E-02	1.856E-03	0.3861
		71.780	9.529E-03	3.738E-02	3.257E-03	0.6726
		61.173	6.842E-03	3.952E-02	3.021E-03	0.6618
		77.667	1.148E-02	3.722E-02	4.069E-03	0.7321
	0.125	36.947	7.265E-03	6.131E-02	5.458E-03	0.4325
		34.885	5.909E-03	6.316E-02	5.518E-03	0.4611
		1.285E+02	2.383E-02	3.935E-02	5.315E-03	0.1100
		1.863E+02	2.981E-02	4.053E-02	6.454E-03	0.3731
		25.739	2.225E-03	7.983E-02	1.659E-02	0.8474
	0.175	42.403	3.241E-02	7.940E-02	2.126E-02	0.6440
		84.196	3.287E-02	5.650E-02	1.151E-02	0.1245
		30.477	1.012E-02	7.548E-02	9.362E-03	0.1215
		24.006	1.024E-02	9.329E-02	1.482E-02	0.5728
		89.196	5.179E-02	7.413E-02	5.397E-02	0.8555
	0.225	43.629	5.827E-02	0.1038	9.386E-02	0.8509
		66.686	4.439E-02	7.412E-02	2.171E-02	0.1920
		33.306	4.132E-02	0.1010	3.553E-02	0.6081
		24.554	2.409E-02	0.1050	2.410E-02	0.4438
		70.464	5.896E-02	8.714E-02	4.080E-02	0.6442
	0.275	27.432	7.000E-02	0.1421	1.233	0.9816
		16.414	3.499E-02	0.1556	0.1073	0.8085
		53.278	5.575E-02	9.276E-02	3.727E-02	0.2419
		99.364	7.710E-02	9.698E-02	5.869E-02	0.5814
		22.535	3.161E-02	0.1193	3.568E-02	0.3197
	0.325	1.340E+02	0.1101	0.1247	0.2228	0.8343
		44.228	8.606E-02	0.1304	0.1156	0.6784
		14.332	9.935E-03	0.1465	4.297E-02	1.116E-02
		11.461	2.259E-02	0.1945	0.1187	0.7497
		24.785	4.522E-02	0.1241	5.329E-02	0.1631
	0.375	11.123	1.302E-02	0.1883	7.112E-02	0.2968
		39.066	8.075E-02	0.1303	9.387E-02	0.3334
		7.632	1.249E-02	0.2692	4.008	0.9898
		10.911	3.780E-02	0.2168	0.1915	0.7546
		17.495	6.146E-02	0.1727	0.1230	0.5652
	0.425	8.040	3.330E-02	0.2739	0.5467	0.8807
		31.959	9.808E-02	0.1580	0.1644	0.4877
		21.423	9.199E-02	0.1816	0.2111	0.6233
		1.012E+02	0.1473	0.1663	0.6801	0.8837
		27.903	8.438E-02	0.1528	0.1345	0.3281

α_1	α_2/α_1	Term 1			Term 2	
		A_1	$\omega_{1,0}$	$\omega_{1,1}$	A_2	$\omega_{2,0}$
0.775	0.475	32.384	0.1428	0.2011	0.8299	0.8660
		17.580	0.1104	0.2180	0.4933	0.7774
		11.002	5.945E-02	0.2315	0.2383	0.5488
		20.018	8.885E-02	0.1827	0.2040	0.4026
		1.047E+02	0.1143	0.1320	0.1795	0.1804
	0.525	6.954	5.938E-02	0.3273	2.026	0.9324
		19.273	8.187E-02	0.1741	0.2422	7.803E-02
		34.231	0.1003	0.1518	0.2473	3.902E-02
		8.456	5.144E-02	0.2708	0.3442	0.5788
		41.013	0.1089	0.1524	0.2474	0.1351
	0.575	6.453	7.539E-03	0.2820	0.2888	0.2077
		20.235	0.1099	0.1969	0.3768	0.3615
		1.030E+02	0.1290	0.1455	0.3416	0.1299
		12.914	0.1320	0.2709	1.766	0.8836
		6.669	4.067E-02	0.3116	0.4989	0.6131
	0.625	56.527	0.1207	0.1482	0.4612	2.987E-02
		8.268	0.1082	0.3173	2.746	0.9015
		8.770	0.1146	0.3116	2.873	0.9053
		5.513	5.129E-02	0.3676	1.732	0.8522
		9.803	6.439E-02	0.2328	0.4481	0.2216
	0.675	7.345	9.061E-02	0.3138	1.549	0.7674
		7.985	6.311E-02	0.2622	0.6570	0.3753
		43.821	0.1248	0.1589	0.6059	0.1693
		7.442	5.619E-02	0.2702	0.6539	0.3768
		1.194E+02	0.1453	0.1582	0.6368	0.2858
	0.725	9.994	8.792E-02	0.2356	0.9223	0.4320
		9.880	6.349E-02	0.1987	0.7609	0.1277
		11.790	8.132E-02	0.1996	0.7836	0.2278
		6.855	3.724E-02	0.2385	0.7560	0.1790
		16.348	8.833E-02	0.1690	0.7671	0.1124
	0.775	66.967	0.1047	0.1223	0.9594	0.1418
		19.345	7.771E-02	0.1359	0.9524	8.193E-02
73.290		9.260E-02	0.1072	0.9563	2.457E-02	
5.806		4.229E-02	0.2788	1.295	0.5160	
17.323		9.114E-02	0.1637	0.9974	0.2547	
0.825	38.191	7.406E-02	0.1007	1.155	0.1497	
	22.543	4.689E-02	8.562E-02	1.141	1.232E-02	
	19.907	5.632E-02	0.1054	1.144	0.1062	
	12.577	5.651E-02	0.1427	1.191	0.2307	
	30.526	6.716E-02	9.972E-02	1.148	0.1240	

α_1	α_2/α_1	Term 1			Term 2	
		A_1	$\omega_{1,0}$	$\omega_{1,1}$	A_2	$\omega_{2,0}$
0.775	0.875	2.086E+02	0.1429	0.1483	36.995	0.9765
		13.021	2.842E-02	9.966E-02	1.395	0.2314
		23.594	7.195E-02	0.1162	1.704	0.4397
		31.661	9.523E-03	3.189E-02	1.312	1.528E-02
		31.941	5.549E-02	8.544E-02	1.435	0.2728
	0.925	1.085E+02	7.582E-02	8.480E-02	3.646	0.7188
		16.319	4.072E-02	9.917E-02	2.613	0.5996
		39.254	5.369E-02	7.772E-02	2.405	0.5607
		5.429	1.623E-03	0.1843	7.794	0.8706
		9.497	3.670E-02	0.1406	5.729	0.8231
	0.975	22.100	9.866E-03	4.840E-02	5.436	0.7888
		76.237	2.788E-02	3.914E-02	11.613	0.9017
		34.831	1.739E-02	4.186E-02	5.738	0.8000
		19.899	9.280E-03	5.222E-02	6.437	0.8220
		18.469	9.591E-03	5.602E-02	9.201	0.8758
0.825	0.025	1.978E+02	2.984E-03	1.310E-02	3.094E-04	0.7712
		1.751E+02	3.035E-03	1.445E-02	3.051E-03	0.9783
		1.652E+02	2.605E-03	1.471E-02	1.045E-03	0.9358
		2.547E+02	3.356E-03	1.121E-02	1.588E-04	0.4431
		1.838E+02	3.229E-03	1.411E-02	4.663E-03	0.9859
	0.075	84.765	1.231E-02	3.590E-02	2.424E-03	0.6739
		66.776	7.224E-03	3.716E-02	1.652E-03	0.5725
		86.830	1.734E-02	4.036E-02	2.433	0.9997
		59.417	5.309E-03	3.896E-02	1.666E-03	0.6215
		69.352	1.371E-02	4.254E-02	4.856E-02	0.9843
	0.125	24.135	6.298E-04	8.344E-02	4.479E-02	0.9681
		31.964	1.402E-03	6.392E-02	2.892E-03	0.4471
		74.254	3.542E-02	6.232E-02	1.911	0.9987
		37.734	1.361E-02	6.655E-02	7.107E-03	0.7055
		50.956	2.856E-02	6.776E-02	0.2002	0.9878
	0.175	26.489	1.147E-02	8.681E-02	7.940E-03	0.4493
		29.992	2.265E-02	8.917E-02	1.351E-02	0.6425
		45.433	2.805E-02	7.194E-02	9.146E-03	0.3671
		62.634	4.483E-02	7.667E-02	2.122E-02	0.7354
		79.787	5.538E-02	8.038E-02	9.806E-02	0.9422
	0.225	22.250	1.840E-02	0.1079	1.421E-02	0.3820
		44.872	6.219E-02	0.1065	7.244E-02	0.8593
		39.277	3.377E-02	8.437E-02	1.441E-02	0.1109
		30.416	4.362E-02	0.1091	3.131E-02	0.6896
36.634		4.416E-02	9.848E-02	2.249E-02	0.5447	

α_1	α_2/α_1	Term 1			Term 2	
		A_1	$\omega_{1,0}$	$\omega_{1,1}$	A_2	$\omega_{2,0}$
0.825	0.275	13.250	2.866E-02	0.1786	0.2385	0.9455
		22.054	3.762E-02	0.1276	2.896E-02	0.4351
		1.709E+02	8.508E-02	9.667E-02	4.262E-02	0.5694
		41.795	5.705E-02	0.1044	2.901E-02	0.3335
		54.326	5.462E-02	9.098E-02	2.585E-02	4.726E-02
	0.325	13.610	3.521E-02	0.1805	6.175E-02	0.6420
		67.644	0.1053	0.1345	0.1167	0.7625
		19.259	3.867E-02	0.1410	3.691E-02	0.2071
		35.565	6.892E-02	0.1243	4.587E-02	0.3290
		26.871	5.259E-02	0.1258	3.944E-02	0.1426
	0.375	11.683	6.862E-02	0.2368	1.903	0.9813
		24.362	6.442E-02	0.1444	6.111E-02	0.1393
51.282		8.231E-02	0.1201	6.464E-02	6.745E-03	
69.484		9.109E-02	0.1191	6.506E-02	0.1308	
36.064		8.629E-02	0.1404	7.098E-02	0.3341	
0.425	53.945	0.1126	0.1484	0.1075	0.3389	
	8.626	1.203E-02	0.2388	7.259E-02	0.3920	
	10.979	5.806E-02	0.2354	0.1447	0.6351	
	34.789	0.1011	0.1566	0.1039	0.3121	
	17.956	8.267E-02	0.1906	0.1151	0.4575	
0.475	22.183	0.1247	0.2108	0.2359	0.6210	
	51.147	0.1215	0.1584	0.1459	0.2230	
	54.510	0.1323	0.1672	0.1638	0.3820	
	28.961	0.1566	0.2226	0.6291	0.8603	
	11.530	7.245E-02	0.2386	0.1654	0.4913	
0.525	48.878	0.1269	0.1638	0.2074	4.184E-02	
	31.890	0.1171	0.1737	0.2051	4.818E-02	
	9.465	0.1191	0.3182	2.179	0.9470	
	8.449E+02	0.1844	0.1866	0.3412	0.6141	
	13.619	8.792E-02	0.2239	0.1978	0.2488	
0.575	14.931	0.1140	0.2339	0.3018	0.3052	
	1.454E+03	0.2222	0.2234	0.9186	0.8048	
	9.817	7.656E-02	0.2587	0.2715	0.2190	
	87.850	0.1563	0.1764	0.2984	0.2023	
	20.612	0.1626	0.2509	0.5329	0.6602	
0.625	8.689	0.1133	0.3153	0.6026	0.5937	
	6.466	4.289E-02	0.3042	0.3555	0.1269	
	14.579	0.1116	0.2223	0.4108	5.853E-02	
	3.801	1.328E-02	0.4929	1.961	0.9096	
	39.865	0.1450	0.1848	0.4227	2.475E-02	

α_1	α_2/α_1	Term 1			Term 2	
		A_1	$\omega_{1,0}$	$\omega_{1,1}$	A_2	$\omega_{2,0}$
0.825	0.675	28.881	0.1834	0.2397	0.7480	0.5018
		54.643	0.2108	0.2409	0.9489	0.6241
		18.554	0.1316	0.2106	0.5786	7.503E-02
		15.417	0.9779	1.000	1.368E+02	0.2658
		4.373	1.853E-02	0.4052	0.5575	0.4457
	0.725	29.591	0.1692	0.2181	0.8499	0.3480
		0.7790	0.1243	1.000	14.148	0.1233
		5.538	0.1246	0.4059	3.754	0.8821
		28.053	0.2286	0.2833	2.924	0.8410
		6.765	9.188E-02	0.3110	0.8439	0.3861
	0.775	5.559	0.1292	0.3815	4.638	0.8712
		10.887	0.1663	0.2929	2.074	0.7002
		86.872	0.1407	0.1529	1.022	8.296E-02
		44.500	0.2088	0.2396	1.899	0.6679
		6.333	0.1004	0.3136	1.334	0.5130
	0.825	8.398	7.629E-02	0.1927	1.293	0.2095
		61.476	9.168E-02	0.1038	1.274	1.353E-02
		6.609	4.943E-02	0.1786	1.263	9.215E-02
		31.408	9.137E-02	0.1165	1.268	4.640E-02
		11.204	0.1680	0.2765	4.408	0.8221
	0.875	23.647	1.917E-02	4.164E-02	1.485	1.103E-02
		8.333	1.386E-02	8.854E-02	1.490	7.514E-02
		15.600	0.1577	0.2244	10.754	0.9107
		9.177	3.187E-03	6.211E-02	1.484	1.698E-02
		5.527	3.372E-02	0.1932	1.680	0.3342
	0.925	8.440E+02	7.791E-02	7.883E-02	2.326	0.4742
		19.040	6.078E-02	0.1020	2.392	0.4920
		8.408	4.200E-02	0.1378	2.613	0.5428
		18.694	6.682E-02	0.1097	2.581	0.5357
		36.157	5.444E-02	7.489E-02	2.097	0.3990
0.975	9.855	1.405E-02	8.608E-02	46.340	0.9722	
	39.148	3.554E-02	5.354E-02	8.580	0.8490	
	5.623E+02	3.087E-02	3.208E-02	4.061	0.6757	
	11.504	1.117E-02	7.204E-02	6.358	0.7956	
	9.887	1.472E-02	8.653E-02	1.020E+02	0.9873	
0.875	0.025	2.434E+03	6.433E-03	7.254E-03	9.834E-05	0.4005
		2.285E+02	3.643E-03	1.240E-02	3.928E-04	0.9017
		2.007E+02	1.031E-03	1.100E-02	5.678E-05	0.5008
		2.706E+02	2.872E-03	1.026E-02	7.854E-05	0.4531
		2.072E+02	1.033E-04	9.755E-03	2.976E-05	0.2438

α_1	α_2/α_1	Term 1			Term 2	
		A_1	$\omega_{1,0}$	$\omega_{1,1}$	A_2	$\omega_{2,0}$
0.875	0.075	85.356	4.904E-03	2.833E-02	4.818E-04	0.1093
		59.696	1.440E-04	3.364E-02	3.789E-04	0.5015
		77.875	9.618E-03	3.529E-02	1.250E-03	0.6768
		1.773E+02	2.163E-02	3.291E-02	7.496E-03	0.9312
		62.777	7.264E-03	3.912E-02	1.922E-03	0.8252
	0.125	30.269	3.876E-03	6.993E-02	5.833E-03	0.8819
		31.032	2.044E-03	6.647E-02	2.917E-03	0.7878
		1.300E+02	2.411E-02	3.948E-02	2.303E-03	0.1501
		71.721	2.662E-02	5.449E-02	5.129E-03	0.7109
		35.202	9.388E-03	6.618E-02	4.396E-03	0.7898
	0.175	47.102	4.556E-02	8.795E-02	0.2720	0.9883
		26.121	1.633E-02	9.281E-02	9.465E-03	0.7706
		23.072	1.366E-02	0.1003	1.948E-02	0.8996
		63.885	3.249E-02	6.374E-02	5.366E-03	0.3259
		19.674	9.955E-04	0.1026	2.432E-02	0.9518
	0.225	46.630	3.563E-02	7.835E-02	8.432E-03	6.590E-02
		1.951E+02	7.582E-02	8.604E-02	3.134E-02	0.7960
		39.099	5.201E-02	0.1030	2.356E-02	0.7509
		29.669	2.061E-02	8.782E-02	6.644E-03	7.877E-02
		8.510E+02	6.313E-02	6.548E-02	1.080E-02	0.3203
0.275	48.808	5.566E-02	9.638E-02	1.584E-02	0.2163	
	13.029	1.693E-02	0.1700	9.003E-02	0.9408	
	40.979	4.889E-02	9.737E-02	1.482E-02	0.1247	
	16.420	4.388E-03	0.1259	6.973E-03	0.3249	
	17.660	3.695E-02	0.1498	3.541E-02	0.7851	
0.325	14.624	1.541E-02	0.1515	1.430E-02	0.2950	
	55.747	8.272E-02	0.1183	3.081E-02	0.4102	
	10.226	1.456E-02	0.2094	0.1773	0.9573	
	19.072	2.964E-02	0.1336	1.762E-02	4.879E-02	
	11.780	2.093E-02	0.1900	3.941E-02	0.7764	
0.375	12.115	1.370E-03	0.1654	1.341E-02	2.731E-02	
	47.206	8.780E-02	0.1295	3.974E-02	0.1924	
	3.308E+02	0.1243	0.1303	5.969E-02	0.5465	
	24.557	6.706E-02	0.1473	3.651E-02	0.2009	
	28.788	0.1169	0.1855	0.2586	0.9051	
0.425	10.706	2.583E-02	0.2103	3.558E-02	0.2834	
	54.290	0.1319	0.1680	9.405E-02	0.5793	
	19.169	7.219E-02	0.1742	5.319E-02	0.1747	
	10.166	6.606E-03	0.2013	2.365E-02	0.1131	
	13.061	4.370E-02	0.1941	4.294E-02	0.1830	

α_1	α_2/α_1	Term 1			Term 2	
		A_1	$\omega_{1,0}$	$\omega_{1,1}$	A_2	$\omega_{2,0}$
0.875	0.475	22.741	0.1571	0.2427	0.4790	0.8868
		14.689	7.201E-02	0.2036	7.560E-02	0.1073
		83.005	0.1972	0.2206	1.587	0.9648
		10.821	4.021E-02	0.2197	6.002E-02	3.098E-02
		6.266	2.002E-03	0.3181	0.1030	0.8137
	0.525	17.585	0.1019	0.2086	0.1264	2.109E-02
		38.833	0.1433	0.1921	0.1375	0.2429
		6.878	2.888E-02	0.3129	9.365E-02	0.5024
		10.977	8.444E-02	0.2595	0.1236	0.3661
		12.250	8.172E-02	0.2372	0.1137	0.1567
	0.575	57.148	0.1660	0.1980	0.2025	0.1542
		8.371	9.758E-02	0.3242	0.2324	0.5563
		7.038	0.1234	0.3937	2.462	0.9603
		6.401	3.726E-02	0.3372	0.1310	0.3873
		24.061	0.2132	0.2914	0.9314	0.8737
	0.625	8.665	0.1869	0.3990	7.854	0.9794
		6.006	0.1273	0.4365	1.750	0.9184
		5.109	6.320E-03	0.3772	0.1349	0.2173
		12.349	0.1279	0.2701	0.2829	0.1380
		6.378	9.800E-02	0.3892	0.3911	0.6352
	0.675	4.482	2.884E-02	0.4327	0.2875	0.3381
		13.547	0.1868	0.3139	0.5507	0.4958
		12.197	0.1623	0.3010	0.4600	0.3297
		8.532	0.1400	0.3421	0.4724	0.4158
		11.372	0.1665	0.3172	0.4954	0.4225
	0.725	7.063	0.1305	0.3474	0.6480	0.2775
		7.789	0.1956	0.4048	1.413	0.7378
		45.845	0.1996	0.2280	0.7071	1.433E-02
		3.765	8.098E-02	0.5328	1.198	0.7504
		13.322	0.2279	0.3490	1.162	0.6666
	0.775	83.672	0.2268	0.2421	1.014	0.2893
		3.286	4.859E-02	0.3884	0.9209	4.057E-02
		25.599	0.2575	0.3130	1.546	0.6257
		14.302	0.1785	0.2617	0.9869	0.1787
		18.549	0.2104	0.2823	1.063	0.3722
	0.825	24.639	0.2267	0.2735	1.748	0.5157
		9.379	0.1303	0.2086	1.356	6.636E-02
		9.192	0.1722	0.2921	1.512	0.4059
		7.935	0.1204	0.2012	1.373	1.075E-02
		4.274	0.1083	0.3739	1.504	0.4251

α_1	α_2/α_1	Term 1			Term 2	
		A_1	$\omega_{1,0}$	$\omega_{1,1}$	A_2	$\omega_{2,0}$
0.875	0.875	4.676	6.687E-02	0.2087	1.714	0.2198
		5.832	3.902E-02	0.1105	1.664	4.895E-02
		3.390	2.389E-03	0.1025	1.667	3.740E-03
		15.547	0.1398	0.1893	1.830	0.3276
		7.171	4.585E-02	0.1041	1.665	4.985E-02
	0.925	29.317	9.349E-02	0.1140	2.394	0.4162
		20.727	5.293E-02	7.744E-02	2.112	0.2936
		7.948	5.108E-02	0.1215	2.232	0.3546
		4.666	1.972E-02	0.1346	2.167	0.3243
		2.507	3.843E-02	0.3382	7.965	0.8433
	0.975	42.125	1.600E-02	2.733E-02	3.286	0.5366
		6.482	2.890E-02	0.1135	13.633	0.8935
		22.974	6.393E-02	8.790E-02	99.798	0.9855
		7.921	1.465E-02	8.013E-02	4.503	0.6710
		5.625	1.980E-03	9.433E-02	4.548	0.6745
0.925	0.025	8.407E+02	4.826E-03	7.205E-03	4.083E-05	0.4238
		2.380E+02	2.626E-03	1.103E-02	0.1398	0.9999
		2.596E+02	9.579E-05	7.801E-03	1.370E-05	0.8801
		2.670E+03	6.318E-03	7.067E-03	5.547E-05	0.5278
		2.789E+02	1.615E-06	7.172E-03	1.622E-05	0.9350
	0.075	1.627E+02	1.536E-02	2.765E-02	8.495E-04	0.7667
		92.055	6.930E-03	2.866E-02	3.494E-04	0.6735
		1.134E+02	1.248E-02	3.012E-02	9.966E-04	0.8315
		1.096E+02	4.220E-03	2.246E-02	1.332E-04	0.1716
		1.336E+02	1.288E-02	2.785E-02	6.369E-04	0.7185
	0.125	48.036	1.337E-02	5.500E-02	3.755E-03	0.9104
		1.104E+02	2.339E-02	4.151E-02	1.331E-03	0.5373
		2.752E+02	3.550E-02	4.277E-02	4.462E-03	0.8511
		63.350	1.714E-02	4.870E-02	1.501E-03	0.6940
		66.205	1.613E-03	3.182E-02	1.243E-04	0.1020
	0.175	43.863	5.235E-03	5.082E-02	4.816E-04	0.1348
		43.878	2.115E-02	6.671E-02	2.275E-03	0.5991
		38.545	5.165E-03	5.704E-02	5.673E-04	0.4539
		56.472	3.486E-02	7.025E-02	6.347E-03	0.8118
		30.925	6.135E-03	7.080E-02	2.752E-03	0.9003
0.225	30.543	2.736E-02	9.279E-02	5.137E-03	0.7013	
	27.755	1.966E-02	9.168E-02	3.667E-03	0.6809	
	22.517	1.539E-02	0.1042	5.253E-02	0.9845	
	67.977	3.498E-02	6.435E-02	3.346E-03	3.191E-02	
	23.496	6.382E-03	9.149E-02	4.802E-03	0.9135	

α_1	α_2/α_1	Term 1			Term 2	
		A_1	$\omega_{1,0}$	$\omega_{1,1}$	A_2	$\omega_{2,0}$
0.925	0.275	47.162	6.876E-02	0.1111	2.418E-02	0.8363
		19.948	1.079E-02	0.1110	3.767E-03	0.7580
		25.323	8.821E-03	8.776E-02	1.478E-03	0.2553
		36.370	4.937E-02	0.1043	8.657E-03	0.5841
		90.314	7.045E-02	9.254E-02	1.122E-02	0.6125
	0.325	36.986	6.692E-02	0.1208	1.387E-02	0.5532
		21.990	5.323E-02	0.1440	1.954E-02	0.7597
		19.016	9.447E-03	0.1146	2.425E-03	0.4649
		23.840	5.907E-02	0.1428	2.207E-02	0.7700
		26.917	5.512E-02	0.1292	1.275E-02	0.5806
	0.375	16.474	1.063E-02	0.1319	3.204E-03	0.3864
		3.634E+02	0.1070	0.1125	2.036E-02	0.4485
		2.452E+02	9.749E-02	0.1056	1.692E-02	0.2678
		34.377	7.905E-02	0.1369	1.861E-02	0.4689
		31.312	5.998E-02	0.1235	1.292E-02	0.1041
	0.425	17.030	6.972E-02	0.1865	2.741E-02	0.5992
		13.690	1.088E-02	0.1568	4.443E-03	0.4381
		16.808	3.867E-03	0.1228	1.897E-03	7.924E-02
		13.961	8.000E-02	0.2225	0.1721	0.9403
		18.472	6.459E-04	0.1089	1.055E-03	6.468E-02
	0.475	11.717	9.631E-02	0.2657	1.706	0.9911
		32.515	0.1207	0.1815	4.497E-02	0.4951
		65.824	0.1194	0.1494	3.582E-02	0.1845
		1.155E+02	0.1457	0.1628	4.935E-02	0.5141
		10.270	6.543E-03	0.2011	1.057E-02	0.8251
	0.525	10.522	1.073E-03	0.1910	4.133E-03	0.6321
		10.824	2.078E-02	0.2047	1.103E-02	0.1815
		13.009	0.1091	0.2609	8.509E-02	0.7028
		19.322	0.1101	0.2119	5.087E-02	0.3523
		1.381E+02	0.2177	0.2319	1.840	0.9821
	0.575	6.381	4.462E-02	0.3561	1.515	0.9917
		11.273	0.1589	0.3328	0.9539	0.9583
		8.249	2.354E-02	0.2648	1.863E-02	0.4657
		32.941	0.2196	0.2789	0.6207	0.9231
		29.957	0.1376	0.2017	7.990E-02	4.525E-03
	0.625	66.910	0.2563	0.2851	0.4056	0.8166
		8.636	0.1178	0.3434	0.1358	0.6180
		15.756	0.1891	0.3116	0.2224	0.6875
		11.613	0.1809	0.3476	0.3449	0.8141
		18.597	0.1520	0.2545	0.1164	0.1977

α_1	α_2/α_1	Term 1			Term 2	
		A_1	$\omega_{1,0}$	$\omega_{1,1}$	A_2	$\omega_{2,0}$
0.925	0.675	17.385	0.1891	0.2962	0.2008	0.3124
		21.565	0.2447	0.3321	0.3758	0.6930
		6.832	0.1685	0.4490	0.8686	0.9038
		16.579	0.1731	0.2834	0.1945	0.1180
		56.400	0.2395	0.2727	0.2334	0.4320
	0.725	4.967	8.692E-02	0.4714	0.1973	0.5412
		3.816	3.525E-02	0.5514	0.7998	0.9623
		1.422E+02	0.2606	0.2728	0.3519	0.2139
		27.868	0.2728	0.3373	0.4552	0.5528
		8.619	0.1949	0.4067	0.3838	0.5470
	0.775	5.585	0.2009	0.5103	0.8060	0.6627
		10.108	0.3148	0.4824	2.681	0.8859
		0.5330	0.4051	1.000	5.866	0.1725
		2.026E+02	0.3743	0.3826	1.487	0.7820
	0.825	4.034	6.393E-02	0.5191	0.2381	0.3105
		23.973	0.2756	0.3211	1.124	0.1924
		4.832	0.1893	0.4619	1.033	0.3389
		43.980	0.3340	0.3651	1.317	0.5189
		2.533	8.688E-02	0.5386	0.8875	3.599E-02
	0.875	12.190	0.2517	0.3303	1.149	9.363E-02
6.805		0.2527	0.3929	2.116	0.5057	
8.679		0.1712	0.1938	1.827	1.277E-02	
2.326		0.1223	0.5796	2.028	0.5385	
1.150		7.795E-02	0.3238	1.799	4.557E-02	
0.925	7.395	0.1703	0.1999	1.822	2.294E-02	
	5.143	1.824E-02	5.899E-02	2.197	0.1851	
	11.763	1.155E-02	2.755E-02	2.181	0.1692	
	4.963	8.605E-02	0.1532	2.321	0.2821	
	1.679	1.858E-02	0.2088	2.296	0.2682	
0.975	3.145	0.1019	0.2415	2.507	0.3773	
	4.815	1.866E-02	8.316E-02	3.865	0.5629	
	3.378	2.814E-02	0.1290	4.687	0.6460	
	3.537	1.783E-02	0.1096	4.168	0.5980	
	2.017	4.021E-03	0.1797	5.329	0.6912	
0.975	2.529	5.297E-02	0.2058	20.344	0.9207	
	1.979E+03	3.190E-03	4.200E-03	4.591E-06	0.4080	
	3.462E+03	3.490E-03	4.068E-03	4.711E-06	0.2569	
	8.875E+02	3.766E-03	6.019E-03	2.697E-05	0.9180	
	4.097E+03	4.089E-03	4.578E-03	1.055E-05	0.7448	
7.091E+02	3.360E-03	6.181E-03	1.960E-05	0.8773		

α_1	α_2/α_1	Term 1			Term 2	
		A_1	$\omega_{1,0}$	$\omega_{1,1}$	A_2	$\omega_{2,0}$
0.975	0.075	2.363E+02	9.325E-03	1.779E-02	3.051E-04	0.9490
		2.336E+02	3.393E-03	1.195E-02	5.405E-05	0.9721
		2.356E+02	6.020E-03	1.451E-02	2.709E-05	0.6344
		2.731E+02	3.497E-03	1.082E-02	6.815E-06	0.3526
		2.851E+02	6.725E-03	1.374E-02	2.775E-05	0.3880
	0.125	2.372E+02	1.482E-02	2.325E-02	1.161E-04	0.4198
		2.243E+02	2.084E-02	2.976E-02	9.448E-04	0.9255
		1.498E+02	5.392E-03	1.874E-02	3.590E-05	0.8921
		2.268E+02	1.706E-02	2.588E-02	1.843E-04	0.6275
		1.619E+02	6.926E-03	1.928E-02	2.634E-05	0.3883
	0.175	89.189	1.898E-02	4.140E-02	9.708E-04	0.9264
		1.715E+02	2.369E-02	3.535E-02	3.280E-04	0.5587
		1.018E+02	1.002E-02	2.966E-02	6.790E-05	0.6533
		3.615E+02	3.153E-02	3.706E-02	7.070E-04	0.7617
		6.598E+02	3.222E-02	3.526E-02	6.108E-04	0.7123
	0.225	3.281E+02	4.729E-02	5.339E-02	1.533E-02	0.9806
		86.480	2.409E-02	4.722E-02	4.156E-04	0.5985
		1.497E+02	3.534E-02	4.869E-02	8.444E-04	0.6808
		3.687E+02	3.168E-02	3.710E-02	4.429E-04	0.1989
		76.485	1.596E-02	4.211E-02	1.809E-04	0.5931
	0.275	3.319E+02	6.065E-02	6.667E-02	0.5773	0.9992
		60.194	3.845E-02	7.167E-02	1.170E-02	0.9762
		53.591	2.005E-02	5.737E-02	9.132E-04	0.9171
		59.673	2.194E-02	5.545E-02	3.862E-04	0.6616
		95.743	2.803E-02	4.891E-02	4.834E-04	0.1333
	0.325	80.237	4.903E-02	7.395E-02	1.730E-03	0.6508
		45.576	4.290E-02	8.678E-02	3.570E-02	0.9898
		50.594	2.460E-02	6.413E-02	4.482E-04	0.6031
		2.683E+02	5.316E-02	6.062E-02	1.308E-03	0.3856
		44.630	2.448E-02	6.929E-02	9.902E-04	0.8758
	0.375	44.740	4.703E-02	9.172E-02	2.252E-03	0.7452
		51.467	2.528E-02	6.413E-02	4.183E-04	0.1768
		1.187E+02	7.822E-02	9.506E-02	1.009E-02	0.8976
		88.170	7.837E-02	0.1010	4.853E-02	0.9793
		96.565	8.030E-02	0.1010	3.338	0.9997
	0.425	36.055	4.177E-02	9.722E-02	1.490E-03	0.6399
		45.456	3.517E-02	7.915E-02	8.751E-04	0.1374
		46.897	2.331E-02	6.595E-02	3.678E-04	4.040E-03
		36.243	3.982E-02	9.499E-02	1.303E-03	0.6230
		46.491	2.123E-02	6.424E-02	2.712E-04	0.1210

α_1	α_2/α_1	Term 1			Term 2	
		A_1	$\omega_{1,0}$	$\omega_{1,1}$	A_2	$\omega_{2,0}$
0.975	0.475	36.725	3.543E-02	8.987E-02	8.667E-04	0.2300
		46.140	8.379E-02	0.1271	7.134E-03	0.7546
		42.000	4.315E-02	9.073E-02	1.444E-03	1.166E-02
		42.541	9.671E-02	0.1437	0.5964	0.9970
		47.133	1.712E-02	5.955E-02	1.403E-04	5.555E-02
	0.525	25.845	3.972E-02	0.1171	1.526E-03	0.7395
		29.542	3.176E-02	9.945E-02	6.507E-04	0.5456
		26.957	3.142E-02	0.1056	1.437E-03	0.8831
		30.076	3.609E-02	0.1026	8.603E-04	0.4039
		31.051	2.438E-02	8.879E-02	5.622E-04	0.8535
	0.575	35.591	7.286E-02	0.1289	4.299E-03	8.151E-02
		1.402E+02	0.1089	0.1231	7.010E-03	0.1883
		24.480	8.698E-02	0.1686	8.938E-03	0.7410
		28.386	2.647E-02	9.692E-02	4.769E-04	0.7851
		26.287	3.041E-02	0.1065	6.752E-04	0.7503
	0.625	36.597	0.1132	0.1677	9.840E-03	0.4104
		24.700	8.184E-02	0.1627	5.542E-03	0.3585
		25.360	7.135E-02	0.1501	4.367E-03	0.1668
		21.095	4.752E-02	0.1423	1.705E-03	0.5581
		25.193	3.916E-02	0.1185	1.006E-03	0.1865
0.675	32.861	2.097E-02	8.183E-02	1.257E-04	0.2115	
	25.805	0.1254	0.2026	1.400E-02	0.4715	
	30.101	2.290E-02	8.934E-02	1.504E-04	0.4423	
	17.719	4.417E-02	0.1570	2.407E-02	0.9885	
	31.049	2.118E-02	8.559E-02	1.295E-04	0.7078	
0.725	16.036	8.502E-02	0.2095	6.747E-03	0.3497	
	5.366E+02	0.1813	0.1850	2.539E-02	0.1012	
	17.830	0.1188	0.2305	1.413E-02	0.3995	
	14.872	5.394E-02	0.1884	7.347E-03	0.9340	
	21.836	3.320E-02	0.1248	4.373E-04	0.4615	
0.775	26.662	2.502E-02	0.1000	1.600E-04	8.419E-02	
	14.273	0.1146	0.2539	1.518E-02	0.2157	
	23.295	2.769E-02	0.1135	2.181E-04	0.7573	
	10.639	0.1457	0.3329	5.765E-02	0.8631	
	13.760	8.342E-02	0.2284	6.583E-03	0.2568	
0.825	8.415	0.1593	0.3956	6.131E-02	0.8099	
	24.451	2.530E-02	0.1071	1.033E-04	0.7430	
	54.042	0.3119	0.3480	0.1413	0.6438	
	59.039	1.001E-02	4.388E-02	2.485E-06	0.4302	
	4.178E-02	0.1534	1.000	12.140	0.1613	

α_1	α_2/α_1	Term 1			Term 2	
		A_1	$\omega_{1,0}$	$\omega_{1,1}$	A_2	$\omega_{2,0}$
0.975	0.875	17.600	3.619E-02	0.1498	2.911E-04	1.943E-02
		5.562	0.2133	0.5686	1.153	0.9796
		9.119	9.229E-02	0.3106	9.253E-03	3.939E-02
		12.248	5.490E-02	0.2181	1.047E-03	0.3695
		5.999	0.1680	0.4992	0.1038	0.8756
	0.925	5.153	0.3899	0.5849	1.147	0.1328
		3.923	0.1951	0.6956	0.1005	0.6415
		33.035	1.784E-02	7.838E-02	2.689E-06	0.5513
		4.189	0.1688	0.6429	4.776E-02	0.7034
		37.126	1.587E-02	6.974E-02	8.831E-06	0.9649
	0.975	1.682	8.906E-02	0.1508	3.924	0.5168
		6.823	0.1068	0.1217	3.899	0.5130
		1.263	0.1205	0.2234	4.223	0.5572
		1.068	2.153E-02	9.694E-02	3.697	0.4808
		0.5512	1.881E-02	0.1973	3.862	0.5077

Curriculum vitae

Name: Sebastian Kelma
Date of birth: 16. Oktober 1985
Place of birth: Bad Oldesloe

Education

2004 Abitur (general qualification for university entrance) at the Wilhelm-Raabe-Schule in Lüneburg
2005-2011 Studies of aerospace engineering at the Universität Stuttgart
Final degree: Diplom-Ingenieur
2023 Promotion at the Institute for Steel Construction of the Gottfried Wilhelm Leibniz Universität Hannover
Final degree: Doktor-Ingenieur

Working experience

2012-2018 Research associate at the Institute for Steel Construction of the Gottfried Wilhelm Leibniz Universität Hannover
since 2019 Project engineer at Jörss - Blunck - Ordemann GmbH in Osnabrück